Anal. Methods Environ. Chem. J. 8 (1) (2025) 5-25

AMECJ

Research Article, Issue 1
Analytical Methods in Environmental Chemistry Journal
Journal home page: www.amecj.com/ir

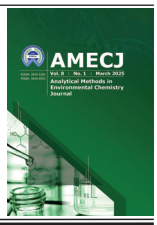

Efficient adsorption of malachite green from wastewater using agricultural biosource waste: Kinetic, isothermal, thermodynamic studies and mechanisms analysis

Smail Imame[a], Hafssa Atlas[a], Mohamed Sadoq[a], Abderahim Kali[a], Abdelouahed Amar [a] and Fatima Boukhlifi[a,*]
[a] *Laboratory of Chemistry and Biology Applied to the Environment, URL-CNRST-N◦13, Faculty of Sciences, Moulay Ismail University, Meknes 50050, Morocco.*

ARTICLE INFO:
Received 7 Nov 2024
Revised form 12 Jan 2025
Accepted 15 Feb 2025
Available online 29 March 2025

Keywords:
Malachite green,
Adsorption,
UV-Vis spectrophotometry,
Sugarcane bagasse

ABSTRACT
Adsorption on biomass has gained popularity recently as a method for reducing pollutants in wastewater before release. This work investigates the adsorption of malachite green (MG) onto sugarcane bagasse (SCB). To optimize the process, the mass of the bio-adsorbent, contact time, temperature, and pH of the MG solution were investigated with the adsorbate and the adsorbent. The observed results indicate that MG adsorption on SCB is more effective in the environment because of the electrostatic interactions between the organic cations of the dye and the negatively charged SCB surface in this pH range. In ideal circumstances, SCB removes 97% of MG. The adsorption of MG on SCB is better described by the pseudo-second-order model, according to adsorption kinetics modeling. UV-Vis spectrophotometers were used to analyze the fluids under study and determine the dye concentration. Malachite green has a limit of quantification (LOQ) of 0.1 mg L^{-1} and a limit of detection (LOD) of 0.06 mg L^{-1} using UV-Vis spectrophotometry. The measuring range of the procedure is 0.1 to 30 mg L^{-1}, which guarantees precise and repeatable results. According to adsorption isotherm modeling, the Freundlich and Langmuir models best describe MG's adsorption on SCB. Given that both the Freundlich parameter 1/n and the Langmuir separation coefficient RL are smaller than 1, it is clear that MG's bio-adsorption on SCB is beneficial. The study's findings demonstrate that SCB, an underutilized agricultural waste, is a reasonably priced bio-adsorbent with a substantial capability for treating wastewater that contains dyes.

1. Introduction

Due to various agricultural practices and industrial and domestic activities, the textile industry's intensive consumption of large quantities of water and chemicals, particularly synthetic dyes, has had a negative impact on aquatic ecosystems and the wider environment [1-3]. Dyes can be measured using UV–Vis spectrometry. The absorbance value ranges from zero to 2. When no light is absorbed, P0 equals P, and transmittance equals one. Consequently, absorption is zero. If the light absorption and transmission are 90% and 10%, respectively, resulting in T = 0.1 (absorbance =1). The resulting spectrum is a graph of absorbance against wavelength. This UV–Vis spectrophotometer range was from 200 to 800 nm. The wavelength of light that different colored

*Corresponding Author: Fatima Boukhlifi
Email: f.boukhlifi@umi.ac.ma
https://doi.org/10.24200/amecj.v8.i01.359

dyes absorb varies. Most dyes are conjugated substances with alternate double and single bonds and generally absorb light in the visible spectrum. Dyes have a narrower energy gap, and electrons are excited by lower-energy light at visible light. Measure the object's spectral reflectance before using a UV–Vis spectrophotometer to assess color. Fluorescein and indigo dye are studied using UV–Vis absorption spectroscopy [3]. Since these chemicals require treatment to lower the pollutant concentration before being released into the atmosphere, they are frequently highly harmful since they are difficult for effluents to biodegrade [4,5]. Malachite Green (MG) is a cationic dye that is extensively utilized in several industries, including the fish business, food additives, paper, leather, wool, and silk dying, as well as distilleries [6]. Although, Malachite green (MG) is harmful to the immunological and reproductive systems and can cause cancer, genotoxicity, mutagenicity, and teratogenicity in fish [6,7]. MG in any fish intended for consumption is severely prohibited in the United States and the European Council due to its excessive buildup in fish tissue [6]. Furthermore, by changing the water's color and lowering the amount of sunlight that reaches the surface, the discharge of MG into nearby waters may modify the environment. Water-soluble MG can, nevertheless, have detrimental effects even at low concentrations, including the suffocation of aquatic vegetation and the development of cancer, mutagenesis, and teratogenic effects in humans [8]. Numerous techniques, including biological treatment for biodegradable pollutants, coagulation-flocculation, electrochemical treatment, nanofiltration, ion exchange, and adsorption, can be used to remove contaminants from wastewater [9,10]. Because of the adsorption process's cost, efficiency, simplicity, and adaptability benefits are utilized increasingly frequently [11-14]. Various agricultural wastes have been employed as biosorbents for wastewater treatment. These include rice husk derivatives [15] which was used to remove crystal violet (CV), nostoc Linckia [15]which was used to remove crystal violet (CV), coffee black [16], argan shell [17]the wood powder from the shell of Argan nuts was used in raw form, or modified form by Sodium hydroxide, as a new economic and ecologic adsorbent. The effectiveness of these materials was evaluated on Methylene Blue (MB), marine macroalga sargassum muticum [18]which has prompted greater research into effective and sustainable removal techniques. Even though there have been major efforts in the previous few decades, more study is still necessary to fully examine the long-term performance and usable applicability of adsorbents and different adsorption techniques for the removal of dye. In the present study, a brown marine macroalga Sargassum muticum was used as an effective and sustainable biosorbent for the crystal violet (CV), and brown seaweed [18] which has prompted greater research into effective and sustainable removal techniques. Even though there have been major efforts in the previous few decades, more study is still necessary to fully examine the long-term performance and usable applicability of adsorbents and different adsorption techniques for the removal of dye. In the present study, a brown marine macroalga Sargassum muticum was used as an effective and sustainable biosorbent for the crystal violet (CV). The fibrous waste left behind after sugarcane is crushed to extract juice in sugar mills and refineries, known as bagasse, has been the subject of numerous scientific investigations highlighting its potential use [17,19]. The material's favorable qualities, including biodegradability, availability, buoyancy, and low cost, have shown it to be successful in eliminating pollutants from wastewater, including heavy metals and dyes. Furthermore, it mainly comprises cellulose, hemicellulose, and lignin, which have polymer structures rich in hydroxyl and carboxyl groups that interact with the chemical contaminants in the treated solution [20-22]. This work aims to investigate and examine the inherent ability of sugarcane bagasse to extract Malachite green by examining the effects of different experimental settings on the adsorption process. These parameters include mass and contact time, solution pH, and temperature. To illustrate

the feasibility of the process, thermodynamic parameters, such as enthalpy, entropy, and free energy, were determined. The thermodynamic characteristics demonstrate the spontaneous nature of the MG adsorption process on SCB.

2. Materials and methods

2.1. Materials

The dye considered in this study is a green color called malachite green or diamond green B (CAS N.: 2437-29-8, CHEMICALS, India) [23]. It was first prepared by Hermann Fischer in 1877. Its molecular structure is shown in Figure 1. It was used as supplied. The colored solutions at varying concentrations were prepared by dilution from a stock solution of 23 mg L^{-1} using distilled water. Analytical-grade chemicals were used for all experiments. Hydrochloric acid (HCl, 99% CAS N.: 7647-01-0) and sodium hydroxide (NaOH, 99%, CAS N.: 1310-73-2) were acquired from Sigma-Aldrich (Saint-Quentin-Fallavier, France).The main characteristics of the dye are described in Table 1.

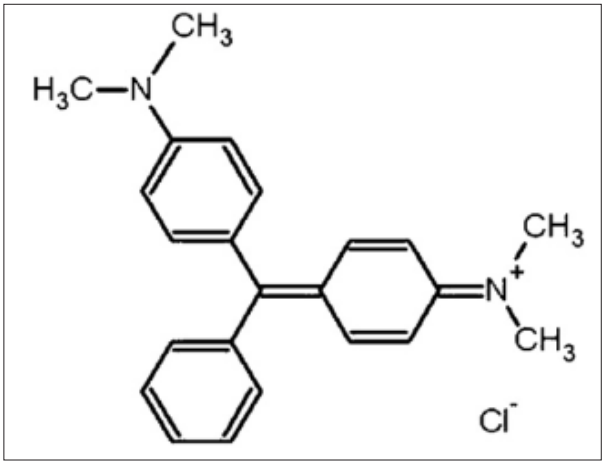

Fig. 1. The chemical structure of the MG [6].

Table 1. Physico-chemical properties of MG

Parameters	Characteristics
Molecular formula	$C_{52}H_{54}N_4O_{12}$
Molecular weight	927.03 $g.mol^{-1}$
Absorption maxima	618.0 nm
Commercial name	Malachite Green oxalate (MG) Green
Appearance	crystalline powder

2.2. Characterization Techniques

The powder X-ray diffraction patterns (XRD) of the sample were collected with a Bruker AXS model (D8-advance A25) diffractometer using Cu-K_α foundation (λ = 1.5418 Å) at 40 Kv, 20 mA, and a scan range 5–70. XRD results were recorded in the 2θ range between 2° and 70° in 0.02° angle increments. Infrared spectra were performed using a Shimizu IRAFFINIY-1S Fourier transform spectrometer (FTIR) equipped with a detector (TGS) and a ceramic source, separated by an optical system using a Michelson interferometer. The samples were prepared as 12 mm diameter pellets with a mass of 3 mg of solid diluted in 97 mg of KBr. Absorption spectra were analyzed with a resolution of 20 cm^{-1} in the wavelength range between 400 and 4000 cm^{-1}. UV-visible spectrophotometry is a qualitative and quantitative analysis method that identifies a chemical species's presence and concentration. For this purpose, the spectrophotometer used is of the type (SHIMADZU-UV 1800) that allows the measurement of the absorbance of a solution at a precise wavelength in the range between (190 to 900 nm) from the concentrations deduced from the Beer-Lambert law: $A = \varepsilon . \ell . C$.

The point of zero charge corresponds to the pH level at which the solid's surface charge becomes neutral; it was determined by the method of addition of solid [24]due to their low cost, availability, cost-effectiveness, and efficiency. In this study, we were interested in the elimination of crystal violet dye, from aqueous solutions, by adsorption on almond shell-based material, as a low-cost and ecofriendly adsorbent. The almond shells were first analyzed by Fourier transform infrared spectroscopy (FTIR). The specific surface of the solid material corresponds to its overall surface per mass unit; it was determined by the method of adsorption of methylene blue.

2.3. Preparation of the solid

Sugar cane bagasse was used as a bio-sorbent in this study. It was collected from a local vendor after the sugar cane had been crushed to extract

the sugar cane juice. It was then washed several times with water to remove dirt. The final rinses were carried out with distilled water to remove chemical residues such as salts and other soluble substances, then dried at 60°C for 24 hours. After drying, the dried sugarcane bagasse was ground using a grinder (mark: FRITSCH, Germany). They were then sieved using a sieve shaker (mark: FRITSCH, Germany), and the particle size used was determined to be less than or equal to 0.2 mm. The final product is stored for experimental studies.

2.4. Adsorption procedure

All the experiments in this work were conducted in the same experimental setup, except for the study of the effect of temperature, in which a water bath was used to set the temperature to the desired value. For this purpose, a series of samples is prepared by suspending a precise quantity in mg of the biomass in a volume of 20 mL of an aqueous solution of the green dye malachite of known initial concentration C_0 (2.5×10^{-5} M). The suspensions are then stirred for a time (t) ranging from 5 to 70 minutes. After this time, the supernatant was extracted by centrifugation. The solution was analyzed by UV-visible spectrophotometry at a wavelength of 618.0 nm. The determination of the adsorbed amounts of MG is performed from the calibration line (Scheme 1).

The adsorbed amounts are calculated using the following Equation 1.

$$q_{ads} = \frac{(C_0 - C_e),\ V}{m}$$

(Eq. 1)

Where C_0 and Ce are the initial and equilibrium concentration of the dye in mg L^{-1}, respectively; m is the mass of the solid in g; V is the volume of the dye solution MG in L, and quads is the adsorbed amount per gram of adsorbent in mg g^{-1}.

2.5. Modeling of adsorption kinetics

To interpret the MG adsorption on SCB experimental data. Three kinetic models were utilized: intra-particle diffusion, pseudo-second-order (PSO), and pseudo-first-order (PPO).

2.5.1.Pseudo-first-order model

The pseudo-first-order model is given by Lagergren, which is expressed by the following Equation 2 [25].

$$\frac{dqt}{dt} = K_1(q_e - q_t)$$

(Eq. 2)

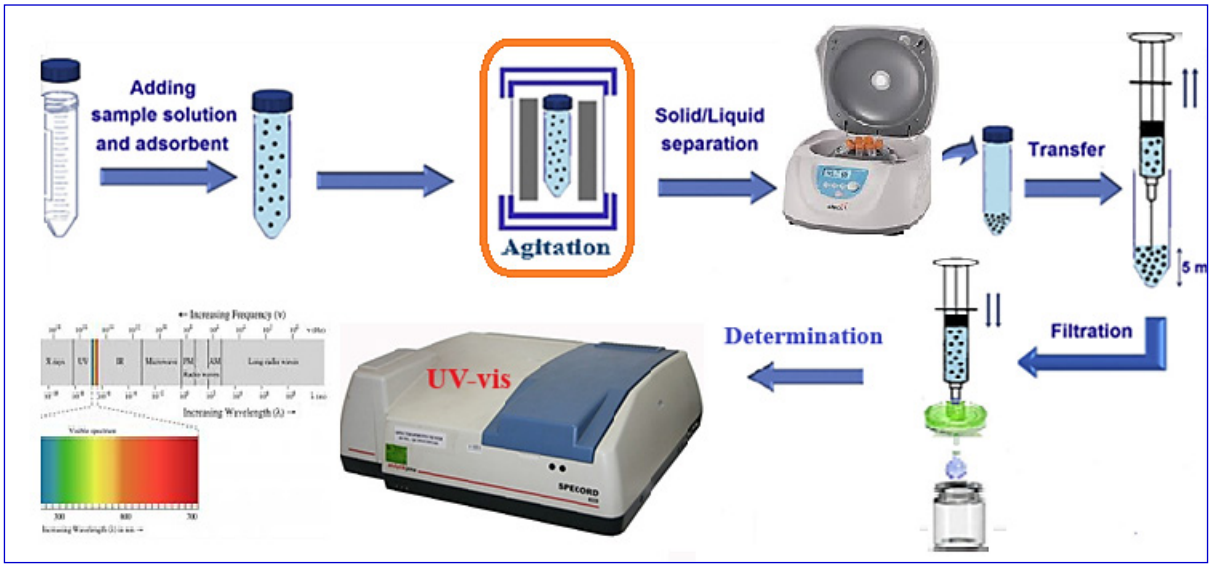

Scheme 1. Procedure for separating MG on SCB by UV-visible.

Where k_1 is the first order reaction rate constant of adsorption of MG on BCS in (min^{-1}), q_e, q_t the amount of MG adsorbed at equilibrium and at time t in (mg g^{-1}), t the contact time in (min).
After integration with initial conditions q_{t0} at t = 0, Equation 3 was obtained. For the representation of Log (qe-qt) = f(t), we obtain a line that gives k_1 and qe.

$$q_t = q_e(1 - e^{K_1 t})$$

(Eq. 3)

2.5.2. Pseudo-second order model

The following expression gives the pseudo-second-order model in Equation 4 [26].Where K_2 is the second-order reaction rate constant of adsorption of MG on SCB in ($g.mg^{-1}.min^{-1}$).

$$\frac{dqt}{dt} = K_2(q_e - q_t)^2$$

(Eq. 4)

After integration of Equation 4, we obtain Equation 5. The linearization of the Equation 5 gives Equation 6.

$$q_t = \frac{K_2 q_e^2 t}{K_2 q_e t + 1}$$

(Eq. 5)

$$\frac{t}{q_t} = \frac{1}{K_2 q_e^2} + \frac{1}{q_e} t$$

(Eq. 6)

The representation of t/qt = f(t) allows us to obtain a line from which we determine k_2 and q_e.

2.5.3. Intra-particle diffusion model

The intra-particle diffusion is described by Equation7 by Weber and Morris [27]. The K_d is the intra-particle diffusion rate constant in (mg g^{-1} $min^{0.5}$), and C is the boundary layer thickness in (mg g^{-1}). In Equation 7, the representation of qt = f ($t_{1/2}$) (allows to calculate k_d and C.

$$q_t = K_d t^{1/2} + C$$

(Eq. 7)

2.6. Thermodynamic parameters

The thermodynamic parameters (ΔG°), (ΔH°), and (ΔS°) for the studied system (MG/SCB) were determined and calculated at different temperatures (25°C, 35°C and 45°C). The adsorption-free energy (ΔG°) is calculated according to the standard Gibbs formula defined by Equation 8.

$$\Delta G° = - RT \ln (K_d),\ K_d = \frac{q_e}{Ce}$$

(Eq. 8)

q_e (mg g^{-1}) represents the amount of adsorbed dye at equilibrium, and Ce (mg L^{-1}) is the residual concentration of the adsorbate at equilibrium.
Also, the thermodynamic parameters of adsorption of the MG on the adsorbent can be estimated from the curve representing the variation ln (K_d) as a function of 1/T, which was shown in Equation 9.

$$\ln K_c = \frac{\Delta S^\circ_{ads}}{R} - \frac{\Delta H^\circ_{ads}}{RT}$$

(Eq. 9)

The values of (ΔH°_{ads}) and (ΔS°_{ads}) are calculated from the slope and intercept of the line obtained by plotting ln (K_c) versus $\frac{1}{T}$, respectively.

2.7. Modeling of adsorption isotherms

2.7.1. Langmuir Isotherm Model

The Langmuir model was initially employed for systems featuring monolayer adsorption occurring on the surface of the adsorbent. This model assumes that all adsorption sites are identical, do not depend on surface coverage, and take place without lateral interaction with the adsorbate molecules. The following Equation 10 represents this model. In equation 10, qm is the maximum

adsorbed quantity in mg g^{-1}, and K_l is the Langmuir constant in L mg^{-1}. To determine the adsorption parameters of this model, we use the linear form of the Langmuir isotherm, represented by Equation 11. In addition, among the essential characteristics of the Langmuir isotherm is the separation factor $R_{L,}$ defined by Equation 12.

$$q_e = \frac{q_m.K_l.C_e}{1+K_l.C_e}$$

(Eq. 10)

$$\frac{1}{qe} = \frac{1}{K_l.q_m.C_e} + \frac{1}{q_m}$$

(Eq. 11)

$$R_l = \frac{1}{1+K_l.C_e}$$

(Eq. 12)

With: C_i is the initial concentration of the dye (mg L^{-1}) and K_L the Langmuir constant (Lmg^{-1}). Values of R_L indicate the shapes of isotherms to be either unfavorable ($R_L > 1$), linear ($R_L = 1$), favorable ($0 < R_L < 1$) [28].

2.7.2. Freundlich Isothermal Model

The Freundlich empirical model is founded on adsorption on heterogeneous surfaces and is represented by Equation 13. The linearization of this equation implies a passage of the terms in logarithmic form.

$$\text{Log}\,(q_e) = \text{Log}(K_f) + \frac{1}{n}\text{Log}(C_e);\ \ q_e = K_F.\ C_e^{1/n}$$

(Eq.13)

Where qe is the amount adsorbed at equilibrium, C_e is the residual concentration of the dye at equilibrium, and n represents the adsorption intensity and indicates whether the adsorption is favorable. If n<1 linear adsorption, if n>1 physical adsorption is favorable [29]. the linear form of the isotherm by plotting Log qe = f(LogCe).

2.7.3. Temkin Isothermal Model

The Temkin isotherm is derived assuming that the decline in adsorption heat follows a linear trend, unlike the logarithmic decrease presumed by the Freundlich equation. Generally, the Temkin isotherm is expressed by Equation 14 [30].

$$q_e = \frac{R.T}{b_T}.\ \text{Ln}(A_T.C_e)$$

(Eq.14)

The b_T and A_T are Temkin isotherm constants, R is the perfect gas constant (8.314 $KJmol^{-1}$), Ce is the equilibrium concentration of dye ions (mg L^{-1}), and T is the absolute temperature.

3. Results and discussion

3.1. Characterizations

3.1.1. XRD Analysis

The XRD diffractogram of sugarcane bagasse is shown in Figure 2. The SCB is mainly composed of lignin, cellulose, and hemicelluloses. The two peaks detected have values of 2ɵ around 16 and 22 due to the semi-crystalline structure of the cellulose contained in the biomass [31]. Moreover, the XRD spectrum resembles that of other lignocellulosic residues [32].

3.1.2. FT-IR analysis

Fourier transform infrared spectroscopy was utilized to analyze the SCB solid, and the resulting FT-IR spectrum is presented in Figure 3. The FT-IR spectra of BCS show the presence of many functions on the surface of the adsorbent such as: The strong band appearing at 3374 cm^{-1}, is attributed to OH groups (alcohols, phenols, and carboxylic acids) [33,34]. The band at 1732 cm^{-1} is characteristic of the stretching vibration of the C=O of xylan carboxylic acids present in hemicelluloses [23].The bands at 1611 cm^{-1} ant 1640 cm^{-1} is attributed to the C=C deformation (aromatic of lignin) [35], thus the band at 1370 cm^{-1} confirms

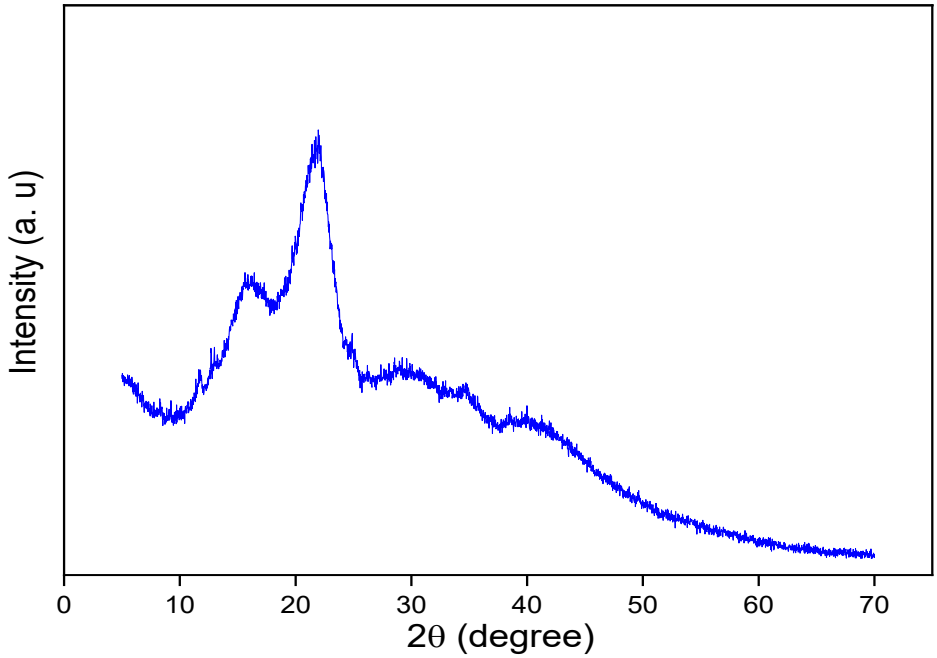

Fig. 2. Powder XRD patterns of SCB.

the presence of methoxy -C-O groups of lignin [36], the bands at 1250 and 1052 cm^{-1} are attributed to the stretching vibration of the C-O bonds of the aromatic compounds and the acid, alcohol, phenol, ether, and ester functions [33],830 cm^{-1} due to the vibration of the aromatic C-H bond, corresponding to the polysaccharides and lignin [37], and the band appears at 606 cm^{-1} due to the elongation of the C-X bond (alkyl halide) [33].

3.1.3.Point of zero charge

In this work seven vials were prepared, each containing 50 ml of sodium chloride NaCl (10^{-3} M). The pH of these vials is adjusted to the initial pH (values between 2 and 12) by adding NaOH or HCl solution (0.1M). After the initial pH adjustment, 100 mg of the solid was added to each vial. The suspensions were kept under stirring, at room temperature, for 24 h, and the final pH was measured.

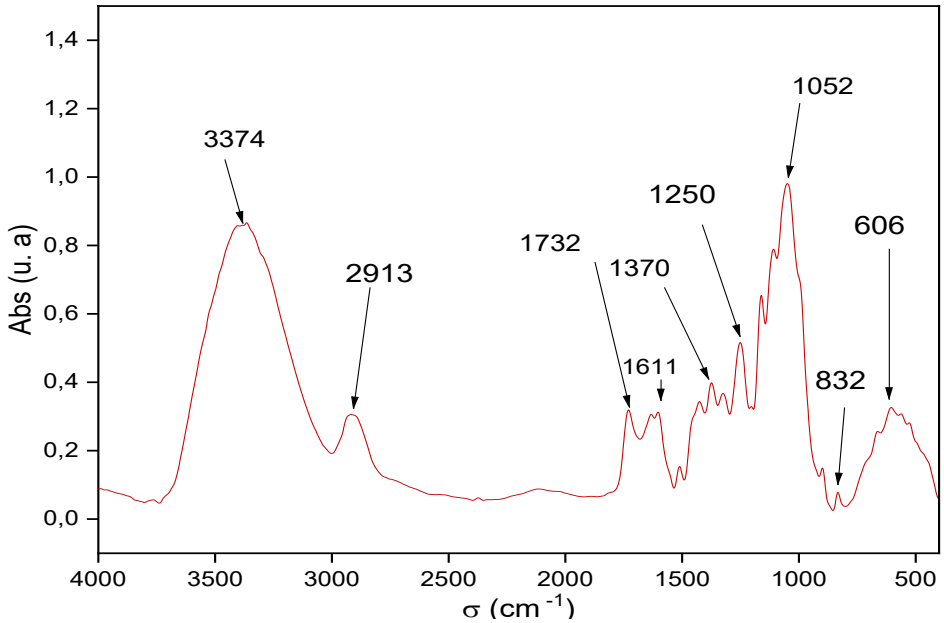

Fig. 3. FT-IR spectra of the BCS solid

The representation of ΔpH = f(pHi) a determines the pH_{pzc} value. The latter results from the intersection of the curve with the x-axis [38]. The representation of ΔpH = f(pHi) a allows us to determine the value of pHpzc, which is ulster in Figure 4. It shows that the pH value at which the solid surface has zero charge corresponds to pH = 7.3, so the solid surface is opposing at pH > 7.3 and positive below pH = 7.3.

3.1.4.Determination of the specific surface

The specific surface area of SCB was determined by the methylene blue adsorption method, which consists in studying the adsorption of methylene blue. A precise mass in mg of the biomass was suspended in a volume of the aqueous solution of methylene blue of known initial concentration, and the kinetics of the process were followed until a maximum value of the adsorption capacity was obtained. The specific value is calculated by Equation 15 [39]. The value of S_{BM} was obtained at 28.44 $m^2 g^{-1}$.

$$S_{BM} = q_m.N_A.S \quad (Eq.15)$$

With SBM: specific surface determined by BM adsorption (m^2g^{-1}); qm: maximum adsorbed quantity (mol g^{-1}); S: the surface of a BM molecule (175 $Å^2$); N_A: Avogadro number.

3.2. Study of MG adsorption on BCS

Various parameters influencing the adsorption phenomenon are examined: the mass of the adsorbate, the solution's initial pH, the adsorbent-adsorbate contact time, and the solution temperature.

3.2.1.Effect of adsorbent mass.

Different adsorbent masses ranging from 0.01 to 0.1 g are added to individual 20 mL samples of an aqueous solution containing 2.5×10^{-5} M of the dye to determine the optimal quantity of adsorbent required to remove the highest amount of dye. The solution is then stirred magnetically for 60 minutes until the adsorption equilibrium is reached. The findings of this experiment are presented in Figure 5. Also, Figure 5 shows that the percentage of dye removal increases with the mass of the bio-adsorbent and a stabilization of the adsorption rate beyond a mass of 50 mg, which indicates that the adsorption equilibrium is reached from 50 mg of adsorbent (saturation). An optimal amount of 50 mg of biomass will be necessary to fix the maximum amount of the dye, corresponding to the removal of 97%.

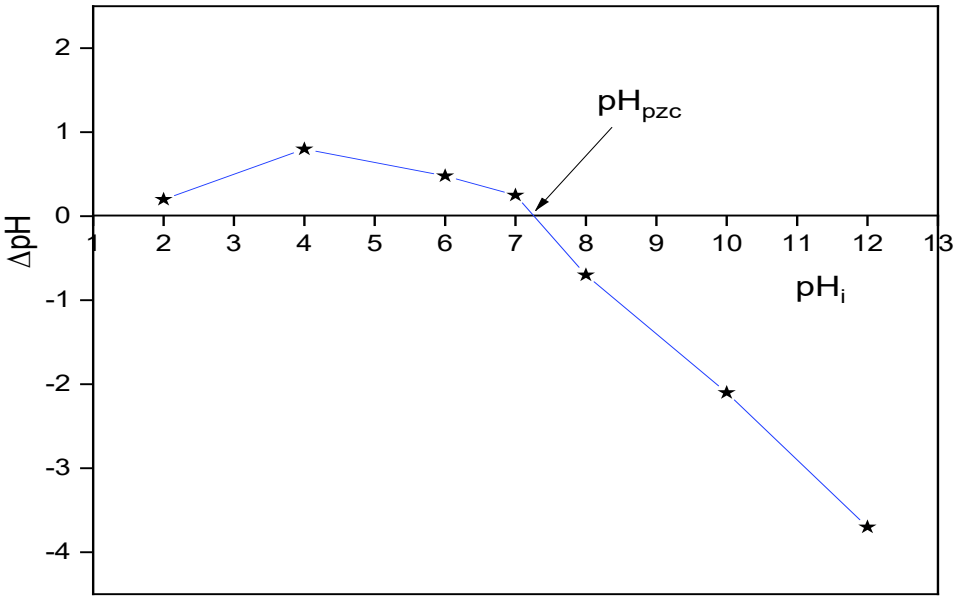

Fig. 4. Point of zero charge of BCS

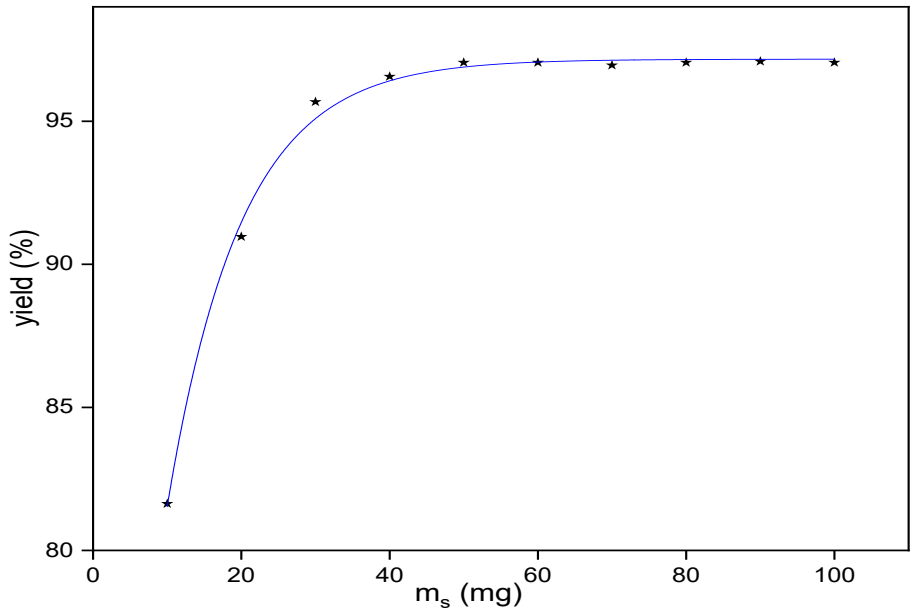

Fig. 5. Percentage of MG removal as a function of bagasse mass.

3.2.2.Effect of temperature

In order to determine the optimal temperature that gives highest capacity of adsorption, studies were done in a water bath at temperatures 25, 30, 35, 40, and 45°C by adding 50 mg of the bagasse in 20mL of the GM solution of a concentration of 2.5 $\times 10^{-5}$M, for one hour under stirring. The results obtained are shown in Figure 6 below. The resulting curve indicates that when temperature increases from 25 to 45°C, the MG adsorption capacity decreases from 12.84 to 12.50 mg g^{-1}. This result, in line with Arrhenius' law, implies that the surface reaction is exothermic and that the contact between the dye molecules and the biosorbent's active sites decreases with increasing temperature, which is detrimental to the adsorption process [40]. The best results are obtained at room temperature.

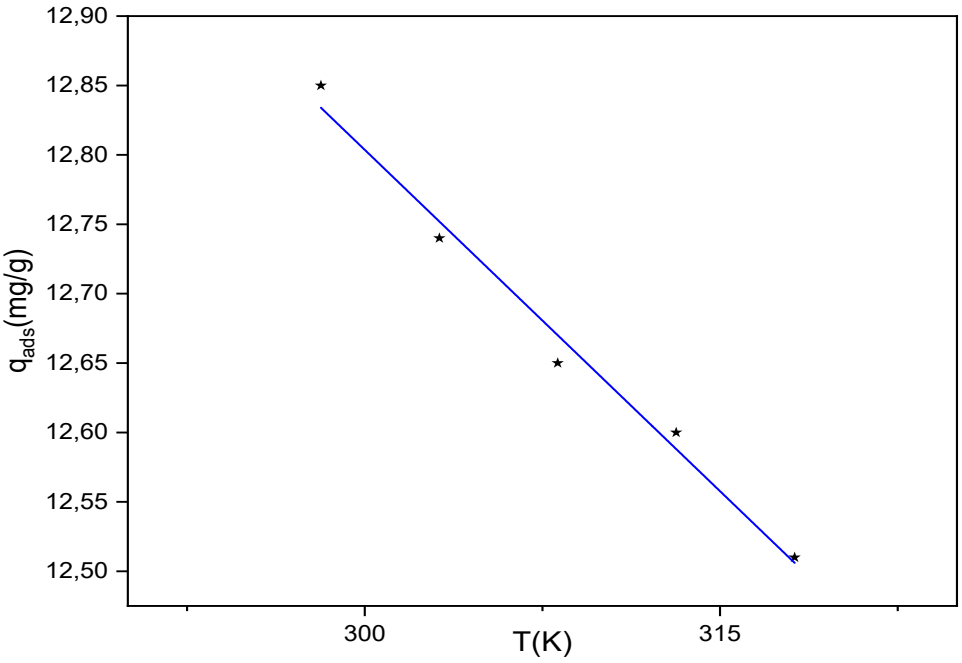

Fig. 6. Influence of the temperature on the amount of adsorbed dye.

3.2.3.Effect of contact time

To determine the time required for saturation of the adsorbate by the adsorbent/maximum retention of the dye, volumes of 20 mL of the dye solution at a concentration of 10^{-4} mol L^{-1} are mixed with 50 mg of the biomass at the following temperatures 25, 35 and 45°C. The whole is stirred at times ranging from 5 to 70 minutes. Separation was performed by centrifugation of the suspension. The residual concentrations were determined using the UV-VIS spectrophotometer at 618 nm. The results are shown in Figure 7. The figures show that the amount of MG adsorbed by biomass adsorbent at different temperatures increases over time until an equilibrium plateau is reached, after 50 minutes. This is because the adsorbent's surface initially has active sites available for use. After this time (the equilibrium time), there is a decrease in adsorption efficiency because fewer free sites remain on the adsorbent's surface [24]. Additionally, the graphs demonstrate that the quantity of MG adsorbed by the biomass is somewhat temperature-sensitive. Raising the temperature has a negative effect on adsorption, indicating an exothermic process. Notably, this adsorption happens quickly, taking place in the first forty minutes after adsorption begins.

3.2.4.Effect of pH

Several tests were conducted to evaluate the effect of the reaction media's pH on the adsorbent's ability to adsorb dye. This required putting biomass suspensions in 20 milliliters of dye solution and changing the pH between 2 and 12 during 50 minutes of contact. By adding 0.1M of HCl or 0.1M of NaOH, the suspensions' pH was brought to the required level. Figure 8 displays the results of varying the adsorption percentage about the solution's pH. The graph shows the significant impact of the character of the mixture on the adsorption of MG by the adsorbate. As a result, effective dye retention is observed over a pH range from 8 to 10, with particularly remarkable performance at pH 10. Above this pH range, a decrease in retention efficiency is observed. To explain the effect of solution pH on these interactions, the pH value of the zero charge point pHpzc was used. Since the pHpzc of the solid used is 7.3, the surface of the adsorbent is positively charged when the pH of the solution is below this value and is negatively charged when the pH of the solution is above this value. As the dye used is cationic, its dissolution releases positively charged ions, so hydrophobic and chemical interactions could be the main

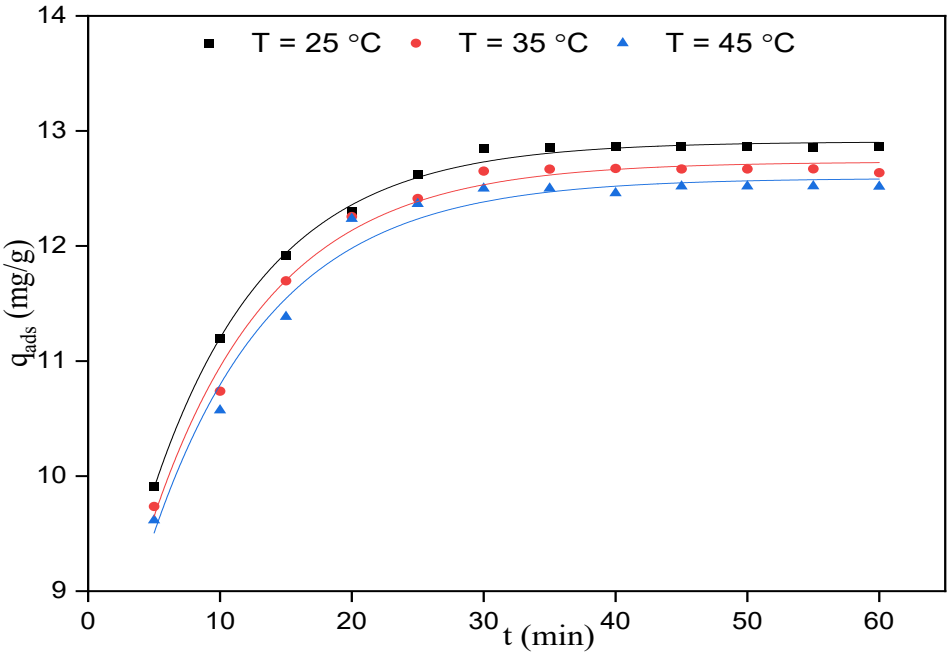

Fig. 7. Effect of contact time.

adsorption forces in the pH range below pHpzc. The significant retention of the dye at pH values above pHpzc can be explained by electrostatic interactions between the different charges in the suspension and the surface of the adsorbent. In addition, MG molecules (pka = 10.3) [6] are protonated in the acid medium and deprotonated at higher pH values, which explains the decrease in dye retention at pH values above 10.

3.3. Thermodynamics parameters

Figure 9 shows the evolution of $\ln(K_c)$ as a function of $\frac{1}{T}$. The activation energy of the adsorption process is determined by applying the Arrhenius equation of $k = A.e^{-Ea/RT}$. The thermodynamic parameters are grouped in Table 2. The results confirm the exothermic nature of MG's adsorption onto the adsorbent ($\Delta H°$ is negative). A decrease in disorder during the adsorption of MG onto the adsorbent is

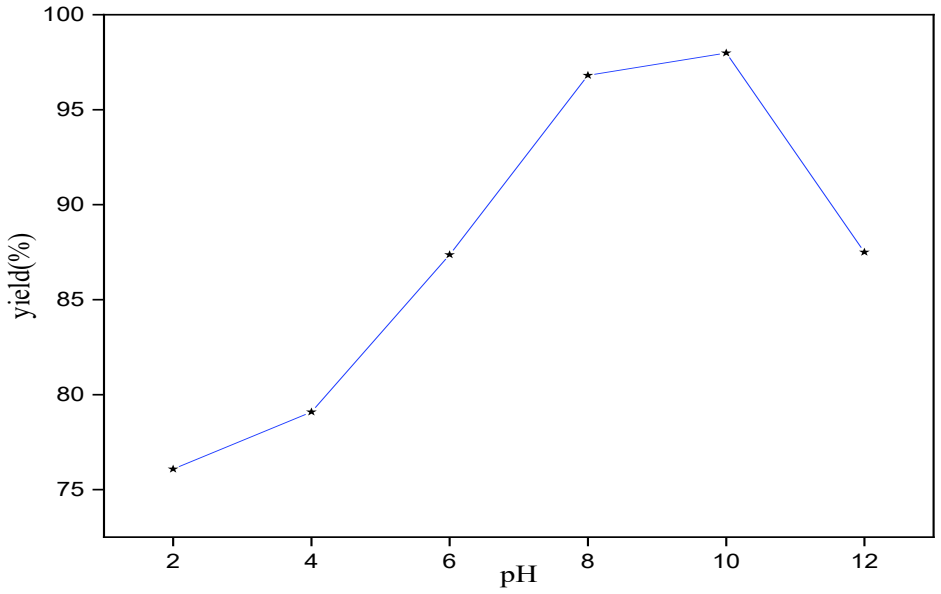

Fig. 8. Influence of pH on MG adsorption

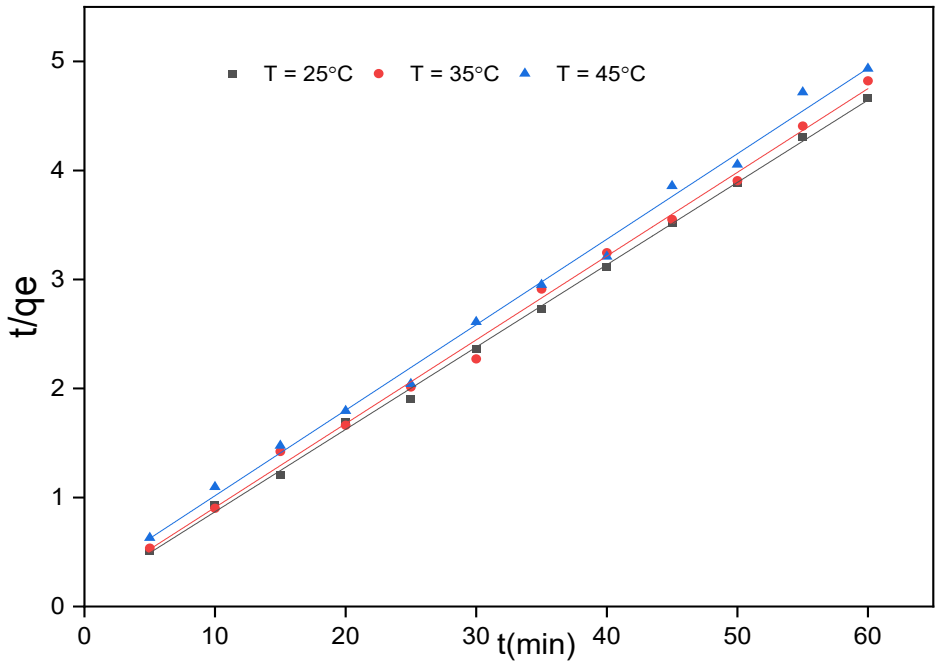

Fig. 9. Evolution of $\ln(K_c)$ as a function of T^{-1}

Table 2. The thermodynamic parameters

Temperature (°K)	$\Delta H°_{ads}$ (Kj mol^{-1})	$\Delta S°_{ads}$ (jK^{-1} mol^{-1})	$\Delta G°_{ads}$ (Kj mol^{-1})	R^2	Ea (Kj mol^{-1})
298			-26.046		
303			-26.048		
308	-25.90	0.49	-26.051	0.998	35.75
113			-26.053		
318			-26.056		

indicated by the negative values of ΔG° and ΔS°, which indicate that the process is spontaneous [41]. The Arrhenius equation was also used to compute the activation energy value, which is less than 40 kj mol^{-1}. This suggests that a physisorption mechanism underlies the adsorption process.

3.4. Modeling of adsorption kinetics

3.4.1.Pseudo-first-order kinetics

The figure shows the results of these models, with the kinetic parameters derived from the slopes and intercepts of the theoretical lines. Table 3 shows the kinetic parameters derived from the linear Lagergren models. The obtained data (Figure 10 and Table 3) demonstrate that the experimental points for this model are not entirely linear, the experimentally adsorbed quantities of malachite green are significantly different from the calculated qcal, and the R^2 coefficients depart considerably from the value of 1. As a result, this model cannot explain the outcomes of the adsorption of malachite green on our adsorbent.

3.4.2.Pseudo-second order kinetics

The experimental results were also compared with the pseudo-second-order kinetic model Figure 11. The results obtained for the linear adsorption kinetics models are shown in the figure 11.

Table 3 shows the kinetic parameters calculated from the slopes and ordinates of the theoretical lines. According to Figure 11, the model with the highest correlation factor is the pseudo-second-order model. The adsorbed quantity values in this model q_{cal} are similar to those obtained experimentally q_{exp}, with correlation coefficients R^2 close to 1. In this way, it can be concluded that the pseudo-second-order model better represents the malachite green adsorption process on the SCB solid. It would appear that the biosorption of MG molecules by the SCB from an aqueous solution proceeds rapidly [42]. This result is similar to that observed in other research [6].

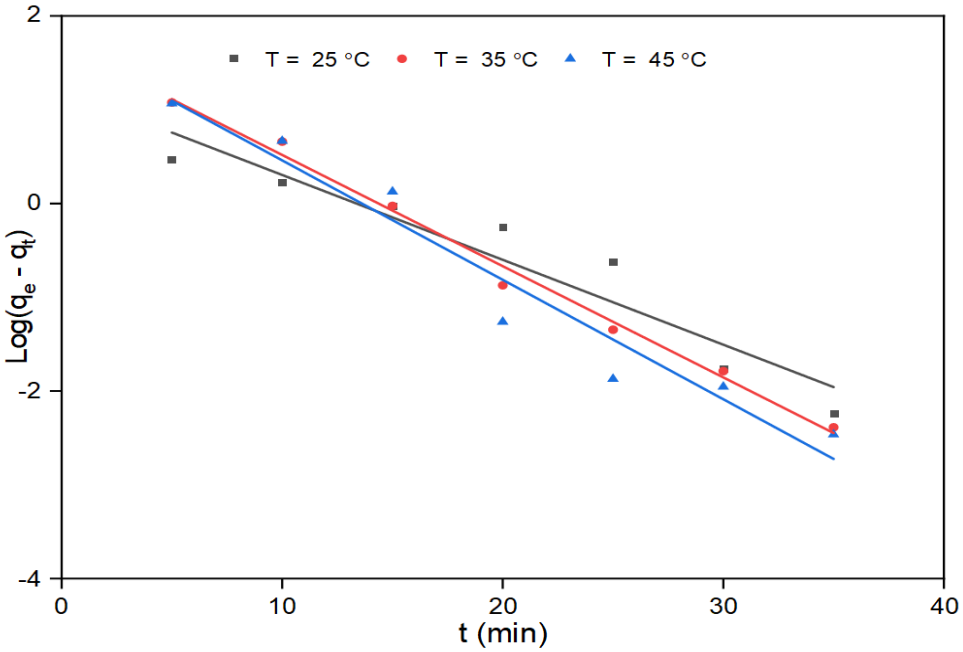

Fig. 10. Application of the pseudo-first-order model on MG-SCB adsorption

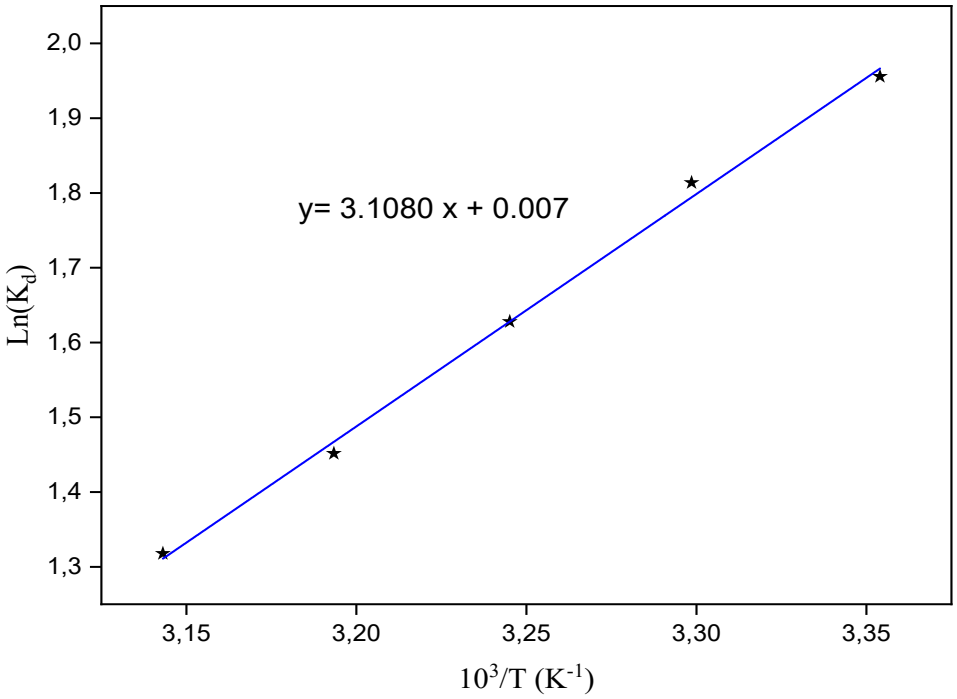

Fig. 11. Application of the pseudo-second-order model on GM-BCS adsorption.

3.4.3.Intra-particle diffusion model

Figure 12 below shows a graphical representation of the variation of the amount of dye adsorbed at each time qt as a function of the square root of time ($t_{1/2}$). According to these results, the curves representing qe = f ($t^{0.5}$) do not pass through the origin, which indicates that the diffusion of the dyes into the biomass pores is not the only mechanism determining the adsorption kinetics, the double linearity of the curves suggests that there is a combination of two different steps. Therefore, the rate of adsorption kinetics varies from one step to the other. Table 4 displays the parameters of the intra-particle diffusion model for the adsorption of MG on SCB. From these results, it can be seen that the diffusion rate constant Kd values in the first step are higher than those in the second step, which indicates that the first step of the dye diffusion kinetics is faster than the second step. The first step represents the dyes' diffusion on the adsorbent's external surface. In contrast, the second step reflects the diffusion of the dye molecules through the internal pores within the biomass particles, which is a slower step [43]. Thus, the values of the constant C are different from 0; this last one expresses the thickness of the diffuse layer; we notice that the intra-particle diffusion is not the only factor that controls the rate of adsorption of malachite green on the adsorbent [44]. Table 4. Parameters of the intra-particle diffusion model of MG on BCS.

Table 3. Kinetic parameters of linear modeling of MG dye adsorption.

Temperature	Adsorbed values	Pseudo-first order model			Pseudo-second order model		
(°K)	q_{exp}(mg.g^{-1})	q_{cal}	K_1	R^2	q_{cal}	K_2	R^2
298	12.86	3.54	2.21	0.914	12.50	0.049	0.999
308	12.66	0.1	2.81	0.866	12.50	0.082	0.998
318	12.51	0.01	0.48	0.965	12.50	1.28	0.999

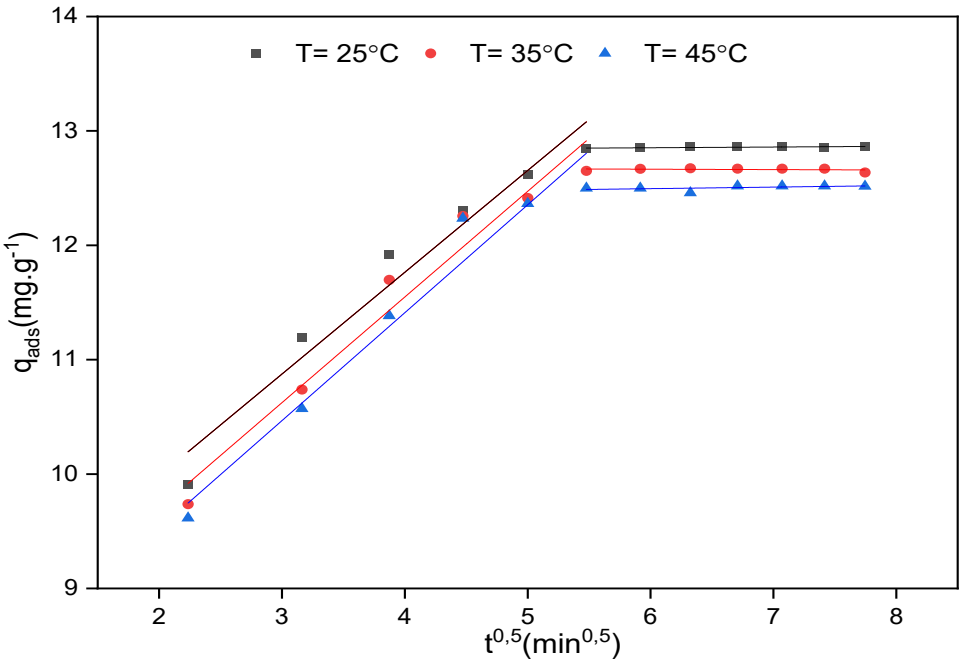

Fig. 12. Application of the external diffusion model to adsorption MG -SCB

According to these results, the curves representing qe = f ($t^{0.5}$) do not pass through the origin, which indicates that the diffusion of the dyes into the biomass pores is not the only mechanism determining the adsorption kinetics, the double linearity of the curves suggests that there is a combination of two different steps. Therefore, the rate of adsorption kinetics varies from one step to the other. Table 4 displays the parameters of the intra-particle diffusion model for the adsorption of MG on SCB. From these results, it can be seen that the diffusion rate constant Kd values in the first step are higher than those in the second step, which indicates that the first step of the dye diffusion kinetics is faster than the second step. The first step represents the diffusion of the dyes on the external surface of the adsorbent, while the second step reflects the diffusion of the dye molecules through the internal pores within the biomass particles, which is more of a slow step [43]. Thus, the values of the constant C are different from 0; this last one expresses the thickness of the diffuse layer; we notice that the intra-particle diffusion is not the only factor that controls the rate of adsorption of malachite green on the adsorbent [44].

3.5. Modeling of adsorption isotherm

3.5.1.Langmuir Isotherm

Figure 13 illustrates the modeling results obtained from the model, while Table 5 summarizes the isotherm's parameters. The data presented in Table 5 shows that the experimental data for MG biosorption on biomass is well described. This is confirmed by the high value of the coefficient of determination (R^2 = 0.98), proving that the biosorption process occurred in a monolayer fashion. In addition, MG dye ions (KL = 0.011 L mg^{-1}) highly refined the biosorption sites on the biomass surface, demonstrating their ability to effectively

Table 4. Parameters of the intra-particle diffusion model of MG on BCS.

Temperature	1st right			2nd right		
(°K)	C	K_1	R^2	C	K_2	R^2
298	0.92	2.23	0.917	12.45	0.057	0.65
308	0.95	2.54	0.94	12.29	0.06	0.58
318	0.96	2.53	0.969	12.01	0.07	0.807

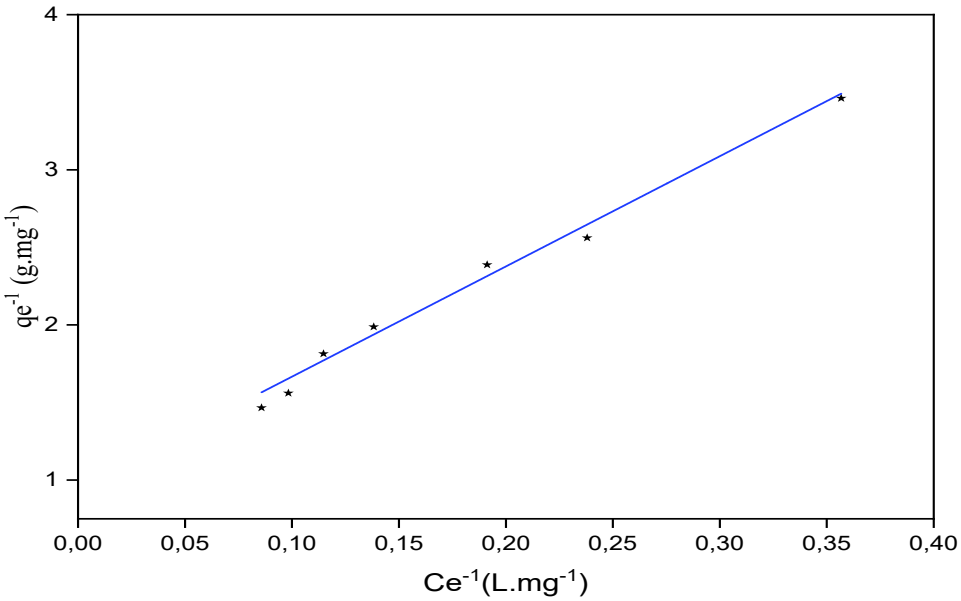

Fig. 13. Linear representation of the Langmuir model of MG adsorption on SCB

remove dye particles from aqueous solutions [18]. Deviations from the linearity of biosorption are considered when determining the Langmuir isotherm model's second parameter (dimensionless factor RL). The value of R_L is between zero and one, indicating favorable biosorption [28]. Furthermore, the maximum dye adsorption amount predicted by this model, qm, closely matches the experimental value (q_{exp}:12.84 mg g^{-1}).

3.5.2. Freundlich isotherm

The outcomes of modeling the adsorption isotherm of the dye on the adsorbent are depicted in the following Figure 14, based on this model. According to Sahu and colleagues [45], it has been reported that the higher the value of n, the more intense the reaction between the adsorbate and the biosorbent. In addition, the increase in the R^2 value (0.98) indicates that multilayer biosorption has an impact on the process. This also shows that the Freundlich isotherm model accurately illustrates the equilibrium of MG biosorption by SCB biomass, with a high affinity between the heterogeneous biomass surface and the MG particles [45].

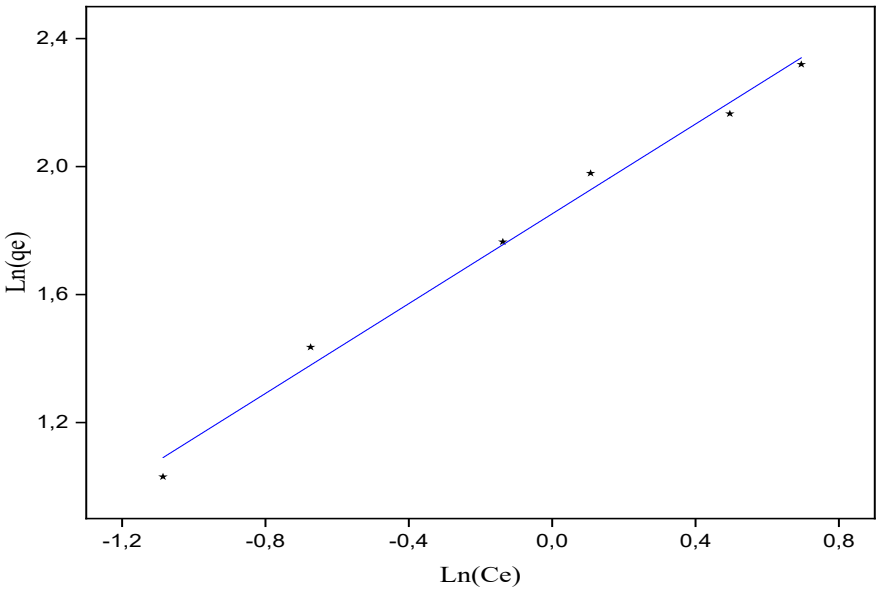

Fig. 14. Linear representation of the Freundlich model of MG adsorption on SCB

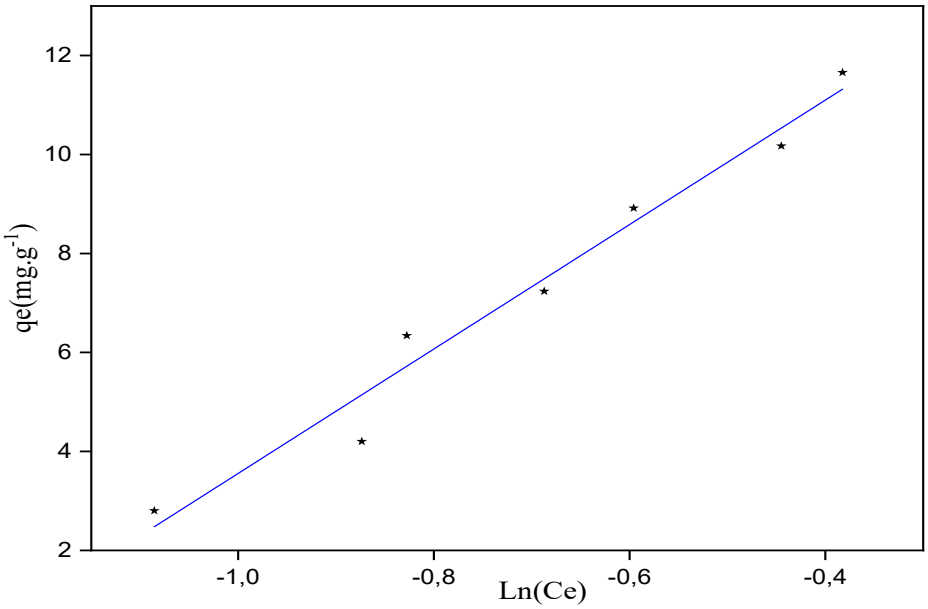

Fig. 15. Linear representation of the Temkin model of MG adsorption on SCB

3.5.3. Temkin isotherm

Figure 15 depicts the outcomes of modeling the dye's adsorption isotherm on the adsorbent, as per this model. According to the results in Table 5, the Temkin model is suitable for the biosorption of MG on biomass, as demonstrated by the high R^2 value (0.97). This also confirms the possibility of heterogeneous sites with different binding energies [46]. The higher b-value (187.1 $Jmol^{-1}$) suggests a strong interaction between MG ions and different functional groups present on the biomass surface, which is associated with the decrease of the adsorption heat of ions in the layer [18]. Furthermore, the adsorption energy of the dye from the aqueous solution, according to the Temkin model (b_T), is positive, suggesting an exothermic nature of the adsorption [47]. According to the Langmuir, Freundlich, and Temkin biosorption isotherms, the R^2 values are all greater than 0.97, which suggests that the biosorption process is multimechanistic and that it is very likely to be a multilayer physisorption.

Table 5. Parameters related to the adsorption models used.

Isotherm	Parameters
Langmuir	$q_m = 12.9$ $K_L = 0.011$ $R_L = 0.8$ $R^2 = 0.98$
Freundlich	$K_F = 2.752$ $\frac{1}{n} = 0.69$ $R^2 = 0.98$
Temkin	$A_T = 1.15$ $b_T = 187.1$ $R^2 = 0.97$

3.6. Mechanism of MG adsorption on SCB

To propose a mechanism for MG adsorption on SCB, Fourier transform infrared spectroscopy is a critical study that must be conducted. This examination is an essential tool for examining the interaction between dye molecules and the solid material's surface-active sites, and it is carried out both before and after MG adsorption. Comparison of the two FTIR spectra (Fig. 16) reveals neither the appearance of new bands nor the disappearance of bands previously observed in the raw SCB alone. The only change detected is a variation in the intensity of the absorption bands. Indeed, there is a reduction in the intensity of the broadband located between 3374 cm^{-1}, corresponding to the elongation of the vibrations of the (OH) groups, suggesting a possible involvement of hydrogen bonds between the hydroxyl groups on the SCB surface and the nitrogen atoms of the MG in the adsorption mechanism. In addition, ion exchange could occur by replacing the sodium, magnesium, and calcium ions present on the biomass cell wall with ions from the MG dye [18]. This would also be a process of electrostatic interaction, as the biosorbent surface is negatively charged at a pH above 7.3 (pH_{pzc}); this facilitates the interaction of the algal surface with the positively charged particles of the MG dye (Schema 2). Thus, it can be concluded that hydrogen bonding, ion exchange, and electrostatic interaction may all play a role in the biosorption of MG dye on SCB biomass.

4. Conclusion

The study focused on using SCB sugar cane bagasse waste in its natural form to remove the malachite green (MG) dye by adsorption in an aqueous medium. The physicochemical characterization of the material has shown that it is rich in hydroxyl groups present in several surface functions, such as acids and alcohols. The specific surface of the adsorbent is estimated at around 28.44 m^2g^{-1}. This surface is opposing at a pH greater than 7.3; the biosorbent is rich in oxygenated functions such as alcohol, acid, and ether, capable of attracting cationic pollutants in an essential medium. UV-Vis spectrophotometry is used to assess the concentrations of MG dye solutions. The performance of BCS in removing MG from wastewater was about 12.84 mg g^{-1}, corresponding to a removal efficiency of 97% at room temperature. The study of the optimization of the conditions showed that the adsorption capacity decreases with the increase in temperature, which represents a strong point for treating this dye. The kinetic and isothermal study results clearly showed that the adsorption of MG on the biosorbent adhered to the pseudo-second-

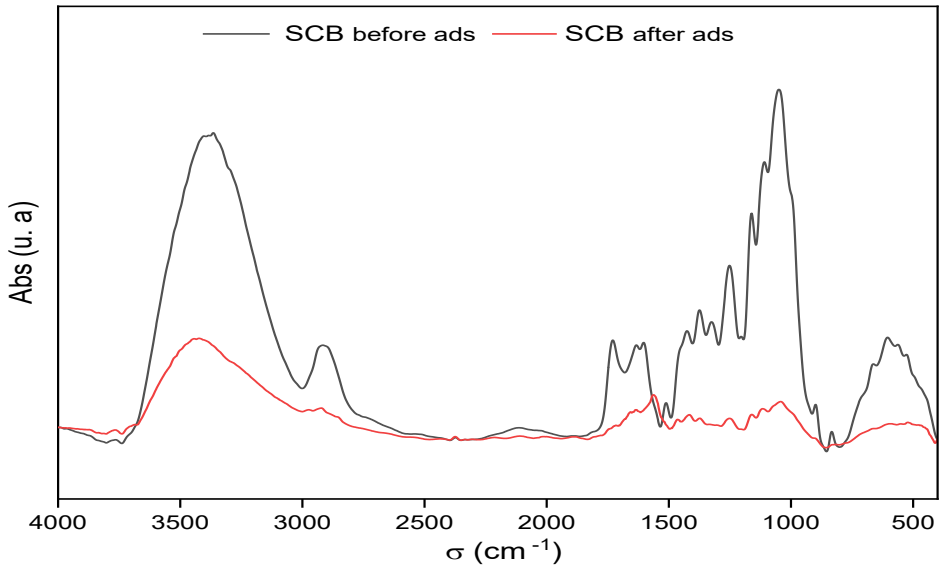

Fig. 16. FT-IR spectra of SCB before and after adsorption of dye molecules.

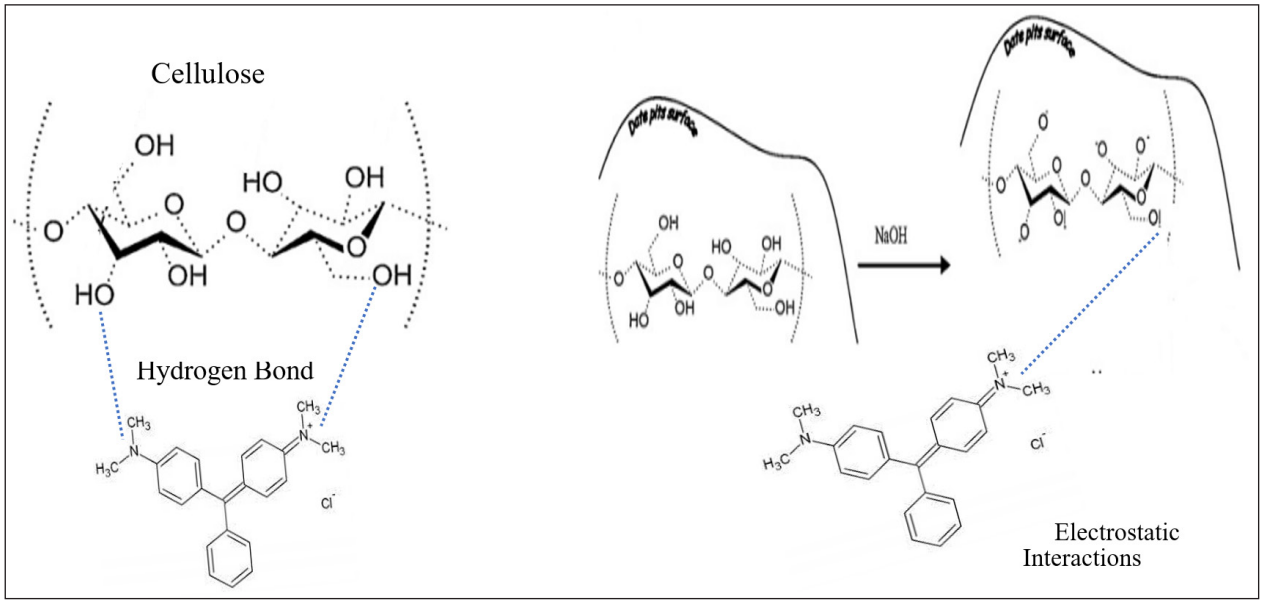

Scheme 2. Proposed mechanism for the retention of MG dye over the SCB solid

order model. The variations in adsorption and Gibbs free energy (ΔG°), entropy (ΔS°), and enthalpy (ΔH°) were computed, revealing that the adsorption of MG occurs spontaneously through an exothermic process. The investigation into the adsorption of MG has shown that this material constitutes an adsorbent abandonment and is economical and practical for the treatment of wastewater loaded with dyes.

5. Acknowledgements

The authors thank the Applied Chemistry and Biology Laboratory, Faculty of Sciences, Moulay Ismail University, Morocco.

6. References

[1] S. Teimoori, H. Shirkhanloo, A. H. Hassani, M. Panahi, N. Mansouri, Rapid extraction of BTEX in water and milk samples based on functionalized multi-walled carbon nanotubes by dispersive homogenized-micro-solid phase extraction, Food Chem., 421 (2023) 136229. https://doi.org/10.1016/j.foodchem.2023.136229

[2] S. Teimoori, H. Shirkhanloo, A. H. Hassani, M. Panahi, N. Mansouri, An immobilization of aminopropyl trimethoxysilane-phenanthrene carbaldehyde on graphene oxide for toluene extraction and separation in water samples, Chemosphere, 316 (2023) 137800. https://doi.org/10.1016/j.chemosphere.2023.137800

[3] M. Arjomandi, A Review: Analytical methods for heavy metals determination in environment and human samples, Anal. Methods Environ. Chem. J., 2 (2019) 97–126. https://doi.org/10.24200/amecj.v2.i03.73

[4] M. B. H. Abadi, H. Shirkhanloo, J. Rakhtshah, Air pollution control: The evaluation of TerphApm@MWCNTs as a novel heterogeneous sorbent for benzene removal from air by solid phase gas extraction, Arab. J. Chem., 13 (2020) 1741–1751. https://doi.org/10.1016/j.arabjc.2018.01.011

[5] J. Rakhtshah, H. Shirkhanloo, N. Esmaeili, A rapid extraction of toxic styrene from water and wastewater samples based on hydroxyethyl methylimidazolium tetrafluoroborate immobilized on MWCNTs by ultra-assisted dispersive cyclic conjugation-micro-solid phase extraction, Microchem. J., 170 (2021) 106759. https://doi.org/ 10.1016/j.microc.2021.106759

[6] S. Arellano-Cárdenas, S. López-Cortez, M. Cornejo-Mazón, J. C. Mares-Gutiérrez, Study of malachite green adsorption by organically modified clay using a batch method, Appl.

Surf. Sci., 280 (2013) 74–78. https://doi.org/10.1016/j.apsusc.2013.04.097

[7] K. Vasanth Kumar, S. Sivanesan, V. Ramamurthi, Adsorption of malachite green onto Pithophora sp., a fresh water algae: Equilibrium and kinetic modelling, Process Biochem., 40 (2005) 2865–2872. https://doi.org/ 10.1016/j.procbio.2005.01.007

[8] A. Dehbi, Comparative study of malachite green and phenol adsorption on synthetic hematite iron oxide nanoparticles (α-Fe2O3), Surf. Interface., 21 (2020) 100637. https://doi.org/ 10.1016/j.surfin.2020.100637

[9] M. Mohammadi Asl, N. Mansouri, S. A. R. Haji Seyed Mirzahosseini, F. Atabi, Simultaneity comparative evaluation of toluene removal from the air by adsorption and UV semi-degradation-based adsorption procedure, Int. J. Environ. Sci. Technol., 21 (2024) 6677-6694. https://doi.org/10.1007/s13762-024-05503-0

[10] M. M. Asl, F. Atabi, Functionalized graphene oxide with bismuth and titanium oxide nanoparticles for efficiently removing formaldehyde from the air by photocatalytic degradation–adsorption process, J. Anal. Test., 7 (2023) 444-458. https://doi.org/10.1007/s41664-023-00272-0

[11] R. Ashouri, Dynamic and static removal of benzene from air based on task-specific ionic liquid coated on MWCNTs by sorbent tube-headspace solid-phase extraction procedure, Int. J. Environ. Sci. Technol., 18 (2021) 2377-2390. https://doi.org/10.1007/s13762-020-02995-4

[12] S. Teimoori, H. Shirkhanloo, A. H. Hassani, M. Panahi, N. Mansouri, New extraction of toluene from water samples based on nano-carbon structure before determination by gas chromatography, Int. J. Environ. Sci. Technol., 20 (2023) 6589–6608. https://doi.org/ 10.1007/s13762-023-04906-9

[13] A. Faghihi-Zarandi, H. Shirkhanloo, C. Jamshidzadeh, A new method for removal of hazardous toluene vapor from air based on ionic liquid-phase adsorbent, Int. J. Environ. Sci. Technol., 16 (2019) 2797–2808. https://doi.org/ 10.1007/s13762-018-1975-5

[14] A. Faghihi-Zarandi, J. Rakhtshah, B. Bahrami Yarahmadi, A rapid removal of xylene vapor from environmental air based on bismuth oxide coupled to heterogeneous graphene/graphene oxide by UV photo-catalectic degradation-adsorption procedure, J. Environ. Chem. Eng., 8 (2020) 104193. https://doi.org/ 10.1016/j.jece.2020.104193

[15] R. F. Wang, L. G. Deng, K. Li, X. J. Fan, W. Li, H. Q. Lu, Fabrication and characterization of sugarcane bagasse–calcium carbonate composite for the efficient removal of crystal violet dye from wastewater, Ceram. Int., 46 (2020) 27484–27492. https://doi.org/ 10.1016/j.ceramint.2020.07.237

[16] I. Loulidi, Adsorptive removal of chromium (VI) using walnut shell, almond shell, coconut shell and peanut shell, Res. J. Chem. Environ., 23 (2019) 25–32. http://www.scopus.com/inward/record.url?eid=2-s2.0-85081283619&partnerID=MN8TOARS

[17] M. El Khomri, N. El Messaoudi, A. Dbik, S. Bentahar, A. Lacherai, Efficient adsorbent derived from Argania Spinosa for the adsorption of cationic dye: Kinetics, mechanism, isotherm and thermodynamic study, Surf. Interface., 20 (2020) 100601. https://doi.org/ 10.1016/j.surfin.2020.100601

[18] M. A. Fawzy, Sustainable use of marine Macroalga Sargassum muticum as a biosorbent for hazardous crystal violet dye: Isotherm, kinetic and thermodynamic modeling, Sustain., 15 (2023) 15064. https://doi.org/ 10.3390/su152015064

[19] N. Ameram, Chemical composition in sugarcane bagasse: Delignification with sodium hydroxide, Malaysian J. Fundam. Appl. Sci., 15 (2019) 232–236. https://doi.org/ 10.11113/mjfas.v15n2.1118

[20] T. L. Bezerra, A. J. Ragauskas, A review of sugarcane bagasse for second-generation bioethanol and biopower production, Biofuel. Bioprod. Bior., 10 (2016) 634–647. https://doi.org/ 10.1002/bbb.1662

[21] V. Yogeshwaran, A. K. Priya, Experimental studies on the removal of heavy metal ion concentration using sugarcane bagasse in batch adsorption process, Desalin. Water Treat., 224 (2021) 256–272. https://doi.org/ 10.5004/dwt.2021.27160

[22] H. Tahir, M. Sultan, N. Akhtar, U. Hameed, T. Abid, Application of natural and modified sugar cane bagasse for the removal of dye from aqueous solution, J. Saudi Chem. Soc., 20 (2016) S115–S121. https://doi.org/ 10.1016/j.jscs.2012.09.007

[23] E. K. Guechi, O. Hamdaoui, Biosorption of methylene blue from aqueous solution by potato (Solanum tuberosum) peel : equilibrium modelling, kinetic, and thermodynamic study, Desalin. Water Treat., 57 (2016) 10270-10285. https://doi.org/10.1080/19443994.2015.1035338

[24] I. Loulidi, Adsorption of crystal violet onto an agricultural waste residue: Kinetics, isotherm, thermodynamics, and mechanism of adsorption, Sci. World J., 2020 (2020) 873521. https://doi.org/ 10.1155/2020/5873521

[25] K. D. Belaid, S. Kacha, Study of the kinetics and thermodynamics of the adsorption of a basic dye on sawdust, J. Water Sci., 24 (2011)131–144. https://doi.org/ 10.7202/1006107ar

[26] E. Sudova, J. Machova, Z. Svobodova, T. Vesely, Negative effects of malachite green and possibilities of its replacement in the treatment of fish eggs and fish: A review, Vet. Med., 52 (2007) 527–539. https://doi.org/ 10.17221/2027-VETMED

[27] M. Sadoq, Elimination of crystal violet from aqueous solution by adsorption on naturel polysaccharide: Kinetic, isotherm, thermodynamic studies and mechanism analysis, Arab. J. Chem., 17 (2024) 105453. https://doi.org/ 10.1016/j.arabjc.2023.105453

[28] B. Shetty, Y. S. R, J. Johns, A Green approach to the removal of Malachite Green dye from aqueous medium using chitosan/cellulose blend, Res. Square, 2022. https://doi.org/ 10.21203/rs.3.rs-1376666/v2

[29] S. Dawood, T. K. Sen, Removal of anionic dye Congo red from aqueous solution by raw pine and acid-treated pine cone powder as adsorbent: Equilibrium, thermodynamic, kinetics, mechanism and process design, Water Res., 46 (2012) 1933–1946. https://doi.org/ 10.1016/j.watres.2012.01.009

[30] D. Kavitha, C. Namasivayam, Experimental and kinetic studies on methylene blue adsorption by coir pith carbon, Bioresour. Technol., 98 (2007) 14–21. https://doi.org/ 10.1016/j.biortech.2005.12.008

[31] M. Ertaş, M. Hakki Alma, Pyrolysis of laurel (Laurus nobilis L.) extraction residues in a fixed-bed reactor: Characterization of bio-oil and bio-char, J. Anal. Appl. Pyrolysis, 88 (2010) 22–29. https://doi.org/ 10.1016/j.jaap.2010.02.006

[32] A. Kali, Efficient adsorption removal of an anionic azo dye by lignocellulosic waste material and sludge recycling into combustible briquettes, Colloids Interfaces, 6 (2022) 22. https://doi.org/ 10.3390/colloids6020022

[33] A. F. Abbas, M. J. Ahmed, Mesoporous activated carbon from date stones (Phoenix dactylifera L.) by one-step microwave assisted K_2CO_3 pyrolysis, J. Water Process Eng., 9 (2016) 201–207. https://doi.org/ 10.1016/j.jwpe.2016.01.004

[34] Z. Belala, M. Jeguirim, M. Belhachemi, F. Addoun, G. Trouvé, Biosorption of basic dye from aqueous solutions by date stones and palm-trees waste: Kinetic, equilibrium and thermodynamic studies, Desalin., 271 (2011) 80–87. https://doi.org/ 10.1016/j.desal.2010.12.009

[35] N. El Messaoudi, M. El Khomri, S. Bentahar, A. Dbik, A. Lacherai, B. Bakiz, Evaluation of performance of chemically treated date stones: Application for the removal of cationic dyes from aqueous solutions, J. Taiwan Inst. Chem. Eng., 67 (2016) 244–253. https://doi.org/ 10.1016/j.jtice.2016.07.024

[36] M. A. Al-Ghouti, J. Li, Y. Salamh, N. Al-Laqtah, G. Walker, M. N. M. Ahmad, Adsorption mechanisms of removing heavy

metals and dyes from aqueous solution using date pits solid adsorbent, J. Hazard. Mater., 176 (2010) 510–520. https://doi.org/ 10.1016/j.jhazmat.2009.11.059

[37] L. Rodier, K. Bilba, C. Onésippe, M. A. Arsène, Utilization of bio-chars from sugarcane bagasse pyrolysis in cement-based composites, Ind. Crops Prod., 141 (2019) 111731. https://doi.org/ 10.1016/j.indcrop.2019.111731

[38] E. N. Bakatula, D. Richard, C. M. Neculita, G. J. Zagury, Determination of point of zero charge of natural organic materials, Environ. Sci. Pollut. Res., 25 (2018) 7823–7833. https://doi.org/ 10.1007/s11356-017-1115-7

[39] K. M. Kifuani, Adsorption d'un colorant basique, Bleu de Méthylène, en solution aqueuse, sur un bioadsorbant issu de déchets agricoles de Cucumeropsis mannii Naudin, Int. J. Biol. Chem. Sci., 12 (2018) 558. https://doi.org/ 10.4314/ijbcs.v12i1.43

[40] E. K. Guechi, O. Hamdaoui, Biosorption of methylene blue from aqueous solution by potato (Solanum tuberosum) peel: equilibrium modelling, kinetic, and thermodynamic studies, Desalin. Water Treat., 57 (2016) 10270–10285. https://doi.org/ 10.1080/19443994.2015.1035338

[41] N. B. Singh, G. Nagpal, S. Agrawal, Water purification by using adsorbents : A review, Environ. Technol. Innov., 11 (2018) 187–240. https://doi.org/ 10.1016/j.eti.2018.05.006

[42] S. D. Ahranjani, A lead analysis based on amine-functionalized bimodal mesoporous silica nanoparticles in human biological samples by ultrasound assisted-ionic liquid trap-micro solid phase extraction, J. Pharm. Biomed. Anal., 157 (2018) 1-9. https://doi.org/10.1016/j.jpba.2018.05.004

[43] Z. Khademi, B. Ramavandi, M. T. Ghaneian, The behaviors and characteristics of a mesoporous activated carbon prepared from Tamarix hispida for Zn(II) adsorption from wastewater, J. Environ. Chem. Eng., 3 (2015) 2057–2067. https://doi.org/ 10.1016/j.jece.2015.07.012

[44] F. Wu, R. Tseng, S. Huang, R. Juang, Characteristics of pseudo-second-order kinetic model for liquid-phase adsorption : A mini-review, Chem. Eng. J., 151 (2009) 1–9. https://doi.org/ 10.1016/j.cej.2009.02.024

[45] S. Sahu, Adsorption of methylene blue on chemically modified lychee seed biochar: Dynamic, equilibrium, and thermodynamic study, J. Mol. Liq., 315 (2020) 113743. https://doi.org/ 10.1016/j.molliq.2020.113743

[46] H. Zeghache, S. Hafsi, N. Gherraf, Adsorption of organic dyes onto commercial activated carbon by using non-linear regression method, Environ. Asia, 12 (2019) 127–142. https://doi.org/ 10.14456/ea.2019.15

[47] P. Sampranpiboon, Equilibrium isotherm models for adsorption of zinc (II) ion from aqueous solution on pulp waste faculty of engineering, WSEAS Trans. Environ. Dev., 10 (2014) 35–47. https://wseas.org/cms.action?id=4031

Anal. Methods Environ. Chem. J. 8 (1) (2025) 26-38

AMECJ

Research Article, Issue 1
Analytical Methods in Environmental Chemistry Journal
Journal home page: www.amecj.com/ir

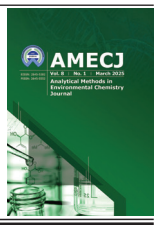

Determination and removal of methylene blue dye via photodegradation using titanium dioxide nanoparticles from watermelon rind

Mohamed Abdelkalik Hussain[a,*] and Wadhah Naji Al Sieadi[b]
[a]*Department of Chemistry, College of Science, University of Baghdad, Baghdad, Iraq*
[b]*Department of Chemistry, College of Science, University of Baghdad, Baghdad, Iraq*

ARTICLE INFO:
Received 2 Dec 2024
Revised form 4 Feb 2025
Accepted 30 Feb 2025
Available online 30 March 2025

Keywords:
Green synthesis,
TiO_2NPs,
Watermelon rind,
Methylene blue dye,
Sol-gel method

ABSTRACT
Water pollution poses significant threats to the environment and human health, applications of photodegradation technology offer a promising solution for mitigating these impacts by utilizing light energy to break pollutants; this technology can effectively clean contaminated water, contributing to a sustainable challenge and enhanced the practicality and efficiency of photodegradation systems. This study compares the photodegradation efficiency of (20 ppm, pH = 6.4) methylene blue dye (MB) under three different types of ultraviolet (UV) irradiation light sources, which are UV type A (365 nm), UV type B (311 nm), UV type C (254 nm) by using new home-made photoreactor. The photodegradation activity of this system comprises various conditions, first on circulation of MB dye in the system without irradiation or adding catalytic, when irradiation MB dye with UV-A, UV-B, and UV-C light sources with circulation, finally, the effect of adding 0.05 g of green synthesis of titanium dioxide nanoparticles (TiO_2NPs) by using watermelon rind extract with irradiation in the system. Different percentage of MB dye removal was reported. The prepared catalytic TiO_2NPs were characterized using ultraviolet−visible spectroscopy (UV-Vis), Fourier transform infrared spectroscopy (FTIR), scanning electron microscope (SEM), energy dispersive analysis (EDX), X-ray spectroscopy (XRD), and atomic force microscopy (AFM). High photodegradation performance was reported under UV-C and UV-B irradiation of MB dye in 90 minutes.

1. Introduction

Nanotechnology science refers to any product or device created by matter manipulated by controlling atoms and molecules at the nanoscale [1]. These materials are known as nanomaterials or nanoparticles (NPs), with no more than 100 nanometers thick in at least one dimension of materials or molecules at the nanoscale. These materials promise great promise for a scientific career when applied to industries like sports, healthcare, and electronics [2,3]. The field of inorganic nanoparticles has been developed in recent years. Metal nanoparticles differentiate from bulk with their physical and chemical properties, including their morphology and geometry, size and distribution, catalytic activity, and magnetic properties. This leads to broad fields of application in biomedical, electronics, environment, and air pollution [4,5]. Different chemical, physical, and biological methods produce metal nanoparticles. The chemical and

*Corresponding Author: Mohammed Abdelkalik Hussain
Email: muhamedabdelkalik@gmail.com
https://doi.org/10.24200/amecj.v8.i01.362

physical methods have their drawbacks, with hazardous products and poisonous creation products [6,7]. Biosynthesis approaches with low-cost, environmentally friendly methods, with one step to generate metal NPs, and using plant parts as a starting point such as (seeds, roots, and fruits) [8,9], or microorganisms which are used in green synthesis of metal nanoparticles [10,11] which contain bioactive agents such as fungi, yeasts, and bacteria [12-14]. A plant extract is used to produce NPs on a large scale, which is cost-effective, simple, and safe. Plant extract contains bioactive compounds that play different roles in green synthesis methods as capping, stabilizing, and reducing agents [15,16], with compounds such as saccharides [17], vitamins [18], antioxidants [19], alkaloids [20], flavonoids [21], as well as various proteins, amino acids, and enzymes [22]. Watermelon fruit (Citrullus lanatus) is one of the most consumed worldwide [23], but only the red flesh is eaten; the green rind is always discarded to waste. However, the rinds contain various bioactive components, proteins, carotenoids, citrulline, pectin, and cellulose [24,25]. Also, it contains soluble carbohydrates up to (45-65%), carotenoids, alkaloids, saponin, and phytates [26]. WMRs also contain various proteins (15-50%), including prolamin, glutelin, albumin, and globulin. Also, it is considered a good source of vitamin B-complex (B_1, B_2, B_3, B_6, and B_{12}) [27]. Water pollution nowadays receives global attention due to organic contaminations [28,29], which cannot be isolated with conventional methods. An increase in pharmaceutical concentration, especially using amino acid products, which affects plants and other living organisms [30-32]. Due to the photocatalytic technology based on the ultraviolet spectrum and TiO2NP substances [33,34], which undergo the generation of reactive oxygen species (ROS), which is considered the key oxidant that decomposes water pollutants [35]. TiO_2NPs are known for low cost, high stability photocatalytic, and non-toxicity. Also, TiO_2NPs are known for one drawback, which is a large band gap in the visible spectrum [36]. Several chemical and physical methods are reported to remove dyes and organic pollutants from water, such as photocatalysis, coagulation-flocculation, adsorption, membrane separation, and electrochemical processes. Among all these methods, photocatalysis has been reported as cheaper, more effective, and preferred over other methods due to its simple design, operation, energy efficiency, eco-friendliness, and cost-effectiveness. Other methods also focus on changing the pollutants from an aqueous solution to a solid state. In contrast, photocatalysis focuses on the degradation of contaminants by an advanced oxidation process on the catalyst's surface [37–40]. The present work reports the degradation of methylene blue dye by photocatalytic method using TiO_2NPs as a photocatalyst and irradiation of different ultra-viable light sources, such as UV-A, UV-B, and UV-C.

2. Materials and Methods

2.1. Chemicals and Materials

Titanium tetrachloride (TiCl4, 99.99%, CASN.: 7550-45-0) was supplied from Sigma Aldrich, America. Methylene blue dye ($C_{16}H_{18}ClN_3S$, ≥95%, CAS N.: 61-73-4) was bought from Merck, America. Ammonia (≥10%, CASN.: 1336-21-6) bought from Prolabo, Canada. All experiments include using deionized water (DW Millipore).

2.2. Preparation of Watermelon rinds Aqueous

Several watermelons are bought from the market; the rinds are separated and washed with water to remove all remaining parts for several days. The rinds were kept in a dark place to dry. The next step was to use a grinder from Al saif-elec., model HM-917, and the dried rinds ground to powder. To prepare the aqueous solution of watermelon rind, 5.0 g of powder was added to 100 mL DW, the mixture was heated using a stirrer hot plate, the temperature kept under 80 ^{0}C, stirring at 200 rpm for 30 minutes, and a green solution was obtained, the aqueous cooled and filtered, stored in a dark brown bottle.

2.3. Preparation of green TiO_2 NPs by the Sol-Gel

To prepare TiO2NPs by sol-gel method, (100ml) of green watermelon rinds were heated and stirred with a hot plate to 70 0C, then (100 mL) of (0.5M) TiCl4 solution was added. The mixture was kept to reach the wanted temperature, a dropwise of ammonia solution was added, and the mixture color changed from white-green to yellow color after (60) minutes; the mixture cooled down, centrifuged, dried, and ground with crystal mortar to obtain the TiO_2NPs powder. The last step, purification, is done by calcinating the powder in the furnace at (400°C) to remove water moisture for three hours and oxidize the entire TiO_2NPs to powder (Fig. 1). The TiO_2NPs characterized by AFM, SEM, FTIR, UV-vis spectrum, XRD, and EDAX.

2.4. Photoreactor and UV light sources

A photoreactor instrument designed to bring photons to reactant is known as a photoreactor; the device consists of a frame bought from the market, attached to a diaphragm pump 24V.16L^{-1} min^{-1}. The frame connected to the ultraviolet chamber barrel consists of a high-quality tube of quartz for UV-light sources, which are (T5 8W) UV-A (365 nm), (T5 8W) UV-B (311 nm), and (T5 8W) UV-C (254 nm). A water cartridge with 10 inches where used, plastic tubes with connectors used to close the system flow. All UV-light sources were bought from the Coospider quartz ultraviolet lamp, 220v, China, as shown in Figure 2.

Fig. 1. Sol-Gel method for green synthesis of TiO_2NPs

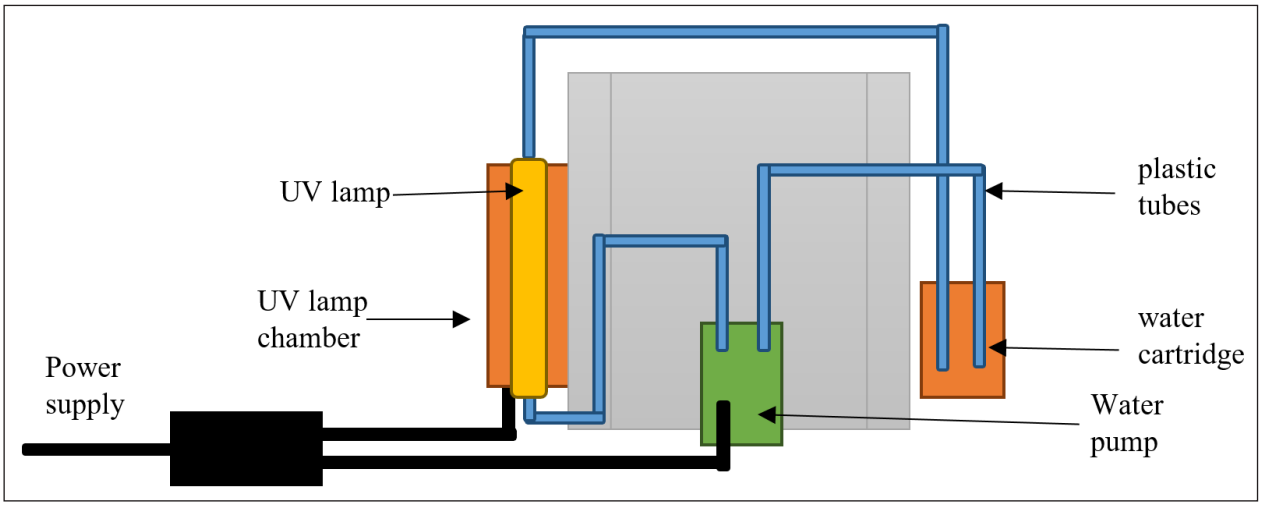

Fig. 2. Photoreactor system design

2.5. The procedure of photodegradation

To ensure the solution flow in the photoreactor device, (320 mL) of methylene blue with concentration (20 mg L^{-1},, PH = 6.4) was selected. An experiment was done to show the impact on MB circulation in the photoreactor. To study the effect of irradiation of three UV lamps, which are UV-A, UV-B, and UV-C, on the circulation of MB in the photoreactor, a set of experiments was done to show the effect. The last set of experiments was done to show the impact of loading (0.05 g) of TiO_2NPs with irradiation with three UV-lamps for degradation of MB, with these set of experiments and to ensure the adsorption-desorption equilibrium of MB on the surface of TiO_2NPs, after adding (0.05 g) of the catalyst, the solution kept for (15) minutes in a dark place. In all experiments, a sample of (2.5 mL) was first collected from the photoreactor; after irradiation started, the sample was collected every (15) minutes using a pipette, and all experiments were done in (90) minutes.

2.6. Instrument and principle of operation

Ultraviolet(UV)radiationisaformofelectromagnetic radiation with shorter wavelengths than visible light; there are three types of UV rays: UV-A, UV-B, and UV-C. To investigate the photodegradation of MB dye, a UV-Vis spectrophotometer with a double beam was used for its capability to analyze the absorption and transmission of light with the dye and degradation products, as this technique provides information about electronics transition and understand the mechanism of degradation and efficiency of the photocatalyst. This instrument is based on the interaction between light and matter; as light passes through a molecule of MB dye, it causes vibration to this molecule, and the wavelength of this absorbed light is called absorption maximum, which can identify the changes in the reaction, the instrument consists of light source which provides illumination at specific wavelength, a monochromator used to select the wavelength, a detector to measure the intensity of light passes through the sample, and a data recorder to record the absorbance or transmission of the light[41].

2.7. Photodegradation kinetic study

The photocatalytic study of TiO_2NPs was tested, and the photodegradation rate of MB dye was calculated by Equation 1 [42,43].

$$\text{MB Degradation (\%)} = \frac{A0-At}{A0} \times 100 \quad \text{(Eq.1)}$$

Where A0 is the absorbance of initial MB; At is the absorbance of the solution after irradiation at time t. According to the first-order kinetics reaction, rate constant k (min^{-1}) was determined using the following relation Equation 2[44,45]. C_0 and C_t are concentrations at the beginning, and at a particular time, t is the irradiation time.

$$\ln\left(\frac{Ct}{C0}\right) = -kt \quad \text{(Eq.2)}$$

2.8. Characterization of Titanium oxide nanoparticles

A BOYN D8000 double-beam UV−vis spectrophotometer (China) was used to identify the compounds' functional groups. The Naio AFM atomic force microscopy model Nano surf AG, Switzerland, measured the surface roughness and mean diameters. Environmental scanning electron microscopy (ESEM) and Energy-dispersive X-ray spectroscopy (EDX) were used for element analysis by Tescan Mira with a resolution of 1.2 nm at 30 kV and 2.3 nm at 3.0 kV. FTIR analysis was performed to measure the absorbances of methylene blue dye (Vertex-80v FTIR spectrometer with a frequency range from 4000–400 cm^{-1}). An XRD persee, China, XD_3 (X-ray diffractometer) was carried out on TiO_2NPs powder to identify the structure and the composition, the range -40-90° at a scanning speed 0.125°-120°min^{-1}, step size of 0.00025° with scanning radius 180 mm.

3. Results and discussion

3.1. Morphological analysis

3.1.1.Scanning Electron Microscope and Energy Dispersive Analysis of X-ray

To characterize the surface morphology of TiO_2NPs prepared by green synthesis, Figure 3

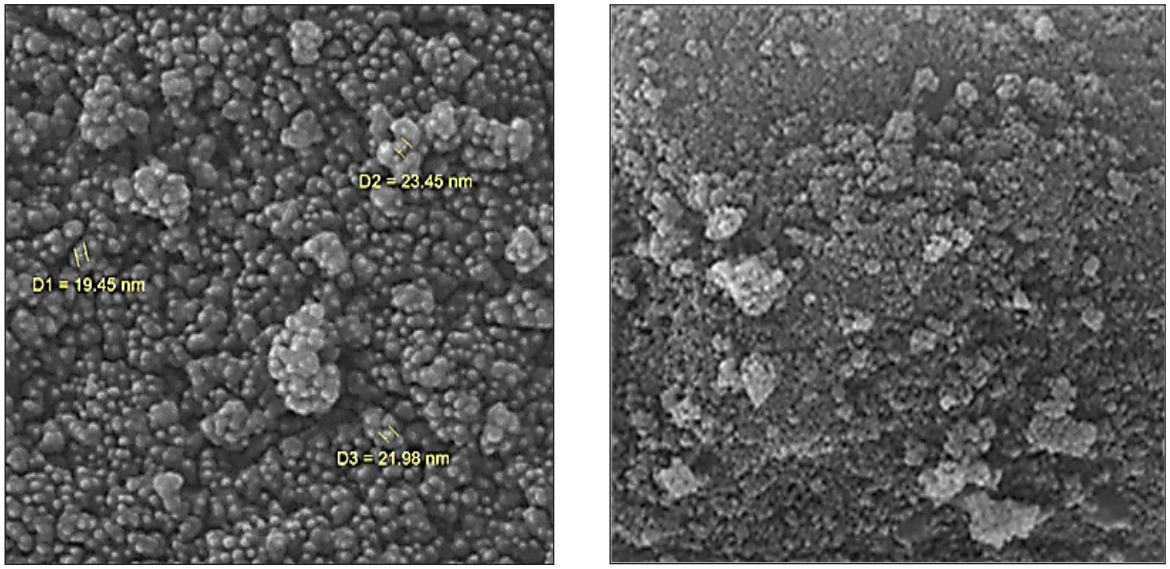

Fig. 3. SEM images of TiO_2NPs view field (left) 200 nm and (right) 1µm

(left) and (right) show the SEM images. The results of these images show the non-uniform distribution of TiO_2NPs, consisting of single particles or clusters with an average size (21 nm) diameter. Also, it is shown from a closer view that the rough surface's slight agglomerations due to high calcination temperature accelerate the crystal growth of TiO_2NPs.

Figure 4 shows an EDAX analysis used to prepare TiO2NPs. The results are described in Table 1, which shows the atomic percentage of oxygen and titanium-grown nanoparticles. This can conclude the right ratio of titanium and oxygen with 1:2. The spectra show different elements from the watermelon rind compounds, as shown in Table 1.

3.1.2.X-ray diffraction (XRD)

Figure 5 shows the results of analyzing the X-ray spectra and studying the structure and crystallization of TiO_2NPs, starting with the Match phase analysis software.

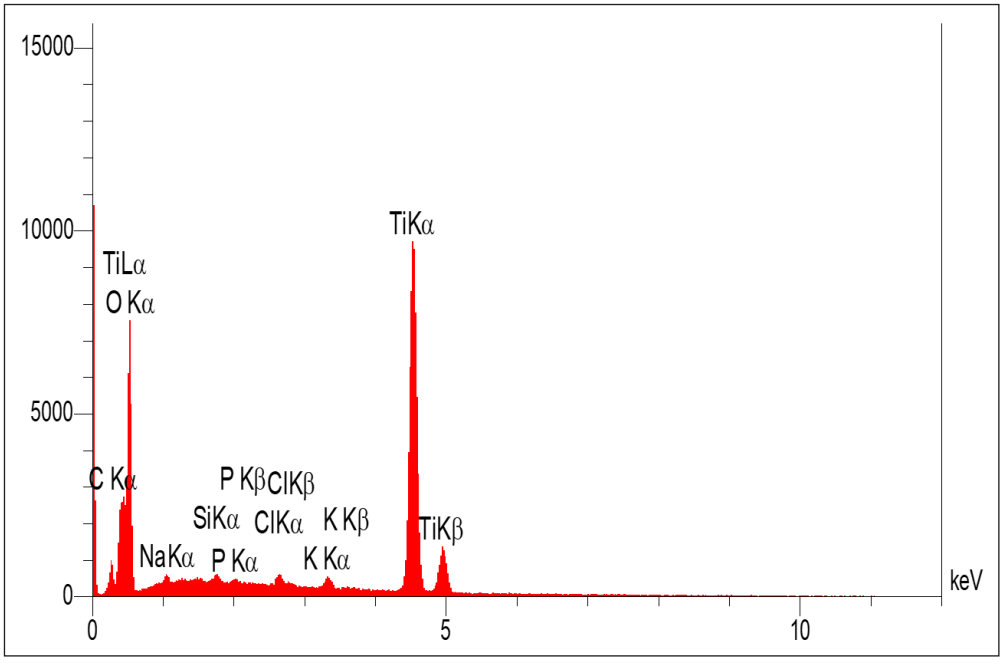

Fig. 4. TiO_2NPs EDAX spectrum

Table 1. Chemical composition of green TiO_2NPs in terms of weight and atomic percentage from (EDAX) measurement

Elements	Weight percentage (Wt. %)	Atomic percentage (%)
C	4.21	7.39
O	54.22	71.39
Na	3.18	2.92
Si	1.67	1.32
P	1.44	0.98
Cl	2.11	1.25
K	2.00	1.08
Ti	31.08	13.76
Total	100.00	100.00

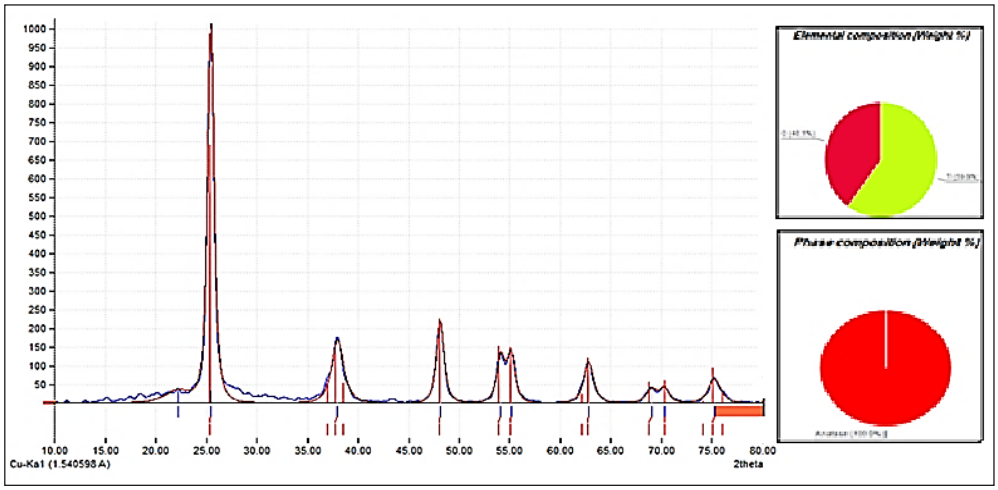

Fig. 5. XRD pattern of green synthesis TiO_2NPs

The diffraction peaks sharp spectrum appeared at 2θ = 22.20°, 25.45°, 38.00°, 48.15°, 54.13°, 55.13°,62.83°, 69.05°, 70.30°, and 75.25°. The spectrum matches with anatase phase patterns of TiO_2NPs from (COD card No. 96-901-5930) [46], with a tetragonal crystal plane and average crystallite size for the TiO_2NPs estimated according to the Debye–Scherrer's Equation 3 [47].

$$D = \frac{K*\lambda}{\beta * \mathrm{Cos}\,\theta} \qquad \text{(Eq.3)}$$

Where K represents the Scherrer constant (0.94), D is the nanoparticle crystalline size, λ is the X-ray wavelength (1.54 A°), θ is the Bragg's diffraction angle, and β is the peak width at half maximum. The average particle size has been calculated in Match software to be (26.69 nm) as shown in Figure 6.

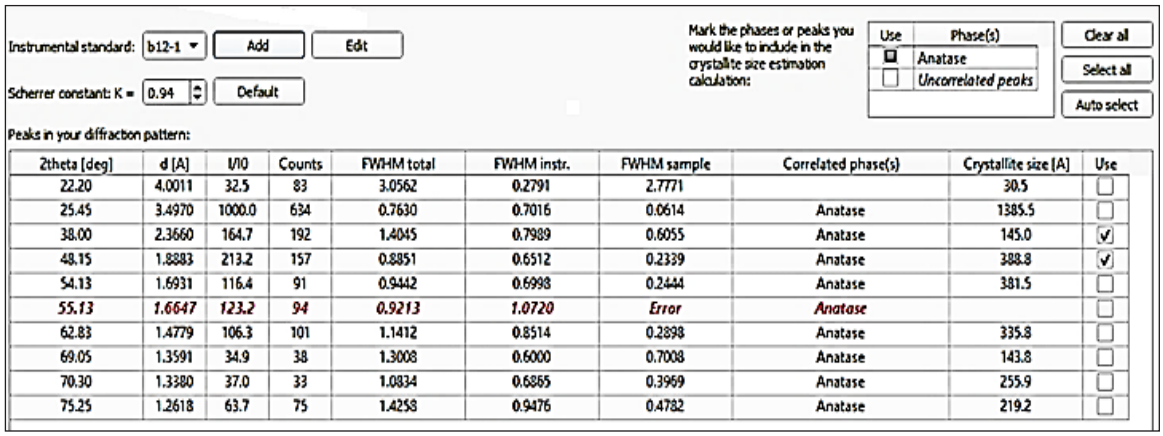

2theta [deg]	d [A]	I/I0	Counts	FWHM total	FWHM instr.	FWHM sample	Correlated phase(s)	Crystallite size [A]	Use
22.20	4.0011	32.5	83	3.0562	0.2791	2.7771		30.5	☐
25.45	3.4970	1000.0	634	0.7630	0.7016	0.0614	Anatase	1385.5	☐
38.00	2.3660	164.7	192	1.4045	0.7989	0.6055	Anatase	145.0	☑
48.15	1.8883	213.2	157	0.8851	0.6512	0.2339	Anatase	388.8	☑
54.13	1.6931	116.4	91	0.9442	0.6998	0.2444	Anatase	381.5	☐
55.13	*1.6647*	*123.2*	*94*	*0.9213*	*1.0720*	*Error*	*Anatase*		☐
62.83	1.4779	106.3	101	1.1412	0.8514	0.2898	Anatase	335.8	☐
69.05	1.3591	34.9	38	1.3008	0.6000	0.7008	Anatase	143.8	☐
70.30	1.3380	37.0	33	1.0834	0.6865	0.3969	Anatase	255.9	☐
75.25	1.2618	63.7	75	1.4258	0.9476	0.4782	Anatase	219.2	☐

Fig. 6. TiO_2NPs Crystallite size calculation

3.1.3. FTIR spectroscopy study

The FTIR spectroscopy of both watermelon rind and prepared TiO_2NPs powders was carried out to determine functional groups as shown in Figure 7. TiO_2NPs spectra (a and b) show three spectrum peaks, the observed peaks at 3452.43 cm^{-1} and 3431.13 cm^{-1}, which are stretching vibration asymmetric and symmetric attributed to the hydroxyl group in (Ti-OH) [48]. The band observed peak in 1618.17 cm^{-1} attributed to the binding vibration of the (OH) group in the water molecule, which adsorbed on the surface of TiO_2NPs [49,50], the peaks at the broadband from 800 to 400 cm^{-1} region is attributed to the Ti-O stretching and Ti-O-Ti vibration absorption from the anatase TiO_2NPs [51,52].

3.1.4. Atomic force microscopy (AFM)

AFM carried out the topography analysis phases of TiO_2NPs. The results show spherical nanoparticles. An image topographic roughness inspection showed an average size of 9nm, as shown in Figure 8.

3.2. Photodegradation Studies

3.2.1. Absorption of MB dye

The concentration of the experimental part chosen 20ppm (6×10^{-5}M) at 662 nm wavelength and (0.680) absorbance as shown in Figure 9, by reference to Beer's law, this concentration of 20ppm which lies between (0.2-0.7) absorbances with least errors and best range for measurements [53].

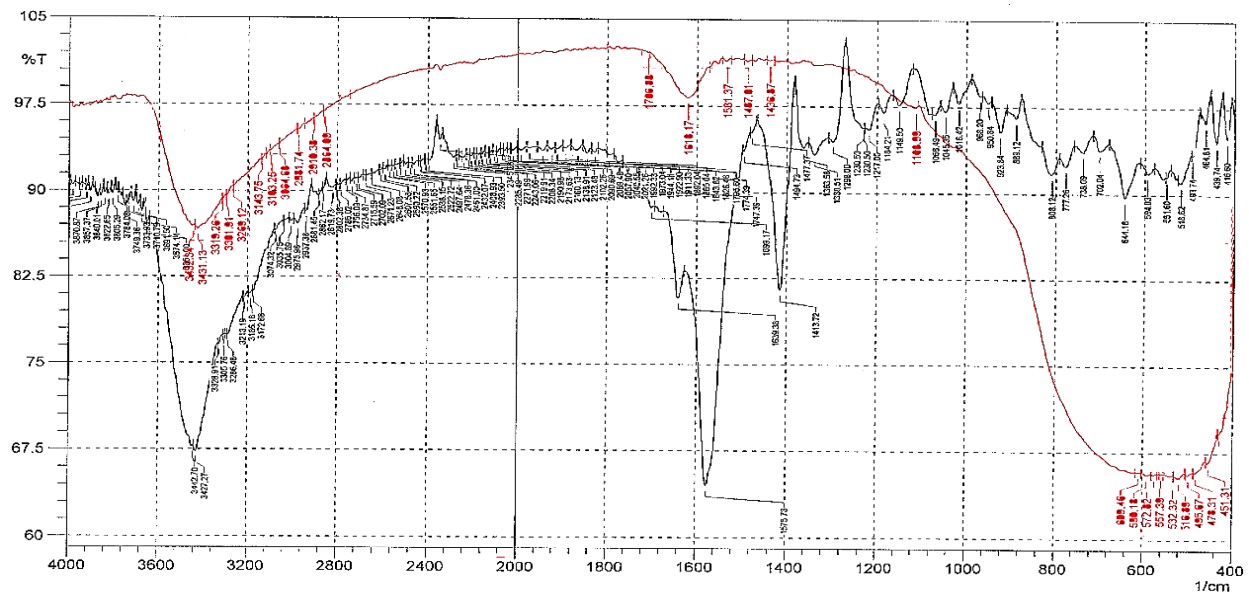

Fig.7. FTIR pattern (a) green synthesis TiO_2NPs (**b**) watermelon rind

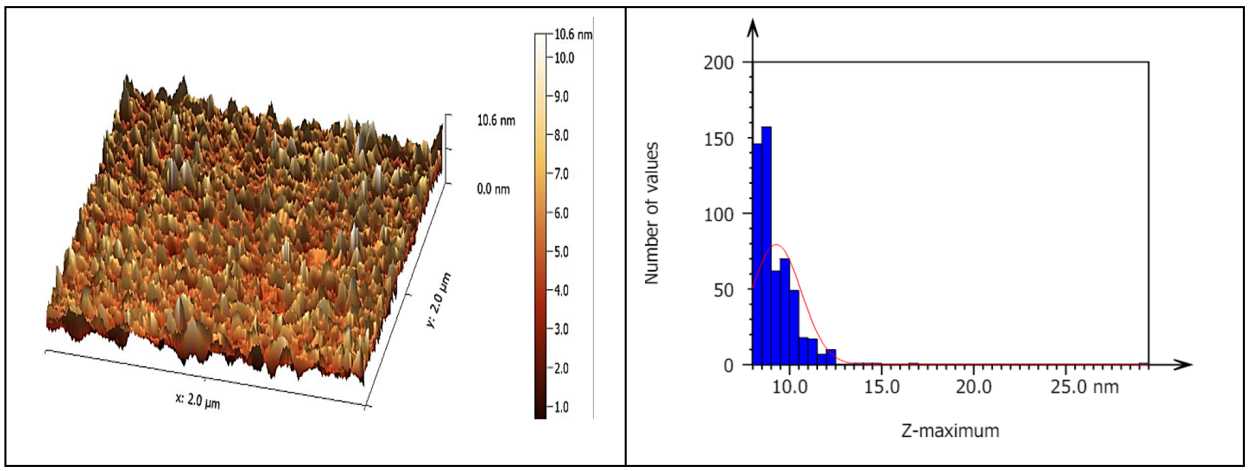

Fig. 8. TiO_2NPs Atomic force microscopy analysis

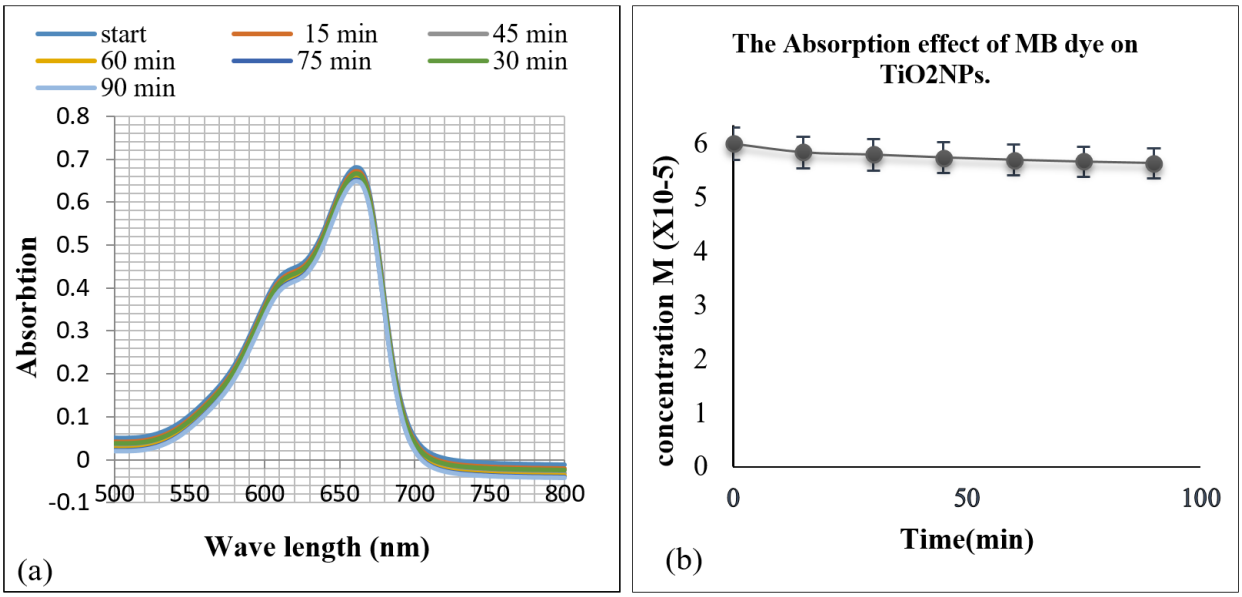

Fig. 9. UV-Vis of MB (**a**) Absorbance vs wavelength (nm), (**b**) Concentration vs time

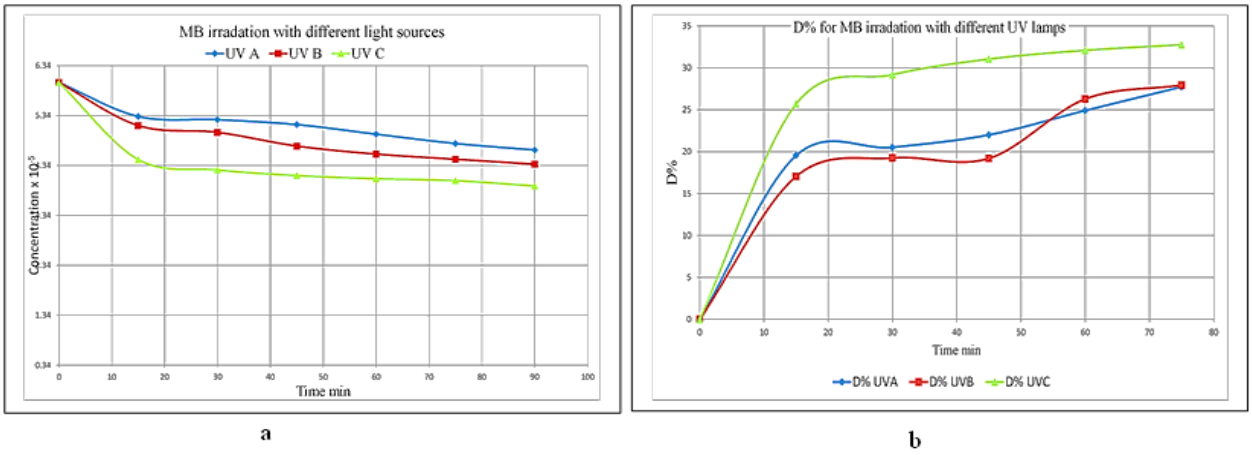

Fig. 10. (a) MB irradiation with different UV-light sources, (b) D% for MB irradiation with different UV lamps, both experiments ([MB] = 20 ppm; TiO_2NPs loading = none)

3.2.2.Irradiation of MB dye with different UV-light sources

Irradiation of MB dye with different lamps (UV-A, UV-B, UV-C) without loading photocatalyst: All these experiments show the MB decreasing in concentration with time in different percentages. Also, the photodegradation process increases with different percentages, as shown in Figures 10 and b. The results show that photodegradation for UVC = 34%, and both UVB and UVA results are 29%.

3.2.3. Photocatalyst loading for photodegradation of methylene blue

The photodegradation of methylene blue with loading (0.05g) TiO_2NPs photocatalyst has been carried out in (90) minutes with irradiation by three different UV lumps, which are UV-A (365 nm), UV-B (311nm), UV-C (254 nm), as in Figure11a, which indicate the decrease of MB dye concentration with time. UV-C reaches 99.9% degradation of MB dye after 75 minutes, while UV-B reaches 96% degradation, and UV-A reaches 50% degradation

after 90 minutes. Figure 11b shows Regression correlation values R2 for each UV tube, UV-A, UV-B, and UV-C. Figures 11c and 11d show that the degradation percentage increases (D%), and all experiments were done in (90) minutes.

The photodegradation of MB dye with UV-C is faster than that with UV-B and UV-A, indicating its photolysis capability, as it has a shorter penetration wavelength and high energy level. The photodegradation kinetic study follows a first-order reaction [54,55]. A graph of ln(C0/Ct) against time was plotted, as shown in Figure 11b, with a high regression correlation value.

4. Conclusion

This study shows the easy procedure to produce TiO_2NPs by the sol-gel method, which was successfully prepared using watermelon rinds for the green synthesis method. The critical role of green synthesis is to prepare metal nanoparticles with their advantages and acceptances in wastewater treatment and for the environment. Photodegrading using semiconductor TiO_2NPs, with a new photoreactor system design, is highly effective in degrading methylene blue dye under different ultraviolet light irradiation. This process can break down harmful organic compounds into less toxic

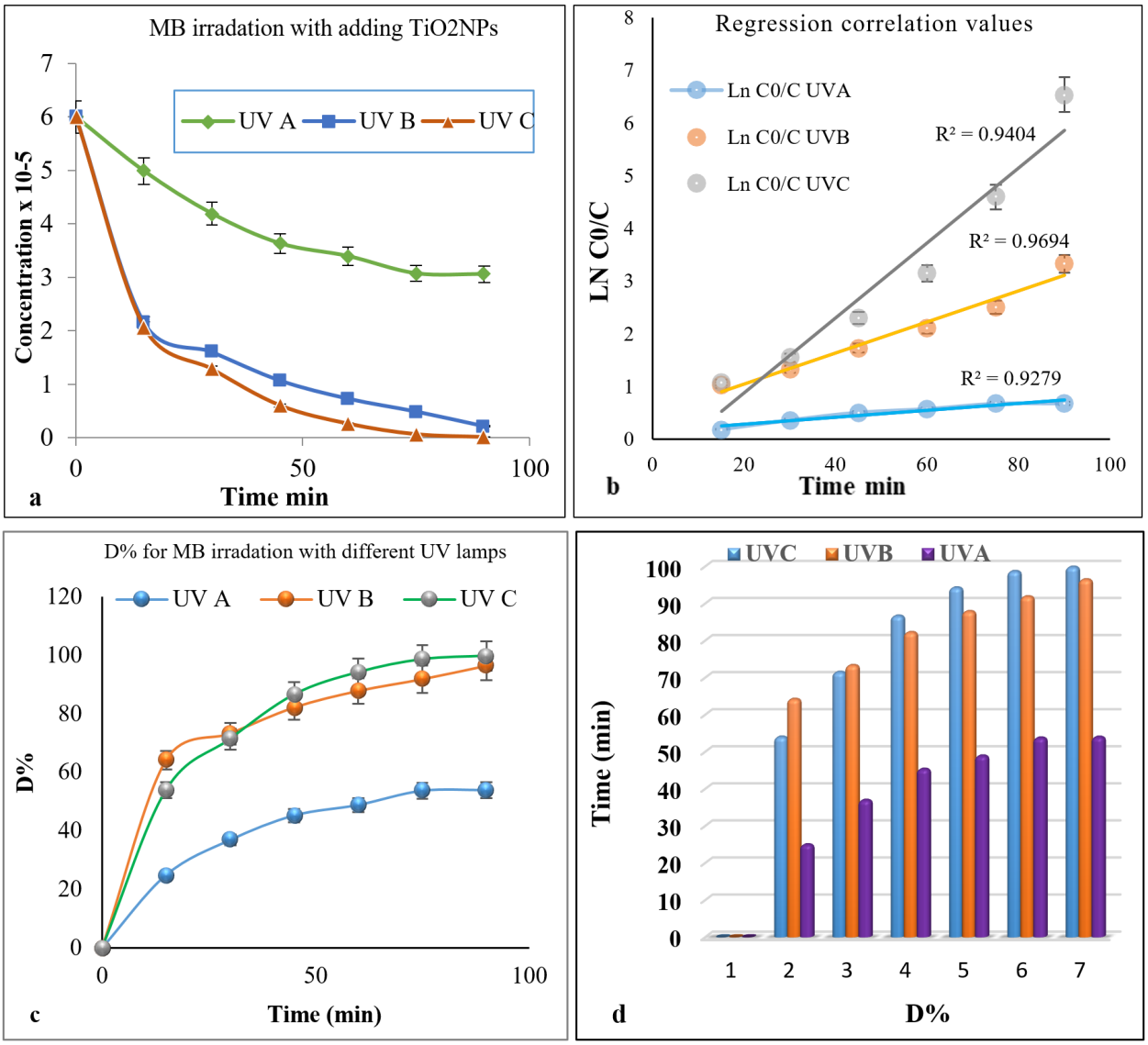

Fig. 11. (**a**) MB Conc. Decrease with time (**b**) Regression correlation values R^2, (**c**) and (**d**) D% for MB irradiation with different UV lamps. all experiments ([MB] = 20 ppm; TiO_2 NPs loading = 0.05g)

or harmless substances. This is particularly useful for treating industrial wastewater and contaminated natural water. The results of the photodegradation process, with loading (0.05g) of TiO_2NPs, indicate the effectiveness of ultraviolet C rays, as they have higher energy and shorter wavelengths. Compared to ultraviolet B and ultraviolet A, this makes them very effective at breaking chemical bonds in methylene blue dye (20 mg L^{-1}, pH=6.4). This indicates their capability in photolysis, as they have a shorter penetration wavelength and high energy level.

5. Acknowledgements

The authors thank the Department of Chemistry, College of Science, University of Baghdad, Baghdad, Iraq.

6. References

[1] N. Joudeh, D. Linke, Nanoparticle classification, physicochemical properties, characterization, and applications: a comprehensive review for biologists, J. Nanobiotechnol., 20 (2022) 262. https://doi.org/10.1186/s12951-022-01477-8.

[2] B. Mekuye, B. Abera, Nanomaterials: An overview of synthesis, classification, characterization, and applications, Nano Select, 4 (2023) 486–501. https://doi.org/10.1002/nano.202300038

[3] R. Griffo, F. Di Natale, M. Minale, M. Sirignano, A. Parisi, C. Carotenuto, Analysis of carbon nanoparticle coatings via wettability, Nanomater., 14 (2024) 301. https://doi.org/10.3390/nano14030301

[4] M. Mohammadi Asl, N. Mansouri, S. A. R. Haji Seyed Mirzahosseini, F. Atabi, Simultaneity comparative evaluation of toluene removal from the air by adsorption and UV semi-degradation-based adsorption procedure, Int. J. Environ. Sci. Technol., 21 (2024) 6677-6694. https://doi.org/10.1007/s13762-024-05503-0

[5] M. M. Asl, F. Atabi, Functionalized graphene oxide with bismuth and titanium oxide nanoparticles for efficiently removing formaldehyde from the air by photocatalytic degradation–adsorption process, J. Anal. Test., 7 (2023) 444-458. https://doi.org/10.1007/s41664-023-00272-0

[6] Y.N. Slavin, J. Asnis, U.O. Häfeli, H. Bach, Metal nanoparticles: Understanding the mechanisms behind antibacterial activity, J. Nanobiotechnol., 15 (2017) 65. https://doi.org/10.1186/s12951-017-0308-z

[7] M. Arjomandi, H. Shirkhanloo, A Review: Analytical methods for heavy metals determination in environment and human samples, Anal. Methods Environ. Chem. J., 2 (2019) 97–126. https://doi.org/10.24200/amecj.v2.i03.73

[8] S. Syamsol Bahri, Z. Harun, S. Khadijah Hubadillah, W. Norhayati Wan Salleh, N. Rosman, N. Hasliza Kamaruddin, F. Hafeez Azhar, N. Sazali, R. Adiba Raja Ahmad, H. Basri, Review on recent advance biosynthesis of TiO2 nanoparticles from plant-mediated materials: characterization, mechanism and application, IOP Conf. Ser. Mater. Sci. Eng., 1142 (2021) 012005. https://doi.org/10.1088/1757-899x/1142/1/012005

[9] P. Sathishkumar, F.L. Gu, Q. Zhan, T. Palvannan, A.R. Mohd Yusoff, Flavonoids mediated 'Green' nanomaterials: A novel nanomedicine system to treat various diseases – Current trends and future perspective, Mater. Lett., 210 (2018) 26–30. https://doi.org/10.1016/j.matlet.2017.08.078

[10] Z. Zahra, Z. Habib, S. Chung, M.A. Badshah, Exposure route of TiO2 nps from industrial applications to wastewater treatment and their impacts on the agro-environment, Nanomater., 10 (2020) 1–22. https://doi.org/10.3390/nano10081469

[11] A.K. Abass, W.N.J. Al Sieadi, A.K.M.A. Al-Sammarraie, Investigation of the electrical, compositional, and magnetic features of hybrid lead oxide nanocomposites, Eurasian Chem. Commun., 4 (2022) 1044–1053. https://doi.org/10.22034/ecc.2022.344547.1479

[12] N. Rousta, M. Aslan, M. Yesilcimen Akbas, F. Ozcan, T. Sar, M.J. Taherzadeh, Effects of

fungal based bioactive compounds on human health: Review paper, Crit. Rev. Food Sci. Nutr., 64 (2023) 7004-7027. https://doi.org/10.1080/10408398.2023.2178379

[13] V. Tadioto, A. Giehl, R.D. Cadamuro, I.Z. Guterres, A.A. dos Santos, S.K. Bressan, L. Werlang, B.U. Stambuk, G. Fongaro, I.T. Silva, S.L. Alves, Bioactive compounds from and against Yeasts in the one health context: A comprehensive review, Ferment., 9 (2023) 363. https://doi.org/10.3390/fermentation9040363

[14] Y. Xie, Q. Peng, Y. Ji, A. Xie, L. Yang, S. Mu, Z. Li, T. He, Y. Xiao, J. Zhao, Q. Zhang, Isolation and identification of antibacterial bioactive compounds from bacillus megaterium L2, Front. Microbiol., 12 (2021) 645484. https://doi.org/10.3389/fmicb.2021.645484

[15] O. Ying Qian, S. Harith, M. Razif Shahril, N. Shahidan, Bioactive compounds in Cucumis melo L. and its beneficial health effect scoping review, Malays. Appl. Biol., 48 (2019) 11-23. https://jms.mabjournal.com/index.php/mab/article/view/1872

[16] A. Rana, K. Yadav, S. Jagadevan, A comprehensive review on green synthesis of nature-inspired metal nanoparticles: Mechanism, application and toxicity, J. Clean. Prod., 272 (2020)122880. https://doi.org/10.1016/j.jclepro.2020.122880

[17] A. Tsakni, A. Chatzilazarou, E. Tsakali, A.G. Tsantes, J. Van Impe, D. Houhoula, Identification of bioactive compounds in plant extracts of greek flora and their antimicrobial and antioxidant activity, Sep. J., 10 (2023) 373. https://doi.org/10.3390/separations10070373

[18] F.M. Vella, R. Calandrelli, D. Cautela, B. Laratta, Natural antioxidant potential of Melon Peels for fortified foods, Foods, 12 (2023) 2523. https://doi.org/10.3390/foods12132523

[19] O. Sytar, I. Smetanska, Bioactive compounds from natural sources (2020, 2021), Molecules, 27 (2022) 1929. https://doi.org/10.3390/molecules27061929

[20] M. Loi, C. Paciolla, A.F. Logrieco, G. Mulè, Plant bioactive compounds in pre- and postharvest management for aflatoxins reduction, Front. Microbiol., 11 (2020) 243. https://doi.org/10.3389/fmicb.2020.00243

[21] M. Kussmann, D.H. Abe Cunha, S. Berciano, Bioactive compounds for human and planetary health, Front. Nutr. 10 (2023) 1193848. https://doi.org/10.3389/fnut.2023.1193848

[22] P.M. Rolim, G.P. Fidelis, C.E.A. Padilha, E.S. Santos, H.A.O. Rocha, G.R. Macedo, Phenolic profile and antioxidant activity from peels and seeds of melon (Cucumis melo L. var. reticulatus) and their antiproliferative effect in cancer cells, Braz. J. Med. Biol. Res., 51 (2018) e6069. https://doi.org/10.1590/1414-431x20176069

[23] A.S. Rini, Y. Rati, R. Fadillah, R. Farma, L. Umar, Y. Soerbakti, Improved photocatalytic activity of ZnO film prepared via green synthesis method using red watermelon rind extract, Evergreen, 9 (2022) 1046–1055. https://doi.org/10.5109/6625718

[24] N. Basavegowda, K.H. Baek, Multimetallic nanoparticles as alternative antimicrobial agents: Challenges and perspectives, Molecules, 26 (2021) 912. https://doi.org/10.3390/molecules26040912

[25] M. Nadeem, M. Navida, K. Ameer, A. Iqbal, F. Malik, M.A. Nadeem, H. Fatima, A. Ahmed, A. Din, A comprehensive review on the watermelon phytochemical profile and their bioactive and therapeutic effects, Korean J. Food Preserv., 29 (2022) 546–576. https://doi.org/10.11002/KJFP.2022.29.4.546

[26] A.S. Rini, H. Adzani, T.S.L. Husain, M.P. Deraf, Y. Rati, Y. Hamzah, Structural and morphological studies of silver nanoparticles prepared using citrullus lanatus rind extract, in: AIP Conf. Proc., Am. Institute Phys. Inc., 2021. https://doi.org/10.1063/5.0037960

[27] W. Chums-ard, D. Fawcett, C.C. Fung, G.E.J. Poinern, Biogenic synthesis of gold nanoparticles from waste watermelon and their antibacterial activity against Escherichia coli and Staphylococcus epidermidis, Int. J. Res. Med. Sci., 7 (2019) 2499. https://doi.

org/10.18203/2320-6012.ijrms20192874

[28] S. Teimoori, H. Shirkhanloo, A.H. Hassani, M. Panahi, N. Mansouri, Rapid extraction of BTEX in water and milk samples based on functionalized multi-walled carbon nanotubes by dispersive homogenized-micro-solid phase extraction, Food Chem., 421 (2023) 136229. https://doi.org/10.1016/j.foodchem.2023.136229

[29] S. Teimoori, H. Shirkhanloo, A.H. Hassani, M. Panahi, N. Mansouri, New extraction of toluene from water samples based on nano-carbon structure before determination by gas chromatography, Int. J. Environ. Sci. Technol., 20 (2023) 6589–6608. https://doi.org/10.1007/s13762-023-04906-9

[30] J. Lee, U. Von Gunten, J.H. Kim, Persulfate-based advanced Oxidation: Critical assessment of opportunities and roadblocks, Environ. Sci. Technol., 54 (2020) 3064–3081. https://doi.org/10.1021/acs.est.9b07082

[31] J. Rakhtshah, H. Shirkhanloo, N. Esmaeili, A rapid extraction of toxic styrene from water and wastewater samples based on hydroxyethyl methylimidazolium tetrafluoroborate immobilized on MWCNTs by ultra-assisted dispersive cyclic conjugation-micro-solid phase extraction, Microchem. J., 170 (2021) 106759. https://doi.org/10.1016/j.microc.2021.106759

[32] Z. Karamzadeh, A novel biostructure sorbent based on CysSB/MetSB@ MWCNTs for separation of nickel and cobalt in biological samples by ultrasound assisted-dispersive ionic liquid- suspension solid phase microextraction, J. Pharm. Biomed. Anal., 172 (2019) 285-294. https://doi.org/10.1016/j.jpba.2019.05.003

[33] A. Faghihi-Zarandi, J. Rakhtshah, B. B. Yarahmadi, A rapid removal of xylene vapor from environmental air based on bismuth oxide coupled to heterogeneous graphene/graphene oxide by UV photo-catalectic degradation-adsorption procedure, J. Environ. Chem. Eng., 8 (2020) 104193. https://doi.org/10.1016/j.jece.2020.104193

[34] A. Romandini, A. Pani, P.A. Schenardi, G.A.C. Pattarino, C. De Giacomo, F. Scaglione, Antibiotic resistance in pediatric infections: Global emerging threats, predicting the near future, Antibiotics, 10 (2021) 393. https://doi.org/10.3390/antibiotics10040393

[35] E.Y. Ahn, S.W. Shin, K. Kim, Y. Park, Facile Green Synthesis of titanium dioxide nanoparticles by upcycling mangosteen (Garcinia mangostana) pericarp extract, Nanoscale Res. Lett., 17 (2022) 40. https://doi.org/10.1186/s11671-022-03678-4

[36] M. Ghosh, P. Chowdhury, A.K. Ray, Photocatalytic activity of aeroxide tio2 sensitized by natural dye extracted from mangosteen peel, Catal., 10 (2020) 917. https://doi.org/10.3390/catal10080917

[37] S. Kumar, W. Ahlawat, G. Bhanjana, S. Heydarifard, M.M. Nazhad, N. Dilbaghi, Nanotechnology-based water treatment strategies, J. Nanosci. Nanotechnol., 14 (2014) 1838–1858. https://doi.org/10.1166/jnn.2014.9050

[38] B. Abebe, H.C.A. Murthy, E. Amare, Summary on adsorption and photocatalysis for pollutant remediation: Mini review, J. Encapsulation Adsorp. Sci., 08 (2018) 225–255. https://doi.org/10.4236/jeas.2018.84012

[39] M.S. Anantha, S. Olivera, C. Hu, B.K. Jayanna, N. Reddy, K. Venkatesh, H.B. Muralidhara, R. Naidu, Comparison of the photocatalytic, adsorption and electrochemical methods for the removal of cationic dyes from aqueous solutions, Environ. Technol. Innov., 17 (2020) 100612. https://doi.org/10.1016/j.eti.2020.100612

[40] S. Teimoori, H. Shirkhanloo, A.H. Hassani, M. Panahi, N. Mansouri, An immobilization of aminopropyl trimethoxysilane-phenanthrene carbaldehyde on graphene oxide for toluene extraction and separation in water samples, Chemosphere, 316 (2023) 137800. https://doi.org/10.1016/j.chemosphere.2023.137800

[41] S. Woo, H. Jung, Y. Yoon, Real-Time UV/VIS spectroscopy to observe photocatalytic degradation, Catal., 13 (2023) 683. https://doi.org/10.3390/catal13040683

[42] S. Alkaykh, A. Mbarek, E.E. Ali-Shattle, Photocatalytic degradation of methylene blue dye in aqueous solution by MnTiO3 nanoparticles under sunlight irradiation, Heliyon, 6 (2020) e03663. https://doi.org/10.1016/j.heliyon.2020.e03663

[43] G. V. Geetha, R. Sivakumar, C. Sanjeeviraja, V. Ganesh, Photocatalytic degradation of methylene blue dye using ZnWO4 catalyst prepared by a simple co-precipitation technique, J. Solgel Sci. Technol., 97 (2021) 572–580. https://doi.org/10.1007/s10971-021-05480-7

[44] T. Nakayama, R. Honda, K. Kuwata, S. Usui, B. Uno, Electrochemical and mechanistic study of reactivities of α-, β-, γ-, and δ-tocopherol toward electrogenerated superoxide in N,N-dimethylformamide through proton-coupled electron transfer, Antioxidants, 11 (2022) 9. https://doi.org/10.3390/antiox11010009

[45] J. Iqbal, B.A. Abbasi, T. Yaseen, S.A. Zahra, A. Shahbaz, S.A. Shah, S. Uddin, X. Ma, B. Raouf, S. Kanwal, W. Amin, T. Mahmood, H.A. El-Serehy, P. Ahmad, Green synthesis of zinc oxide nanoparticles using Elaeagnus angustifolia L. leaf extracts and their multiple in vitro biological applications, Sci. Rep., 11 (2021) 20988. https://doi.org/10.1038/s41598-021-99839-z

[46] X. Jaramillo-Fierro, J. Ramón, E. Valarezo, Cyanide removal by $ZnTiO_3/TiO_2/H_2O_2$/UVB system: A theoretical-experimental approach, Int. J. Mol. Sci., 24 (2023) 16446. https://doi.org/10.3390/ijms242216446

[47] R. Ahmadiasl, G. Moussavi, S. Shekoohiyan, F. Razavian, Synthesis of Cu-doped TiO2 nanocatalyst for the enhanced photocatalytic degradation and mineralization of gabapentin under UVA/LED irradiation: Characterization and photocatalytic activity, Catal., 12 (2022) 1310. https://doi.org/10.3390/catal12111310

[48] X. Li, Y. Gao, H. Xiong, Z. Yang, The electrochemical redox mechanism and antioxidant activity of polyphenolic compounds based on inlaid multi-walled carbon nanotubes-modified graphite electrode, Open Chem., 19 (2021) 961–973. https://doi.org/10.1515/chem-2021-0087

[49] R.D. Desiati, M. Taspika, E. Sugiarti, Effect of calcination temperature on the antibacterial activity of TiO_2/Ag nanocomposite, Mater. Res. Express., 6 (2019) 095059. https://doi.org/10.1088/2053-1591/ab155c

[50] D.R. Eddy, S.N. Ishmah, M.D. Permana, M.L. Firdaus, I. Rahayu, Y.A. El-Badry, E.E. Hussein, Z.M. El-Bahy, Photocatalytic phenol degradation by silica-modified titanium dioxide, Appl. Sci., 11 (2021) 9033. https://doi.org/10.3390/app11199033

[51] M. M. Eskandari, B. Kalantari, Dispersive liquid-liquid microextraction based on task-specific ionic liquids for determination and speciation of chromium in human blood, J. Anal. Chem., 70 (2015) 1448-1455. https://doi.org/10.1134/S1061934815120072

[52] K.E. Al Ani, A.E. Ramadhan, W.N. Al Sieadi, Fourier-transform infrared spectroscopic study of plasticization effects on the photodegradation of poly(fluorostyrene) isomers films, J. Vinyl Add. Technol., 24 (2018) 75–83. https://doi.org/10.1002/vnl.21529

[53] W.B. Baker, A.B. Parthasarathy, D.R. Busch, R.C. Mesquita, J.H. Greenberg, A.G. Yodh, Modified beer-lambert law for blood flow, Biomed. Opt. Express, 5 (2014) 4053. https://doi.org/10.1364/boe.5.004053

[54] A.S. Rini, Y. Rati, R. Dewi, S. Putri, Investigating the influence of precursor concentration on the photodegradation of methylene blue using biosynthesized ZnO from pometia pinnata leaf extracts, Baghdad Sci. J., 20 (2023) 2532–2539. https://doi.org/10.21123/bsj.2023.9176

[55] S.A. Mousa, S. Tareq, E.A. Muhammed, Studying the photodegradation of Congo red dye from aqueous solutions using bimetallic Au-Pd/TiO_2 photocatalyst, Baghdad Sci. J., 18 (2021) 1261–1268. https://doi.org/10.21123/BSJ.2021.18.4.1261

Anal. Methods Environ. Chem. J. 8 (1) (2025) 39-53

AMECJ

Research Article, Issue 1
Analytical Methods in Environmental Chemistry Journal
Journal home page: www.amecj.com/ir

Electrochemical Spectroscopy: Evaluation and determination of Carbon dioxide reduction based on tin oxide doped ethyl cellulose as electrocatalyst by H-type cell and reversible hydrogen electrode

Ali Hussein Ghanim[a, *] **and Khulood Abid Salah**[b]
[a]*University of Baghdad, Collage of Science, Chemistry Department, Iraq*
[b]*University of Baghdad, Collage of Science, Chemistry Department, Iraq*

ARTICLE INFO:

Received 17 Nov 2024
Revised form 2 Feb 2025
Accepted 26 Feb 2025
Available online 28 March 2025

Keywords:
CO_2 reduction,
Catalyst,
Tin oxide,
Electrochemical spectroscopy,
Electrocatalytic reduction

ABSTRACT

Electrocatalytic Carbon dioxide (CO_2) reduction to carbon products on SnO_2-doped ethyl cellulose (EC) was prepared by dispersion of nano-sized tin oxide (SnO_2, 25 nm) in ethyl cellulose through sonication by an ultrasonic probe (600 W) for 60 min. The SnO_2-EC catalyst is characterized by field emission scanning electron microscopy (FESEM), atomic force microscopy (AFM), and X-ray diffraction (XRD). The electrocatalytic performance for CO_2 reduction was investigated by loading SnO_2-EC paste on a 306S.S. rotated disc. The CO_2 electroreduction occurred in an H-type cell with three electrodes in 0.1M $KHCO_3$ saturated with CO_2 at different potential ranges of -1.0 V to -1.8V vs. reversible hydrogen electrode (RHE) for 3 hours. The oxygen content of liquid products was collected and determined using a chemical oxygen demand (COD,15–300 mg L^{-1}) kit, which was quantified by a colorimeter. A higher oxygen content concentration was obtained at -1.2V vs. RHE (-2 mA cm^{-2}) and found to be 235 mg L^{-1}, while the oxygen content tends to decrease with a more negative applied potential of -1.4V, -1.6V, and 1.8V vs. RHE with current densities of -2.5 mA cm^{-2}, -7.3 mA cm^{-2}, and -15.6 mA cm^{-2}, respectively.

1. Introduction

The scientific community attributes the causes of climate change to the increased production of carbon dioxide (CO_2) through human activity. CO_2 is one of the principal greenhouse gases contributing to global warming. To minimize the continuous growth of its atmospheric concentration, CO_2 can be used as raw material to obtain products with high energy value [1]. Electrochemical CO_2 reduction reaction (CO_2RR) is recognized as one of the most attractive and environmentally friendly approaches for reducing CO_2 emissions. This approach is especially effective when integrated with the utilization of renewable energies [2-3]. Carbon dioxide (CO_2) is a highly stable molecule that requires considerable energy to transform into useful compounds. Scientists have identified several methods to convert CO_2 into valuable chemicals, including carbon monoxide (CO) [4]. hydrocarbons, and oxygenated hydrocarbons. These methods include gas-phase, liquid-phase, electrochemical, and photocatalytic reactions. Gas-phase reactions involve dry reforming of methane ($CH_4 + CO_2 \rightarrow 2CO + 2H_2$) and hydrogenation of CO_2 ($CO_2 + H_2 \rightarrow CO + H_2O$, which is also known as the water-gas shift reversal reaction; $CO_2 + 4H_2 \rightarrow CH_4 + 2H_2O$). On the other hand, the liquid-phase technique uses CO_2 dissolved

*Corresponding Author: Ali Hussein Ghanim
Email: ali.ghanem@sc.uobaghdad.edu.iq
https://doi.org/10.24200/amecj.v8.i01.364

in an aqueous solution ($CO_{2(aq)} + H_{2(aq)} \rightarrow COOH$) to produce formic acid (HCOOH) [4–8]. Carbon dioxide (CO_2) electroreduction is a process that involves different numbers of electrons and protons to produce specific products. Metallic catalysts such as gold (Au), silver (Ag), palladium (Pd), zinc (Zn), lead (Pb), bismuth (Bi), tin (Sn), indium (In), mercury (Hg), and copper (Cu) have shown remarkable selectivity towards different products. Depending on the catalyst used, the major products of CO_2 electroreduction can be classified into three categories: (1) CO is produced by Au, Ag, Pd, and Zn; (2) formic acid/formate is produced by Pb, Bi, Sn, In, and Hg; [9–11] (3) various hydrocarbons are produced by Cu [12–15]. Despite this promising progress, these catalysts are still far from being industrially applicable, especially regarding current density. To have a sustainable impact on the environment and climate, it is crucial to conduct industrially relevant research. Therefore, urgent efforts are needed to develop more efficient and cost-effective catalysts for CO_2 electroreduction [16]. The CO2 reduction reaction (CO2RR) process faces challenges such as high overpotential and low current density [17-18]. Additionally, if the reaction occurs in an aqueous solution, the hydrogen evolution reaction competes with the desired product formation [19]. Therefore, the selectivity of product formation is influenced by several factors, such as the concentration of CO_2 in the electrolyte, electrode potential, temperature, electrolyte solution, and electrocatalyst used [15]. Electrocatalytic reduction of CO_2, also known as CO_2RR, is a challenging process due to the thermodynamic stability of CO_2, which causes slow reaction kinetics. Moreover, CO_2 conversion often competes with hydrogen evolution reaction (HER), leading to reduced selectivity of carbon products. Therefore, there is a need for highly effective, selective, and stable electrocatalysts to meet the requirements for practical applications of CO_2RR [20]. In electrocatalysis, several techniques have been developed to improve the performance of catalysts. These methods include alloying, surface modification, element doping, oxidative treatment, and shape control [21]. Alloying is widely regarded as one of the most effective ways to enhance electrocatalytic activity. This is because bimetallic alloying can modify not only the conventional electronic and geometric structures but also the ensemble effects of the metal active sites. By introducing a second metal into the catalyst, alloying can create new active sites or modify the electronic properties of existing sites, leading to improved catalytic activity and selectivity. Overall, alloying as a strategy for enhancing electrocatalytic performance has shown great promise in many research studies [22-23]. Tin (Sn) based catalysts have recently emerged as a promising metal for catalyzing the electrochemical reduction of CO_2. These are highly efficient, selective, and cost-effective, making them an attractive alternative to noble metal-based catalysts [24]. Sn-based catalysts can selectively convert CO_2 to formate, a valuable chemical feedstock. A wide range of Sn-based catalysts has been reported for CO2RR, including single metals, alloys, oxides [25,26], sulfides, and hybrids with carbon nanomaterials such as carbon nanotubes and graphene. These hybrids offer improved catalytic activity and stability and enhanced selectivity towards formate production. Furthermore, Sn-based catalysts are eco-friendly, non-toxic, and abundant in nature, making them a sustainable alternative to traditional catalysts. Currently, formate and CO can achieve Faradaic efficiencies of ~ 100% and over 90%, respectively [27-31]. We experimented to test the effectiveness of adding ethyl cellulose (EC) to SnO_2 nanoparticles (NPs) and applying it onto a rotated disk of 306 stainless (306S.S) steel using the drop-casting technique. The resulting SnO_2-EC@306S.S electrode was used as a catalyst for CO_2 reduction. Ethylcellulose helps to improve the adhesion of SnO_2 NPs to the substrate and prevent degradation. We analyzed the structure and composition of the SnO_2-EC@306S.S electrode using various methods, including atomic force microscopy (AFM), Field emission scanning electron microscopy (FESEM), X-ray diffraction (XRD), and Fourier transform infrared spectroscopy (FT-IR). To evaluate the catalyst's efficiency in promoting the reduction of CO_2, we used an H-type cell equipped with three electrodes and a solution of 0.1M $KHCO_3$ with a continuous flow of CO_2 gas. We applied a negative potential ranging from -1.8V to -1V at intervals of 0.2V. The CO_2 liquid products were

analyzed using the chemical oxygen demand (COD) method, and it was found that the oxygen content reached a maximum value of 226 mgL^{-1} at a potential of -1.2 mV.

2. Material and Methods

2.1. Reagents

Tin oxide nanoparticles (SnO_2 NPs, 305nm, CAS No:18282-10-5) were purchased from Hongwu International Group, China. At the same time, ethyl cellulose (EC, 99%, CAS No:9004-57-3) was procured from Sigma Aldrich, Germany. Potassium hydrogen carbonate ($KHCO_3$, 99.99%, CAS No:298-14-6) was prepared from Fluke, Germany. Nafion (5 wt.%, CAS No:31175-20-9) solution was purchased from Wuhan Golden Kylin industry, and Ethanol (EtOH, 99.9%, CAS No:64-17-5) was purchased from Chem-lab company, Belgium. The carbon dioxide (CO_2, 99.999%, CAS No:124-38-9) and Nitrogen gas (N_2, 99.999%, CAS No:7727-37-9) supplied Gulf company for industrial gases, Baghdad, Iraq.

2.2. Characterization instruments

Field Emission-Scanning Electron Microscope (FE-SEM, Sigma VP-Zeiss equipped with EDS-EBSD-Mapping-Line, Oxford Instrument Co) was used to examine the morphology of SnO_2 and EC-SnO_2 catalysts. Additionally, an Atomic Force Microscope (CoreAFM, Nanosurf, Switzerland) was used to measure the coated catalyst's particle size, roughness, adhesion force, and hardness. XRD diffraction (PANalytical XPert Pro XRD, Philips, Holland) was employed to estimate grain size, and electrocatalytic CO_2 reduction was carried out using the Vertex One Potentiostat equipped with Electrochemical Impedance Spectroscopy (EIS, Ivium Technologies, Holland). Finally, a Colorimeter (Lovibond, Germany) was employed to measure COD content.

2.3. Preparation of SnO_2-Doped Ethyl Cellulose (SnO_2-EC)

In a one-neck round-bottom flask (25 mL), 8 mg of ethyl cellulose (EC) was dissolved in 20 mL of ethanol and sonicated for 30 min. Then, 92 mg of SnO_2 NPs was added to the solution, and the mixture was stirred at room temperature for 120 min. After that, the solution was concentrated by evaporating the solvent at 50°C for 60 min. The thick solution was decanted into a Petri dish, and the yellow powder was collected and dried at 60°C for 10 hours. The resultant composite was donated as SnO_2-EC.

2.4. Preparation of Working Electrode (SnO_2-EC@306S.S)

To prepare the catalyst, 50 mg of SnO_2-EC powder was mixed with 500 µL ethanol and 100 µL Nafion (5 wt.%). An ultrasonic probe sonicated the mixture for 10 minutes, after which thick ink dropped-casted onto a rotating disc of 1 cm^2 306 stainless steel and allowed to dry at room temperature, as illustrated in Figure 1.

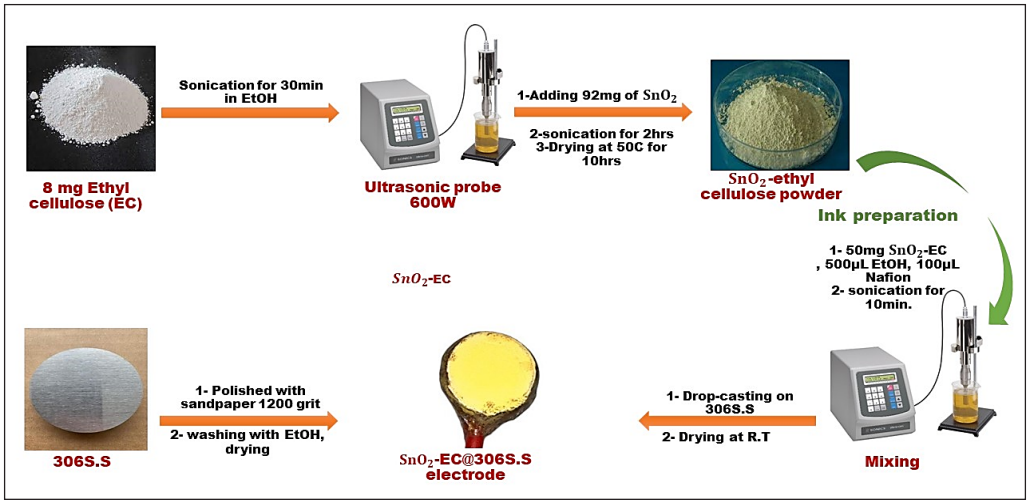

Fig. 1. Illustrate the route of electrocatalyst and ink preparation

2.5. Electrochemical Measurements

Experiments were carried out to reduce CO_2 using an H-type electrochemical cell. A Nafion 117 proton exchange membrane separated the cathodic and anodic compartments. A three-electrode system was used with the electrocatalyst deposited on 306 stainless steel, which served as the working electrode, a high-surface-area platinum plate as the counter electrode (area = 1 cm^2), and a $Hg/HgCl_2$ (saturated KCl) as the reference electrode, as shown in Figure 2. All electrochemical experiments were conducted using a Potentiostat (Vertex One, Ivium Technologies, Netherlands).

The cathodic and anodic compartments were filled with a fresh solution of 110 mL of 0.1M $KHCO_3$. The pH of the catholyte solution was initially measured to be 8.45 before purging with CO_2 gas. After saturating the solution with CO_2 for 60 minutes, the pH decreased to 7.23. This significant change in pH demonstrates the strong influence of CO_2 on the solution's acidity. Linear sweep voltammetry (LSV) curves were conducted in an N_2 and CO_2-saturated electrolyte at a flow rate of 10 mL per seconds with an applied potential in the range of 0 to -2 V vs. RHE with a scan rate of 10 mV per seconds. All potentials were calibrated against the reversible hydrogen electrode (RHE) using Equation1.

$$E_{RHE} = V_{SCE} + 0.24 + 0.0592 \times pH \quad \text{(Eq.1)}$$

Electrochemical impedance spectroscopy (EIS) was carried out under the same electrolyte and electrodes with an amplitude of 10 mV and a frequency ranging from 0.1 Hz to 100 kHz at AC potential.

3. Result and Discussion

3.1. Morphology Characterization

The FE-SEM equipped with EDX was used to characterize the morphology of SnO_2 nanoparticles and ethyl cellulose doped with SnO_2 nanoparticles, as shown in Figures (3A and 3B). The microscopic images of SnO_2 nanoparticles at low (50kx) and high (100kx) magnifications, as displayed in Figure 3A, clearly demonstrate that the particles exhibit a uniform spherical shape with a diameter ranging from 12.67nm to 16.20nm. Furthermore, the surface appeared rougher due to the small sizes of the SnO_2 nanoparticles.

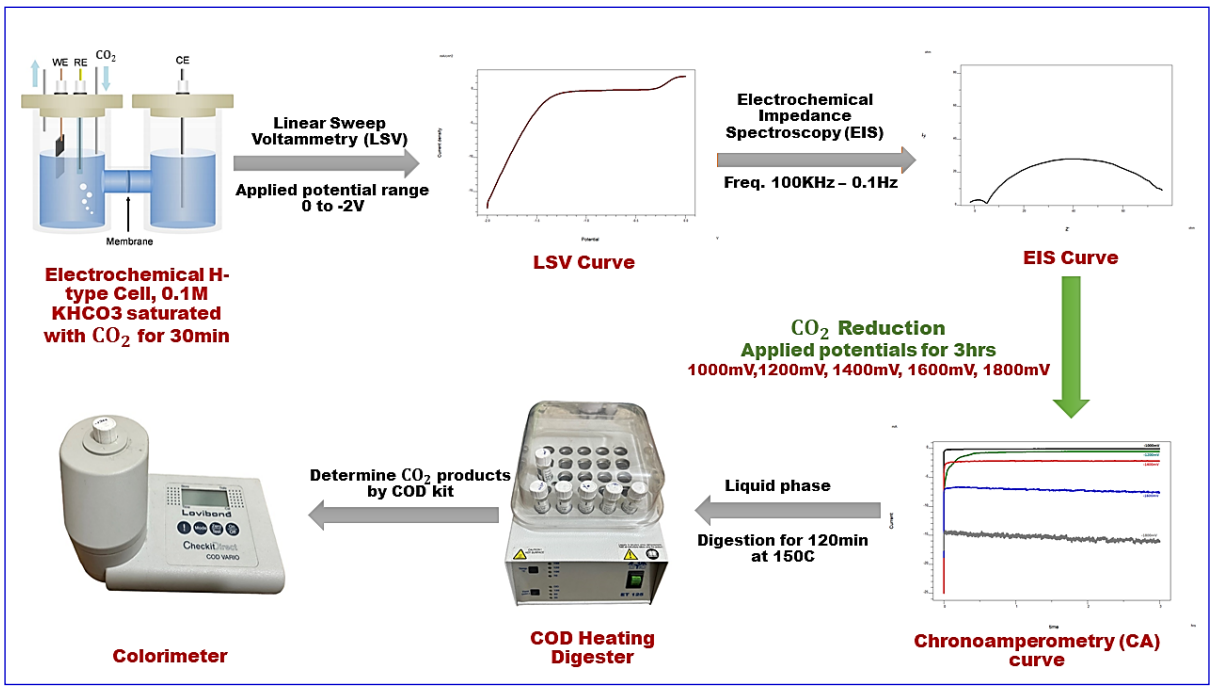

Fig. 2. Electrochemical measurement steps using an H-type cell with three electrode systems

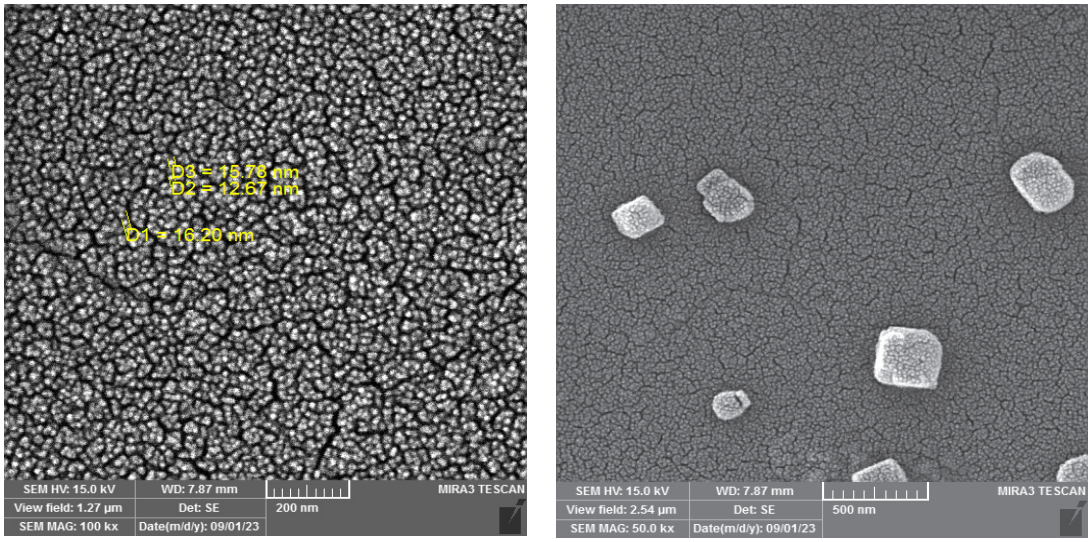

Fig. 3A. FESEM images of SnO_2 nanoparticles with low (left) and high (right) magnification**.**

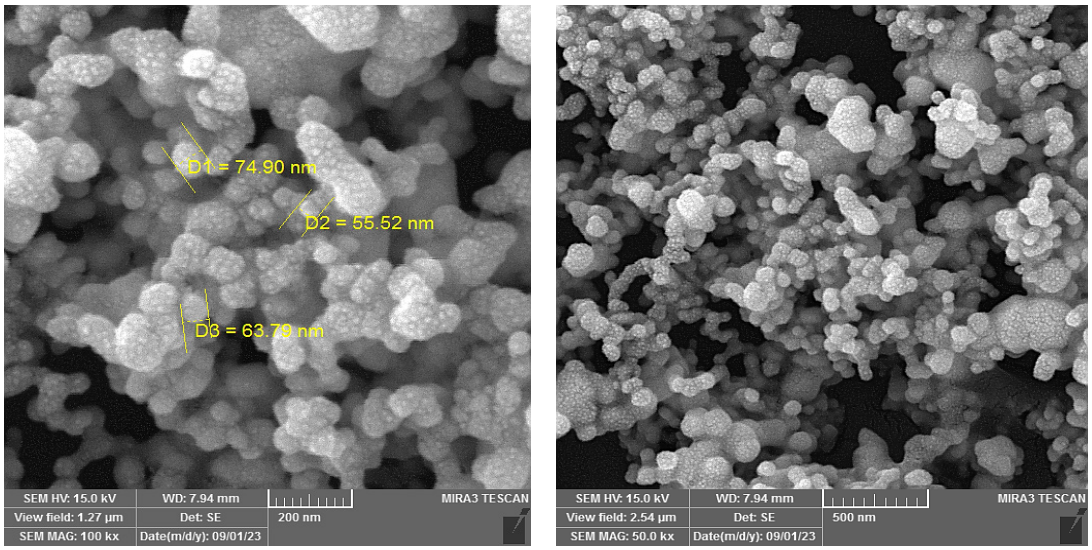

Fig. 3B. FESEM images of SnO_2 NPs-doped ethyl cellulose as clusters

Doping SnO_2 nanoparticles into ethyl cellulose (EC) resulted in individual nanoparticle clusters, each containing more than ten particles. The stiffening action of ethyl cellulose improves the surface adherence of SnO_2 nanoparticles, which causes the size of the particles to increase and become variable, ranging from 55.52 nm to 74.90 nm, as shown in Figure 3B.

3.2. AFM Characterization

An atomic force microscope (AFM) is a technique that provides two and three-dimensional high-resolution images that result in information about topography and morphology. In brief, all prepared electrodes were measured in tapping mode, the most common dynamic mode type used in AFM. In this mode, the cantilever (Tap300-G, reflected coating with 30nm Au, Resonance freq. 300KHz and force constant 42N/m) oscillated with its resonance frequency near the surface. The SnO_2@306S.S electrode with scanned area (2 × 2um) observed spherical-like shapes with uniform distribution of SnO_2 nanoparticles over 306S.S surface, while ethyl cellulose doped with SnO_2 NPs demonstrated aggregation of SnO_2 NP within EC layer that led to increase particle size as

compared with pure SnO_2 NPs which was shown in Figure 4. Regarding surface roughness, the SnO_2-EC@306S.S electrode exhibited higher roughness than the SnO2@306S.S electrode; the mean diameter, root mean square height (Sq), and surface roughness (Sa) calculated using SPIP mountains software are listed in Table 2.

Force-distance (FD) spectroscopy is an AFM mode that can measure the nano-mechanical properties of various materials, such as adhesion force, hardness, adhesion energy, and work function. The force-distance curve is obtained by allowing the cantilever tip to approach the sample surface, leading to an attractive force (Van der Waals forces). When the tip comes into contact with the surface, a rise in repulsive force (electrostatic forces) occurs, pushing the tip away from the surface and causing the cantilever to bend to overcome the tip-sample adhesion forces. The tip is then pulled sharply toward its equilibrium position, and the value of tip-surface deflection is monitored and recorded as a function of tip-surface displacement [32-35] as illustrated in Figure 5. This data is then plotted as a force-distance curve, which is used to estimate the adhesion force (pull-off force).

The force-distance curve of the SnO_2-EC@306S.S

Table 2. Mean diameters, root mean square height (Sq), and surface roughness (Sa) of prepared catalyst.

No.	Electrode	Sq (nm)	Sa (nm)	Mean diameter (nm)
1	SnO2@306S.S	7	5	31.29
2	SnO2-EC@306S.S	56	35	98.30

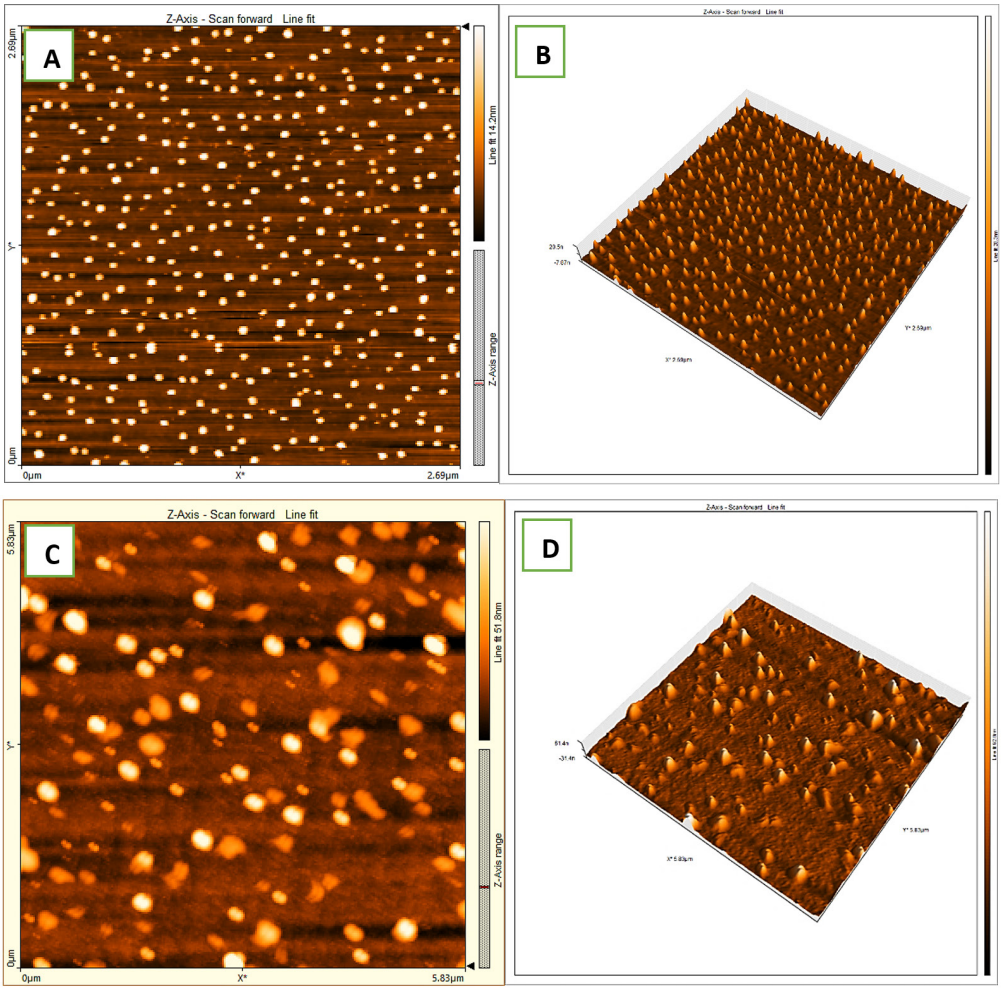

Fig. 4. 2D and 3D-dimensional of SnO_2 NPs (A, B) SnO_2 NPs-doped ethyl cellulose (C, D)

electrode showed a large pull-off force of 0.519 nN and a hardness of 1.601 MPa. In contrast, the SnO_2@306S.S electrode exhibited a lower adhesion force of 0.093 nN and a hardness of 52 kPa, as depicted in Figure 6. The higher adhesion value of the SnO_2-EC@306S.S electrode may be attributed to the presence of OH-groups in the structure of ethyl cellulose, which plays an important role in holding SnO_2 NPs on the stainless-steel surface through hydrogen bonding with vapour water, making the surface hydrophilic. Therefore, more force is required to pull the tip away from the surface. Additionally, the higher surface roughness of the SnO_2-EC@306S.S electrode resulted in a higher adhesion force compared to the lower roughness of the SnO_2@306S.S electrode. All force-distance spectroscopy measurements were conducted in contact mode in an air environment, using a cantilever with a backside aluminium reflective coating (30 nm), a force constant of 0.2N/m, a frequency of 13 KHz, and a tip radius of 10nm.

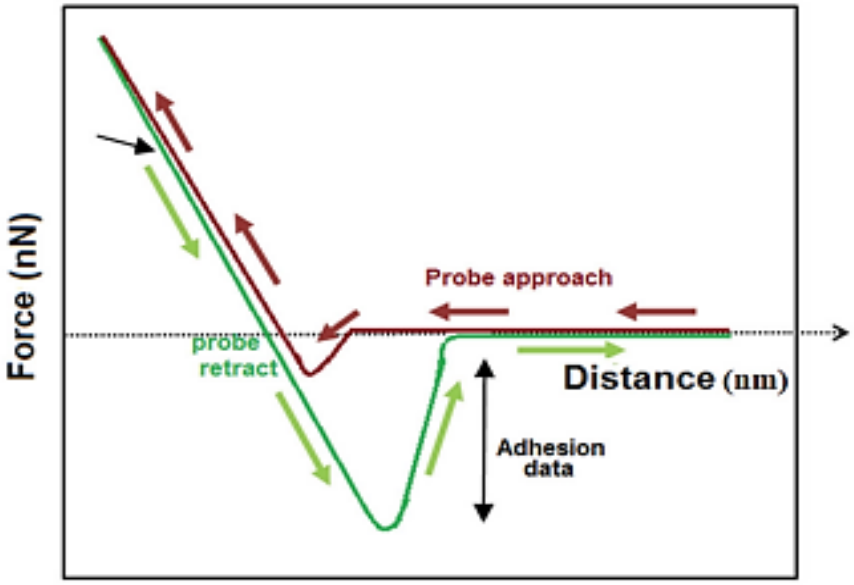

Fig. 5. Diagram of force–distance curve [35]

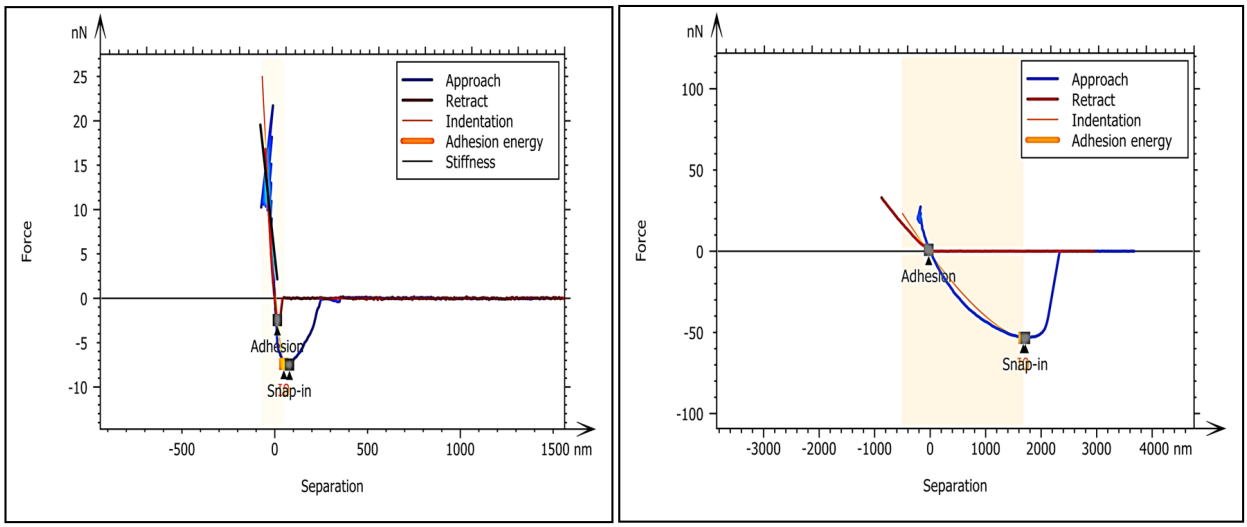

Fig. 6. Force-distance curve of SnO_2-EC@306SS (left) and of SnO_2@306SS (right) electrodes.

3.3. X-Ray Diffraction Analysis

The diffractograms for both sonicated ethyl cellulose (EC) and SnO_2-doped ethyl cellulose as shown in Figure 7. Ethyl cellulose pattern showed a broad peak at a position of 17.06°, corresponding to a d-spacing of 0.5193 nm. This broad peak could be attributed to the amorphous structure and nano-size effect after treatment with an ultrasonic probe for 60 minutes.

The average crystalline size was calculated using the Debye-Scherer formula [36-40] as illustrated in Equation 2 and was found to be 45 nm.

$$D = \frac{0.9\,\lambda}{\beta\,COS\theta} \qquad \text{(Eq.2)}$$

Where D is the crystalline grain size, B = FWHM, = angle of diffraction and = wavelength of x-ray. The XRD pattern of SnO_2-doped ethyl cellulose powder displayed more than ten peaks with different intensities and positions listed in the Table 3. The narrow and sharp diffraction peaks revealed no impurities in the prepared catalyst, indicating good crystallinity. The average size estimated to be 44.21 nm, which is in close agreement with results obtained by FESEM and AFM.

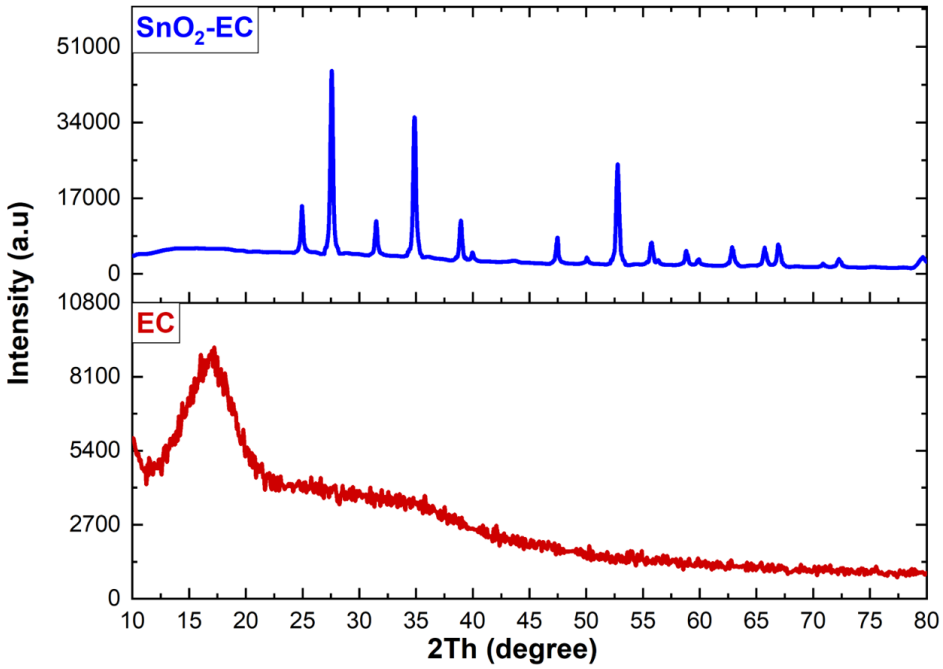

Fig. 7. XRD pattern of ethyl cellulose (EC) and SnO_2-doped EC.

Table 3. XRD parameters of SnO_2-doped ethyl cellulose

No.	FWHM [°2Th]	Peak pos. [°2Th]	Crystallite size (nm)	No	FWHM [°2Th]	Peak pos. [°2Th]	Crystallite size (nm)
1	0.197	24.944	43.0	8	0.216	55.975	43.3
2	0.108	27.540	81.8	9	0.276	58.794	34.0
3	0.177	31.470	48.8	10	0.236	59.913	40.2
4	0.197	34.822	44.1	11	0.236	62.880	40.8
5	0.216	38.966	40.5	12	0.276	65.696	35.3
6	0.197	47.488	45.9	13	0.236	66.921	41.8
7	0.187	52.782	49.5	14	0.336	72.250	30.0

3.4. Electrochemical Performance

Conducted linear sweep voltammetry tests on three electrodes (306S.S, EC@306S.S, and SnO_2-EC@306S.S) in 0.1M $KHCO_3$ electrolytes saturated with N_2 and CO_2, in the voltage range of 0 to -2V (Fig.8). The onset potential for all three electrodes was -1V, indicating stability within the applied potential range. In CO_2-saturated conditions, the current densities for both electrodes (306S.S and EC/306S.S) were measured at -5 mA/cm^2 and -8 mA/cm^2, respectively. This suggests that the use of rotated disc and ethyl cellulose loaded on 306 stainless steels did not contribute to ECO_2RR due to low current densities. From the LSV curve, we observed that the SnO_2-EC@306S.S electrocatalyst exhibited a significant increase in current density in CO_2-saturated electrolytes, reaching -33 mA cm^{-2}, compared to -0.205 mA cm^{-2} in N_2-saturated conditions. This indicates lower current density in the absence of CO_2 (N_2-saturated) due to hydrogen production from the hydrogen evolution reaction (HER) in the cathodic region, which is considered a side product competing with CO_2RR and reduces faradaic efficiency. The higher current density contributes to CO_2 reduction and HER, demonstrating that the prepared catalyst is more electrically active towards CO_2 electrochemical reduction despite the production of H_2 gas.

The double layer capacitances (Cdl) and charge transfer resistance (Rct) parameters of 306S.S, EC/306S.S, and SnO_2-EC/306S.S electrodes were estimated after fitted electrical equivalent circuit using the electrochemical impedance spectroscopy technique at a potential of -1.2V vs RHE, as listed in Table 4. The Nyquist plot resulting from the EIS investigation shows a smaller semicircle due to the higher conductivity of the SnO_2-EC/306S.S electrode. The 306S.S electrode exhibited a low Cdl

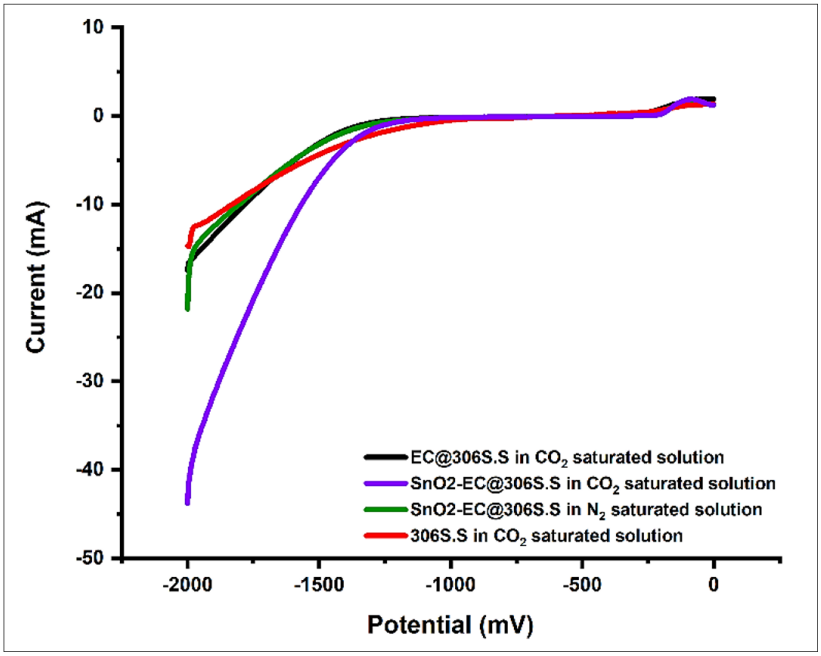

Fig. 8. Linear sweep voltammograms of 306S.S, EC@306S.S, and SnO_2-EC@306S.S in 0.1M $KHCO_3$ electrolyte saturated with N_2 and CO_2 gas.

Table 4. Charge transfer resistance (R_{ct}) and double layer capacitance (C_{dl}) of prepared electrodes

Electrode	Charge transfer resistance Rct (ohm)	Double layer capacitances C_{dl} (F cm^{-2})
SnO_2-EC/306S.S	5.519E+01	6.432E-04
EC/306S.S	5.902E+01	6.421E-04
306S.S	6.157E+01	6.412E-04

(0.0006412 F cm^{-2}), followed by EC/306S.S, which showed a slight increase in Cdl (0.0006421 Fcm^{-2}). However, the SnO_2-EC/306S.S electrocatalyst showed a higher Cdl (0.0006432 F cm^{-2}) as illustrated in Figure 9. The higher value of Cdl indicates that the catalyst has a high electrochemically active surface area (ECSA) and more active sites in the SnO_2-EC/306S.S catalyst, which leads to enhanced electrocatalytic activity of the desired electrode for the CO_2 reduction reaction. The higher conductivity of the SnO_2-EC/306S.S electrocatalyst could be attributed to the lower charge transfer resistance (Rct 5519 ohm) that improves electrocatalytic CO_2 reduction, while electrodes 306S.S and EC/306S.S exhibited high Rct (low conductivity).

The electrocatalytic performance of the SnO_2-EC/306S.S electrode was investigated using chronoamperometry to determine the oxygen content of products under different applied potentials (ranging from -1 to -1.8 mV) for 180 minutes at each potential in a 0.1M $KHCO_3$ solution saturated with CO_2 gas, as shown in Figure 10. The current density of the SnO_2-EC/306S.S electrode increased with the increase in applied potential and remained constant without any drop during CO_2 reduction, indicating its good stability.

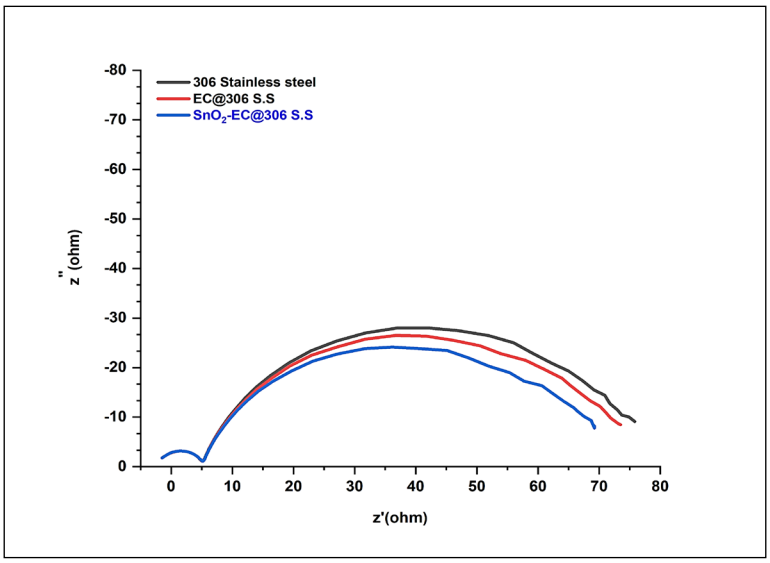

Fig. 9. Nyquist plots of 306S.S, EC@306S.S, and SnO_2-EC@306S.S in 0.1M $KHCO_3$ electrolyte saturated with CO_2 gas

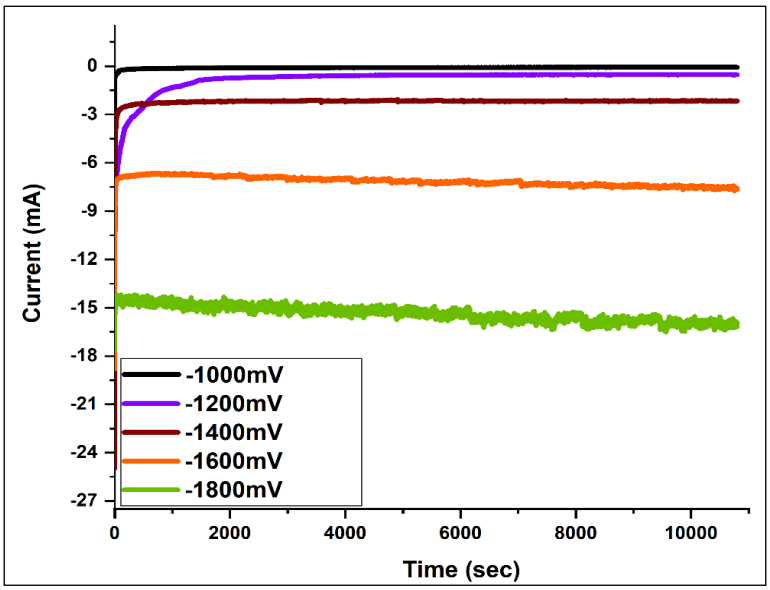

Fig. 10. Chronoamperometry curves at different applied potentials for 3 hrs.

The liquid products at each potential are collected and analysed using a chemical oxygen demand (COD) test. This method is used to detect the amount of oxidizable organic compounds in liquid and waste based on the reduction of potassium dichromate (K_2CrO_7) to chromium salt at high temperatures reaching 150°C [41]. The absorbance is then determined using a colorimeter as shown in Figure 11.

The SnO_2-EC/306S.S electrode demonstrated high electrocatalytic performance with a high oxygen content at an applied potential of -1.2V vs. RHE (-2mA cm^{-2}) and a concentration of 235 mgL^{-1}. This was indicated by a colour change in the dichromate from yellow to black, showing the oxidation of organic products. As the potential increased towards the more negative cathodic region, the oxygen content decreased, measuring 46 mgL^{-1}, 31 mgL^{-1}, and 17 mgL^{-1} for potentials of -1.4V vs. RHE (-2 mA cm^{-2}), -1.6V vs. RHE (-7.3 mA cm^{-2}), and -1.8V vs. RHE (-15.6 mA cm^{-2}), respectively. This suggests that high potentials were not favorable for CO_2 reduction due to the competing hydrogen evolution reaction (HER), leading to a decrease in oxygen content in the liquid products. The COD test indicated no reduction process at a potential of -1V vs. RHE (-0.7 mA cm^{-2}) when CO_2 reduction occurred at a less harmful potential, as listed in Table 5.

Fig 11. Colour of oxidized CO_2 products at different applied potentials

Table 5. Oxygen content of CO_2 products at different applied potentials

No	Potential (mV)	Current (mA cm^{-2})	Temp. (^oC)	COD (mg L^{-1})	Colour
1	Blank	----	25	----	Yellow
2	-1000	0.7	25	0	Yellow
3	-1200	2.0	25	235	Black
4	-1400	2.5	25	46	Yellow
5	-1600	7.3	25	31	Yellow
6	-1800	15.6	25	17	Yellow

4. Conclusion

This study doped SnO_2 nanoparticles (30 nm) with ethyl cellulose ultrasonically to enhance their adhesion to a rotated disc made of 306S.S. This was done to prevent degradation of the catalyst-coated layer in the electrolyte during CO_2 reduction. Ethylcellulose played a key role by making the SnO_2 nanoparticles more rigid, resulting in increased hardness from 52 kPa to 1.601 MPa and surface roughness from 5 nm to 35 nm. Electrochemical CO_2 reduction using a three-electrode setup was performed in a 0.1 M $KHCO_3$ solution saturated with CO_2. Among the three electrodes tested (306S.S., EC@306S.S., and SnO_2-EC@306S.S.), only SnO_2-EC@306S.S. exhibited a high current density of -33 mA cm^{-2} via LSV. This was due to its low charge transfer resistance (Rct 5519 ohm) and high electrical conductivity (Cdl 0.0006432 F cm^{-2}), making it a well-suited electrode for the CO_2 reduction reaction. The electrode also showed high oxygen demand through COD testing at a potential of -1.2V, estimated at 235 mg L^{-1}.

5. Acknowledgements

This research is reinforced by Chemical Analysis Centre (CAC), Baghdad, Iraq

6. References

[1] M. Rumayor Villamil, A. Domínguez Ramos, J.Á. Irabien Gulías, Formic acid manufacture: carbon dioxide utilization alternatives, Appl. Sci. *8* (2018) 914. https://doi.org/10.3390/app8060914

[2] J. Qiao, Y. Liu, F. Hong, J.J.C.S.R. Zhang, A review of catalysts for the electroreduction of carbon dioxide to produce low-carbon fuels, Chem. Soc. Rev., 43 (2014) 631-675. https://doi: 10.1039/c3cs60323g

[3] M. Schreier, F. Héroguel, L. Steier, S. Ahmad, J.S. Luterbacher, M.T. Mayer, J. Luo, M.J.N.E. Grätzel, Solar conversion of CO_2 to CO using Earth-abundant electrocatalysts prepared by atomic layer modification of CuO, Nat. Energy, 2 (2017) 17087. https://doi.org/10.1038/nenergy.2017.87

[4] N. Mozaffari, Alireza Haji Seyed Mirzahosseini, and Niloofar Mozaffari. A new kinetic models analysis for CO adsorption on palladium zeolite nanostructure by roll-coating technique, Anal. Method Environ. Chem. J., 3 (2) (2020) 92-107. https://doi.org/10.24200/amecj.v3.i02.106

[5] Y. Zhang, X. Su, L. Li, H. Qi, C. Yang, W. Liu, X. Pan, X. Liu, X. Yang, Y.J.A.C. Huang, Ru/TiO_2 catalysts with size-dependent metal/support interaction for tunable reactivity in Fischer–Tropsch synthesis, ACS Catal., 10 (2020) 12967-12975. https://doi.org/10.1021/acscatal.0c02780

[6] J. Kang, S. He, W. Zhou, Z. Shen, Y. Li, M. Chen, Q. Zhang, Y.J.N.c. Wang, Single-pass transformation of syngas into ethanol with high selectivity by triple tandem catalysis, Nat. Commun., 11 (2020) 827. https://doi: 10.1038/s41467-020-14672-8

[7] W.-H. Wang, Y. Himeda, J.T. Muckerman, G.F. Manbeck, E.J.C.r. Fujita, CO_2 hydrogenation to formate and methanol as an alternative to photo and electrochemical CO_2 reduction, Chem. Rev., 115 (2015) 12936-12973. https://doi: 10.1021/acs.chemrev.5b00197

[8] W. Li, H. Wang, X. Jiang, J. Zhu, Z. Liu, X. Guo, C.J.R.a. Song, A short review of recent advances in CO_2 hydrogenation to hydrocarbons over hetero-geneous catalysts, RSC Adv., 8 (2018) 7651-7669. https://doi.org/10.1039/C7RA13546G

[9] R. Kortlever, I. Peters, S. Koper, M.T.J.A.C. Koper, Electrochemical CO_2 reduction to formic acid at low overpotential and with high faradaic efficiency on carbon-supported bimetallic Pd–Pt nanoparticles, ACS Catal., 5 (2015) 3916-3923. http://dx.doi.org/10.1021/acscatal.5b00602

[10] A.A. Miran Beigia, Mojtaba Shamsipur, Biochemistry Method: Simultaneous determination of formaldehyde and methyl

tert-buthyl ether in water samples using static headspace gas chromatography mass spectrometry, Anal. Method Environ. Chem. J., 2 (2019) 33-42. https://doi.org/10.24200/amecj.v2.i01.40

[11] X. Zhang, T. Lei, Y. Liu, J.J.A.C.B.E. Qiao, Enhancing CO_2 electrolysis to formate on facilely synthesized Bi catalysts at low overpotential, Appl. Catal. B: Environ., 218 (2017) 46-50. https://doi.org/10.1016/j.apcatb.2017.06.032

[12] Y. Li, Y. Li, Y. Wan, Y. Xie, J. Zhu, H. Pan, X. Zheng, C.J.A.E.M. Xia, Perovskite oxyfluoride electrode enabling direct electrolyzing carbon dioxide with excellent electrochemical performances, Adv. Energy Mater., 9 (2019) 1803156. http://dx.doi.org/10.1002/aenm.201803156

[13] M. Ma, K. Djanashvili, W.A.J.A.c.i.e. Smith, Controllable hydrocarbon formation from the electrochemical reduction of CO_2 over Cu nanowire arrays, Angewandte Chem., 55 (2016) 6680-6684. https://doi.org/10.1002/anie.201601282

[14] B. Parsazadeh, H. Asilian Mahabadi, N. Damyar, Removal and determination of carbon monoxide based on copper oxide immobilized on Zeolite 13X Nanocatalyst by catalytic oxidation process and gas flow analyzer, Anal. Method Environ. Chem. J., 6 (2023) 37-51. https://doi.org/10.24200/amecj.v6.i04.259

[15] Z. Weng, J. Jiang, Y. Wu, Z. Wu, X. Guo, K.L. Materna, W. Liu, V.S. Batista, G.W. Brudvig, H.J.J.o.t.A.C.S. Wang, Electrochemical CO_2 reduction to hydrocarbons on a heterogeneous molecular Cu catalyst in aqueous solution, J. Am. Chem. Soc., 138 (2016) 8076-8079. https://doi.org/10.1021/jacs.6b04746

[16] Y.Y. Birdja, J.J.C. Vaes, Towards a critical evaluation of electrocatalyst stability for CO_2 electroreduction, Chem. Electro. Chem., 7 (2020) 4713-4717. https://doi.org/10.1002/celc.202001227

[17] G. Centi, S. Perathoner, G. Winè, M.J.G.C. Gangeri, Electrocatalytic conversion of CO_2 to long carbon-chain hydrocarbons, Green Chem., 9 (2007) 671-678. https://doi.org/10.1039/B615275A

[18] M. Gattrell, N. Gupta, A.J.J.o.e.C. Co, A review of the aqueous electrochemical reduction of CO_2 to hydrocarbons at copper, J. Electroanal. Chem., 594 (2006) 1-19. https://doi.org/10.1016/j.jelechem.2006.05.013

[19] D.T. Whipple, P.J.J.T.J.o.P.C.L. Kenis, Prospects of CO_2 utilization via direct heterogeneous electrochemical reduction, J. Phys. Chem. Lett., 1 (2010) 3451-3458. https://doi.org/10.1021/jz1012627

[20] A. á Loiudice, P. á Lobaccaro, E. á Kamali, T. á Thao, B.J.A.C. á Huang, Int. Ed, JW áAger, R. áBuonsanti, Tailoring Copper Nanocrystals towards C_2 Products in Electrochemical CO_2 Reduction, Angewandte Chem., 55 (2016) 5789. https://doi.org/10.1002/anie.201601582

[21] H.-K. Lim, H. Shin, W.A. Goddard III, Y.J. Hwang, B.K. Min, H.J.J.o.t. A.C.S. Kim, Embedding covalency into metal catalysts for efficient electrochemical conversion of CO_2, J. Am. Chem. Soc., 136 (2014) 11355-11361. https://doi.org/10.1021/ja503782w

[22] D. Kim, J. Resasco, Y. Yu, A.M. Asiri, P.J.N.c. Yang, Synergistic geometric and electronic effects for electrochemical reduction of carbon dioxide using gold–copper bimetallic nanoparticles, Nat. Commun., 5 (2014) 4948. https://doi.org/10.1038/ncomms5948

[23] A.S. Agarwal, Y. Zhai, D. Hill, N.J.C. Sridhar, The electrochemical reduction of carbon dioxide to formate/formic acid: engineering and economic feasibility, ChemSusChem., 4 (2011) 1301-1310. https://doi.org/10.1002/cssc.201100220

[24] Y. Hori, H. Wakebe, T. Tsukamoto, O.J.E.A. Koga, Electrocatalytic process of CO selectivity in electrochemical reduction

of CO_2 at metal electrodes in aqueous media, Electrochim. Acta, 39 (1994) 1833-1839. https://doi.org/10.1016/0013-4686(94)85172-7

[25] H. Asdollahzadeh, Development of electrochemical sensor based on carbon paste electrode modified with ZnO nanoparticles for determination of chlorpheniramine maleate, Anal. Method Environ. Chem. J., 4 (2021) 16-25. https://doi.org/10.24200/amecj.v4.i01.130

[26] K. Ibrahim Alabid, and Hajar Naser Nasser, Determine methylene blue based on carbon paste electrode modified with nanoparticles of nickel oxide-nitrogen carbon quantum dots and carbon structures by cyclic voltammetry, Anal. Method Environ. Chem. J., 7 (2024) 17-29. https://doi.org/10.24200/amecj.v7.i01.272

[27] X. Hou, Y. Cai, D. Zhang, L. Li, X. Zhang, Z. Zhu, L. Peng, Y. Liu, J.J.J.o.m.c.A. Qiao, 3D core–shell porous-structured Cu@Sn hybrid electrodes with unprecedented selective CO_2-into-formate electroreduction achieving 100%, J. Mater. Chem. A, 7 (2019) 3197-3205. https://doi.org/10.1039/C8TA10650A

[28] X. Bai, W. Chen, C. Zhao, S. Li, Y. Song, R. Ge, W. Wei, Y.J.A.C. Sun, Exclusive formation of formic acid from CO_2 electroreduction by a tunable Pd-Sn alloy, Angewandte Chem., 129 (2017) 12387-12391. https://doi.org/10.1002/anie.201707098

[29] T. Lai, K. Shi, P.J.T.J.o.A. Huang, Adhesion force behaviors between two silica surfaces with varied water thin film due to substrate temperature studied by AFM, J. Adhesion, 96 (2020) 855-872. https://doi:10.1080/00218464.2018.1523725

[30] M. N. Jassim, Z. S. Rasheed, Enhancement optical characterized of tin oxide in polymer polyvinyl alcohol colloid prepared by laser ablation method, Baghdad Sci. J., 21 (2024) 2425-2425. https://doi.org/10.21123/bsj.2023.8494

[31] A. Alwash, The green synthesize of zinc oxide catalyst using pomegranate peels extract for the photocatalytic degradation of methylene blue dye, Baghdad Sci. J., 17 (2020) 0787-0787. https://doi.org/10.21123/bsj.2020.17.3.0787

[32] M. Trought, K.A.J.J.o.C.E. Perrine, Investigating the relationship between adhesion forces and surface functionalization using atomic force microscopy, J. Chem. Educ., 98 (2021) 1768-1775. http://dx.doi.org/10.1021/acs.jchemed.0c00558

[33] K. Ono, Y. Mizushima, M. Furuya, R. Kunihisa, N. Tsuchiya, T. Fukuma, A. Iwata, A.J.A. Matsuki, Direct measurement of adhesion force of individual aerosol particles by atomic force microscopy, Atmosphere, 11 (2020) 489. https://doi.org/10.3390/atmos11050489

[34] S. Sadegh Hassani, M. Daraee, Z.J.J.o.A.S. Sobat, Technology, Application of atomic force microscopy in adhesion force measurements, J. Adhesion Sci. Technol., 35 (2021) 221-241. http://dx.doi.org/10.1080/01694243.2020.1798647

[35] R. Sharma, V. Kumar, Y.J.C.l. Goswami, Excellent flexible Tin Oxide-metal sulfide nanocomposites grown by spin coating chemical route, Chalcogenide Lett., 18 (2021) 473-479. http://dx.doi.org/10.15251/CL.2021.188.473

[36] T. Kondo, Y. Tamura, M. Hoshino, T. Watanabe, T. Aikawa, M. Yuasa, Y.J.A.c. Einaga, Direct determination of chemical oxygen demand by anodic decomposition of organic compounds at a diamond electrode, Anal. Chem., 86 (2014) 8066-8072. https://doi.org/10.1021/ac500919k

[37] S. A. Hamdan, Characterization study of neodymium doped Tin oxide films for optoelectronic applications, Iraqi J. Sci., 65 (2024) 2479-2489. https://doi.org/10.24996/ijs.2024.65.5.12

[38] A. Nada Mohammed, A. A. Baqer, A selective NH3 gas sensor based on (Ag_2O) 1-x (SnO_2) x nanocomposites thin films at various operating temperatures, Baghdad Sci. J., 21 (2024) 1391-1391. https://doi.org/10.21123/bsj.2023.8117

[39] M. K. Alshujery, K. Abid Saleh Al-Saadie, Anodizing of aluminum 6061 alloy with incorporated nanoparticles to inhibits the aluminum corrosion, Int. J. Health Sci., 6 (2022) 930-940. https://doi.org/10.53730/ijhs.v6nS1.4847

[40] M. M. Abbas, A. Ab-M. Shehab, N. A. Hassan, A. K. Al-Samuraee, Effect of temperature and deposition time on the optical properties of chemically deposited nanostructure PbS thin films, Thin Solid Films, 519 (2011) 4917-4922. https://doi.org/10.1016/j.tsf.2011.01.053

[41] A.E. Rodríguez-Mata, L.E. Amabilis-Sosa, A. Roé-Sosa, J.M. Barrera-Andrade, J.G. Rangel-Peraza, Quantification of recalcitrant organic compounds during their removal test by a novel and economical method based on chemical oxygen demand analysis, Korean J. Chem. Eng., 36 (2019) 423-432. http://dx.doi.org/10.1007/s11814-018-0203-9

Anal. Methods Environ. Chem. J. 8 (1) (2025) 54-77

AMECJ

Research Article, Issue 1
Analytical Methods in Environmental Chemistry Journal
Journal home page: www.amecj.com/ir

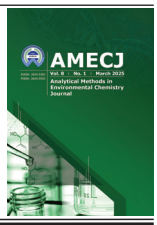

Effectiveness of blended modified biomaterials and coagulants in removing heavy metal ions from drinking water before determination by ICP-OES

David Obasi Igwe[*,a], Chukwunonso Peter Okoli[b], George C. Mbaeyi[c], Omaka Omaka Ndukaku[a], and Aka Beatrice Lebechi[c]

[a]*Department of Chemistry, Alex Ekwueme Federal University, Ndufu-Alike, Abakaliki, Ebonyi State.*
[b]*Department of Mathematics and Statistics, Alex Ekwueme Federal University, Ndufu-Alike, Abakaliki, Ebonyi State.*
[c]*Department of Chemistry, University of Agriculture and Environmental Sciences, Umuagwo, Imo State,*

ARTICLE INFO:

Received 19 Oct 2024
Revised form 16 Jan 2025
Accepted 10 Feb 2025
Available online 28 March 2025

Keywords:
Dissolved Heavy Metals,
Inductively coupled plasma optical emission spectroscopy,
Biomaterial,
Scrap Iron,
River water,
Borehole Water

ABSTRACT

The effectiveness and characterization of blended composite materials made of modified biomaterials and iron (III) sulfate coagulant to remove selected dissolved heavy metals from water-chosen samples were determined during the rainy and dry seasons by inductively coupled plasma optical emission spectroscopy (ICP-OES). Water samples were mechanically batch agitated at their prevailing pHs with optimal composite doses. Following the treatment during the rainy season, the results indicated a percent elimination range of 62.16-99.19 percent. Cu > Zn > Pb > Cd; Zn > Cu > Pb > Cd; Pb > Cu > Cd > Zn; and Zn > Cu > Cd > Pb were the percent removal trends in the Funai borehole water (FBW), Assemblies of God church borehole water(ABW), Ebonyi River water (EBRW), and Eziyiaku river water, Akaeze (ERWA) samples, respectively. During the dry season, a removal range of 93.70 – 100 percent was recorded in all samples. Concentrations of all residual metals except Cd satisfied the World Health Organization and Nigerian Standard Organization permissible levels. Interactions of the variables at ($p<0.05$, $p<0.01$, and $p<0.001$) indicated a statistically significant difference. The reduced linear model of analysis of variance (ANOVA) and response surface methodology employed to predict the responses of main and interaction effects of variables for the dosage optimization of composite materials indicated suitability and statistical significance.

1. Introduction

The increasing population with industrialization has been implicated in impacting significantly environmental pollution with chemical compounds, with surface water and groundwater increasingly becoming sinks for heavy metal ions. Mining activities have contributed significantly to water pollution with dissolved heavy metals in recent years [1]. Household waste, discarded electronic devices, and industrial solid wastes dumped indiscriminately have also contributed to trace metal pollution of water bodies [2]. Furthermore, heavy metal poisoning of water supplies has been linked to the overuse of herbicides, pesticides, and fertilizers. Heavy metals have been found in various thick laminated leaves used to cover food products like *eba*, *moi-moi*, and *agidi*, according to [3]. The leaves degrade due to heavy precipitation and runoff; the released heavy metals enter rivers and percolate into aquifers,

*Corresponding Author: David Obasi Igwe
Email: digwe53@yahoo.com
https://doi.org/10.24200/amecj.v8.i01.378

poisoning water bodies. The authors also implicated small-scale road-side mechanics and petroleum motor spirit road-side traders, sometimes known as "black marketers," in the pollution of the environment with heavy metals. Water contamination is also caused by the dissolution of heavy metal-containing rocks and soils and bush burning [4]. Chemical elements with a specific gravity of at least 5 times that of water are known as heavy metals. They are neither biodegradable nor biodegradable in environmental matrices. Mercury in water was determined using multiwall carbon nanotubes [5]. They can be found in colloidal, particulate, and dissolved forms in surface waters, but their concentrations are typically modest [5, 6]. According to Misihairabgwi et al. [7], colloidal and particulate phases may occur as hydroxides, oxides, silicates, or sulfides; or absorbed into clay, silicate, or organic matter, while the dissolved phase is in the form of ions or unionized organometallic chelates or complexes [3]. As much as some of these heavy metals (e.g., copper, cobalt, iron, manganese, molybdenum, vanadium, strontium, selenium, and zinc) are essentially needed in very low levels in the human body to maintain metabolism when their concentrations in drinking water are above the threshold limit, they become poisonous. Because they build up in living tissues, they can cause disorders including neurological and renal breakdown, brain damage, high blood pressure, convulsions, cancer, metabolic acidosis, and mouth ulcers, among others [6, 7, 8]. linked these heavy metals' toxicity to developing complexes in human cells with organic molecules containing oxygen, sulfur, or nitrogen groups. Some enzymes are inactivated, protein structure is altered, cells lose their capacity to function normally, or cells die [6, 9]. Children are more susceptible to heavy metal toxicity than adults, particularly when exposed to lead poisoning, due to their faster rate of absorption. According to [9,10], the toxicity of these metal ions is determined by their stability, bioavailability, and environmental mobility, as well as the speciation, concentration, and type of heavy metal. Due to epileptic power supply, lack of maintenance culture, and high operational expenses, governments and donor agencies' efforts to solve potable water scarcity for 3 million Ebonyians never achieved any positive outcomes, according to [11]. As a result, drinking water is not properly treated, treatment plants are under-equipped or moribund, and distribution pipes are broken, causing regrowth. Neuropsychological effects of long-term exposure to heavy metal reported by Bagheri et al. [12]. According to [11], the demand for water in Ebonyi State has increased due to the growing population, and people are now sourcing their drinking water from boreholes, hand-dug wells, streams, and rivers. Ebonyi State is endowed with large deposits of heavy metals. However, the rate of accumulation of these heavy metals into the water bodies in virtually all three senatorial zones of the State due largely to the mining of these solid minerals and discharge of the untreated effluents has become a serious health concern, especially to natives who source their drinking water from these water bodies [13]. Many poor countries are increasingly interested in developing water treatment techniques that can efficiently and affordably remove heavy metal ions from drinking water [14]. Membrane filtration (candle, packed column, or beds) [15] ion exchange, reverse osmosis, solid-liquid trap phase extraction, and solid-phase microextraction [16, 17], as well as gas field separation consolidation process [18], are not cost-effective for use in treating water in the developing countries. Electrodialysis, or chemical precipitation, to treat water at home is costly, especially if the volume of water is large. In addition to incomplete removal at low metal levels, the operations are difficult for non-skilled users. In multi-metals systems, studies have demonstrated that single strategies of heavy metal removal, such as adsorption using activated carbons, are challenged by interaction effects and competition for adsorption sites, lowering the removal effectiveness of one heavy metal over the others [19]. The present study used different blends of modified biomaterials and coagulants to absorb selected heavy metals in water samples naturally containing multi-metal cations. The choice allowed interaction effects and competition for sites on the modified biomaterials to be avoided through the synergic effects of charge

separation and sweep flocculation. This method has advantages over the traditional methods in that the precursor materials are abundant locally (from local markets and refuse dumpsites), sustainable, require unskilled operators, cost-effective, and accessible to rural dwellers. Nevertheless, the potential shortcoming of this method lies in the fact that the recommended optimum dose of the different blended composites used in this present study might fall short of the required dose if the level of pollution of the river and borehole waters increases for increased anthropogenic activities and vice-versa. Information abounds in the literature concerning the pollution of the major water resources (Ebonyi River and Ezeiyiaku River, in Ebonyi North and Central, and Ebonyi South senatorial zones, respectively, and groundwater) by heavy metals as a result of the mining of lead, zinc ores, and other metal ores in all the senatorial zones of Ebonyi State. Nevertheless, besides the works of Igwe *et al*. [20, 21], there is a dearth of information regarding efficient techniques for the removal of pollutants such as heavy metals, which can be affordable to the economically less privileged Eboyians, who depend on these water sources for drinking and other domestic purposes, especially in the rural areas.

Therefore, the current study created a composite material using local sodium chloride-activated carbon derived from coconut shell, counter softwood, and iron(III) sulfate derived from scrap iron metal and evaluated its potential in the removal of heavy metals (HMs), notably lead (Pb), cadmium (Cd), mercury (Hg), and nickel (Ni), from borehole and river samples (through a multi-barrier treatment strategy).

2. Experimental

2.1. Instruments

The following instruments were used in this study: muffle furnace (carboniser) supplied by the Industrial Chemistry Department, Ebonyi State University, Abakaliki, pH meter (LF 90, Germany), Benchtop pH Meter, Orion Star A221 pH Portable Meter, labtech digital turbidity meter (probe), SEM (Phenom-Prox, Phenom world Eindhoven the Netherlands) and EC meter (WKW, Germany). Others include TDS Meter (CD650, ELUTECH Instruments), Micromeritics ASAP 2020 Surface Area and Porosity Analyzer: Norcross (GA 30093-2901, U.S.A.), ICP-OES (Perkin Elmer 8000 ICP-OES), and FOV (537 µm, Mode: 15kV - Image, Detector: BSD Full DSM 9872 Gemini SEM) were used.

2.2. Reagents

The chemicals used in this study were of analytical grade, which includes acetone (Hainan Starry, CAS N: 67-64-1, China), concentrated sulphuric acid (Merck Millipore, CAS N: 7664-93-9, Darmstadt, Germany), hydrochloric acid (Merck Millipore, CAS N: 7647-01-0, Darmstadt, Germany), and Hydrogen peroxide (JIGS Chemical, CAS N: 7722-84-1, India). Others are copper sulfate (Spectrum Chemical, CAS N: 7758-99-8, New Jersey, USA), Iodine (Merck Millipore, CAS N: 7553-56-2, Darmstadt, Germany), Sodium thiosulphate (Sigma Aldrich, CAS number 7772-98-7, Massachusetts), Sodium hydroxide (Sigma Aldrich, CAS N: 1310-73-2, Massachusetts), and Potassium chloride (Sigma Aldrich CAS N: 7447-40-7, Massachusetts). Some of materials such as Granulated coconut shell carbon (GCSC), Akparata (counter)softwood carbon (ACSC), and Iron(III) sulphate coagulant (ISC) were prepared. The major drinking water sources in Ebonyi State are borehole water (motorized and mechanical) and surface water (rivers and streams). Therefore, water samples were taken at the Ebonyi River and Eziyiaku River, precisely at Mgbo and Ndiachi Akaeze, in Abakaliki and Ivo local government areas of Ebonyi State. The locations were chosen due to the heavy settlement of locals along these rivers. Alex Ekwueme Federal University, Ndufu-Alike, and Assemblies of God Church Avenue, Abakaliki, were selected for borehole water sampling due to the use of these waters for cooking/drinking by students and inhabitants in the capital city, Abakaliki, respectively. The sampling was carried out in August, September, and October 2022, representing the rainy season, and December 2022, January, and February 2023, representing the dry seasons.

2.3. Study area

Abakaliki, AEFUNAI Ikwo, and Akaeze are in

Ebonyi State's North, Central, and South Senatorial Zones, respectively. Mgbo is located on longitude 80° 15′ E and Latitude 60° 22′ N, Assemblies of God Church Avenue is situated on Longitude 80° 10′ E and Latitude 60° 20′ N. AE-FUNAI is on Longitude 80° 17′ E and Latitude 60° 8′ N, while Ndiachi, Akaeze is located on Longitude 70° 45′ E and Latitude 50° 55′ N [21]. The study areas are defined by two distinct seasons: the dry season (November to March) and the rainy season (April to October) [21]. The rainy season peaks between July and August. Cretaceous sedimentary rocks underlie the Albian Esu River and Turonian Eze-Aku Formations in the three research locations. The lithology of Abakaliki (containing Abakaliki urban and Ikwo) is highly folded, faulted, and fractured by tectonic activity [22]. Dark grey shale, volcaniclastics, mudstone, manganiferous sandstone, siltstone, and limestone comprise most of the rock [23]. In the geology of the study areas, especially Abakaliki and Ikwo [24], there is a significant deposit of lead-zinc mineralization, Galena (PbS) and Sphalerite (ZnS) veins, and this occurrence in the fracture led to mining activities along the hydrothermal Pb-Zn vein lodes. Groundwater availability in Abakaliki and Ikwo is inadequate due to underlying shale or aquiclude and limited groundwater recharge. According to [25], the geology of the Abakaliki basin is characterized by compressional tectonic pressures, resulting in low primary porosity, which indicates slow movement. The Esu River facies are notable for insufficient water recharge [26]. Only the Eze-Aku and Agwu formations in the Esu River, Eze-Aku, Agwum Nkporo, and Mamu formations in the Cross River basin are suitable aquifers [21]. The Turonian Eze-Aku group comprises substantial grey and black calcareous shale, limestone, and siltstone. The principal shale unit of this group has its kind of locality near the Eze-aku River in Akaeze.

2.4. Sample collection

The water samples were collected using conventional procedures. Plastic bottles (1 liter) were washed in warm liquid soap, rinsed thoroughly with warm de-ionized water, and then immersed for 48 hours in 10 % nitric acid [27]. They were then thoroughly cleaned in de-ionized water and securely protected. To obtain representative samples, the motorized borehole taps were allowed to run for 5 minutes, after which the bottles were cleaned 3-4 times before collecting three replicate samples by 7:20 a.m. The river was agitated with the sample bottle at the sampling point (banks and center of the river), then uncapped and rinsed three times with the water sample before plunging about 30 cm below the water's surface.

2.5. Activated carbon preparation and synthesis of iron (III) sulfate

2.5.1. Coconut shell and Akparata counter softwood modification and pyrolysis

Different masses (of impregnation ratios of 1:1, 1:2, 1:3, and 2:1) of the coconut shell and *akparata* (counter) softwood were soaked with the local sodium chloride solution and boiled until the mixture became pasty [20, 21]. They were filtered and dried in an oven for 2 hours, after which they were carbonized using a muffle furnace between the temperature range of 450 and 650 °C. The activated biomaterials were washed thoroughly with distilled water and dried in the oven (Gen lab) for another 2 hours before use.

2.5.2. Preparation of coagulant and adsorbent

The coagulant was made using the [20, 21] method. A 23.5 g scrap iron metal was first degreased and soaked in 2 liters of 40 % concentrated sulphuric acid in a capped amber bottle and was allowed to react for 24 hours. The resulting iron (II) sulfate crystals were removed, washed with enough distilled water, and crushed to a fine size. Oxidization of the iron (II) sulfate crystal was done by careful addition of 30 – 40 % hydrogen peroxide solution in the presence of 10 mg per 50 mL of copper sulfate as a catalyst at a temperature of 80 °C in 500 mL beaker using temperature, and time regulated magnetic hot-plate stirrer until a brownish yellow paste was formed. It was allowed for about 3 hours for complete oxidation to iron (III) sulfate. The iron(III) sulfate paste was then dried in the oven at 120°C for 2 hours. An iron (III) sulfate lump formed and was then ground into anhydrous powder.

2.6. Characterization of GCSC, ACSC and ISC

2.6.1. Degree of pore development (DPD)

The iodine test assessed the DPD distribution using the Igwe *et al*. [20] technique. A 1.0 g of the different impregnated ratios of the GCSC and ACSC was separately wetted with 5 ml of 5 % w/v of concentrated hydrochloric acid and mechanically shaken in a 100 ml conical flask. This was stirred for 1 hour with 25 ml of 0.1 M iodine solution in a magnetic stirrer; the mixture was then filtered. A standardized 0.1 M sodium thiosulphate solution was titrated against 25 mL of the filtrate to a cloudy solution using starch solution as an indicator. The iodine values of the different impregnated biomaterials were obtained using Equation 1.

$$DPD\ (X_m) = \frac{[M_i \times 126 \times V_i) - (V_i + V_A/V_F \times (M_T \times 126.93)\ V_T]}{W_{MB}} \quad \text{(Eq. 1)}$$

In equation 1, V_i is the volume of iodine solution added to the flask, V_A is the volume of 5 % HCl used, M_i is the molar concentration of the iodine stock solution, V_T is the volume or average titre of the thiosulphate solution, W_{MB} is the weight of the adsorbent, and X_m is the adsorbent's iodine number in mg g^{-1}. VF is the volume of filtrate used. M_T and V_T are thiosulfate molar concentration and volume or average titer, respectively.

2.6.2. Surface charges of GCSC, ACSC and ISC

The approach of [21] was used to make this determination. With 0.1 M NaOH and HCl solutions, seventeen sets of 100 ml beakers containing 50 mL of 0.1 M potassium chloride (KCl) solution with initial pH values ranging from 2.00 to 10.00 were prepared. 0.150 of adsorbents and 0.002 g of coagulant were soaked individually in the initial pH of KCl solutions for 48 hours to achieve equilibrium. The ultimate pH values of the various contents of the beakers were evaluated after two days.

2.6.3. Surface morphology of the GCSC and ACSC

For surface and morphological characterization, a scanning electron microscope (SEM) (Phenom-Prox, Phenom-World Eindhoven, the Netherlands) was used.

2.6.4. Elemental composition of the GCSC and ACSC

Energy Dispersive X-ray (EDX) was employed to characterize the ultimate analysis of the biomaterials.

2.7. General procedure

The procedure is followed by schema 1. During the rainy and dry seasons, a 250 mL sample of Funai borehole water(FBW) was batched separately and mechanically agitated with five sets of GCSC/ACSC/ ISC composite materials masses (0.500, 0.500, and 0.005; 0.500, 1.000, and 0.010; 1.000, 0.500, and 0.015; 1.500, 0.500, and 0.020; 0.500, 1.500, and 0.025; 2.000, 2.000, and 0.030) to determine the optimum dose of the composite treatment materials needed for the removal of DHMs in the water samples. At the water sample's prevailing pH, each mix was physically stirred for 60 minutes before sedimentation. After filtering the untreated and treated FBW water samples, the concentrations of the untreated and treated FBW water samples were determined using an inductively coupled plasma optical emission spectrophotometer (Perkin Elmer 8000 ICP-OES) [28]. The optimal doses treated the other water samples during both seasons. The water samples were treated using the same procedure as the optimization process. The percentage of DHMs removed from the water samples was estimated using Equation 2.

The rationale behind the choice of the specific combinations of the blended composite materials was based firstly on the information obtained from past studies that modified coconut shell carbon is rigid (in terms of abrasion resistance) and effective in adsorbing contaminants in aqueous system (in terms of low macroporosity and high carbon yield)

$$\%\ \text{Removal} = \frac{\text{Conc. of DHMs in untreated sample} - \text{Conc. of DHMs in treated sample}}{\text{Conc. of DHMs in untreated sample}} \times 100 \quad \text{(Eq. 2)}$$

[29]. Furthermore, modified coconut shell carbon contains more micropore distributions, while modified wood carbon contains more mesopore/ macropore distributions [30]. By combining these different adsorbents, the effectiveness of removing both small and large size-cations contaminants in the water samples would have been enhanced. Secondly, since the medium from which the DHMs are being removed is a multi-component metal system that has shown to present competition amongst the different size cations during adsorption, the inclusion of the third component-the iron(III) sulphate coagulant-synergically removes any recalcitrant adsorbate by neutralization and sweep-floc mechanisms due to the high density of its floc formed [31].

3. Results and discussion

3.1. The impact of modification of GCSC and ACSC on the pore development (iodine test)

Table 1 presents the values of the iodine test carried out to determine the extent of pore development on the surface of the GCSC and ACSC. Table 1 indicated that the iodine values for the GCSC and ACSC at different impregnation ratios ranged from 1204 to 1613 and 1115 to 1532 mg/g, respectively. The lowest values were observed with an impregnation ratio of 3:1. It can be inferred from Table 1 that the iodine values obtained for ACSC at the different impregnation ratios at 500 C were lower than the corresponding iodine values for GCSC. This may be attributed to the different types of precursor biomaterial containing various degrees of cellulose and hemicellulose. An increase in a biomaterial's cellulose and hemicellulose content has been observed to impart a higher degree of microporosity when activated [32]. It was equally observed that increasing the impregnation ratio resulted in increased iodine values of the biomaterials up to a 2:3 impregnation ratio for both GCSC and ACSC. The highest iodine values obtained at an impregnation ratio of 2:3 for both adsorbents were 1613 and 1532 mg g^{-1}. At a 0.3 impregnation ratio, the activating agent penetrated the inner structure to widen the pores. This increase in iodine value with an increase in impregnation ratio reached its plateau at an impregnation ratio of 0.7. This is due to the extensive dehydration and catalytic actions of the alkali metal (Na, the activating agent) on the cellulose and hemicellulose components of the adsorbent [33]. Further, an increase in the impregnation ratio resulted in the excessive carbon born-off and collapse of carbon structure as well as a reduction in the surface area of both GCSC and ACSC due to micropores transition to mesopores and macropores [34] and at the impregnation

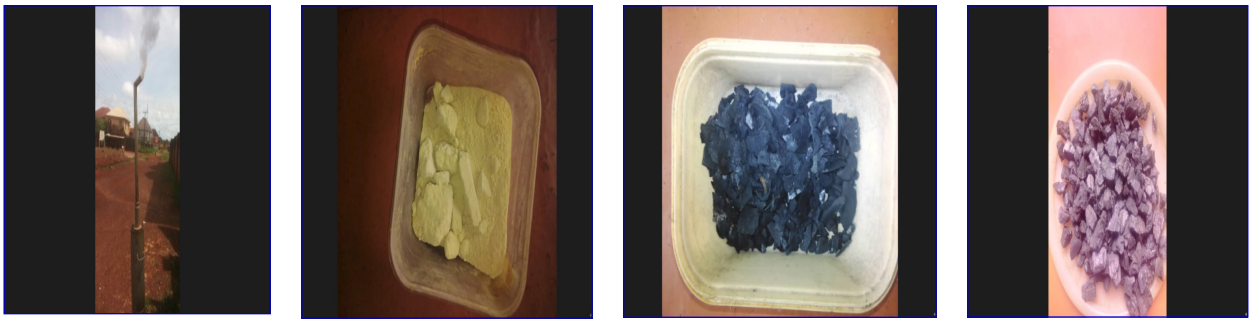

a b c d

Schema 1. Muffle furnace **(a)** used prepared iron(III) sulphate coagulant from scrap iron (**b**), granulated activated coconut shell carbon **(c)**, and counter wood carbon **(d)**.

Table 1. Iodine Value Test for the Modified Biomaterials, Iodine Value (mg g^{-1})

Impregnation Ratio	1:3	1:2	2:3	1:1	2:1	3:1
GCSC	1306	1489	1613	1383	1351	1204
ACSC	1287	1441	1532	1310	1286	1115

ratio of 3, the lowest iodine values for the two adsorbents were achieved.

Table 2 presents the results of the characteristics of the water samples. The mean values of the TDS and EC for the untreated water samples recorded during the rainy and dry seasons (Table 2) showed that the highest mean values (43.05 ± 0.17, and 72.61 ± 0.20; 113.55 ± 0.11, and 206.41 ± 0.16) were observed in FBW samples while the highest mean pH values (8.01 ± 0.16, and 8.05 ± 0.12) were observed in Assemblies of God church borehole water (rainy season) and FBW (dry season), respectively. After treatment, the highest mean TDS and EC values obtained (31.73 ± 0.22 and 5.35 ± 0.05; 84.90 ± 0.30, and 41.62 ± 0.09) were observed in FBW samples for both seasons, while 7.64 ± 0.08, and 7.42 ± 0.25 mean pH values were recorded for ABW and FBW samples, respectively. Total dissolved solids (TDS) measure all the dissolved cations and anions, including carbonates, chlorides, sulfates, nitrates, sodium, potassium, calcium, and magnesium [35]. The results indicated that the untreated surface water samples' mean TDS and EC values (ERWA and EBRW) were lower than those for groundwater (FBW and ABW) during the rainy season. This could result from dissolved solid mineral contents in the aquifer of these study areas [23, 24, 25]. During the dry season, both the surface and groundwater samples were noted to have mean values higher than their corresponding values during the rainy season. This trend has been attributed to the dilution of the ions by rainwater by many researchers [36]. After the treatment of the water samples during both seasons, the mean values of the TDS and EC were found to reduce. The mean values obtained were all within the allowable range of the (World Health Organization [WHO] [37] and Standard Organization of Nigeria [SON] [38]. This shows that the composite materials used were effective in reducing the values. All the pH values of the untreated and treated water samples during both seasons were alkaline and slightly acidic. The slight increase in the mean pH values of the surface water samples during the dry season may be traced to human activities, such as laundry, around the River (Fonddriest Environmental, Inc [FEI] [39]. Generally, the pHs of the treated water samples were all lower than their corresponding untreated samples. This may result from the decreasing pH nature of ISC [40].

3.2. Effect of surface charge and physicochemical characteristics

Figure 1 displays the points of zero charge (pHpzc) for GCSC, ACSC, and the generated iron(III) sulphate coagulant. GCSC and ACSC had pHpzc values of 7.32 and 7.12, respectively, whereas the ISC had a pHpzc of 2.92. Figure 1 shows that at pH 7.32 and 7.12, the net charge on the surface of both adsorbents was equal to zero. Therefore, when the pH of the solution is below these values, i.e.,

Table 2. Mean Values of Physicochemical Parameters of the Untreated and Treated Water Samples during the Rainy and Dry Seasons

		Rainy Season		Dry Season	
		Untreated	Treated	Untreated	Treated
Parameter	Sample	Mean ± Std	Mean ± Std	Mean ± Std	Mean ± Std
TDS (mg L^{-1})	ERWA	15.60 ± 0.13	5.20 ± 0.14	20.52 ± 0.74	2.11 ± 0.46
	EBRW	10.17 ± 0.52	4.46 ± 0.37	16.18 ± 0.12	0.88 ± 0.23
	FBW	43.05 ± 0.17	31.73 ± 0.22	72.61 ± 0.20	5.35 ± 0.05
	ABW	30.33 ± 0.18	27.25 ± 0.20	51.48 ± 0.17	1.25 ± 0.20
EC (µS cm^{-1})	ERWA	98.44 ± 0.35	67.72 ± 0.44	146.58 ±0.88	38.22 ± 0.34
	EBRW	58.63 ± 0.18	27.86 ± 0.52	93.56 ± 0.14	16.75±0.08
	FBW	113.55 ± 0.11	84.90 ± 0.30	206.41 ± 0.16	41.62 ±0.09
	ABW	69.89 ± 0.14	62.07 ± 0.18	100.02 ± 0.22	30.76 ± 0.41
pH	ERWA	6.84 ± 0.07	6.68 ± 0.10	7.66 ± 0.18	6.94 ± 0.26
	EBRW	7.02 ± 0.16	6.70 ± 0.14	7.54 ± 0.19	7.16 ± 0.24
	FBW	7.97 ± 0.08	7.05 ± 0.05	8.05 ± 0.12	7.42 ± 0.25
	ABW	8.01 ± 0.16	7.64 ± 0.08	7.57 ± 0.30	6.72±0.27

if the solution is acidic, the hydrogen ions in the solution bind with the surface functional groups of the adsorbent, creating a positive charge on the adsorbent surface. This development will hence facilitate the adsorption of anions in the solution. However, if the pH of the solution is above the pHpzc of the adsorbent, the surface functional groups will lose protons, thereby making the adsorbent's surface negatively charged. This will enhance the adsorption of cations such as dissolved heavy metals by electrostatic attraction [41]. On the other hand, the alkaline nature of the water samples resulted in the precipitations of the heavy metal ions as hydroxides, which were swept down by the settling coagulant flocs, resulting in the removal of the dissolved heavy metals. Nanographene oxide nanomagnetic composite for removal of aluminum in wastewaters, water samples, and Al precipitations have occurred as aluminum hydroxide at basic pH [42].

3.3. Physical surface structures of the granulated activated biomaterials

Figures 2a-f illustrate the results of the GCSC and ACSC morphologies. Figures 2a- c Scanning electron micrographs of granulated coconut shell carbon at 8000, 9000, and 10,000 magnifications showing few micropores with non-uniform mesopores. Figures 2d- f Scanning electron micrographs of apparatus counter softwood carbon at 8000, 9000, and 10,000 magnifications show a flaky, honeycomb-like surface with many micropore distributions. The SEM at 8 000, 9 000, and 10 000 magnifications was employed to view the morphologies and pore structures/ distribution on the surfaces of the GCSC and ACSC. It was observed that there were few micropores on the surface of GCSC in addition to non-uniform larger pores (mesopores and pore channels-macropores). The larger pore cavities observed may have resulted from high activation temperature, which led to the conversion of already formed micropores to mesopores and macropores [34], and hence, smaller surface area. [33] attributed this to the evolution of oxygen functional groups of the activated carbon. Figures 2d-f showed the pore structure and distribution of ACSC magnified at 9,000 and 10,000. It was found that the surface was flaky and honeycomb-like, with many micropore distributions, resulting in a larger surface area. The increased pore network and volumes may be attributed to the dehydrating action of NaCl and escaping Na^+ and Cl^- during the activation process, as posited by [33] in Equation 3.

$$NaCl + 2nH_2O \rightarrow Na^+(H_2O)_n + Cl^-(H_2O)_n \quad \text{(Eq.3)}$$

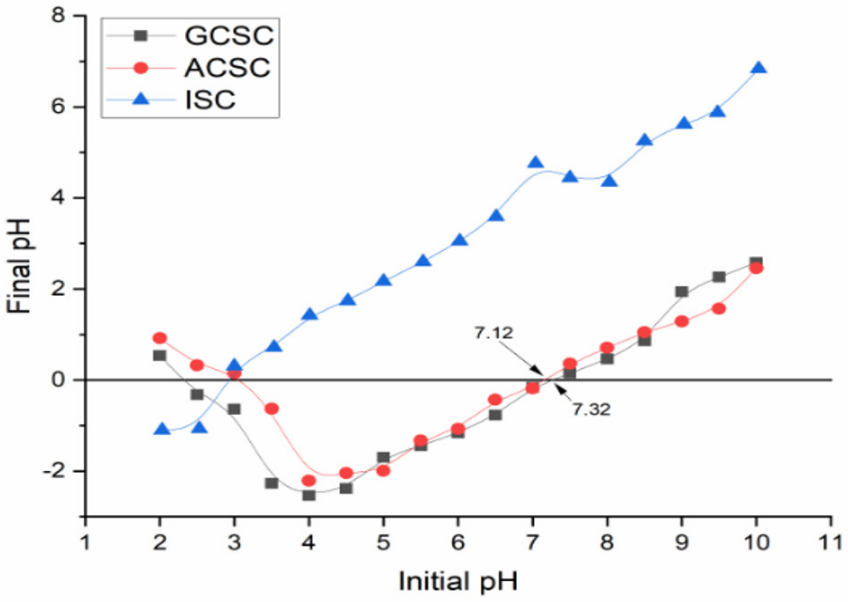

Fig. 1. Points of Zero Charge (pH_{pzc}) for ISC, GCSC and ACSC

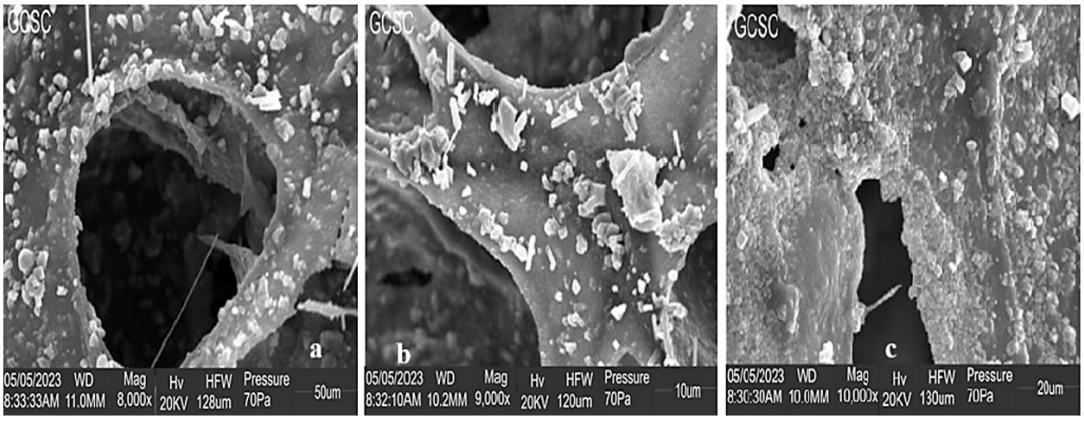

Fig. 2 (a, b, and c). Scanning Electron Micrographs of the GCSC

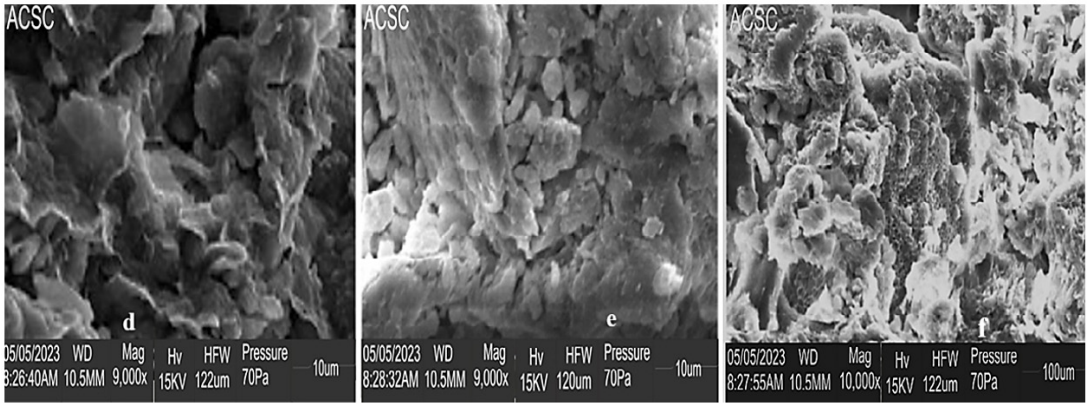

Fig. 2 (d, e, and f). Scanning Electron Micrographs of the ACSC

3.4. Ultimate analysis of GCSC and ACSC

The results for assessing the elemental compositions of the activated GCSC and ACSC are presented in Figure 3 (a and b). The results showed that GCSC contains Cl, C, Na, Si, S, O, N, and Fe, while ACSC contains Cl, C, Na, Si, S, O, N, and Zn. Carbon has the highest percentage composition, while chlorine was observed to have the lowest percentage composition in GCSC. On the other hand, silicon was the most abundant in ACSC, while zinc had the lowest percentage composition.

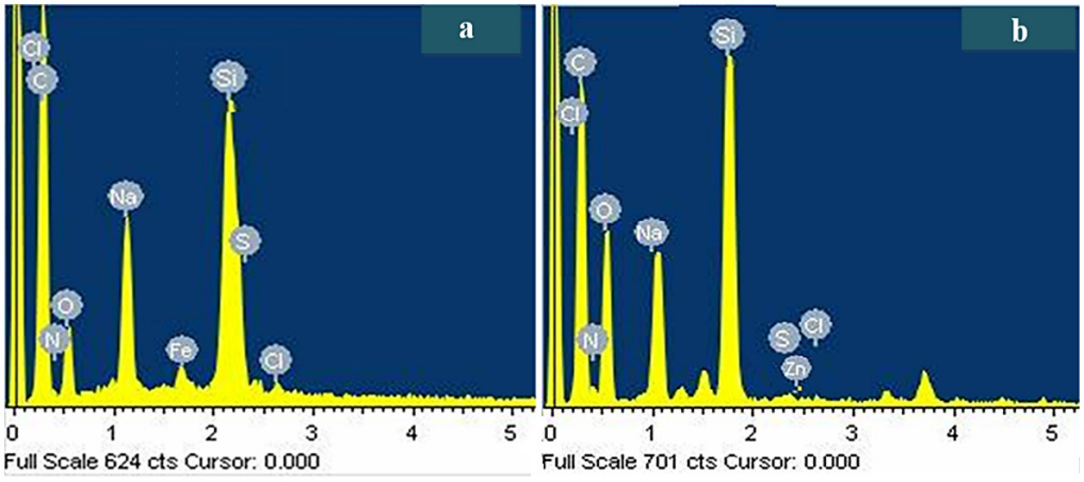

Fig. 3. Energy Dispersive X-ray of GCSC and ACSC (Left side, a): Energy dispersive x-ray of granulated coconut shell carbon indicating that it contained elements such as Cl, C, Na, Si, S, O, N, and Fe, (Right side, b): Energy dispersive x-ray of *akparata* counter softwood carbon showing the composition of Cl, C, Na, Si, S, O, N, and Zn.

3.5. Effect of dose optimization of the composite materials

Table 3 presents the experimental design, indicating the process variables and observed responses for the dosage optimization of composite materials using FBW samples. The initial amounts of Pb, Zn, Cd, and Cu in the FBW sample were 0.205, 0.148, 0.068, and 0.078 mg L^{-1}, respectively. Hence, 0.5, 1.5, and 0.025 g of GCSC, ACSC, and ISC, respectively, were the best dosages of composite materials for achieving the maximum percentage of heavy metals removal.

It is to be noted, however, that the efficiency of removal of the DHMs by the blended composite treatment materials may be affected by the seasonal variations in the pH and temperature of the water samples. Studies have shown that the temperature of the water is affected by many factors, including air temperature and discharges (domestic and industrial) into the water body [43]. In this present study, it was observed that anthropogenic activities (bathing and laundry) were higher during the dry season than the rainy season as the volume of the river waters got reduced (became shallow) due to evaporation, vis-à-vis, increase in air temperature. As expected, the pH of water bodies may rise or fall if there is an increase in the water temperature. An increase in temperature usually stimulates phytoplankton photosynthetic activity, causing more carbon dioxide consumption, which increases pH [44]. Conversely, at higher water temperatures, there is low diffusion of gases, which causes microorganisms to decompose organic matter in the water by anaerobic means, which introduces more CO2 in the water, resulting in low pH. Therefore, the pH of water bodies may correlate inversely or directly with temperature, depending on other factors. In this present study (Table 1), it was observed that there was a slight increase in the average pH of all the water samples during the dry season against the average pH recorded for all the water samples during the rainy season. Table 4 and Table 5 presented the results of the percent removal of the DHMs from the various water samples during rainy and dry seasons, respectively. Pb had the highest mean concentrations in all the untreated water samples during the rainy season, while the mean concentrations of Cu and Zn were the least observed in FBW and ABW, EBRW, and ERWA samples, respectively, after treatment. Furthermore, the average levels of dissolved Pb and Cd in untreated FBW, ABW, EBRW, and ERWA samples exceeded the World Health Organization, 2004 according to [39] maximum acceptable limits of 0.01 and 0.003 mg/L, respectively, for drinking water, while the mean concentration of Zn in the EBRW sample exceeded the maximum allowable limits of 3.0-5.0. The mean amounts of the examined dissolved heavy metals in all water samples were below the Regulatory Bodies' recommended limits throughout the dry season. FBW, ERWA, EBRW, and ERWA had the highest % removal of dissolved Cu, Zn, Pb, and Cd during the rainy season, whereas FBW, EBRW, ERWA, and ABW had the lowest percentage removal of dissolved Cu, Zn, Pb, and Cd during the rainy season. The observed trend in the degree of removal was consistent with other previous studies, and this might be explained by Cu and Zn strong attachment to the active sites or pores of the modified biomaterials due to the effective cationic radius [45]. Pb, Cd, Zn, and Cu have effective ionic radius of 0.2655, 0.2305, 0.2165, and 0.2065 nm, respectively [46]. Speciation of lead in human samples based on MWCNTs@DMP was obtained by the ionic liquid-suspension-micro-solid phase [47]. According to [48], heavy metal removal could also be due to initial metal ion concentrations, which

Table 3. Experimental Design Showing the Process Variables and Observed Responses

Run	GCSC	ACSC	ISC	Cu	Zn	Cd	Pd
1	0.500	0.500	0.005	33.330	24.320	38.240	40.980
2	0.500	1.000	0.010	65.390	50.000	77.940	67.810
3	1.000	0.500	0.015	89.740	93.240	88.240	77.560
4	1.500	0.500	0.020	96.150	95.960	88.240	85.370
5	0.500	1.500	0.025	97.440	98.650	88.240	89.760
6	2.000	2.000	0.030	93.590	97.300	88.240	85.850

is the driving force to overcome all mass transfer resistance of metal between the aqueous and solid phases. However, as the prevailing pH of the solutions increased, the adsorption of the DHMs increased. The level of dissolved DHMs in untreated water samples was below the detection limits of the instrument used during the dry season. After treatment, 100 percent removal of the detected dissolved components was achieved in the FBW, ABW, and EBRW samples. Though some of the water samples were alkaline and could have antagonized the effective adsorption of the DHMs by the GACSC [48], however, the ISC which is acidic in nature lowered the pH of the solution and enabled the removal (adsorption and coagulation) of the heavy metals from the water samples. Tables 4 and 5 indicated that during the rainy season, the efficiency of removal of the DHMs followed the order Zn>Cu>Pb>Cd for FBW, ABW, and ERWA samples, while during the dry season, the efficiency of removal was in the order Zn=Cu=Pb in all the samples. Furthermore, the river waters were slightly more alkaline during the dry season in the present study due to increased water temperature necessitating increased photosynthesis by aquatic plants. The efficiency of removal of the DHMs depends on many factors, including the surface chemistry of the modified biomaterial and the pH range upon which the iron(III) floc (amorphous hydroxide) remains stable. At low pH, there is competition for adsorption of available sites between the DHMs and protons, resulting in lower removal efficiency. As pH increases, there is deprotonation on the surface of the modified biomaterials, causing the surface to be negatively charged and, hence, increasing removal efficiency. On the other hand, it has been revealed that the soluble monomeric hydrolytic species of Fe(III) in equilibrium with the amorphous hydroxide occur over a wider pH range (4.0 –10.0). The solubility of amorphous species, $Fe(OH)_3$, is least at pH 4 but increases to its plateau at pH 9 and then steeps above pH 9 [49]. Furthermore, an increase in the temperature of the aqueous solution has been revealed to result in an increase in the efficiency of coagulants [30]. Therefore, it might be reasonable to posit in the present study that the removal efficiency of the DHMs by the blended composite treatment materials was enhanced as the temperature and pH of the water samples increased during the dry season. This is in tandem with many other findings [50].

Table 4. Degree of Removal of Dissolved Heavy Metals in Water Samples during Rainy Season

Sample	Metals	Initial pH	Untreated Mean Conc. (mg L^{-1})	Treated Mean Conc. (mg L^{-1})	% Rm Permissible Limit
FBW	Pb	7.97	0.205 ± 0.021	0.021 ± 0.002	89.76
	Zn		0.148 ± 0.015	0.005 ± 0.001	96.62
	Cd		0.068 ± 0.007	0.012 ± 0.001	82.35
	Cu		0.078 ± 0.008	0.121 ± 0.001	97.44
ABW	Pb	8.01	0.161 ± 0.016	0.010 ± 0.001	93.79
	Zn		0.109 ± 0.011	0.002 ± 0.000	98.17
	Cd		0.026 ± 0.003	0.006± 0.001	76.92
	Cu		0.096 ± 0.009	0.005 ± 0.001	94.79
EBRW	Pb	7.02	1.371 ± 0.053	0.011 ± 0.001	99.19
	Zn		11.153 ± 0.643	4.220 ± 0.342	62.16
	Cd		0.044 ± 0.002	0.008 ± 0.000	81.81
	Cu		0.101 ± 0.004	0.006 ± 0.000	94.06
ERWA	Pb	6.84	0.100 ± 0.002	0.018 ± 0.001	82.00
	Zn		0.099 ± 0.005	0.002 ± 0.000	97.98
	Cd		0.023 ± 0.002	0.004 ± 0.000	82.60
	Cu		0.042 ± 0.003	0.005 ± 0.001	88.10

Where ND represents not detected
WHO and SON Maximum(n=3): Pb=0.01, Zn=3.0-5.0, Cd=0.003, Cu=1.0

Table 5. Degree of Removal of Dissolved Heavy Metals in Water Samples during Dry Season

Sample	Metals	Initial pH	Untreated Mean Conc. (mg L^{-1})	Treated Mean Conc. (mg L^{-1})	% Rm Permissible Limit
FBW	Pb	8.05	0.701 ± 0.032	ND	100
	Zn		0.143 ± 0.006	ND	100
	Cd		ND	ND	ND
	Cu		0.230 ± 0.012	ND	100
ABW	Pb	7.57	ND	ND	ND
	Zn		0.101 ± 0.005	ND	100
	Cd		ND	ND	ND
	Cu		ND	ND	ND
EBRW	Pb	7.54	0.100 ± 0.004	ND	100
	Zn		ND	ND	ND
	Cd		ND	ND	ND
	Cu		0.101 ± 0.005	ND	100
ERWA	Pb	7.66	ND	ND	ND
	Zn		ND	ND	ND
	Cd		ND	ND	ND
	Cu		ND	ND	ND

Where ND represents not detected

WHO and SON Maximum(n=3): Pb=0.01, Zn=3.0-5.0, Cd=0.003, Cu=1.0

3.5.1. Statistical relevance of the optimization process

The statistical relevance of the optimization process of the composite materials for the removal of the DHMs in the FBW sample was carried out using a reduced linear model of analysis of variance (ANOVA) as shown in Table 6. There was evidence that the model was suitable and statistically significant in describing the experimental data based on their probability >F values being less than 0.05 except for the percent removal of Cd where the probability >F values were greater than 0.05. The probability>F values showed that the ISC component of the composite had a much-pronounced effect on the percent removal of Cu, Cd, and Pb, while ACSC and GCSC contributed latently in influencing the percent removal of the DHMs. This apparent non-contribution by the GCSC and ACSC to the removal of the DHMs was attributed to the reduced linear model used, which does not imply that the adsorbents did not entirely have an effect on the removal of the DHMs.

The relevance of the reduced linear model in describing the experimental data was collaborated by the plot of predicted percent removal of DHMs from the model against actual or experimental percent removal of DHMs in Fig 4 (a to d). For removing Cu, Zn, Cd, and Pb, the determination coefficient (R2) values were 0.7202, 0.9147, 0.5636, and 0.7654, respectively. These values indicated that the regression model did not capture 0.2798, 0.0853, 0.4364, and 0.2346 % of the total

Table 6. F-values and Prob >F from analysis of Variance for the Reduced Linear Model

	Cu		Zn		Cd		Pb	
Response	**F-value**	**Prob>F**	**F-value**	**Prob>F**	**F-value**	**Prob>F**	**F-value**	**Prob>F**
RL	10.32	0.0325	16.09	0.0249	5.17	0.0855	13.05	0.0225
ISC	10.32	0.0325	26.60	0.0141	5.17	0.0855	13.05	0.0225
ACSC	----	----	5.71	0.0968	----	----	----	----
Removal %	97.440		98.650		88.240		89.760	

RL: Reduced Linear

possible variations. Furthermore, the adjusted determination coefficients (R^2a) for the various heavy metals, CuR^2a (0.6509), ZnR^2a (0.8579), CdR^2a (0.4545), and PbR^2a (0.7068), were of high linear relationship for Zn and Pb, moderate for Cu but was weak for Cd. R^2a adjusts the R^2 for the regression model's sample size and number of variables. Figure 4a shows the plot of the predicted percent removal of Cu against the experimental percent with a square of regression of 0.7202. Figure 4b plots the expected percent removal of Zn against the experimental percent with a square of regression of 0.0853. Figure 4c is a plot of the predicted percent removal of Cd against the experimental percent with the square of regression of 0.5636. Figure 4d plots the predicted percent removal of Pb against the experimental percent with a square of regression of 0.7654.

To predict both the main and interaction effects in this study, it was necessary to use a 3D response surface plot and the corresponding x/y 2D contour plot on the response variables. The response surface plots showing the effects of the experimental variables on the percent removal of Cu, Zn, Cd, and Pb in the ABW sample were presented in Figures 5, 6, 7, and 8, respectively. Figure 5a shows the main and interaction effects of ISC and ACSC on the percent removal of Cu while keeping GCSC constant. It was observed from the plot that irrespective of the incremental amount of ACSC, there was no influence on the percentage of dissolved Cu removed. Nevertheless, there was a positive correlation between the amount of ICS used and the percentage of dissolved Cu removed. The same trend was observed in Figure 5b for the main and interaction effects of ISC and GCSC on the percent removal of Cu while keeping the amounts of ACSC constant.

The main and interaction effects of the amounts of GCSC and ACSC on the percent removal of Zn while keeping the amounts of ISC steady are shown in Figure 6a. The amounts of ACSC used varied directly with the percent removal of Zn, though minimally. In contrast, the effect of the GCSC on the percent removal of Zn remained constant, irrespective of the increment in amounts. There was a positive correlation between ACSC and the

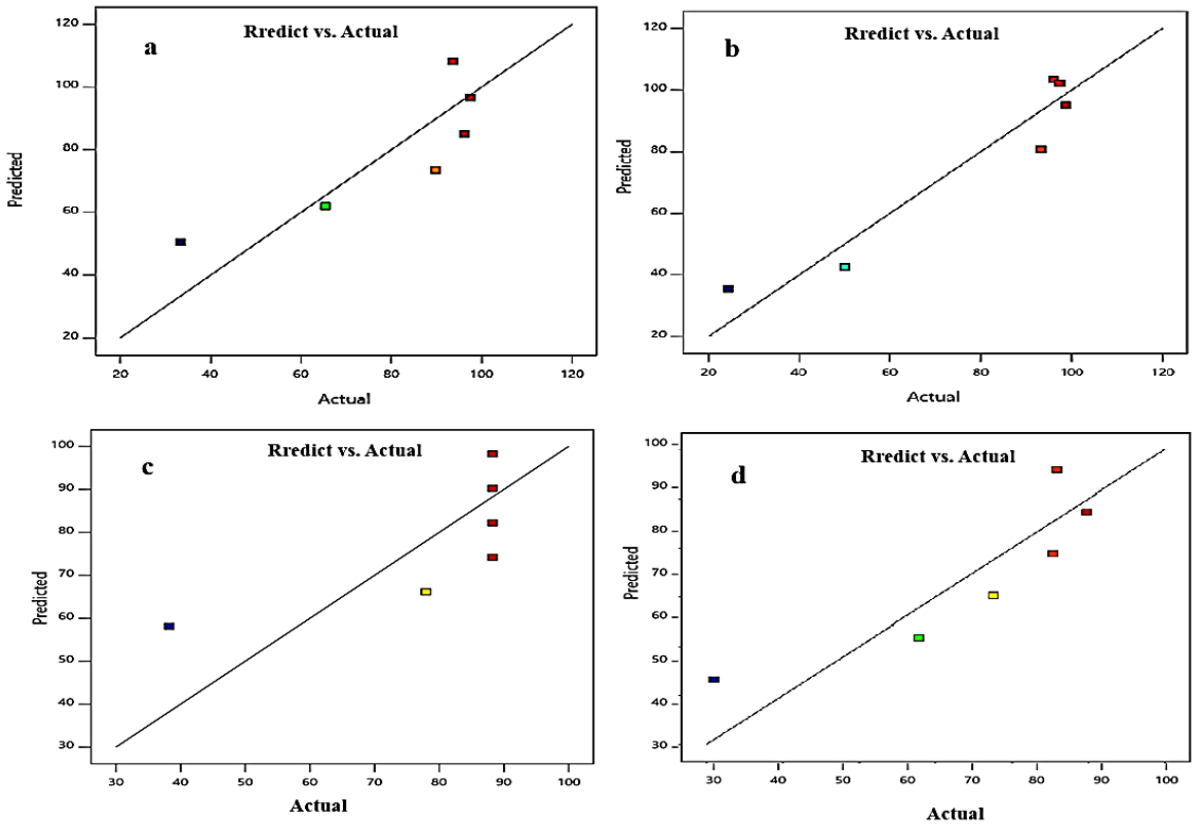

Fig. 4 a – 4d. Plots of Predicted against Actual Values for Percent Removal of Cu, Zn, Cd, and Pb, respectively.

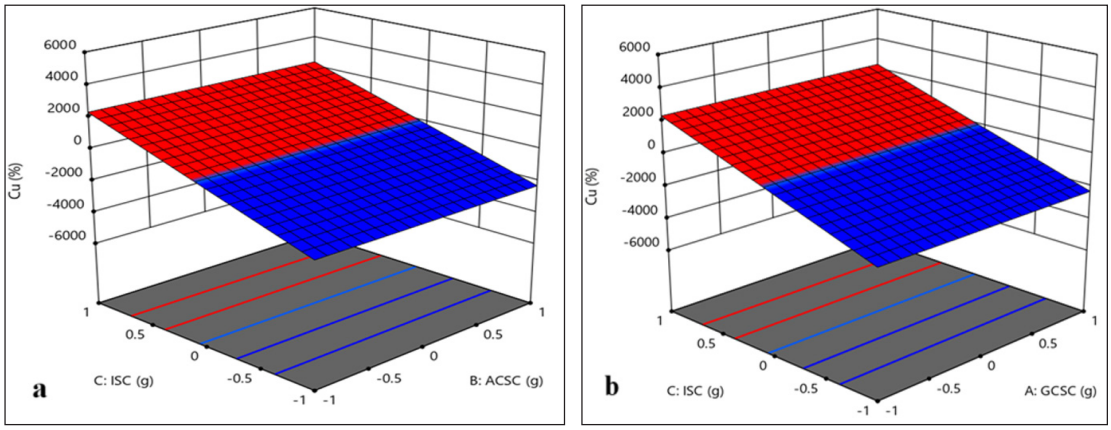

Fig. 5. a) Main Interaction and Effects of ISC and **b**) ACSC, and ISC and GCSC on the Percent Removal of Cu.

percent removal of Zn, while GCSC did not show a positive correlation. Figure 6b revealed that ISC had a significant positive correlation with the percent removal of Zn, while ACSC had no influence on the removal of Zn. Figure 6c shows a positive correlation between ISC and the percent removal of Zn. On keeping the amounts of GCSC constant, Figure 6b shows the main and interaction effects of the amounts of ACSC and ISC on the percent removal of Zn. Compared to the observation in Figure 6a, ISC had a more significant influence on the percent removal of Zn than the removal of Cu, while ACSC had no effect on the percent removal of Zn. The same trend was observed in Figure 6c when the impact of ACSC was kept constant, and the main and interaction effects of ISC and GCSC on the percent removal of Zn were investigated. Figures 7a and 7b show the main and interaction

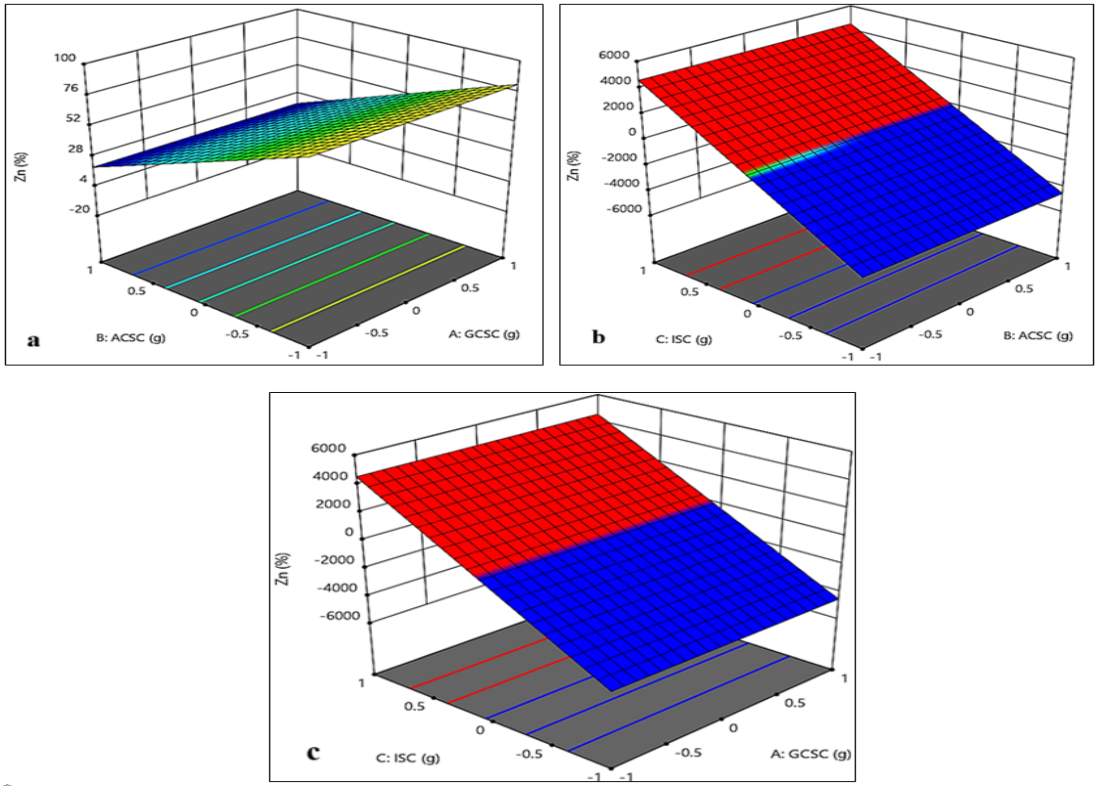

Fig. 6. a) Main Interaction and Effects of ACSC and GCSC, **b**) ISC and ACSC, and ISC, and **c**) GCSC on the Percent Removal of Zn.

influences of the amounts of ISC and ACSC, ISC and GCSC on the percent removal of Cd while keeping the effects of the amounts of GCSC and ACSC steady, respectively. Both plots showed the same trend: only the ISC had moderate positive correlations with the percent of Cd removed from the FBW sample.

Figures 8a and b present the response surface plots for the primary and interaction effects of ISC and GCSC and ISC and ACSC on the percent removal of Pb while maintaining the amounts of ACSC and GCSC constant, respectively. Figures 8a and b revealed that the ISC varied directly with the percent removal of Pb, while the GCSC and ACSC had no relationship with this. There are two response surface plots in which Figure 8a shows the interaction between GCSC and ISC, with a positive correlation between ISC and the percent removal of Pb. Figure 8b shows the interaction between ACSC and ISC in which a positive correlation existed between ISC and the percent removal of Pb.

3.5.2. Statistical Analysis of the Mean Levels of DHMs in Treated Water Samples

Table 7 presented the result for testing the season's significance, untreated/treated water samples, and metals in removing dissolved heavy metals. At the conventional 5 % level of significance, there was evidence of significant difference ($p<0.05$) only in the means of the two seasons. However, at a 10 % level of significance, there was evidence of a significant difference ($p<0.1$) in the degree of removal of heavy metals between the untreated and treated water samples. This implies that the composite materials used were synergetic in removing heavy metals. None of the various samples and metals showed evidence of a significant mean difference in the degree of removal of dissolved heavy metals. This may result from the surface water and groundwater samples during both seasons experiencing the same technique of heavy metals removal. With mean values of 0.006 and 0.0135, the removal of heavy metals seems higher during the dry season and for treated water, respectively. Even though no significant evidence was established for both the samples and metals, the degree of heavy metal removal appears higher for ERWA and lower for EBRW. This may be attributed to the initial concentrations of the heavy metals in the two River samples. In the same way, removal was also higher with samples containing Cd and lowest with water samples containing Zn.

Table 8 shows the interactions between the DHMs

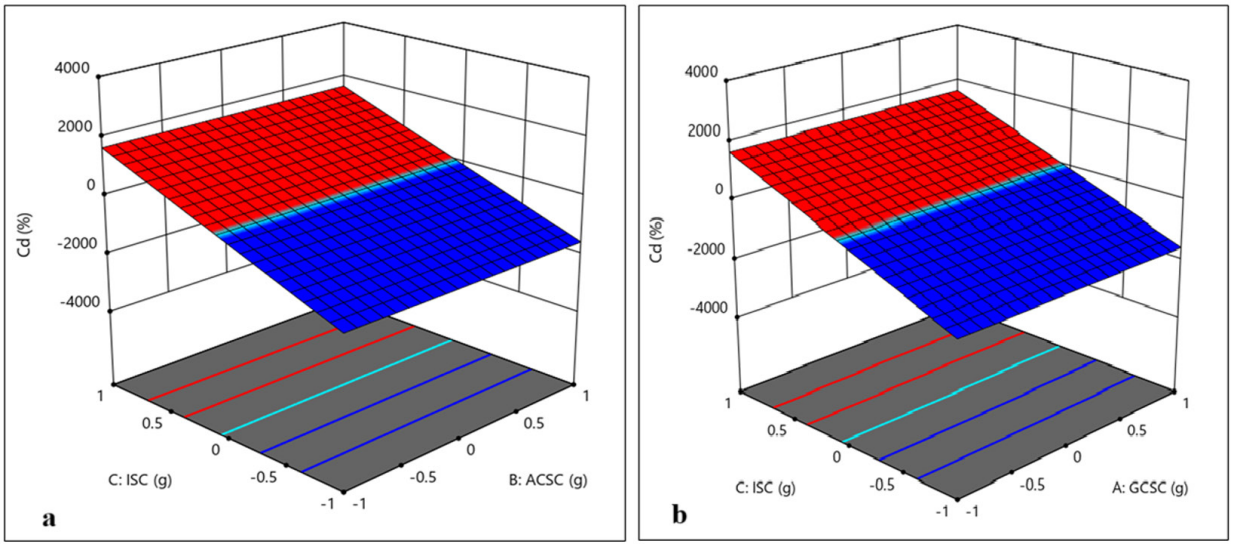

Fig. 7. Main Interaction and Effects of ACSC and GCSC on ISC, **a**) ACSC vs. ISC and **b**) GCSC vs. ISC for Removal of Cadmium

and the water samples. The interest was to investigate if all possible interaction effects of metals and water samples produced the same degree of removal. Generally, at as small as a 1 % significance level, there was evidence of a significant ($p<0.01$) mean difference in the degree of heavy metal removal for all the possible interactions. At a 1 % level of significance, the variable interactions showed that Zn demonstrated higher interactions with the samples by having the highest mean values. Pb, Cu, and Cd followed this in a decreasing order of mean values. Cd-ERWA produced the highest degree of heavy metal removal, followed by Cd-ABW, Cu-ERWA, and so on, while removal was lowest in Zn-

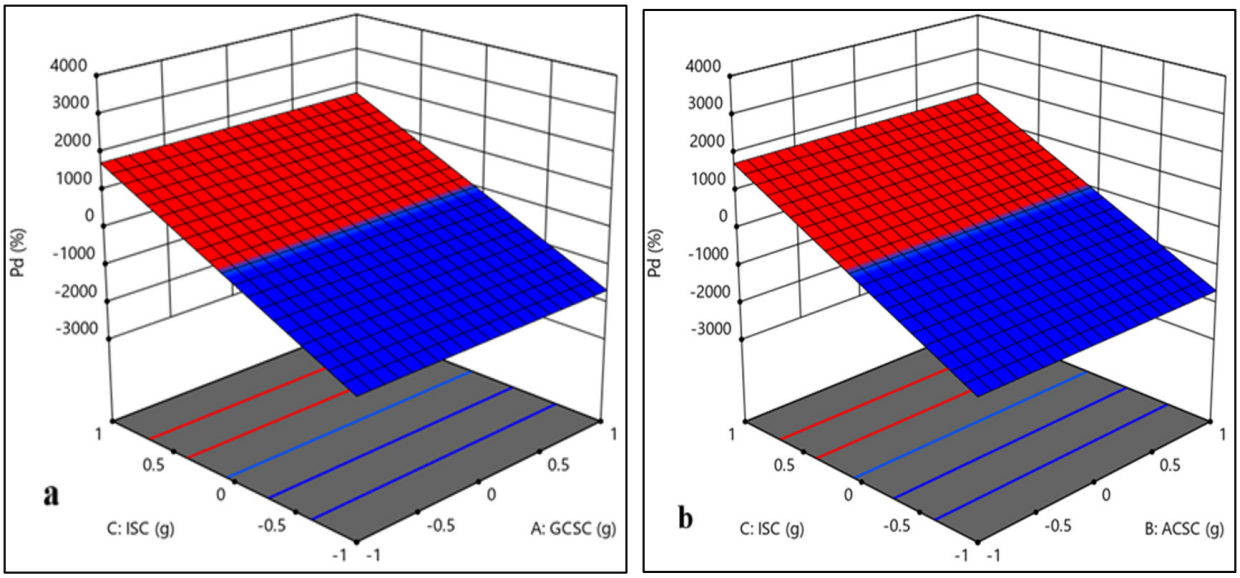

Fig. 8. Main Interaction and Effects of ISC and GCSC, and ISC and ACSC on the Percent Removal of Lead (Pb)

Table 7. Test of Significance: season, untreated/treated water samples, water, and metals in removing dissolved heavy metals

Factors	Variables	Mean sd	Sig. value ($p<0.05$)
Season	Rainy	0.567 ± 0.028	0.001
	Dry	0.006 ± 0.000	
Water	Untreated	0.438 ± 0.011	0.072
	Treated	0.135 ± 0.005	
Samples	FBW	0.044 ± 0.002	0.354
	ABW	0.027 ± 0.001	
	EBRW	1.057 ± 0.055	
	ERWA	0.018 ± 0.001	
Metal	Pb	0.118 ± 0.005	0.419
	Zn	0.993 ± 0.045	
	Cd	0.012 ± 0.000	
	Cu	0.022 ± 0.001	

EBRW. It can also be observed that interaction with ERWA produced a high degree of removal for each of the four metals. In contrast, most metal interactions with EBRW resulted in a low degree of removal. This observation in this work implied that there were different factors (i.e., pH, initial cation concentrations in the multi-metal system, effective ionic radius, etc.) responsible for removing heavy metals from the individual water samples for both seasons. This was in line with the investigations of [45, 47, 48].

Table 9 shows the multivariate test for the factors (season, water, samples, and metal) and their corresponding variables at 1, 5, and 10 % levels of significance. It was used to check for evidence of a significant mean difference between vector means relating to two groups. Concentrations 1, 2, and 3 were considered independent variables. At the 1 % significance level, there was evidence of a significant difference in means for samples, whereas the season was not substantial; water and metal at 1 %, 5 %, and even as high as 10 % were insignificant. This showed that with the observations made independently at three concentrations, heavy metal removal patterns were not the same for the samples.

Table 10 presented the result for testing the significant mean difference in the degree of heavy metal removal for both rainy and dry seasons. Table 10 revealed significant values of the variables during the rainy and dry seasons, which ranged from <0.001 to 0.002 and <0.001 to 0.004, respectively. For both seasons, there was evidence of a significant difference ($p<0.05$) in the degree of removal of heavy metals for treated and untreated water. Whereas the degree of removal is high for treated water, the dry season seems to present a tendency for a higher removal of heavy metals. Lower concentrations of the DHM in water samples during the dry season contributed to this, as evidenced by the lower mean values across all samples and metals.

Table 11 shows the result of the investigation

Table 8. Metal-sample interaction between the DHMs and the water samples

Variable	Interaction	Mean sd	Sig. value
Cu	FBW	0.026	<0.001
	ABW	0.025	<0.001
	EBRW	0.027	<0.001
	ERWA	0.012	<0.001
Zn	FBW	0.074	<0.001
	ABW	0.030	<0.001
	EBRW	3.843	<0.001
	ERWA	0.025	<0.001
Cd	FBW	0.020	<0.001
	ABW	0.008	<0.001
	EBRW	0.013	<0.001
	ERWA	0.007	<0.001
Pb	FBW	0.056	<0.001
	ABW	0.043	<0.001
	EBRW	0.345	<0.001
	ERWA	0.027	<0.001

Table 9. Multivariate Hotelling's Test, Concentrations 1, 2, and 3 were considered independent variables

Factor	Variable	Conc..	Sig. value
Season	Rainy	0.567 ± 0.024	0.116
	Dry	0.006 ± 0.001	
Water	Untreated	0.438 ± 0.024	0.393
	Treated	0.135 ± 0.006	
Sample	FBW	0.044 ± 0.002	0.107
	ABW	0.027 ± 0.001	
	EBRW	1.057 ± 0.051	
	ERWA	0.018 ± 0.011	
Metal	Pb	0.118 ± 0.005	0.156
	Zn	0.993 ± 0.045	
	Cd	0.012 ± 0.001	
	Cu	0.022 ± 0.001	

Table 10. Test of Significance during the rainy and dry seasons

Factors	Variables	Mean sd	Sig. value	Mean sd	Sig. value
		Rainy Season		Dry Season	
Water	Untreated	0.864 ± 0.043	0.002	0.012 ± 0.001	0.004
	Treated	0.270 ± 0.013		ND	
Samples	FBW	0.066 ± 0.003	<0.001	0.022 ± 0.002	<0.001
	ABW	0.052 ± 0.002		ND	
	EBRW	2.114 ± 0.107		ND	
	ERWA	0.035 ± 0.001		ND	
Metals	Pb	0.235 ± 0.012	<0.001	ND	0.002
	Zn	1.967 ± 0.112		0.019 ± 0.001	
	Cd	0.024 ± 0.001		ND	
	Cu	0.042 ± 0.002		ND	

to ascertain whether there was an increment or reduction in the DHMs removal due to the interaction of each of the metals with all the water samples during both seasons. The interactions of the heavy metals with the samples during rainy season in the order of decreasing removal was as follows: Cd-ERWA > Cd-ABW > Cu-ERWA > Cd-EBRW > Cu-FBW > Zn-ERWA > Cu-ABW > Cu-EBRW > Pb-ERWA > Zn-ABW > Zn-FBW > Pb-ABW > Pb-FBW > Pb-EBRW > Zn-EBRW. During dry season, the decreasing order is as follows: Cd-ABW = Cd-EBRW = Cd-ERWA = Cd-FBW = Cu-ABW = Cu-ERWA = Pb-ABW = Pb- EBRW = Pb- ERWA = Pb-FBW = Zn-EBRW = Zn-ERWA > Cu-EBRW > Pb-FBW > Zn-ABW > Cu-FBW > Zn-FBW.

At $p<0.001$ in the two seasons, there was evidence of a significant difference in the degree of heavy metal removal. Again, the dry season presented evidence of increased removal of heavy metals across all metal-sample interactions. As in the overall case presented in Table 8, Cd-ERWA interaction enabled higher removal, followed by Cd-ABW interaction, then Cu-ERWA interaction, and so on, down to Zn-EBRW, which had reduced heavy metal removal. Generally, metal interactions with ERWA appeared to encourage high removal of heavy metal, while metal interactions with EBRW lowered the degree of heavy metal removal. The result was in tandem with the initial metal ions concentrations in the untreated water samples (Table 5 and Table 6) and other previous works due to surface saturation [48].

During both seasons, the interaction of heavy metals and treatment materials was presented in Table 12, which showed higher removal in treated samples than in untreated samples. The result also showed evidence of significance between composite treatment materials (i.e., GCSC, ACSC, and ISC), heavy metals, and water samples. A P-value of <0.001 implied enough evidence of significance in the degree of metal removal concerning treatment materials-metals-samples interaction. Removal was notably high in treated-Cu-FBW, treated-Zn-ABW and treated-Zn-ERWA. This was closely followed by treated Cd-ERWA, while removal was lowest in treated Zn-EBRW.

Table 11. Metal-sample Interaction by Season

Variable	Interaction	Mean sd Rainy season	Sig. Value	Mean sd Dry season	Sig. value
Cu	FBW	0.040 ± 0.002	<0.001	0.011 ± 0.001	<0.001
	ABW	0.051 ± 0.003	<0.001	ND	<0.001
	EBRW	0.053 ± 0.004	<0.001	ND	<0.001
	ERWA	0.024 ± 0.001	<0.001	ND	<0.001
Zn	FBW	0.077 ± 0.008	<0.001	0.072 ± 0.003	<0.001
	ABW	0.055 ± 0.006	<0.001	0.015 ± 0.001	<0.001
	EBRW	7.687 ± 0.256	<0.001	ND	<0.001
	ERWA	0.050 ± 0.004	<0.001	ND	<0.001
Cd	FBW	0.040 ± 0.002	<0.001	ND	<0.001
	ABW	0.016 ± 0.001	<0.001	ND	<0.001
	EBRW	0.026 ± 0.001	<0.001	ND	<0.001
	ERWA	0.014 ± 0.002	<0.001	ND	<0.001
Pb	FBW	0.109 ± 0.005	<0.001	0.013 ± 0.001	<0.001
	ABW	0.086 ± 0.004	<0.001	ND	<0.001
	EBRW	0.690 ± 0.036	<0.001	ND	<0.001
	ERWA	0.054 ± 0.001	<0.001	ND	<0.001

Table 12. Test of Significance for Treatment-Metal-Sample Effect

Treatment	Heavy Metal	FBW	ABW	EBRW	ERWA
Untreated	Pb	0.106	0.081	0.686	0.050
	Zn	1.460	0.060	5.577	0.050
	Cd	0.034	0.013	0.022	0.012
	Cu	0.050	0.048	0.051	0.021
Treated	Pb	0.006	0.005	0.005	0.004
	Zn	0.003	0.001	2.110	0.001
	Cd	0.006	0.035	0.004	0.002
	Cu	0.001	0.003	0.003	0.003
P-value		<0.001	<0.001	<0.001	<0.001

4. Conclusion

The results show that 0.5 g, 1.5 g, and 0.025 g masses of the blended composite were successful in removing DHMs in separate 250 ml water samples during the rainy and dry seasons and determined by ICP-OES, respectively, with 62.16 - 99.19 percent and 100 percent removal efficiency. The statistical relevance of the optimization process of the composite materials for the removal of the DHMs using a reduced linear variance analysis model showed evidence of the model being suitable and statistically significant to describe the experimental data. The probability>F values indicated that the ISC component of the composite had a much-pronounced effect on the percent removal of Cu, Cd, and Pb. At the same time, ACSC and GCSC contributed latently in influencing the percent removal of the DHMs due to the reduced linear model used, and this does not imply that the adsorbents did not entirely have an effect on the removal of the DHMs. Furthermore, at ($p< 0.001$, $p< 0.01$, $p< 0.05$, and $p<0.1$), there were indications of significant mean differences in the following interactions: individual heavy metals with all the water samples during both seasons: DHMs and water samples, and in the vector mean of the water samples; between untreated and treated water, between water samples and their vector mean, and between the heavy metals during both seasons; as well as between the rainy and dry seasons, between the untreated and treated water, and in the vector mean of the water samples, respectively. With a p-value of <0.001, there was a significant mean difference concerning the interaction of treatment materials-metals-samples. It is recommended that a composite of 0.5 g GCSC, 1.5 g ACSC, and 0.025 g ISC be used to treat 250 ml of river or borehole water samples for DHMs removal. Additional research should be conducted to comparatively assess all possible effects of separately treating the water samples with the GCSC, ACSC, and ISC while varying the initial pH of the water samples.

5. Abbreviations

FBW	Funai borehole water
ABW	Assemblies of God church borehole water
EBRW	Ebonyi River water
ERWA	Eziyiaku river water, Akaeze
GCSC	Granulated coconut shell carbon
ACSC	*Akparata* (counter)softwood carbon
ISC	Iron(III) sulphate coagulant
DHMs	Dissolved heavy metals

6. Acknowledgment

I am grateful to the staff of the International Institute of Tropical Agriculture (IITA), Ibadan - where the dissolved heavy metals were quantified using an inductively coupled mass spectrometer; Department of Chemical Engineering, Ahmadu Bello University, Zaria; for obtaining the surface morphology and the electron dispersive x-ray analysis of the adsorbents. I salute my fellow staff of the Department of Chemistry, Alex Ekwueme Federal University, Ndufu-Alike, for their assistance during this study. The authors hereby disclose that they have no known competing financial interests or personal relationships that could have appeared to influence the work reported in this paper.

7. References

[1] S. J. Cobbina, A. B. Duwiejuah, R.Quansah, Comparative assessment of heavy metals in drinking water sources in two small-scale mining communities in northern Ghana, Nigeria, Int. J. Environ. Res. Public Health, 12 (2015)10620–10634. https://doi.org/10.3390/ijerph120910620

[2] B.O. Oladunni, A. Tejumade, A.O. Otolorin, Heavy metal contamination of water, soil, and plants around an electronic waste dumpsite,Pol. J. Environ. Stud., 22(2013) 1431-1439. https://www.pjoes.com/pdf-89108-22967?filename=22967.pdf

[3] J. Rakhtshah, H. Shirkhanloo, M. Dehghani Mobarake, Simultaneously speciation and determination of manganese (II) and (VII) ions in water, food, and vegetable samples based on immobilization of N-acetylcysteine on multi-walled carbon nanotubes, Food Chem., 389 (2022) 133124. https://doi.org/10.1016/j.food chem.2022.133124

[4] J.O. Jeje, K.T. Oladepo, Assessment of heavy metals of boreholes and hand dug wells in Ife North Local Government Area of Osun State, Nigeria. Int. J. Sci. Technol., 3 (2014) 209-214. https://sciencetechnology.uz/index.php/s

[5] J. Rakhtshah, Ultrasound assisted-dispersive-modification solid-phase extraction using task-specific ionic liquid immobilized on multiwall carbon nanotubes for speciation and determination mercury in water samples, Microchem. J., 154 (2020) 104632. https://doi.org/10.1016/j.microc.2020.104632

[6] A. Rouhollahi, Speciation, and determination of trace amount of inorganic arsenic in water, environmental and biological samples, J. Chin. Chem. Soc., 58 (2011) 623-628. https://doi.org/10.1002/jccs.201190097

[7] J.M. Misihairabgwi, K.. Abisha, A. Peter, C.J. Colin, P.A. Tanya, N. Ignatius, Adsorption of heavy metals by agroforestry waste derived activated carbons applied to aqueous solutions. Afr. J. Biotech., 13(2014) 1579-1587. https://doi.org/10.5897/AJB2013.12115

[8] S. D. Ahranjani, A lead analysis based on amine-functionalized bimodal mesoporous silica nanoparticles in human biological samples by ultrasound assisted-ionic liquid trap-micro solid phase extraction, J. Pharm. Biomed. Anal., 157 (2018) 1-9. https://doi.org/10.1016/j.jpba.2018.05.004

[9] M. M. Eskandari, B. Kalantari, Dispersive liquid-liquid microextraction based on task-specific ionic liquids for determination and speciation of chromium in human blood, J. Anal. Chem., 70 (2015) 1448-1455. https://doi.org/10.1134/S1061934815120072

[10] O.P. Igboji, J.A. Ayodele, Quality of FADAMA and EBSCA boreholes in Abakaliki, Southeastern Nigeria, Am. Eur. J. Agri. Environ. Sci., 16 (2016) 470-478. https://doi.org/10.5829/idosi.aejaes.2016.16.3.12841

[11] J.N. Edeh, L.E. Udu, M.C. Nwankamma, S.O. Chima, Effects of financial corruption on socio-economic development in Ebonyi State: A study of selected Local Government Areas, Int. Digit. Org. Sci. Res., 4 (2019) 24-41. https://www.idosr.org/wp-content/uploads/2019/07/IDOSR-JAM-42-24-41-2019-LU-P1.pdf

[12] M. Bagheri Hosseinabadi, N. Khanjani, M.D. Mobarake, Neuropsychological effects of long-term occupational exposure to mercury among chloralkali workers, Work, 66 (2020) 491-498. https://doi.org/10.3233/WOR-203194

[13] V.C. Ezennubia, A.A. Onunkwo, O. Ozotta,

Baseline verification of heavy metal distribution in surface water bodies of Okposi and environs, Ohaozara Local Government Area, Ebonyi State, Southeastern Nigeria, Int. J. Adv. Acad. Res. Sci. Technol. Eng., 5 (2019) 82-92. https://doi.org/10.46654/ij.24889849

[14] F. Cherono, N. Mburu, B. Kakoi, Adsorption of lead, copper and zinc in a multi-metal aqueous solution by waste rubber tires for the design of single batch adsorber, Heliyon, 7(2021) e08254. https://doi.org/10.1016/j.heliyon.2021.e08254

[15] F. Golbabaei, Z. Sadeghi, A. Vahid, A. Rashidi, On-line micro column preconcentration system based on amino bimodal mesoporous silica nanoparticles as a novel adsorbent for removal and speciation of chromium (III, VI) in environmental samples, J. Environ. Health Sci. Eng., 13 (2015) 1-12. https://doi.org/10.1186/s40201-015-0205-z

[16] M. D. Mobarake, Ultrasound-assisted solid-liquid trap phase extraction based on functionalized multi-wall carbon nanotubes for preconcentration and separation of nickel in petrochemical waste water, J. Anal. Chem., 74 (2019) 865-876. https://doi.org/10.1134/S1061934819090090

[17] S. Davari, F. Hosseini, Dispersive solid-phase microextraction based on aminefunctionalized bimodal mesoporous silica nanoparticles for separation and determination of calcium ions in chronic kidney disease, Anal. Methods Environ. Chem. J., 1 (2018) 57-66. https://doi.org/10.24200/amecj.v1.i01.37

[18] F. Golbabaei, A. Vahid, A. Faghihi Zarandi, A novel nano-palladium embedded on the mesoporous silica nanoparticles for mercury vapor removal from air by the gas field separation consolidation process, Appl. Nanosci., 12 (2022) 1667-1682. https://doi.org/10.1007/s13204-022-02366-0

[19] I. Andrew-Oha, K. Mosto-Onuoha, S. Sunday-Dada, Contrasting styles of lead-zinc-barium mineralization in the lower Benue trough, Southeastern Nigeria, Earth Sci. Res. J., 21 (2017) 7-16. https://doi.org/10.15446/esrj.v21n1.39703

[20] D. Igwe, J. Afiukwa, F. Nwabue, Seasonal evaluation of total organic carbon removal from river samples using scrap metal-based coagulant and local salt modified-biomaterials for point-of-use water treatment, Int. J. Environ. Anal. Chem., 103 (2021a) 1-21. https://doi.org/10.1080/030673192021.1875451

[21] D.O. Igwe, J.N. Afiukwa, F.I. Nwabue, Evaluation of the anti-microbial efficiency of scrap metal-based coagulant and local salt modified-biomaterial for point-of-use water treatment, Int. J. Phy. Sci., 16 (2021b) 36-51. https://doi.org/10.5897/IJPS2020.4926

[22] J.E. Obarezi, J.I. Nwosu, Structural controls of Pb-Zn mineralization of Enyigba District, Abakaliki, Southeastern Nigeria, J. Geo. Min. Res., 5 (2013) 250-261. https://doi.org/10.5897/JGMR13.0189

[23] O.C. Okeke, E.C. Dioha, I.B. Umeorizu, M.C. Mmerole, N.I. Nwakwasi, Physico-chemical and bacteriological characteristics and quality assessment of groundwater from shallow aquifer in Abakaliki town, Southeastern Nigeria, Int. J. Adv. Acad. Res. Sci. Technol. Eng., 2(12) (2016) 60-73. https://www.ijaar.org/about-ijaar/

[24] M.O. Eyankware, Hydrogeochemical evaluation of groundwater for irrigation purpose in Ekaeru Inyimagu and its Adjoining Area, Ebonyi State, Nigeria, Discovery, 65 (2020) 681-694. https://mail.discoveryjournals.org/discovery/current_issue/v56/n298/A4.pdf?

[25] T.I. Mgbeojedo, L.S. Al-Naimi, Hydrogeochemical and physico-chemical studies of the groundwater within Afikpo and Abakaliki, Southeastern Nigeria, Geosci., 8 (2018) 32-43. https://doi.org/10.5923/j.geo.20180802.02

[26] F.K. Onu, The southern Benue trough and Anambra basin, Southeastern Nigeria: A stratigraphic review, J. Geo. Environ. Earth Sci. Int., 12 (2017) 1-16. https://doi.org/10.9734/JGEESI/2017/30416

[27] F. D. Wilde, Techniques of Water Resources Investigations (TWRI), Preparations for water

sampling, Book 9 (version 2.0, 1/05), U.S Geological Survey, pp. 1-46, 2004. https://pubs.usgs.gov/twri/twri9a1/Ch1.pdf

[28] B. Mahesh, B. Chandu, B. Sakala, S. Nama, S. Domatoti, Inductively coupled plasma mass spectrometry (ICP-MS), Int. J. Res. Pharm. Chem., 2 (2012) 671-680. https://doi.org/10.4135/9781446247501.n2037

[29] W. Heschel, E. Klose, On the suitability of agricultural by-products for the manufacture of granular activated carbon, Fuel, 74 (1995) 1786–1791. https://doi.org/10.1016/0016-2361(95)80009-7

[30] R. Ansari, F.N. Khoshbakhat, Application of polypyrole coated on wood sawdust for removal of Cr(VI) ion from aqueous solutions, React. Funct. Polym., 67 (2007) 367–374. https://doi.org/10.1016/j.reactfunctpolym.2007.02.001

[31] T. Xiaomin, Z. Huaili, T. Houkai, S. Yongjun, G. Jinsong, X. Wanying, Y. Qingqing, C. Wei, Chemical coagulation process for the removal of heavy metals from water: A review, Desalin. Water Treat., 57 (2016) 1733-1748. https://doi.org/10.1080/19443994.2014.977959

[32] D. Jiang, X. Tianyi, W. Haiyan, Z. Anmin, W. Yong, Effects of cellulose, hemicellulose, and lignin on the structure and morphology of porous carbons, ACS. Sust. Chem. Eng., 4 (2016) 3750-3756 https://doi.org/10.1021/acssuschemeng.6b00388

[33] M. Seri, H. Gewa, A. Irvan, I. Heri, Quality comparison of activated carbon produced from oil palm fronds by chemical activation using sodium carbonate versus sodium chlorid, J. Korean Wood Sci. Technol., 48 (2020) 503-512. https://doi.org/10.5658/WOOD.2020.48.4.503

[34] J. Sahira, K.C. Bishnu, Synthesis and characterization of sugarcane bagasse based activated carbon: Effect of impregnation ratio of $ZnCl_2$, J. Nepal Chem. Soc., 41 (2020) 74-79. https://doi.org/10.3126/jnes.v41i1.30490

[35] A.J. Nwinyimagu, G.N. Nwonumara, C. Ani, I.O. Ukeje, Evaluation and management of the physicochemical variables of Asu river, Southeast, Nigeria, J. Sust. Dev., 9 (2016) 54-66. https://doi.org/10.5539/jsd.v9n2p54

[36] N. Hannington, B. Denis, N. Emmanuel, Effects of seasonal variations in physical parameters on quality of gravity flow water in Kyanamira Sub-county, Kabale District, Uganda, J. Water Res. Pro., 8 (2016) 1297-1309. https://doi.org/10.4236/jwarp.2016.813099

[37] World Health Organization (WHO), Guideline for drinking water quality fourth Edition incorporating the first addendum, Geneva, 541p, 2017. https://www.who.int/

[38] Standard Organization of Nigeria (SON), Nigeria Industrial Standard for Drinking Water Quality, NIS 977:2017, National Standard for Drinking Water Quality from Standard Organization of Nigeria, 22p, 2017. https://son.gov.ng/

[39] pH of Water, Fundamentals of Environmental Measurements, Fondriest Environmental, Inc., 2013. http://www.fondriest.com/environmental-measurements/parameters/water-quality/pH

[40] J. Bratby, Coagulation and flocculation in water and wastewater treatment (third ed), International Water Association (IWA) Publishing, London, UK, 450 pages, 2006. www.iwapublishing.com

[41] A.A.O. El-Amin, Removal of resorcinol from aqueous solution by activated carbon: Isotherms, thermodynamics and kinetics, Am. Chem. Sci. J., 16 (2016) 1-13. https://doi.org/10.9734/ACSJ/2016/27637

[42] M. K. Abbasabadi, F. Hosseini, Nanographene oxide modified phenyl methanethiol nanomagnetic composite for rapid separation of aluminum in wastewaters, foods, and vegetable samples by microwave dispersive, Food Chem., 347 (2021) 129042. https://doi.org/10.1016/j.foodchem.2021.129042

[43] S. Haddouta, K.L. Priyab, A.M. Hoguanec, J.C.C. Casilad, I. Ljubenkove, Relationship of salinity, temperature, pH, and transparency to dissolved oxygen in the Bouregreg estuary (Morocco): First results, Water Pract. Technol., 17 (2022) 2654. https://doi.org/10.2166/wpt.2022.144

[44] F. Sinada, M.E. Abdel-Rahman, Water chemistry

and quality of the white nile at Khartoum, Sudan J. Sci., 5 (2013), 1-14. http://sciencejournal.uofk.edu/

[45] K. Roshanak, B.A. Mansor, R.F.M. Hamid, S. Kamyar, B. Mahiran, K. Katayoon, Rapid adsorption of copper (II) and lead (II) by rice straw/Fe_3O_4 nanocomposite:Optimization, equilibrium isotherms, and adsorption kinetics study, PLOS ONE, 10 (2015) e0120264. https://doi.org/10.1371/journal.pone.0120264

[46] B. Das, N.K. Mondal, R. Bhaumik, P. Roy, Insight into adsorption equilibrium, kinetics and thermodynamics of lead onto alluvial soil, Int. J. Environ. Sci. Technol., 11 (2014) 1101-1114. https://doi.org//10.1007/s13762-013-0279-z

[47] N. Esmaeili, J. Rakhtshah, E. Kolvari, A. Rashidi, H. Shirkhanloo, Rapid speciation of lead in human blood and urine samples based on MWCNTs@DMP by dispersive ionic liquid-suspension-micro-solid phase extraction, Biol. Trace Elem. Res., 199 (2021) 2496–2507. https://doi.org/10.1007/s12011-020-02382-7

[48] M.N. Saifuddin, P. Kumaran, Removal of heavy metal from industrial wastewater using chitosan coated oil palm shell charcoal, Electronic J. Biotechnol., 8 (2005) 43-53. https://doi.org/10.4067/S0717-34582005000100008

[49] M. K. Abbasabadi, Speciation of cadmium in human blood samples based on Fe_3O_4-supported naphthalene-1-thiol- functionalized graphene oxide nanocomposite by ultrasound-assisted dispersive magnetic micro solid phase extraction, J. Pharm. Biomed. Anal., 189 (2020)113455. https://doi.org/10.1016/j.jpba.2020.113455

[50] P.W. Olupot, J. Wakatuntu, M. Turyasingura, J. Jjagwe, E. Menya, M. Okure, Optimization of heavy metal removal by activated carbon obtained as a co-product from fast pyrolysis of rice husks, Results Mater., 21 (2024) 100545. https://doi.org/10.1016/j.rinma.2024.100545

Anal. Methods Environ. Chem. J. 8 (1) (2025) 78-99

AMECJ

Research Article, Issue 1
Analytical Methods in Environmental Chemistry Journal
Journal home page: www.amecj.com/ir

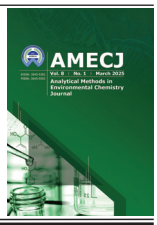

Determination and investigation of phenolic compounds in Citrus pulps and zests by Ultra-high performance liquid chromatography

Amal Sammama [a,b,*], Hasnaa Sammama[c,d], Rachid Bengueddour [a]

[a]*Natural Resources and Sustainable Development Lab, Department of Biology, Faculty of Science, Ibn Tofail University, Kenitra, Morocco*

[b]*Center of Analysis and Characterization, University Cadi Ayyad, Marrakech, Morocco*

[c]*Laboratory of Phyto-Bacteriology, Plant Protection Research Unit, National Institute of Agricultural Research, Marrakesh, Morocco*

[d]*Laboratory of Agro-Biotechnology and Bioengineering, Department of Biology, Faculty of Sciences and Technologies-Gueliz, Cadi Ayyad University, Marrakesh, Morocco*

ARTICLE INFO:

Received 21 Nov 2024

Revised form 27 Jan 2025

Accepted 18 Feb 2025

Available online 30 March 2025

Keywords:
Antioxidant activities;
Analysis;
Citrus;
Phenolic composition;
Ultra-high-performance-liquid-chromatographic-diode array;
2.2-diphenyl-1-picrylhydrazyl

ABSTRACT

This study aimed to evaluate in vitro the influence of extraction methods (maceration and soxhlet) and solvents (hexane, dichloromethane, ethyl acetate and methanol) on the phenolic composition and antioxidant activity of tree citrus species: *C. limon, C. limetta and C. aurantifolia*. The results showed that the soxhlet remains the best extraction method for quantifying polyphenols, flavonoids and condensed tannins. Polar solvents (ethyl acetate and methanol) make it possible to obtain the best extraction yields and high polyphenols and flavonoids. *Citrus aurantifolia* shows the highest contents for epicarps and pulps, respectively in polyphenols (326.73 mg and 443.57 mg Gallic acid equivalent (EAG) per gram of fresh weight; FW) and in flavonoids (133.00 mg and 138.62 mg Equivalent (EQ) per gram of FW). The evaluation of the antioxidant activity using the 2.2-diphenyl-1-picrylhydrazyl (DPPH) for the different extracts showed that methanol and ethyl acetate extracts by soxhlet possess the best antioxidant activities. A strong antiradical power was noted for the epicarps and the pulps of *C. aurantifolia* fruit, respectively of 5.13 and 4.89 µg mL^{-1}. 15 phenolic compounds were tentatively identified by an ultra-high-performance-liquid-chromatographic-diode array (UHPLC-DAD) in the polar *Citrus* pulp and epicarp extracts. In fact, the identification of three flavonols (rutin, kaempherol and quercetin), two flavanones (hesperidin and naringin), a flavone (3,4,5,7-tetrahydroxyflavone)and a phenolic acid (pyrogallic acid) were the major compounds identified in polar citrus pulp and epicarp extracts.

1. Introduction

According to current nutritional theories, one secret to good health is to absorb more antioxidants, which promote the proper aging of the body's various organs. This is one of the major reasons why a Mediterranean diet rich in fresh fruit and vegetables is recommended [1].

The ingestion of secondary metabolites via fruit and vegetables could enable our bodies to strengthen their defenses against the oxidation processes that threaten our cells on a daily basis. However, the mechanisms involved probably go far beyond the direct reduction of reactive oxygen species by secondary metabolites such as phenolic compounds [2]. *Citrus* (*Citrus L. de Rutaceae*) is one of the world's major fruit crops. It is widely cultivated in tropical and subtropical

*Corresponding Author: Amal Sammama
Email: sammama.amal@gmail.com
https://doi.org/10.24200/amecj.v8.i01.1006

regions of the world and in many other areas. *Citrus* cultivation is the world's largest fruit production sector, with more than 161.8 million tons annually in 2021 [3]. *Citrus* is a highly valuable matrix due to its wealth of functional ingredients (essential oils, fibers, carotenoids, vitamin C, phenolic compounds) with a wide range of applications in the food, cosmetics and nutraceutical industries, as well as in the production of biofuels and biodegradable materials [4]. However, various epidemiological studies have suggested that citrus fruits positively affect a range of degenerative disorders [5]. *Citrus* consumption has expanded dramatically in recent years due to its beneficial effects on human health. *Citrus* peels represent a major source of phenolic compounds, mainly flavonoids and phenolic acids. *Citrus* flavonoids include glycosylated flavanones and polymethoxylated flavones [6]. *Citrus* peel flavonoids are characterized by their antioxidant, therapeutic, antiviral, antifungal and antibacterial activity [7]. Indeed, recent research has focused on by-products that extract natural antioxidants to replace synthetic antioxidants [8]. In addition, most industries have focused on fruit and vegetable by-products to transform them into exploitable products [9]. Indeed, our study evaluate firstly the effect of extraction methods (maceration and soxhlet) and the different solvents (hexane, dichloromethane, ethyl acetate and methanol) on the quantification of total phenols, flavonoids and condensed tannins contained in *Citrus Limon Burm, Citrus Limetta Risso and Citrus Aurantiifolia (Christm.) Swingle*. Secondly, evaluating the effect of the extraction methods and the different solvents on the antioxidant activity of the studied extracts. Thus, the various phenolic compounds of polar citrus extracts are characterized by UHPLC-DAD.

2. Material and Methods

2.1. Plant material

At the maturity stage, the fruits of C. limetta, C. limon, and C. Aurantiifolia were randomly harvested from all the trees. The fruits were washed, the pulp and epicarp were manually separated and seeded. 25.0 g of fresh pulp or epicarp was extracted by maceration (250 ml) and soxhlet (300 mL) in increasing solvent polarity for 24h at room temperature and in the dark. The extracts were evaporated using a rotavapor, then taken up with various volumes of methanol and stored at -4°C.

2.2. Reagents

All thirty-three standards used for analyses were obtained from Sigma-Aldrich (Berin, Germany): blend 1: pyrogallic acid (CAS Number: 87-66-1), vannilic acid (CAS Number: 121-34-6), caffeic acid (CAS Number: 331-39-5), ferulic acid (CAS number: 1135-24-6), hesperidin (CAS Number: 520-26-3) and salicylic acid (CAS Number: 69-72-7). The blend two including: Gallic acid (CAS Number: 149-91-7), Catechin (CAS Number: 7295-85-4), chlorogenic acid (CAS Number: 327-97-9), epicathechin (CAS Number: 490-46-0), vanillin (CAS Number: 121-33-5), p-coumaric acid (CAS Number: 501-98-4), sinapic acid (CAS Number: 530-59-6), naringin (CAS Number: 10236-47-2), rutin (CAS number: 153-18-4), quercetin (CAS number: 117-39-5) and kaempferol (CAS number: 520-18-3). Also, the blend three including: catechol (CAS number: 120-80-9), hydroxybezoic acid (CAS Number: 99-96-7), syringic acid (CAS Number: 530-57-4), 3,4 dimethoxybezoic acid (CAS Number: 93-07-2), 2-hydroxynaphthoic acid (CAS Number: 2283-08-1), rosmarinic acid (CAS Number: 20283-92-5), 4'.5.7 trihydroxyflavanone (CAS Number: 67604-48-2), 3',5,7 trihydroxy-4'-methoxyflavone (CAS Number:520-33-2). And the blend four including: 3-hydroxybenzoic acid (CAS Number: 99-06-9), 4-hydroxybenzoic acid (CAS Number: 99-96-7), 3,4-dihydroxycinnamic acid (CAS Number: 331-39-5), 4-hydroxy-3,5-dimethoxycinnamic acid (CAS Number: 530-59-6), ellagic acid (CAS Number: 476-66-4), tannic acid (CAS Number: 1401-55-4), 3',4',5,7-tetrahydroxyflavone (CAS Number: 491-70-3), curcumin (CAS Number: 458-37-7). Reactif Folin-Ciocalteu (CAS Number: 12111-13-6), 2,2-Diphenyl-1-picrylhydrazyl (CAS Number: 1898-66-4), and Ascorbic acid (CAS Number: 50-81-7, Sigma).

2.3. Determination of total phenolics, total flavonoids and tannins

The polyphenols were determined by the Folin-Ciocalteu method according to Li *et al*. [10]. The

results were reported in milligrams of gallic acid equivalent per gram of fresh weight (mg GE g^{-1} FW). The flavonoids were characterized by the aluminum trichloride ($AlCl_3$) method according to Shraim researcher [11]. Results were expressed as micrograms of quercetin equivalent per gram of fresh weight (mg QE g^{-1} FW). The condensed tannins were determined by the vanillin acid method [12]. Results were expressed as milligrams of catechin equivalent per gram of fresh weight (mg CE g^{-1} FW).

2.4. Analysis of DPPH radical scavenging activity

According to Awika et al. [13], antioxidant activity was measured using the DPPH method. The methanol dissolved the DPPH radical at a 5.5 mg mL^{-1} concentration. Then, it was sonicated for 3 minutes and kept at -4 °C for 1 hour at obscurity. Briefly, 1.0 mL of each extract of pulp or epicarp was added to 2.5 mL of DPPH solution, and the absorbance was measured after 30 min at 515 nm. DPPH trapping was determined using Equation 1.

$$IC50\% = [1 - (Abs\ (t\ =\ 30)/Abs\ (t = 0))] * 100 \quad \text{(Eq. 1)}$$

Abs (t = 0): absorbance of the *DPPH* radical at t = 0 min
Abs (t = 30): absorbance of the *DPPH* radical + phenolic extracts at t = 30 min.
The positive control was a solution containing the standard antioxidants: ascorbic acid, gallic acid, and quercetin. The absorbance of the solution was evaluated under identical conditions as the samples. For each concentration, the test was repeated three times.

2.5. Determination of phenolic compound

The Dionex Ultimate 3000 chromatography system (CA, USA), which is furnished with a quaternary pump (HPG 3400 RS), an autosampler (WPS 3000 TSL) and a column oven (TCC 3000), was used to carry out the chromatographic separation. A Kinetex C18 reversed phase column (250 × 4,6 mm, Eurospher 100-5) provided by Thermo Fisher Scientific (CA, USA) was used for the proposed technique. The separation and identification of phenolic compounds was performed using the method of Puigventós et al. [14]. Retention times and UV spectra were compared to standards to identify the compounds investigated in the methanolic and ethyl acetate extracts (Schema 1).

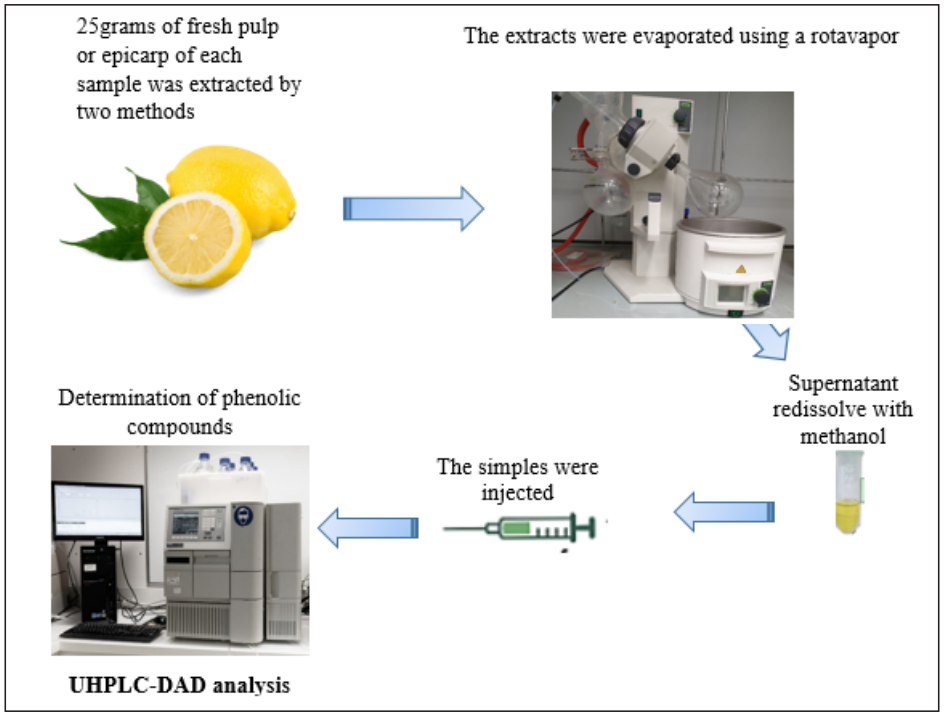

Schema 1. Schematic of study stages including the sampling, the extraction method, and analysis of phenolic compounds by UHPLC-DAD

Also, the Chromatographic profile of pulp from methanolic extracts of C. limon (Cp1), C. limetta (Cp2) and C. aurantifolia (Cp3) by two extraction methods maceration M and soxhlet S were shown in Figure 1a. Chromatographic profile of epicarp from methanolic extracts of C. limon (Cz1), C. limetta (Cz2) and C. aurantifolia (Cz3) by two extraction methods maceration M and soxhlet S were shown in Figure 1b. Chromatographic profile of pulps from ethyl acetate extracts of C. limon (Cp1), C. limetta (Cp2) and C. aurantifolia (Cp3) by two extraction methods, maceration M and soxhlet S, were shown in Figure 1c. Chromatographic profile of epicarp from methanolic extracts of C. limon (Cz1), C. limetta (Cz2) and C. aurantifolia (Cz3) by two extraction methods maceration M and soxhlet S. was shown in Figure 1d. The chromatographic profile of the multi-standards is shown in Figure 1e and Table 1.

Table 1. The multi standards with their retention times

Compounds	Retention time
Blend 1	
Pyrogallic Ac	5.45
Vanillic Ac	11.81
Cafeic Ac	12.18
Furelic Ac	16.51
Hesperidin	18.76
Salicyclic Ac	19.48
Blend 2	
Gallic Ac	5.86
Catechin	9.44
Chlorogenic ac	10.87
Epicathechin	12.13
vanillin	12.72
p-coumaric	15.41
Sinapic Ac	16.87
Naringin	19.04
Rutin	20.31
Quercetin	24.84
Kaempferol	26.82
Blend 3	
Catechol	8.07
Hydroxybezoic Ac	10.76
Syringic Ac	12.54
dimethoxybezoic Ac 3,4	16.46
hydroxynaphthoic Ac 2	19.20
Rosmarinic Ac	20.14
trihydroxyflavanon 4,5,7	24.05
trihydroxy-4'-methoxyflavon 5,7,'3	25.34
Blend 4	
hydroxybenzoic Ac-3	7.74
hydroxybenzoic Ac-4	10.76
dihydroxycinnamic Ac 3,4	12.20
hydroxy-3,5-dimethoxynnamic-4	16.90
Ellagic Ac	21.74
Tannic Ac	24.87
tetrahydroxyflavon-5,7,'4,'3	26.15
Curcumin	28.16

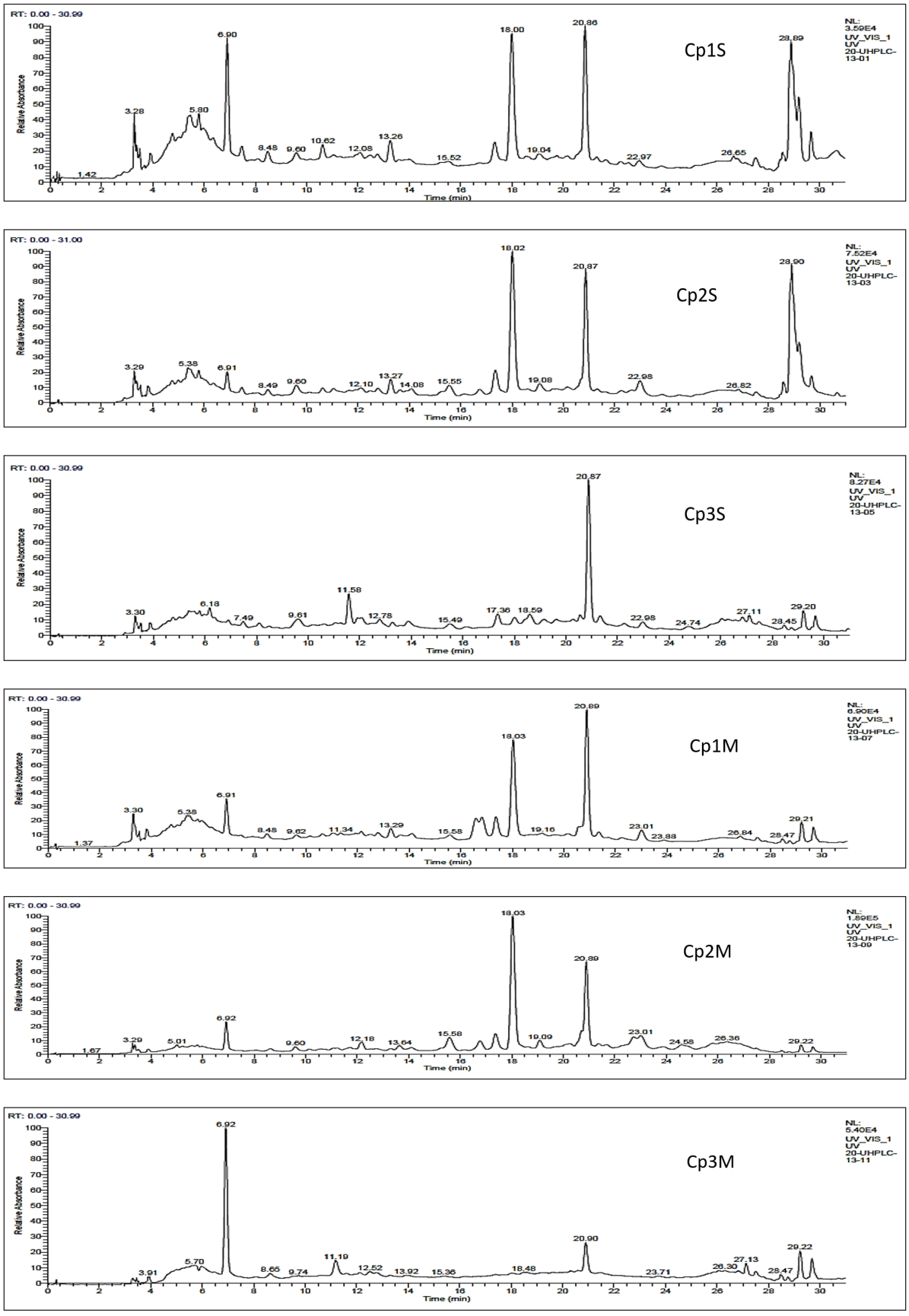

Fig. 1a. Chromatographic profile of pulp from methanolic extracts of *C. limon (Cp1), C. limetta (Cp2) and C. aurantifolia (Cp3)* by two extraction methods maceration M and soxhlet S.

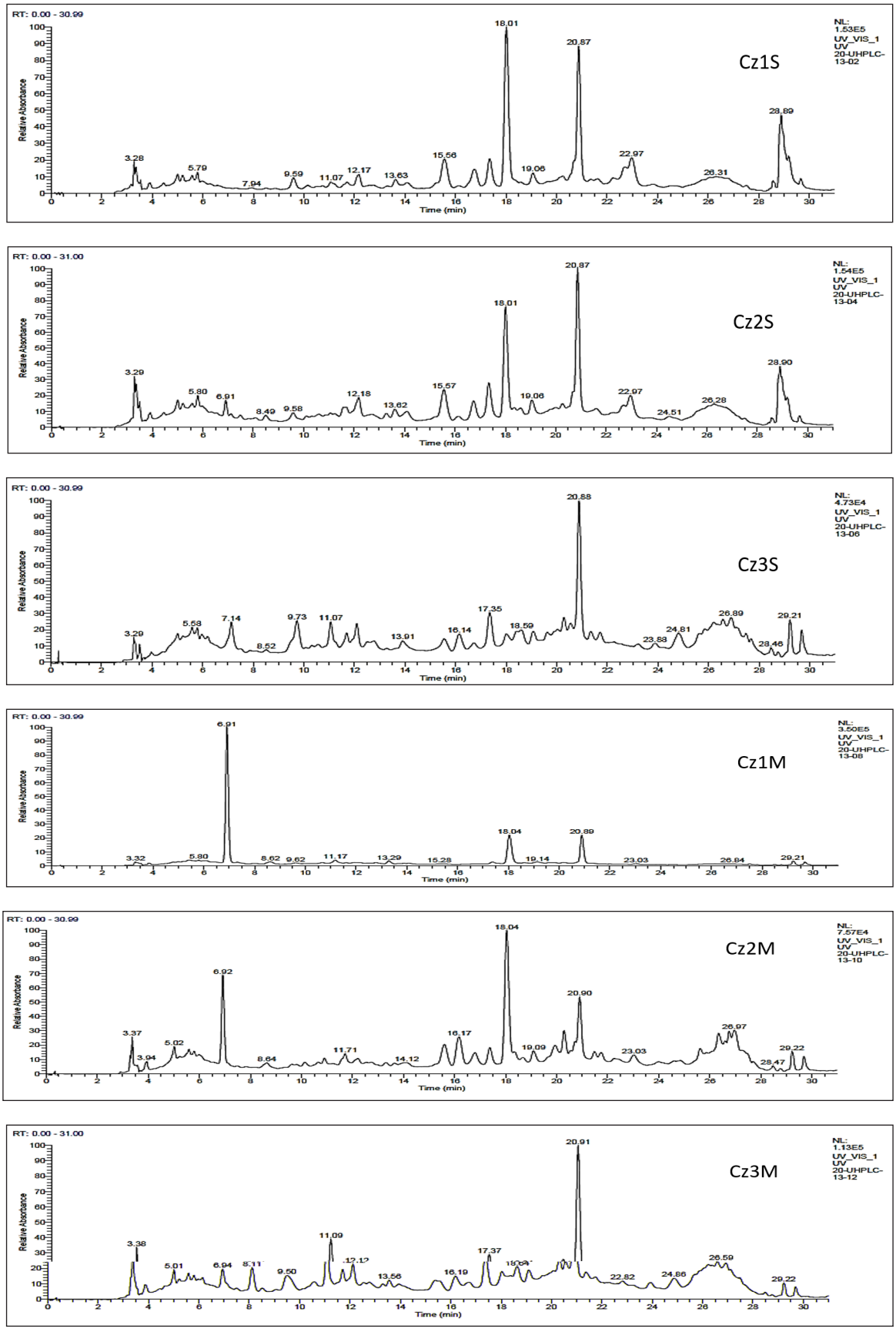

Fig. 1b. Chromatographic profile of epicarp from methanolic extracts of *C. limon (Cz1), C. limetta (Cz2) and C. aurantifolia (Cz3)* by two extraction methods maceration M and soxhlet S.

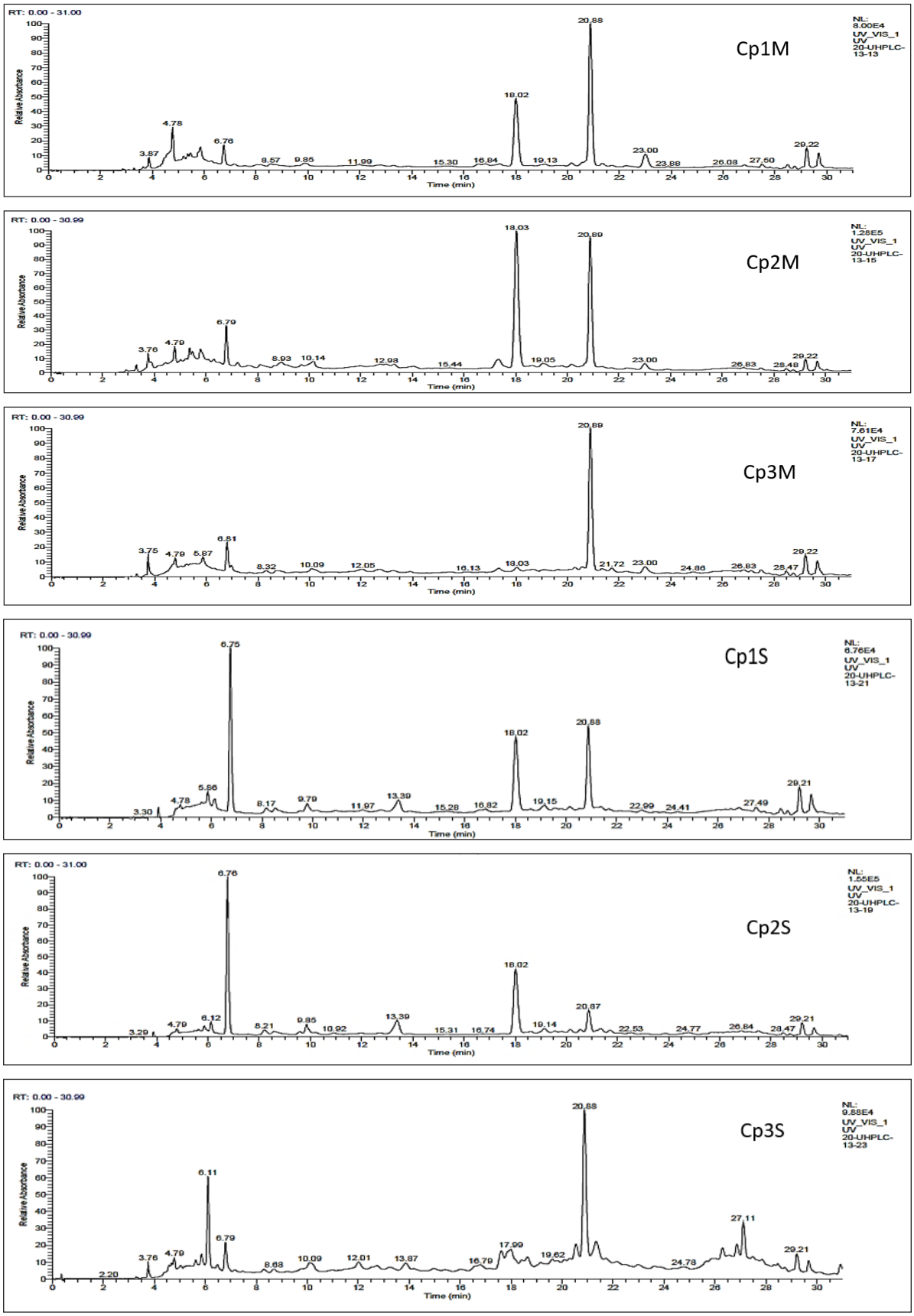

Fig. 1c. Chromatographic profile of pulps from ethyl acetate extracts of *C. limon (Cp1), C. limetta (Cp2) and C. aurantifolia (Cp3)* by two extraction methods maceration M and soxhlet S

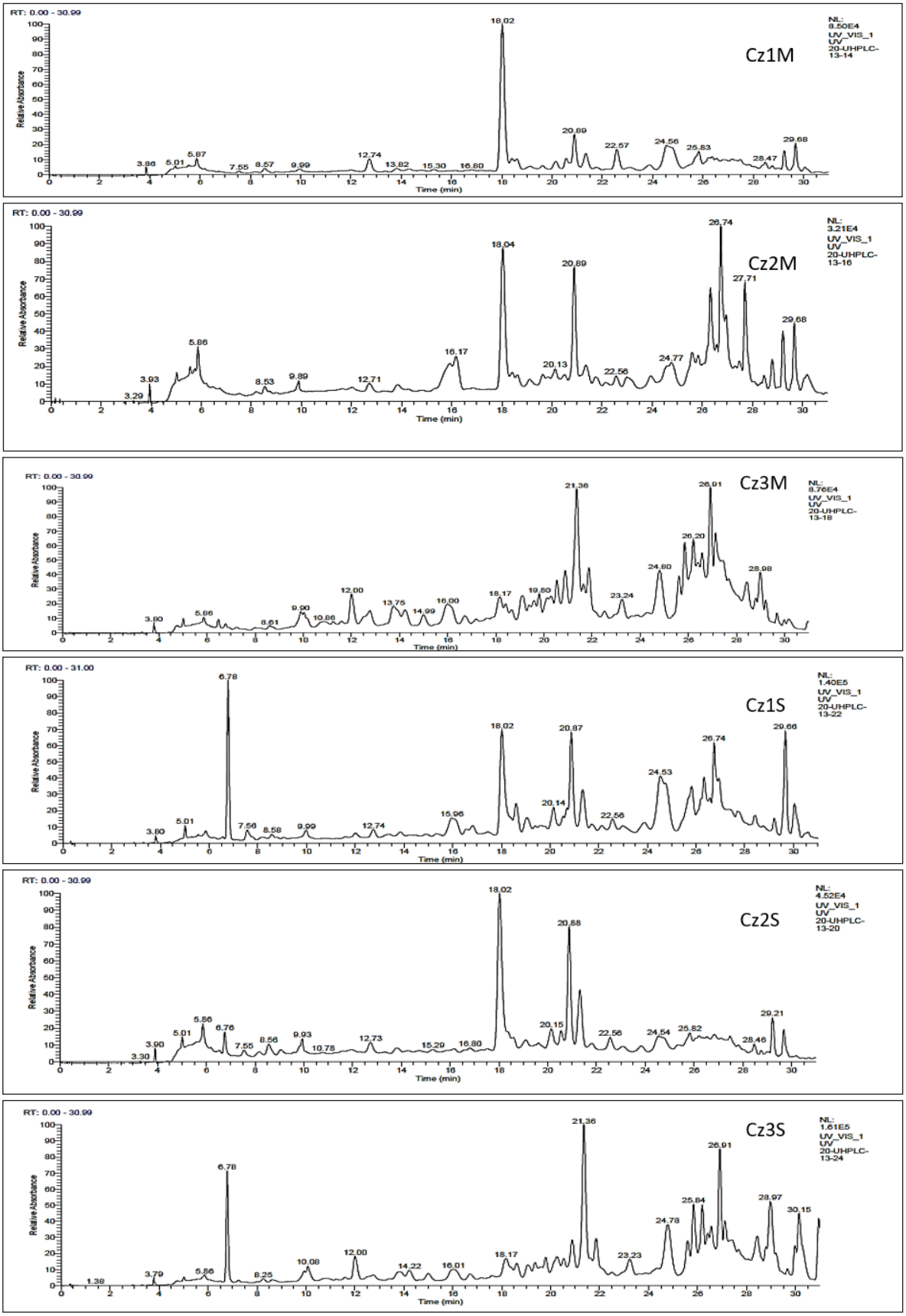

Fig. 1d. Chromatographic profile of epicarp from methanolic extracts of *C. limon (Cz1), C. limetta (Cz2) and C. aurantifolia (Cz3)* by two extraction methods maceration M and soxhlet S.

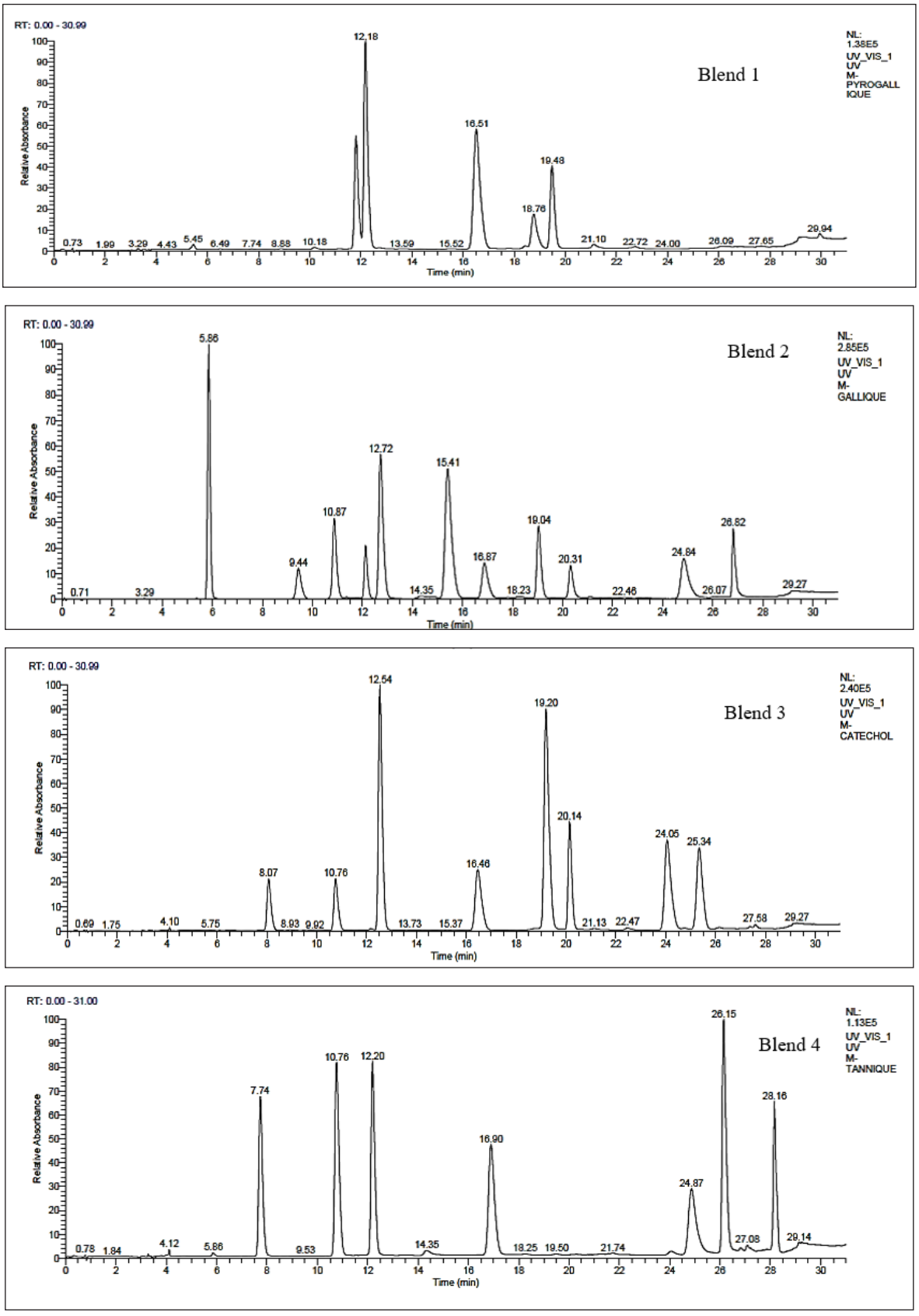

Fig.1e. Chromatographic profile of multi standards

2.6. Statistical Analysis

Data were subjected to a two-factor analysis of variance (*ANOVA*) using the statistical software SPSS for windows (version 20.0, IBM-SPSS Inc., Chicago, IL, USA). Significant differences among treatments were determined using the student-Newman-Keuls (*SNK*) post-hoc test. Mean data followed by different letters are significantly different at $p<0.05$.

3. Results and Discussion

3.1. Crude extracts yield

The edible part*:* The result in Figure 2 showed that the Soxhlet extraction gave higher yields than the maceration method. For both extraction methods, the best yield was obtained with ethyl acetate in *C. limon* (*Cp1*) followed by *C. limetta* (*Cp2*) and *C. aurantifolia* (*Cp3*). At the same time, the lowest yield was with hexane in all three species. The non-edible part*:* We found that the yields of soxhlet extraction varied considerably compared to the yields by maceration (Fig. 3). The recorded percentages ranged from 0.62% to 12.46%. The methanol gave the best yield in *C. limetta* (*Cz2*) followed by *C. limon* (*Cz1*) and finally by *C. aurantifolia* (*Cz3*). On the other hand, the yield of dichloromethane was the lowest for all three species.

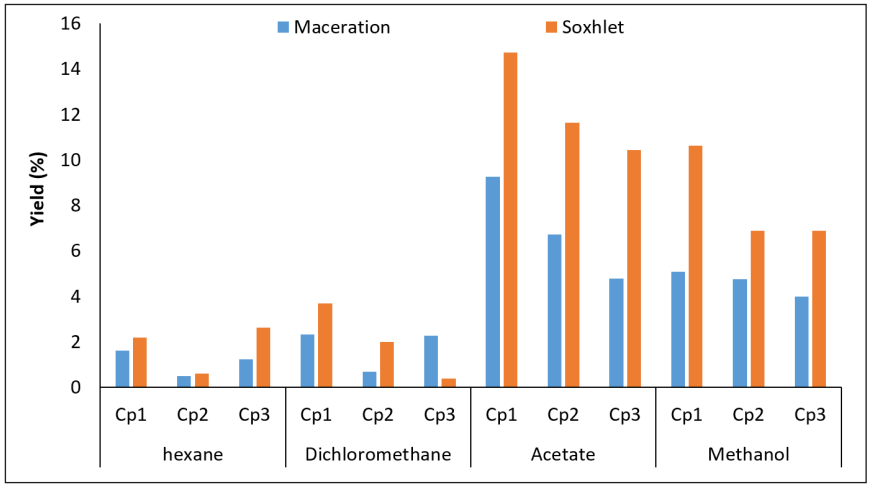

Fig. 2. Crude pulp extract yield (%) of *C. limon (Cp1), C. limetta (Cp2), C. aurantifolia (Cp3)* by two extraction methods (maceration, soxhlet) and four solvents (hexane, dichloromethane, ethyl acetate, methanol). Data are means of 3 replicates ± standard deviation. Different letters above the bars represent a significant difference ($p < 0.05$) between treatments according to Student-Newman-Keuls test.

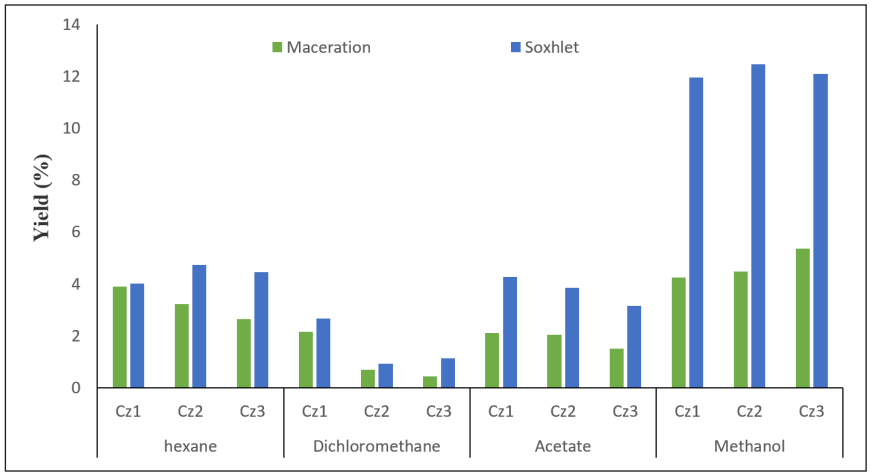

Fig. 3. Crude epicarp extract yield (%) of *C.limon (Cz1), C.limetta (Cz2), C.aurantifolia (Cz3)* by two extraction methods (maceration, soxhlet) and four solvents (hexane, dichloromethane, ethyl acetate, methanol). Data are means of 3 replicates ± standard deviation. Different letters above the bars represent a significant difference ($p < 0.05$) between treatments according to Student-Newman-Keuls test.

3.2. The effect of solvents and extraction methods on phenolic components

Figures 4 and 5 present the results of a quantitative comparison of total phenols, flavonoids, and condensed tannins in the pulp and epicarp parts of three studied citrus species. The edible part: in Figure 4, the results related to the amounts of total phenols, flavonoids, and condensed tannins in the extracts of the pulp of the three species studied showed that Soxhlet extraction as a method and ethyl acetate as a solvent gave the best results. The results obtained in Figure 4A showed that Citrus aurantifolia contained the highest polyphenol content (443.57±3.10 mg g^{-1} FW), followed by Citrus limon (273.75±0.43 mg g^{-1} FW) and, at the end, *Citrus limetta* (245.81±5.58 mg g^{-1} FW). Regarding flavonoid content, it was higher in *Citrus aurantifolia* (138.62±3.21 mg g^{-1} FW), followed by *Citrus limetta* (101.34±9.56 mg g^{-1} FW) and by *Citrus limon* (83.85±1.86 mgg^{-1} FW) (Fig.4B). In contrast, the condensed tannin contents obtained in *Citrus limetta, Citrus aurantifolia and Citrus limon* are 46.90±1.15 mgg^{-1} FW, 46.32±6.76 mg g^{-1} FW and 44.68±5.95 mgg^{-1} FW, respectively (Fig.4C). The non-edible part: in Figure 4, the results related to the amounts of total phenols, flavonoids, and condensed tannins in extracts of the epicarp of the three species studied showed that Soxhlet extraction as a method and methanol as a solvent gave the best results. The results of the assay revealed that the highest amounts of total phenols were recorded in *Citrus aurantifolia* with 326.73±9.82 mgg^{-1} FW, followed by *Citrus limetta* with 229.08±8.59 mgg^{-1} FW and by *Citrus limon* with 183.16±1.40 mgg^{-1} FW (Fig.5A). The flavonoid content was abundant in *Citrus aurantifolia* (133.00±3.55 mgg^{-1} FW) followed by *Citrus limetta* (104.59±4.54 mgg^{-1} FW) and by *Citrus limon* (81.19±8.19 mgg^{-1} FW) (Fig.5B). Concerning, the condensed tannin contents found in *Citrus limetta, Citrus aurantifolia* and *Citrus limon*, we note 49.19±12.17 mg g^{-1} FW, 31.34±1.15 mgg^{-1} FW and 43.86±0.00 mgg^{-1} FW respectively (Fig.5C).

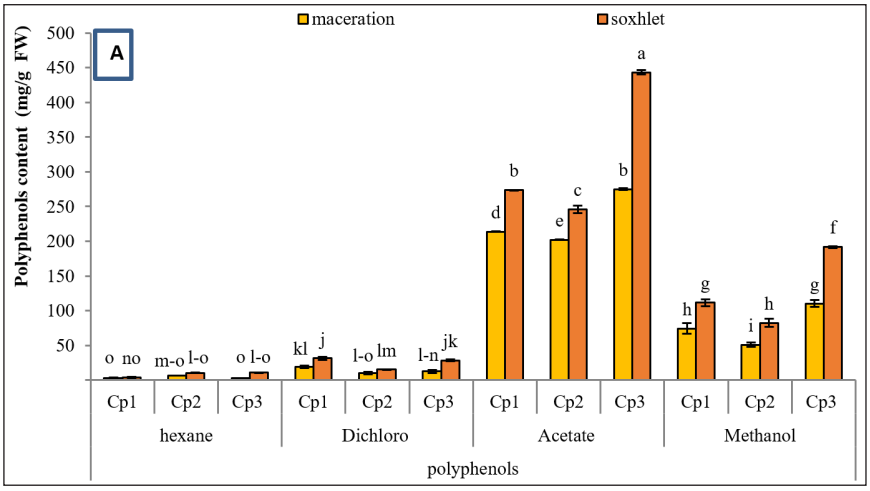

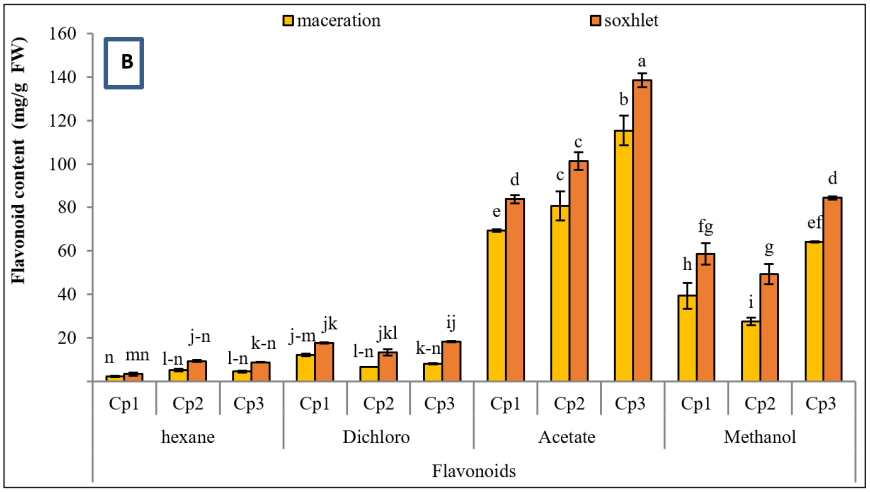

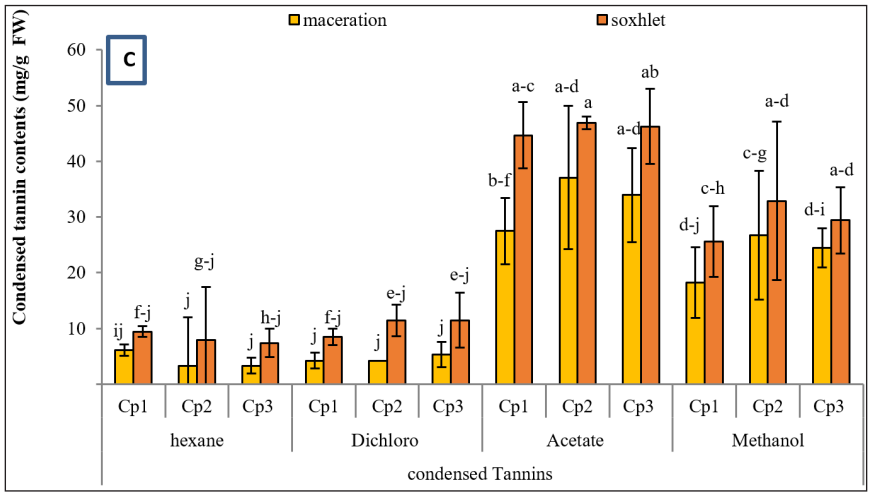

Fig. 4. The polyphenol (A), flavonoid (B) and condensed tannin (C) content of *Citrus Limon Burm (Cp1), Citrus Limetta Risso (Cp2)* and *Citrus Aurantiifolia* (Christm.) Swingle (Cp3) pulps by two extraction methods (maceration, soxhlet) and four solvents (hexane, dichloromethane, ethyl acetate and methanol). Data are means of 3 replicates ± standard deviation. Different letters above the bars represent a significant difference ($p < 0.05$) between treatments according to Student-Newman-Keuls test.

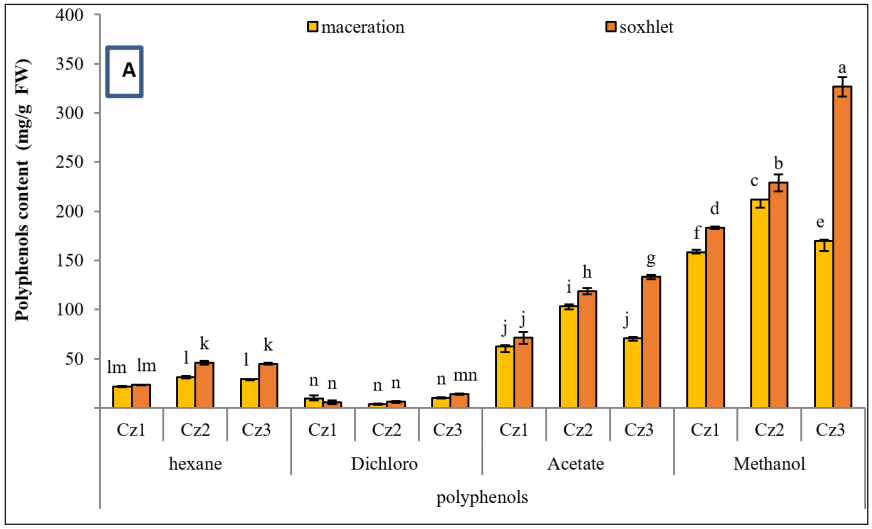

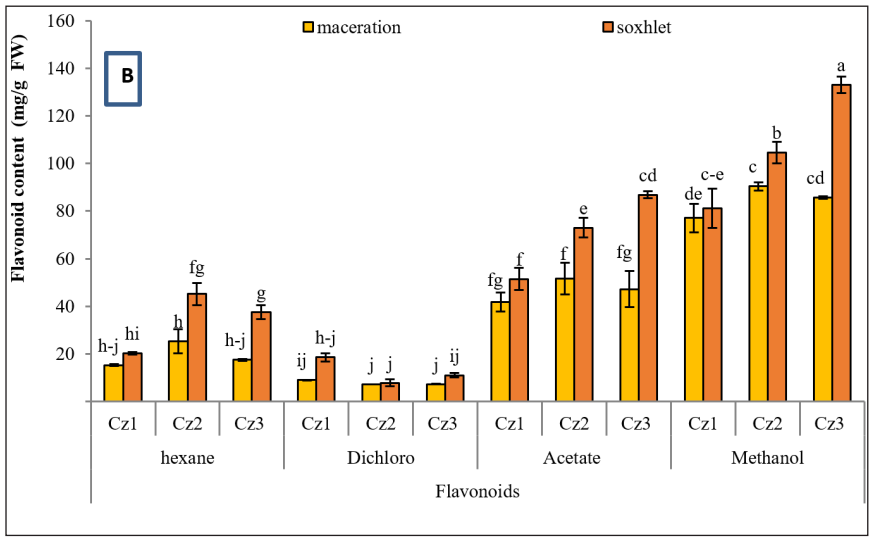

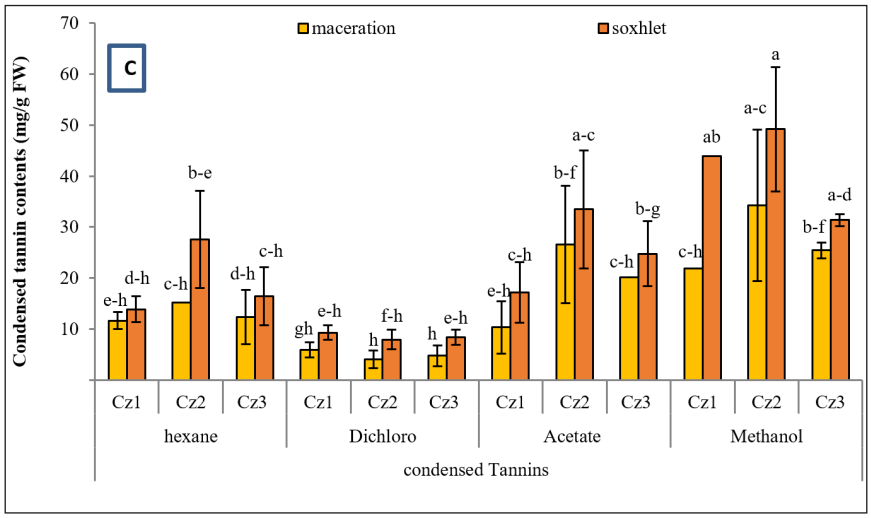

Fig. 5. The polyphenol (A), flavonoid (B) and condensed tannin (C) content of *Citrus Limon Burm* (*Cz1), Citrus Limetta Risso* (*Cz2*) and *Citrus Aurantiifolia (Christm.) Swingle* (*Cz3*) epicarp by two extraction methods (maceration, soxhlet) and four solvents (hexane, dichloromethane, ethyl acetate, methanol). Data are means of 3 replicates ± standard deviation. Different letters above the bars represent a significant difference ($p < 0.05$) between treatments according to Student-Newman-Keuls test

3.3. The effect of solvents and extraction methods on the antioxidant activity (DPPH)

The edible part: from the results obtained on the pulps, statistical analysis showed that the solvents used presented a significant difference ($p<0.05$). Thus, the profiles of the *DPPH*- test obtained revealed that all the extracts tested possessed dose-dependent antiradical activity (Fig. 6). The ethyl acetate extracts showed a high inhibition of the *DPPH*- radical very close to those of the control solutions (gallic acid, quercitin and ascorbic acid); 4.89±0.15 µg ml^{-1} for *Citrus aurantifolia*, 9.54±0.15 µg ml^{-1} for *Citrus limon* and 9.74±0.22 µg ml^{-1} for *Citrus limetta*, followed by the methanol extracts. On the other hand, a very low antiradical activity was noted in hexane and dichloromethane extracts. Regarding the extraction method, the antiradical activities of the analyzed samples showed a significant difference ($p<0.05$). The results obtained showed that the extracts obtained by Soxhlet have the highest antioxidant capacity compared to that of maceration, regardless of the extraction solvent. For comparative purposes, three standard antioxidants were used, gallic acid, quercitin and ascorbic acid (Fig. 6). They showed a high free radical scavenging activity with IC_{50} values in the range of 7.80 ± 0.25 µg ml^{-1}, 4.06 ± 0.26 µg ml^{-1} and 2.48 ± 0.32 µg ml^{-1}, respectively. The lower *the IC50 value, the more potent the extract was considered* an antioxidant. The non-edible part*:* the antiradical activities of the analyzed samples revealed significant differences ($p<0.05$) (Fig.7). We also found that almost all the extracts studied have antioxidant activity and were able to scavenge the *DPPH* radical. We noted that the extracts that showed the best inhibitory activity were the methanolic and ethyl acetate extracts, with IC50 values that vary from 5.13 µg.ml^{-1} to 31,13 µg.ml^{-1}. However, the highest free radical scavenging activity was observed in the methanolic extracts of *Citrus autantifolia* (5.13±0.12 µg ml^{-1}) followed by *Citrus limetta* (6.16±0.10 µg ml^{-1}) and *Citrus limon* (10.78±0.12 µg.ml^{-1}). The activity of these extracts evolves in the same direction as those of gallic acid with 7.80±0.25 µg.ml^{-1} and quercitin with 4.06±0.26 µg ml^{-1}, while ascorbic acid showed the highest antiradical activity with 2.48±0.32 µg.ml^{-1}. On the other hand, the lowest antiradical activity was obtained with hexane and dichloromethane (57.24 µg ml^{-1} and 138.70 µg ml^{-1}, respectively).

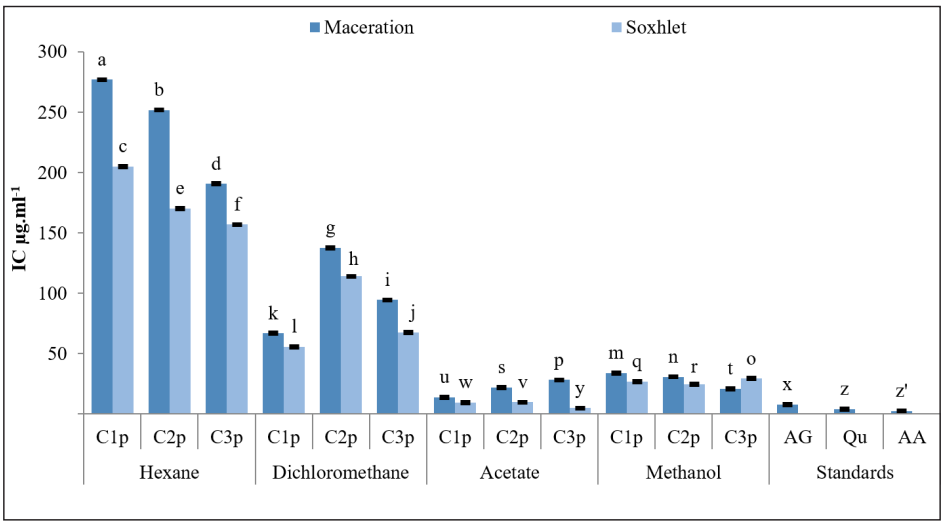

Fig. 6. Antiradical activity of *Citrus Limon Burm* (*Cp1*), *Citrus Limetta Risso* (*Cp2*) and *Citrus Aurantiifolia (Christm.) Swingle* (*Cp3*) pulp by two extraction methods (maceration, soxhlet) and four solvents (hexane, dichloromethane, ethyl acetate, methanol). Data are means of 3 replicates ± standard deviation. Different letters above the bars represent a significant difference ($p < 0.05$) between treatments according to Student-Newman-Keuls test.

3.4. Determination of phenolic compound by *UHPLC-DAD*

In this study, a method of high-performance liquid chromatography (*UHPLC*) coupled to a diode array detector (*DAD*), was used for the characterization of the phenolic compounds of the methanolic and ethyl acetate extracts of the edible and non-edible par of three *Citrus* species studied (*Citrus Limon Burm, Citrus Limetta Risso and Citrus Aurantiifolia (Christm.) Swingle)* for the two extraction methods (maceration and soxhlet). Thirty-three standards were divided into 4 blends to identify the different metabolites. Fifty-five phenolic compounds were tentatively identified in the polar *Citrus* pulp and epicarp extracts based on their maximum wavelength UV absorption and using the peaks of the standards. Among them, the identification of three flavonols (rutin, kaempferol and quercetin), two flavanones (hesperidin and naringin), a flavone (3', 4', 5, 7-tetrahydroxyflavone) and a phenolic acid (pyrogallic acid) which have been confirmed alongside literature data on the chemical composition of *Citrus*. The edible part*:* the three *Citrus* studied contained two flavonoids, of which hesperidin (6.62 g L^{-1}) was the highest in the methanolic extract of *C. limetta* by maceration, followed by rutin (2.52 g L^{-1}) in the ethyl acetate extract of *C. limetta* by maceration, then a phenolic acid, whose pyrogallic acid (1.48 g L^{-1}) was moderately high in the methanolic extract of *C. limetta* by Soxhlet. While the other metabolites (Gallic, Catechol, Catechin, Pcoumaric, Naringin, Ac hydroxybezoic, Sinapic, 3', 4', 5, 7 - tetrahydroxyflavone, Kaempferol, Quercetin, 3',5,7 trihydroxy-4'-methoxyflavone and Epicathechin) were present at trace levels (Table 2). The non-edible part*:* in the ethyl acetate and methanol extracts of *C. limetta* by Soxhlet, high contents of hesperidin (4.34 g L^{-1}) and rutin (3.39 g L^{-1}) were recorded, followed by pyrogallic acid (1.79 g L^{-1}) in the methanolic extract of C. aurantifolia by Soxhlet and then naringin (1.77 g L^{-1}) in the methanolic extract by Soxhlet of *C. limon*. On the other hand, the other metabolites presented in trace amounts (Table 3). According to these results, we suggest that the phenolic compounds content in the pulps of three species was higher than that of the epicarp. The highest concentration of phenolic compounds in juice is generally due to the very hydrophilic nature of these components.

Table 2. Provisional identification of phenolic compounds of the edible part of *Citrus Limon Burm* (*Cp1*), *Citrus Limetta Risso* (*Cp2*) and *Citrus Aurantiifolia* (*Cp3*) by *UHPLC-DAD*.

Extraction methods	Solvent	PA	GA	C	Ca	P-C	Nar	Hes	Rut	HbA	Sin	THF	Kaem	Quer	TMF	Epi
Maceration		0.51	0.04	0.02	0.03	----	0.01	1.36	1.72	----	0.02	0.01	----	----	----	0.02
	acetate	1.17	0.06	0.16	0.05	0.01	0.06	4.40	2.52	----	----	----	0.05	----	----	----
		0.15	0.03	0.03	----	----	----	0.08	----	----	----	----	0.02	0.01	----	----
		0.93	0.02	0.04	0.05	0.02	0.02	1.78	1.5	----	0.2	0.04	0.05	----	----	----
	Methanol	----	----	----	0.15	0.14	0.14	6.62	1.63	----	0.31	0.21	0.20	0.13	----	----
		0.4	0.01	0.04	0.01	----	----	----	0.25	----	----	0.02	0.03	----	----	----
Soxhlet		----	0.03	0.11	0.22	----	0.06	2.33	0.53	0.03	0.01	----	0.05	0.06	----	----
	Acetate	----	0.03	0.05	0.09	----	0.03	1.09	0.77	----	0.02	----	0.05	----	----	----
		0.59	0.03	0.04	----	----	----	0.18	0.06	0.07	----	0.05	0.09	0.04		0.11
		1.48	0.02	0.05	0.07	0.01	----	1.11	0.75	0.06	----	----	----	----	----	----
	Methanol	1.17	0.03	0.05	0.14	0.04	0.05	2.60	1.38	----	----	0.05	----	----	0.01	----
		0.53	0.02	0.06	0.18	0.02	0.04	0.27	1.74	0.05	----	----	----	----	----	----

*(PA) Pyrogallic Acid, (GA) Gallic Acid, (C) Catechol, (Ca) Catechin, (P-C) p-coumaric, (Nar) Naringin, (Hes)Hesperidin, (Rut) Rutin, (HbA) Hydroxybezoic Acid, (Sin) Sinapic Acid, (THF) 3',4',5,7-tetrahydroxyflavone, (Kaem) Kaempferol, (Quer) Quercetin, (TMF) 3',5,7 trihydroxy-4'methoxyflavone, (Epi) Epicathechin.

Table 3. Provisional identification of phenolic compounds of the non-edible part of Citrus Limon Burm (Cz1), Citrus Limetta Risso (Cz2) and Citrus Aurantiifolia (Cz3) by UHPLC-DAD

Extraction methods	Solvent	species	PA	GA	C	Ca	P-C	Nar	Hes	Rut	HbA	Sin	THF	Kaem	Quer	TMF	Epi
Maceration	acetate	Cz1	1.13	0.04	0.05	0.05	0.01	----	3.01	0.14	0.02	0.01	----	----	0.45	----	----
		Cz2	----	0.02	0.02	0.04	0.04	----	1.03	0.47	----	----	0.12	0.31	0.12	0.05	----
		Cz3	----	0.03	----	0.02	0.04	0.21	0.57	0.32	0.09	----	0.33	0.62	0.67	0.15	0.38
	Methanol	Cz1	0.81	0.02	0.16	----	0.01	0.04	2.7	1.63	----	----	0.07	0.06	----	----	----
		Cz2	0.73	----	0.08	----	0.07	0.07	2.61	0.76	----	0.16	0.09	0.13	----	----	----
		Cz3	1.66	0.03	0.35	0.47	0.04	0.19	----	2.37	----	----	0.23	0.25	----	----	0.34
Soxhlet	Acetate	Cz1	0.58	0.03	0.07	0.09	----	0.04	1.71	0.72	0.03	0.02	----	----	0.13	----	----
		Cz2	1.02	0.03	0.08	0.19	0.15	0.18	4.34	1.83	0.18	----	0.21	0.64	0.55	----	----
		Cz3	----	0.04	0.08	----	----	0.17	0.51	0.69	----	----	0.33	1.12	1.11	0.18	----
	Methanol	Cz1	----	0.03	----	0.28	0.19	1.77	1.03	0.31	----	0.43	1.04	0.27	----	0.05	----
		Cz2	----	0.05	0.11	0.22	0.19	0.17	3.95	3.39	----	0.4	0.41	----	0.1	0.08	----
		Cz3	1.79	0.03	0.01	0.29	0.02	0.04	0.16	0.94	0.16	----	0.09	0.13	----	----	----

*(PA) Pyrogallic Acid, (GA) Gallic Acid, (C) Catechol, (Ca) Catechin, (P-C) p-coumaric, (Nar) Naringin, (Hes)Hesperidin, (Rut) Rutin, (HbA) Hydroxybezoic Acid, (Sin) Sinapic Acid, (THF) 3',4',5,7-tetrahydroxyflavone, (Kaem) Kaempferol, (Quer) Quercetin, (TMF) 3',5,7 trihydroxy-4'methoxyflavone, (Epi) Epicathechin.

3.5. Discussion

The main objective of this study was to assess *in vitro* the influence of solvents and extraction methods on the phenolic composition and antioxidant activity of three *Citrus* species extracts using the *DPPH* free radical scavenging method. The data collected demonstrated that each solvent's yield of the crude extracts differed depending on the extraction method and species (0.40% to 14.72%). Similarly, Ibrahim and Hegazy [15] found that the yield of orange epicarp extracts using various solvents ranged from 8.27% to 28.32%. The samples' nature and differences in solvent diffusion explained this variation. It was also due to several factors, including the interaction of the plant with the environment (climate, soils, etc.), the time and place of harvest, cultural practices, and the age of plant material [16]. Maceration and Soxhlet are considered the conventional phenolic compound extraction methods approved by various authors for their efficiencies [17]. Our results showed that the extraction method significantly influences the yield and phenolic compound contents in *citrus limon, citrus aurantifolia, and citrus limetta.* Soxhlet extraction allowed an enrichment in phenolic compounds compared to maceration. Similarly, several works have presented similar results, which indicated a significant variation in the contents of these compounds depending on the technique used [18]. In another study, the Lebanese Eryngium Creticum was extracted using three conventional techniques: maceration, reflux, and Soxhlet. The results showed that among these techniques, reflux and Soxhlet gave approximately the same results compared to maceration [19]. Thus, a comparison between the two methods showed that soxhlet remains the preferred method for extraction [20]. Similarly, Teimoori et al [21] have suggested other extraction methods based on ultrasonic dispersive solid-phase micro-extraction. In our study, solvents of increasing polarity (hexane, dichloromethane, ethyl acetate, and methanol) were used to extract three *Citrus* species, to have as many secondary metabolites of different natures as possible and to separate these metabolites according to their degree of solubility in the solvent. Thus, their degree of glycosylation mainly depends on the number of hydroxyl groups, molecular weight and carbon chain length [22]. Indeed, the hexane extract is generally composed of lipids and highly methoxylated aglycone flavonoids, the dichloromethane extract is richer in aglycone flavonoids, ethyl acetate extract contains glycosylated flavonoids, mainly mono-, di- and tri-glycosylated flavonoids, and the methanolic extract contains flavonoids, amino acids, terpenes, waxes and tannins [23]. According to our results, the quantification of polyphenols, flavonoids and condensed tannins by different solvents showed that methanol and ethyl acetate extracts presented high contents of these molecules compared to hexane and dichloromethane extracts. Ghasemzadeh *et al*. [24] and Barchan *et al*. [25] worked on three species of Mantha from Morocco and two varieties of young ginger from Malaysia, respectively. They also showed that polar solvents (methanol, acetone) yielded higher phenolic compounds than apolar solvents (hexane, dichloromethane, and chloroform). However, other studies reported by Mendes Harcke *et al*. [26], in *Gac* fruit respectively, found that ethyl acetate extracts exhibited high contents of phenolic compounds. Moreover, Al Juhaimi et al. [27] on methanolic and ethyl acetate extracts of some plants grown in Turkey revealed that both solvents showed almost the exact contents of phenolic compounds conducted a study. In this study, we noted that pulp and epicarp parts of the *Citrus* fruit accumulate the highest contents of polyphenols and flavonoids. The comparative analysis showed that *Citrus aurantifolia* was more nutritious than *Citrus limetta* and *Citrus limon* due to its relatively high content of polyphenols and flavonoids. These findings are consistent with those obtained by Khalfan Al-Musharf *et al*. [28] on six citrus species in Oman, who showed that *Citrus limon* juice presented a higher content of total phenols (0.569± 0.0019 mg EAG mL^{-1}) than *Citrus aurantifolia* (0.468± 0.0019 mg EAG mL^{-1}). Another study conducted in South India on the fruits of six *Citrus* species, revealed that *Citrus aurantifolia* possessed

a relatively high content of total phenols (125 µg EAG mg^{-1} for epicarp and 59.05µg EAG mg^{-1} for pulp) and flavonoids (36.49 µg EQ mg^{-1} for epicarp and 15.19 µg EQ mg^{-1} for pulp) [29]. In addition, Ghasemi *et al*. [30] reported that the fruit of *Citrus limon* from Iran, recorded relatively high content of polyphenols (131 mg EAG g^{-1} epicarp and 102.2 mg EAG g^{-1} pulp) and flavonoids. On the other hand, the *Citrus limetta* juice from Mexico showed high levels of polyphenols (786 ± 73.58 mg EAG.g^{-1}) and flavonoids (63.24 ± 3.66 EQ mg g^{-1}) [31]. In view of these results presented, it appears that the extraction of phenolic compounds is a crucial step for the valorisation of active ingredients. It depends on the extraction method, the solvent, the species and the nature of the studied part. From the results reported in Figures 6 and 7, we noticed that only polar extracts (methanol and ethyl acetate) by Soxhlet could inhibit the *DPPH* radical than apolar extracts (hexane and dichloromethane). Also, some other organic compounds were determined by nanotechnology coupled with a chromatography analyser [32-34]. Thus, for gallic acid, quercetin, and ascorbic acid, the percentage of *DPPH* inhibition was still high for these extracts. Because these extracts are rich in phenolic compounds (suitable donors of proton H+). Similarly, Kumaran and Joel, Karunakaran, [35] showed that polyphenols, flavonoids and condensed tannins can reduce and decolorize *DPPH* due to their ability to donate hydrogen. For example, Narayana *et al.* [36] found that flavonoids could inhibit the lipid peroxidation by scavenging free radicals. Indeed, the antioxidant activity is related to the structure of phenolic compounds. Thus, it depends on the O-H bonds' dissociation energy, the phenol radical's electronic delocalization, and the steric hindrance of the substituent groups of the hydrogen atoms of the aromatic ring [37]. The antioxidants influence biological systems by neutralizing free radicals and chelation of toxic metal [38]. Based on the results presented in Tables 1 and 2, ethyl acetate and methanol extracts can be considered the most interesting regarding antioxidant capacity, strongly related to the presence of phenols and polyphenolic compounds, such as flavonoids [39]. This led us to suggest that these extracts contain essential molecules that can serve as a source of natural antioxidants. These minor compounds give the three species important nutritional and therapeutic qualities. In addition, several authors have proposed other types of chromatography (GC-FID, GC-TCD, GC-MS) to identify these organic substances [40-43].

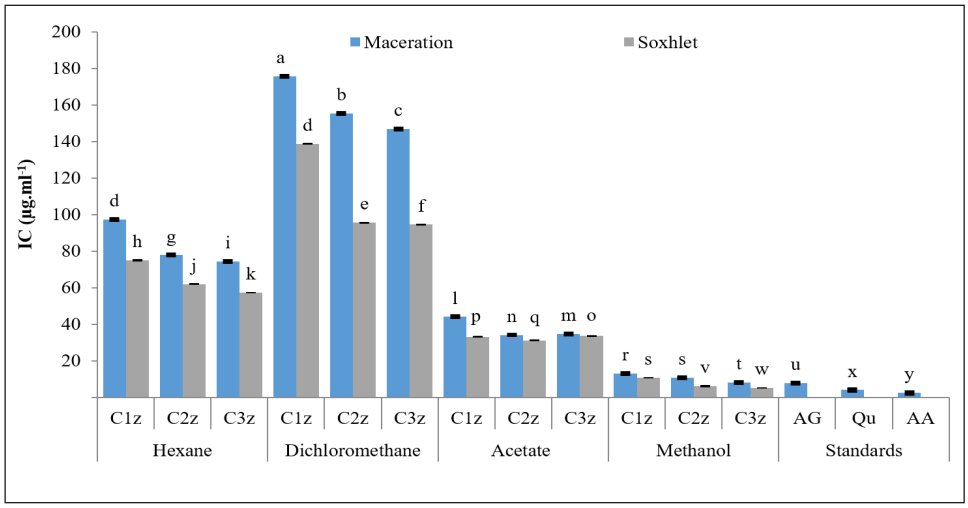

Fig. 7. Antiradical activity of *Citrus Limon Burm* (*Cz1*), *Citrus Limetta Risso* (*Cz2*) and *Citrus Aurantiifolia (Christm.) Swingle* (*Cz3*) epicarp by two extraction methods (maceration, soxhlet) and four solvents (hexane, dichloromethane, ethyl acetate, methanol). Data are means of 3 replicates ± standard deviation. Different letters above the bars represent a significant difference ($p < 0.05$) between treatments according to Student-Newman-Keuls test.

4. Conclusion

This study concluded that the best source of polyphenols among the three citrus species is in the following order for the edible part: *Citrus aurantifolia* > *Citrus limon* > *Citrus limetta*. On the other hand, for the non-edible part the order is as follows: *Citrus aurantifolia* > *Citrus limetta* > *Citrus limon*. The best source of flavonoids in both parts of the fruit is in the following order: *Citrus aurantifolia* > *Citrus limetta* > *Citrus limon*. The three species presented the exact amounts of condensed tannins for both parts of the fruit. Statistical analysis showed significant differences ($p<0.05$) for the content of polyphenols and total flavonoids in the three species studied. Regarding the extraction method, the antiradical activities of the analysed samples showed a significant difference ($p<0.05$). The results showed that the extracts obtained by Soxhlet had the highest antioxidant capacity compared to those of maceration, whatever the extraction solvent. Citrus epicarp and pulp of the three species studied showed intense antioxidant activity, making the fruit a viable source of natural antioxidants for the food industry. It is interesting to examine its use as a natural antioxidant ingredient in several finished food products.

5. Acknowledgment

The authors are very thankful to the Department of Biology, Faculty of Science, Ibn Tofail University, Kenitra, Morocco; University Cadi Ayyad, Marrakech, Morocco; National Institute of Agricultural Research, Marrakesh, Morocco and Department of Biology, Faculty of Sciences and Technologies-Gueliz, Cadi Ayyad University, Marrakesh, Morocco. All authors read and approved the final version of the manuscript.

6. References

[1] D. Mastorakou, M. Rabée, P. Salen, G. Pounis, M. de Lorgeril, Mediterranean diet: A health-protective dietary pattern for modern times, Analysis in Nutrition Research, Chapter 9, Book Elsevier Publisher, p.p. 233-258, 2019. https://doi.org/10.1016/C2017-0-01792-5

[2] C. T. Gallardo-Rivera, A. Lu, M. Z. Treviño-Garza1, E. García-Márquez, C. Amaya-Guerra, C. Aguilera, J. G. Báez-González, Valorization of almond (*Prunus serotina*) by obtaining bioactive compounds, Fron. Nut., 8 (2021) 663953. https://doi.org/10.3389/fnut.2021.663953

[3] Food and Agriculture Organizations (FAO) of the United Nations 2025. http://www.fao.org/faostat/en/#data.

[4] R. K. Saini, A. Ranjit, K. Sharma, P. Prasad, X. Shang, K. G. M. Gowda, Y. S. Keum, Bioactive compounds of *Citrus* Fruits: A review of composition and health benefits of carotenoids, flavonoids, limonoids, and terpenes, Antioxidants, 11 (2022) 239. https://doi.org/10.3390/antiox11020239

[5] X. Lu, C. Zhao, H. Shi, Y. Liao, F. Xu, H. Du, H. Xiao, J. Zheng, Nutrients and bioactives in *citrus* fruits: Different *citrus* varieties, fruit parts, and growth stages, Crit. Rev. Food Sci. Nutr., 63 (2021) 1–24. https://doi.org/10.1080/10408398.2021.1969891

[6] M. Addi, A. Elbouzidi, M. Abid, D. Tungmunnithum, A. Elamrani, C. Hano, An overview of bioactive flavonoids from *Citrus* fruits, Appl. Sci., 12 (2022) 1-29. https://doi.org/10.3390/app12010029

[7] B. Singh, J. P. Singh, A. Kaur, N. Singh, Phenolic composition, antioxidant potential and health benefits of *citrus* peel, Food. Res. Int., 132 (2020) 109-114. https://doi.org/10.1016/j.foodres.2020.109114

[8] A. Iqbal, P. Schulz, and S. S. Rizvi, Valorization of bioactive compounds in fruit pomace from agro-fruit industries: Present Insights and future challenges, Food. Biosci., 44 (2021) 101-384. https://doi.org/10.1016/j.fbio.2021.101384.

[9] R. Ashouri, S. A. H. Mirzahosseini, H. Shirkhanloo, A. Rashidi, N. Mansouri, Synthesis of carbon quantum dots from olive stones for efficient adsorption of benzene

from the ambient air, J. Nanostruct., 11 (2021) 480–497. https://doi.org/10.22052/JNS.2021.03.007

[10] H. B. Li, K. W. Cheng, C. C. Wong, K. W. Fan, F. Chen, Y. Jiang, Evaluation of antioxidant capacity and total phenolic content of different fractions of selected microalgae, Food Chem., 102 (2007) 771–776. https://doi.org/10.1016/j.foodchem.2006.06.022

[11] A. M. Shraim, T. A. Ahmed, Determination of total flavonoid content by aluminum chloride assay: A critical evaluation, LWT, 150 (2021) 111932. https://doi.org/10.1016/j.lwt.2021.111932

[12] A. E. Hagerman, Tannin Handbook, 2éme edition, Miami University, Oxford, USA, 116, 2002. https://cir.nii.ac.jp/crid/1570291225292849152

[13] İ. Gulcin, S. H. Alwasel, DPPH radical scavenging assay, Processes, 11 (2023) 2248. https://doi.org/10.3390/pr11082248

[14] L. Puigventós, M. Navarro, E. Alechaga, Determination of polyphenolic profiles by liquid chromatography-electrospray-tandem mass spectrometry for the authentication of fruit extracts, Anal. Bioanal. Chem., 407 (2015) 597–608. https://doi.org/10.1007/s00216-014-8298-2

[15] M. I. Ibrahim, A. E. Hegazy, Antioxydant activities of orange peel extract, Food. Sci. Tech., 18 (2012) 684–688. https://doi.org/10.5829/idosi.wasj.2012.18.05.64179

[16] D. Atmani, N. Chaher, M. Berboucha, K. Ayouni, H. Lounis, H. Boudaoud, N. Debbache, Antioxidant capacity and phenol content of selected Algerian medicinal plants, Food. Chem., 112 (2009) 303–309. https://doi.org/10.1016/j.foodchem.2008.05.077

[17] O. R. Alara, N. H. Abdurahman, Extraction of phenolic compounds: A review, Curr. Res. Food Sci., 4 (2021) 200-214. https://doi.org/10.1016/j.crfs.2021.03.011

[18] R. Murugan, T. Parimelazhagan, Comparative evaluation of different extraction methods for antioxidant and anti-inflammatory properties from *Osbeckia parvifolia Arn.* –An in vitro approach, J. King. Saud. Univ. Sci., 26 (2014) 267–275. https://doi.org/10.1016/j.jksus.2013.09.006

[19] R. Damaj, A. Sabbah, G. Nasser, M. B. Francis, A. Hijazi, H. Annan, A. A. A. AlRekaby, H. Rammal, Antioxidant activity and chemical composition of the ethanolic extract from leaves and stems of the Lebanese *Eryngium Creticum*, J. Multi. Eng. Sci. Tech., 3 (2016) 5813-5823. https://www.jmest.org/wp-content/uploads/JMESTN42351824.pdf

[20] S. Zeidan, A. Hijazi, H. Rammal, A. Kobaissi, B. Badran, Extraction of phenolic compounds and flavonoids from *eryngium creticum L.* by conventional and non-conventional extraction techniques, World J. Phar. Phar. Sci., 3 (2014) 1889–189. https://www.wjpps.com/

[21] S. Teimoori, A. H. Hassani, M. Panahi, N. Mansouri, An immobilization of aminopropyl trimethoxysilane-phenanthrene carbaldehyde on graphene oxide for toluene extraction and separation in water samples. Chemosphere, 316 (2023) 137–800. https://doi.org/10.1016/j.chemosphere.2023.137800

[22] Z. Mohammedi, F. Atik, Impact of solvant extraction type on total polyphenols content and biological activity from *Tamarixaphylla (L.).* karst, Int. J. Pharma. Bio. Sci., 2 (2011) 609–615. https://ijpbs.net/abstract.php?article=NTk1

[23] O. M. Andersen, K. R. Markham, Flavonoid: Chemistry, Biochemistry, and Applications, Taylor and Francis Group United States of America, 2005. https://doi.org/10.1201/9781420039443

[24] A. Ghasemzadeh, H. Jaafar, A. Rahmat, Effects of solvent type on phenolics and flavonoids content and antioxidant activities in two varieties of young ginger (*Zingiber officinale Roscoe*) extracts, J. Med. Plants Res., 5 (2011) 1147–1154.

https://academicjournals.org/article/article1380532263_Ghasemzadeh%20et%20al.pdf

[25] A. Barchan, M. Bakkali, A. Arakrak, R. Pagán, A. Laglaoui, The effects of solvents polarity on the phenolic contents and antioxidant activity of three *Mentha* species extracts, Int. J. Curr. Microbiol. App. Sci., 3 (2014) 399–412. http://www.ijcmas.com

[26] A. C. Mendes Hacke, J. A. Marques, J. C. Rebuglio Vellosa, A. A. Boligon, F. D. D'Avila da Silva, D. Souza, J. S. Bonini, J. B. Teixeira Rochad, R. Picada Pereira, Ethyl acetate fraction of *Cymbopogon citratus* as a potential source of antioxidant compounds, New J. Chem., 42 (2018) 3642–3652. https://doi.org/2018/NJ/C7NJ04352J

[27] F. Al juhaimi, C. Saglam, M. Musaozcan, Antioxidant properties and total phenolic content of two solvent extraction extracts of some plants belong to *Labiatae* family, Asian J. Chem., 25 (2013) 3011–3013. https://doi.org/10.14233/ajchem.2013.13482

[28] N. Khalfan Al-Musharfi, H. Suliman Al-Wahaibi, S. Alam Khan, Comparison of ascorbic acid, total phenolic content and antioxidant activities of fresh juices of six fruits grown in Oman, Food. Process. Tech., 6 (2015) 513. https://doi.org/10.4172/2157-7110.1000513

[29] M. Pallavi, C. K. Ramesh, V. Krishna, N. Sameera Parvee, L. Nanjunda Swamy, Quantitavie phytochemical analysis and antioxydant activities of some *citrus* fruits of South India, Asian J. Pharm. Clinical. Res., 10 (2017) 198–205. https://doi.org/10.22159/ajpcr.2017.v10i12.20912

[30] A. A. Damián-Reyna, J. C. González-Hernández, R. Maya-Yescas, C. J. Cortés-Penagos, M. C. Chávez-Parga, Polyphenolic content and bactericidal effect of Mexican *Citrus limetta* and *Citrus reticulatade*, J. Food. Sci. Technol., 54 (2017) 531–537. https://doi.org/10.1007/s13197-017-2498-7

[31] K. Ghasemi, Y. Ghasemi, M. A. Ebrahimzadeh, Antioxydant activity, phenol and flavonoide contents of 13 *citrus* species peels and tissues, Pak. J. Pharm. Sci., 22 (2009) 277-281. https://pubmed.ncbi.nlm.nih.gov/19553174/

[32] S. Teimoori, A. H. Hassani, New extraction of toluene from water samples based on nano-carbon structure before determination by gas chromatography, Int. J. Environ. Sci. Technol., 20 (2023) 6589–6608. https://doi.org/10.1007/s13762-023-04906-9

[33] R. Ashouri, N. Mansouri, Dynamic and static removal of benzene from air based on task-specific ionic liquid coated on MWCNTs by sorbent tube-headspace solid-phase extraction procedure, Int. J. Environ. Sci. Technol., 18 (2021) 2377-2390. https://doi.org/10.1007/s13762-020-02995-4

[34] A. Faghihi-Zarandi, H. Shirkhanloo, C. Jamshidzadeh, A new method for removal of hazardous toluene vapor from air based on ionic liquid-phase adsorbent, Int. J. Environ. Sci. Technol., 16 (2019) 2797-2808. https://doi.org/10.1007/s13762-018-1975-5

[35] A. Kumaran, R. Joel Karunakaran, *In Vitro* antioxidant activities of methanol extracts of five *Phyllanthus* species from India, LWT-Food Sci. Technol., 40 (2007) 344-352. https://doi.org/10.1016/j.lwt.2005.09.011

[36] K. R. Narayana, M. S. Reddy, M. R. Chaluvadi, D. R. Krishna, Bioflavonoids classification, pharmacological, biochemical effects and therapeutic potential, Indian. J. pharm., 33 (2001) 2–16. https://journals.lww.com/iphr/pages/default.aspx

[37] C. Sánchez-Moreno, J. A. Larrauri, F. Saura-Calixto, A procedure to measure the antiradical efficiency of polyphenols, J. Sci. Food. Agric., 76 (1998) 270–276. https://doi.org/10.1002/(SICI)1097-0010(199802)76:2<270::AID-JSFA945>3.0.CO;2-9

[38] M. Arjomandi, H. Shirkhanloo, A review: Analytical methods for heavy metals

determination in environment and human samples, Anal. Methods Environ Chem. J., 2 (2019) 97–126. https://doi.org/10.24200/amecj.v2.i03.73

[39] L. Rubió, M. J. Motilva, M. P. Romero, Recent advances in biologically active compounds in herbs and spices: a review of the most effective antioxidant and anti-inflammatory active principles, Critical Rev. Food Sci. Nut., 53 (2013) 943–953. https://doi.org/10.1080/10408398.2011.574802

[40] M. M. Asl, H. Shirkhanloo, N. Mansouri, S. A. R. H. Seyed Mirzahosseini, F. Atabi, Functionalized graphene oxide with bismuth and titanium oxide nanoparticles for efficiently removing formaldehyde from the air by photocatalytic degradation–adsorption process, J. Anal. Test, 7 (2023) 444–458. https://doi.org/10.1007/s41664-023-00272-0

[41] A. Faghihi-Zarandi, J. Rakhtshah, B. B. Yarahmadi, A rapid removal of xylene vapor from environmental air based on bismuth oxide coupled to heterogeneous graphene/ graphene oxide by UV photo-catalectic degradation-adsorption procedure, J. Environ. Chem. Eng., 8 (2020) 104–193. https://doi.org/10.1016/j.jece.2020.104193

[42] S.Teimoori,A. H. Hassani, M. Panahi, N. Mansouri, Rapid extraction of BTEX in water and milk samples based on functionalized multi-walled carbon nanotubes by dispersive homogenized-micro-solid phase extraction, Food Chem., 421 (2023) 136–229. https://doi.org/10.1016/j.foodchem.2023.136229

[43] M. Mohammadi Asl, N. Mansouri, S.A.R Haji Seyed Mirzahosseini, F. Atabi, Simultaneity comparative evaluation of toluene removal from the air by adsorption and UV semi-degradation-based adsorption procedure, Int. J. Environ. Sci. Technol., 21 (2024) 6677–6694. https://doi.org/10.1007/s13762-024-05503-0

Anal. Methods Environ. Chem. J. 8 (1) (2025) 100-114

AMECJ

Research Article, Issue 1
Analytical Methods in Environmental Chemistry Journal
Journal home page: www.amecj.com/ir

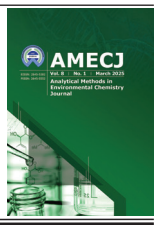

Evaluation of acridine orange dye adsorption using a new epoxy resin hardener, and degradation efficiency through the Fenton method

Saja H. Muhammed[a], Ali Abdulrazzaq Abdulwahid[a,*] and Tahseen A. Saki[a]
[a] *University of Basra, Al-Ashar–Corniche Street, postal code: 61004, Basra, Iraq*

ARTICLE INFO:
Received 25 Oct 2024
Revised form 11 Jan 2025
Accepted 14 Feb 2025
Available online 29 March 2025

Keywords:
Adsorption,
Epoxy Resin,
Fenton,
Acridine Orange,
Dye Degradation,
UV– visible spectroscopy

ABSTRACT
This research uses the Fenton process and adsorption to treat cationic Acridine Orange dye (AO) in aqueous solutions. In the Fenton method the effects of dye concentration, H_2O_2/ Fe^{2+} ratio, pH, and reaction time are considered to optimize the oxidative process. The experimental results regarding the removal percentage of AO dye are reported. UV-visible spectroscopy determined the amount of AO dye at 492nm. The optimal reaction conditions to degrade dye from aqueous solutions were: pH 4; 1.0 mM Fe^{2+} and 1.0 mM H_2O_2. On the other hand, four more robust epoxy resins, denoted E1 through E4, were synthesized using 4-aminopyridine, 3,3-diaminobenzidine (EDAB), 4-aminobenzoyl hydrazine and polyamine, and characterized using thermogravimetric analysis (TGA), and Fourier transform infrared spectroscopy (FTIR). These epoxy resins proved effective for removing AO dye from an aqueous solution at pH 10, and their adsorption behavior was in keeping with Langmuir's adsorption model. Comparison between the adsorption and photo-Fenton oxidation process for Acridine Orange (AO) was carried out under different application conditions. Epoxy resins exhibited the maximum adsorption capacity with 980.39, 1515.2, 1694.9, and 1851.9 mg g^{-1} for E1-E4 respectively at 25 °C after 1.0 h of shaking time while 81.87% of AO was utterly degraded after 10 min of photo-Fenton process.

1. Introduction

Dyes in wastewater can be harmful to people and the environment. They can be toxic, mutagenic, or carcinogenic. Water contamination is common because industries release a lot of dyes into the environment [1]. Removing dyes from wastewater is a big challenge. Many methods have been tried, including coagulation, oxidation, membrane filtration, and adsorption [2]. Adsorption stands out among these methods for removing dyes from wastewater because it's simple, easy to use, affordable, and effective. Polymeric sorbents, which can be customized in many ways and easily handle organic pollutants, are particularly promising [3]. Epoxy resins, a synthetic material, have been underused in designing adsorbents for dye removal. They're cheap, stable, and can be modified to have the right properties. While epoxy resins are increasingly used in other fields, they've seen little application in wastewater treatment. This is an area worth exploring further [4]. Epoxy resins get cross-linked when the resin reacts with a specific crosslinker's functional groups (oxirane

*Corresponding Author: Ali Abdulrazzaq Abdulwahid
Email: ali.abdulwahid@uobasrah.edu.iq
https://doi.org/10.24200/amecj.v8.i01.1013

rings). The linear resins in the curing process change into a spatially network, which makes the polymer gain many specifications such as high mechanical strength, hardness and brittleness, high chemical resistance and electrical isolation, good adhesion to metals, glass, wood and others [5]. Due to its basicity and nonhydrolyzability, ligation chemistry with low molecular weight amines such as ethylene diamine and diethylene triamine is also interesting. Consequently, it would be intriguing to create and synthesize polymeric network-type sorbents that combine the structural characteristics of amines and epoxy [6]. Recently, a novolac - based network polymer with ethylenediamine units was studied for its potential to remove azo dyes. Adding these units and using the polymer's chemical properties, a new version with diethylenetriamine sites is needed for better dye removal [7]. It would be exciting to make polymeric network sorbents that combine the best features of epoxy resins and amines. Epoxy resins are ideal because they're cheap, stable, and easy to modify. They have many uses and can be made into unique structures. Cross-linkable epoxy resin is perfect for creating these new sorbents. Having multiple functional groups like amino, hydroxy, and ether in the network could help remove dyes more effectively [8]. Numerous techniques, such as extraction, micro-solid phase extraction, micro column preconcentration, UV semi-degradation, advanced oxidation, photocatalytic degradation–adsorption process, adsorption, and membrane filtration, have been proposed to treat industrial sewage in recent years. Each technique has pros and cons and removal efficiency [9-13]. The Fenton process is one of the best methods for eliminating organic contaminants since it is easy to use and maintain, has a high oxidation power, oxidizes quickly, and uses less energy when iron catalyst is present.

The research approach involves introducing various amine compounds units and utilizing polyfunctionality to promote adsorption within the network for the adsorptive removal of cationic Acridine Orange (AO) dye and comparing adsorption systems with the Fenton process.

2. Experimental

2.1. Material

Epoxy resin (Diglycidyl ether of bisphenol A) and commercial hardener polyamine were purchased from Kuwait Corporation Chemical Supplier in KUWAIT. 4-aminopyridine (CAS Number: 504-24-5), 3,3-diaminobenzidene (CAS Number: 7411-49-6) was obtained from RDH Chemical Company, Germany, and 4-aminobenzoyl hydrazine (CAS Number: 5351-17-7) and Acridine Orange (CAS Number: 65-61-2) dye from Sigma, Germany. Dimethyl formamide (CAS Number: 68-12-2) DMF from Fluka, Germany. Ethanol, Methanol and 1,4-dioxane from Alpha Chemika, India.. The dye has a molecular formula and weight of $C_{17}H_{19}N_3$ and 265.36 g·mol^{-1} respectively. The dye stock solutions were prepared in concentration (1000 mg L^{-1}) using double distilled water. The pH was adjusted through dilute solutions (0.1-0.01 mol L^{-1}) of NaOH and HCl from VWR. Fourier-transform infrared spectroscopy (FT-IR) was recorded on Shimadzu, FTIR-8400S spectrometer/Japan as KBr pellets, and Thermal Gravimetric Analysis (TGA) was also applied to determine the weight loss behavior of the epoxy resin with various amino compounds as curing agents.

The AO dye absorbance was measured at a wavelength of 492nm, using a UV-visible spectrophotometer (PG Instrument T80 + UV/VIS). The removal efficiency of dye was expressed as a percentage (%Removal Efficiency) for the Fenton approach, Equation1, while the amount of AO dye adsorbed per unit weight of the adsorbent at a specific time, q (mg g^{-1}), was determined through the utilization of Equation 2.

$$\%\ Removal\ Efficiency = \frac{C_0 - C_e}{C_e} \times 100 \quad \text{(Eq.1)}$$

$$q = \frac{(C_0 - C_e)V}{M} \quad \text{(Eq.2)}$$

Where, Ce and C_0 are references to the concentration at temperature (T) and initial concentration of AO dye in (mg) per (L), V represents the volume of the dye in (L), while M is the weight of the epoxy adsorbents in (g).

2.2. Preparation of Hardener Epoxy Resin

2.2.1.Preparation of cured Epoxy resin for 4-aminopyridine (E1)

A mixture of epoxy resin (2.6 g), 4-aminopyridine (1.34 g), 1,4-dioxane (4.8 mL), and methanol (2.4 mL) was refluxed at 95-100 °C for 3 hr. The cured product was purified by thoroughly washing with dioxane/methanol several times. Cured epoxy was collected and crushed as a particle for identification and characterization [14].

2.2.2.Preparation of cured Epoxy resin for both 3,3-diaminobenzidine (E2) and 4-aminobenzoyl hydrazine (E3)

Epoxy resin 5 mL (Diglycidyl ether of bisphenol A) dissolved in solvent 70 mL DMF. Then amino compounds (3,3-diaminobenzidene or 4-aminobenzoyl hydrazine) were added at 250 °C, the mixture was cast on the petri-dish uniformly. The petri-dish was dried in a hot air oven at 150-155 °C and left in a hot oven for 1 hr. The cured epoxy resin was taken out and washed with DMF several times. Then cured epoxy was crushed as a particle for identification and characterization [15-17].

2.2.3.Preparation of cured Epoxy resin for polyamine (E4)

Epoxy resin and polyamine (curing agent) were used in a 3:2 equivalent ratio (excess quantity of agent was used to ensure remaining free amino groups), mixed together until a homogeneous mixture was well blended. Next, the mixed system was washed with ethanol several times to remove trace unreacted polyamine, then poured into the metal mold and left in a hot air oven at 100°C for 4 h. Finally, the cured system was ground and collected for identification and characterization. Figure 1 represented prepared hardener epoxy compounds [18].

2.3. Degradation of Acridine Orange by Fenton Process

In this study, four variables: pH (2-12), contact time (2-20) minutes, dye concentration (100-1200 mg L^{-1}), and ratio of Fenton reagent (1:0.5 - 1:10) were considered. The four steps of this method were completed at room temperature: Initially, the ideal dye concentration investigated using a range of color concentrations at pH_{pzc}, a 5-minute contact period, and a 1:1 H_2O_2/Fe^{2+} ratio. Various dye concentrations (100, 200, 400, 600, 800, 1000 and 1200 mg L^{-1}) were created in this phase. Following this, the samples were centrifuged for five minutes. The filtrate was then moved to a spectrophotometer to determine the remaining dye concentration and the absorbance

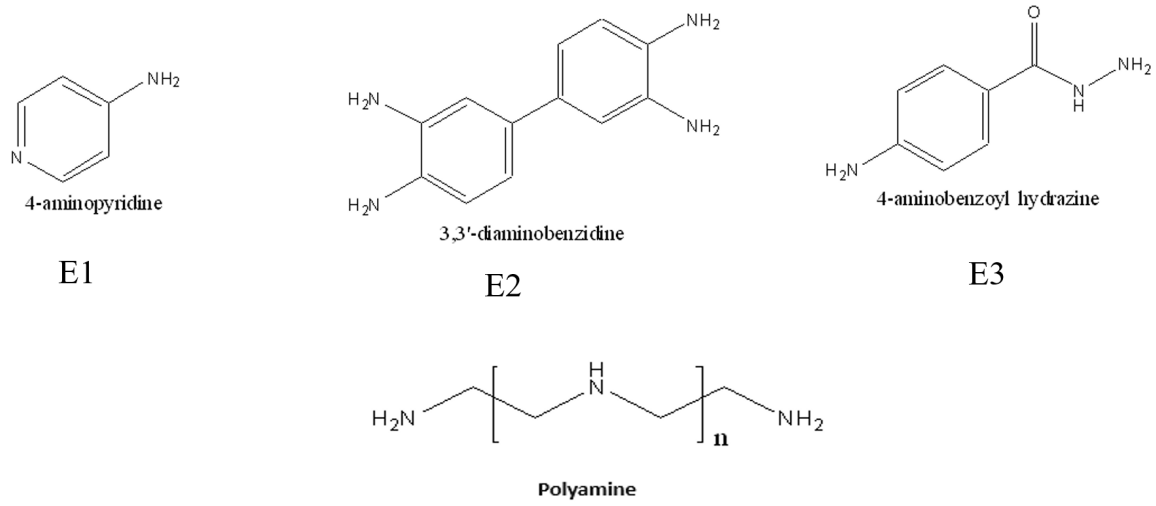

Fig. 1. Structures of prepared hardener epoxy E1-E4

measured at 492nm. Six different pH values (2, 4, 6, 8, 10 and 12) were studied in the second step to investigate the optimum pH. By fixing the optimum dye concentration (800 mg L^{-1} from the previous step), other variables, namely the reaction time (5 minutes) and the H_2O_2/Fe^{2+} ratio (1:1) were kept constant like the first step. In this step, the optimum pH was determined 4. The optimum H_2O_2/Fe^{2+} ratio determined by applying six deferent ratios (1:0.5, 1:1, 1:2, 1:4, 1:8, 1:10) under the optimum conditions, namely C_0=800 mg L^{-1}, pH 3, and 5 minutes of reaction time. After centrifugation for 5 minutes, method solutions were transferred to the spectrophotometer and the optimal ratio of 1:4 was obtained for H_2O_2/Fe^{2+}. In the last Fenton optimization step, the reaction time of Fenton degradation was studied at five different times (2, 5, 10, 15, 20 minutes).

2.4. Batch Adsorption Experiments

Batch adsorption experiments of AO dye were conducted to assess the adsorption parameters and factors influencing the adsorption. A 100mL solution (500.0 mg L^{-1} of AO dye) kept in contact with 100.0 mg of adsorbents E1, E2, E3 and E4 by a thermostat shaker at 25 °C and 245 rpm for a specific period (15–180 min). After the end of each agitation time, the epoxy resins were separated from the solution by simple filtration. The remaining amount of AO dye was determined by UV– visible spectroscopy at 492nm [19,20].

2.5. Characterization of Prepared Epoxy Resins

2.5.1.Fourier transform infrared spectroscopy (FTIR)

Based on Figure 2, the FTIR spectrum of epoxy resin (Neat) shows bands at 3402 cm^{-1} and 916 cm^{-1} wavenumber bands, which indicate the presence of (OH) and epoxy ring CH_2-O-CH. Also, band at 3049 cm^{-1} assigned to the -CH-(O-CH_2) epoxy, band at 1028 cm^{-1} to the -C-O-C- present in the structure. The vibration of C-O bonding of the hydroxyl group can be observed at 1028 cm^{-1}. For 4-Aminopyridine (E1) the bands observed at 3342, 3236, and 1658 cm^{-1} are attributed to the N–H asymmetric, symmetric, and in-plane deformation stretching vibration v, respectively. Band at 2923 cm^{-1} is assigned to the C-H aliphatic stretching. Band at 1603 cm^{-1} is related to the C=N stretching vibration of the pyridine ring. Two absorption bands at 1504 and 1456 cm^{-1} were observed, attributed to the C=C stretching vibration of the pyridine. The presence of the aminopyridine units was further substantiated with the appearance of C–N stretch band at 1384 cm^{-1} [21]. The FTIR study of cured epoxy resin with 3,3-diaminobenzidine (E2) of the cured epoxy resin shows broad band appearance at 3350 cm^{-1}, which is from N–H secondary amine and primary hydroxy group stretching vibration, also there were no band at 916 cm^{-1} (band due to epoxy groups) [22] as represented by Figure 3. The FT-IR spectrum of epoxy-4-aminobenzoyl hydrazine (E3) was shown in Figure 4. Due to conjugated effect between carbonyl and benzene, the carbonyl C=O absorb at lower frequency 1658 cm^{1} contribute to stretching vibration of benzoyl hydrazine. The absorption band at 1288 cm^{-1} was mixed, including C-N and N-H bending stretching vibration. The epoxy group (Oxirane ring) band 916 cm^{-1} was reduced [23]. For Polyamine (E4) the bands of the epoxy group at 3049 cm^{-1} and 916 cm^{-1} decrease during the curing process, as shown in the FTIR spectrum (Fig. 5). The bands for aliphatic -CH_2 bending and -CH_3 symmetrical and asymmetrical vibrations are observed between 2300-2400 cm^{1} for both the polyamine. Polyamine containing a distinct broad N–H stretching absorption around 3363 cm^{-1}, while the epoxy resin has a band at 3402 cm^{-1}, which belongs to hydroxyl stretching vibration. However, it is difficult to evaluate the band attributed to polyamine stretching vibration, due to the overlapping with the epoxy resin stretching bands. Like agents above, the curing was confirmed that the relative intensity of the oxirane ring band (916 cm^{-1}) disappeared [24].

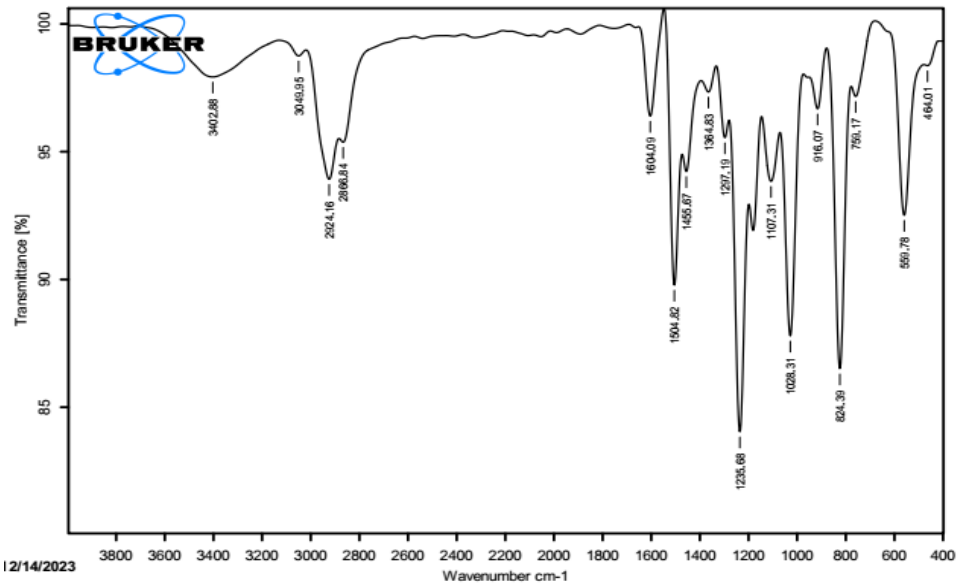

Fig. 2. FTIR spectra for 4-Aminopyridine (E1)

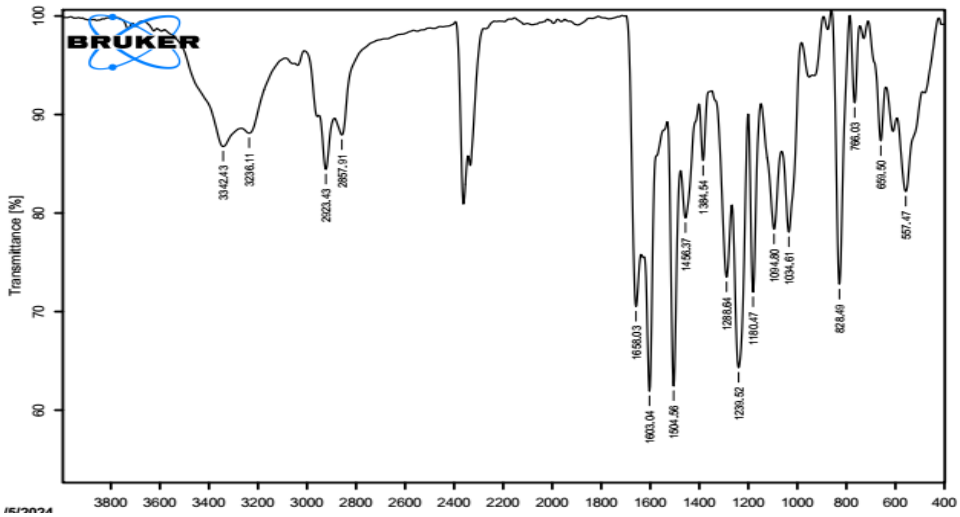

Fig. 3. FTIR spectra for 3,3-diaminobenzidine (E2)

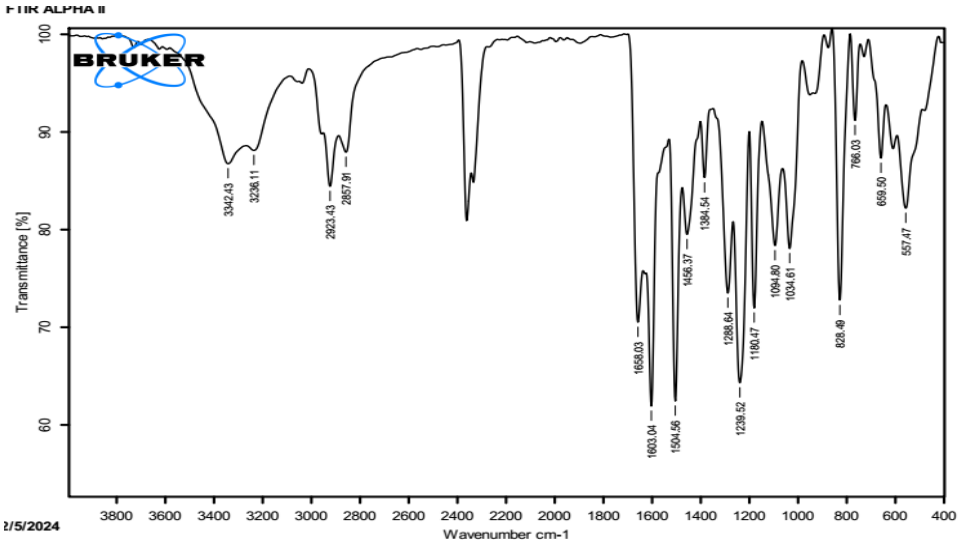

Fig. 4. FTIR spectra for 4-aminobenzoyl hydrazine (E3)

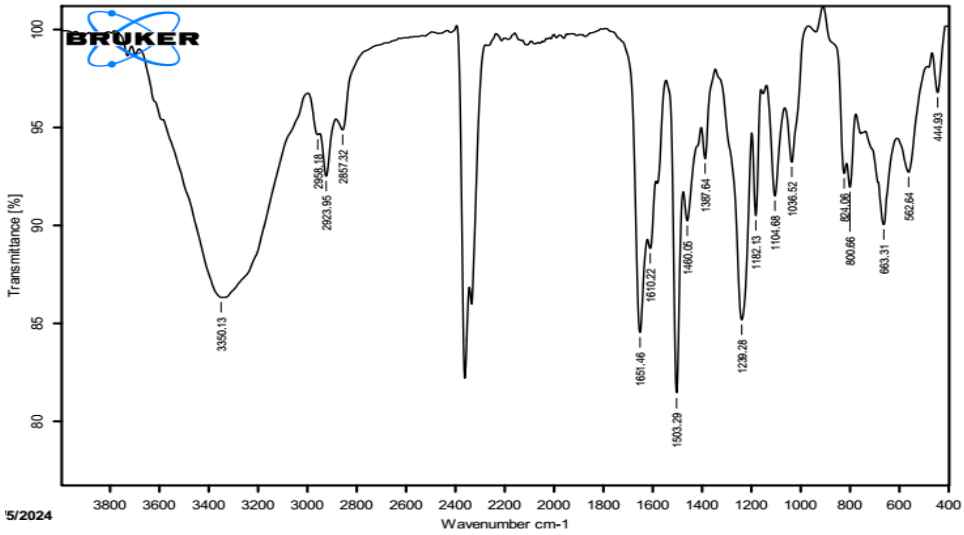

Fig. 5. FTIR spectra for polyamine (E4)

2.5.2. Thermogravimetric analysis (TGA)

A thermogravimetric analysis (TGA) was used to determine the epoxy resin's weight loss behavior with various amino compounds as curing agents. The degradation process was run at a maximum temperature of 550 °C in an inert atmosphere. The crosslinked resin's weight loss was calculated, and Table 1 displays the weight loss rates as a function of temperature. E1-E4 were thermally stable at 200 ◦C of EDAB and EAPy and 350 °C of EABH and EPAm. They decompose in a single step in the 215 to 360°C. Furthermore, it is evident from the curves analysis that the inclusion of aromatic rings improves thermal stability, especially true of EDAB, which develops char content around 20% after reaching the temperature above 550 °C. The products have a slight mass loss due to physically adsorbed water on the EABH surface, visible at temperatures between 98 and 100 °C. As shown in the results data listed in Table 1, thermal stability of resins occurred when the 3,3-diaminobenzidine reacted with epoxy resin due to diaromatic rings (char content 20%). Compared with curing epoxy resin by commercial polyamine hardener, which had a lower char content of 5%, this may have returned to the aliphatic nature of polyamine chemical structure.

Table 1. Thermal Gravimetric Analysis (TGA) of Epoxy systems

Epoxy Resin	UDT (°C)	WL%	TWL (°C)	RD (%/min)	CC% (550 °C)
E1	215	25	330	4.2	20
		50	365		
		75	490		
E2	235	25	340	4.31	7
		50	375		
		75	410		
E3	363	25	158	3.58	14
		50	390		
		75	460		
E4	360	25	360	10	5
		50	380		
		75	410		

UDT: Ultimate Decomposition Temperature °C
WL%: Weight Loss%
TWL: Temperature at Weight Loss °C
RD: Rate of Decomposition %/min
CC%: Char Content %

3. Results and Discussion

3.1. Degradation of AO dye by Fenton Process

3.1.1.Effect of Dye Concentration

Figure 6 illustrates the effect of dye concentration on the removal efficiency, when the dye concentration was between 100-400 mg L^{-1}, the removal percentage was obtained at 99.0-89.7%, respectively. However, when the dye concentration increased, the removal rate decreased; therefore, 800.0 mg L^{-1} dye solution was chosen as the initial dye concentration (C0), corresponding to about 60% removal. The concentration that corresponds to this ratio was chosen because it can be increased when examining the trade-off process for other factors like pH, the H_2O_2/Fe^{2+} ratio, and contact time. Such outcomes were likewise attained by Fahimeh Moghadam et.al. [25].

3.1.2.The Effect of pH in the Dye Removal

Studying the effect of pH value is an essential point in the Fenton process [26]. According to the results obtained, Figure 7 shows that the maximum dye removal efficiency was observed at pH 4, and the high removal efficiency was obtained in the low pH values (acidic). Iron ions were often insoluble under acidic media conditions, giving hydroxyl radicals a potent oxidizing ability. Acids contribute to hydrogen peroxide's stability. Studies show that pH values of 3 to 4 are optimal for Fenton tests because higher or lower pH values allow the ferrous (Fe^{3+}) ions to be liberated as sludge from the reaction media [26,27]. When pH exceeds 3, Fe^{3+} precipitates as $Fe(OH)_3$ and decomposes H_2O_2 into H_2O and O_2. In chemical processes, the concentration of iron ions is reduced by elevated pH levels [28]. On the other hand, ferric ion precipitation in the form of hydroxide can lead to high pH values. In this instance, iron converts H_2O_2 into H_2O and O_2 [29], and the oxidation rate of the oxidation process becomes less due to the decrease of hydroxyl radical [30].

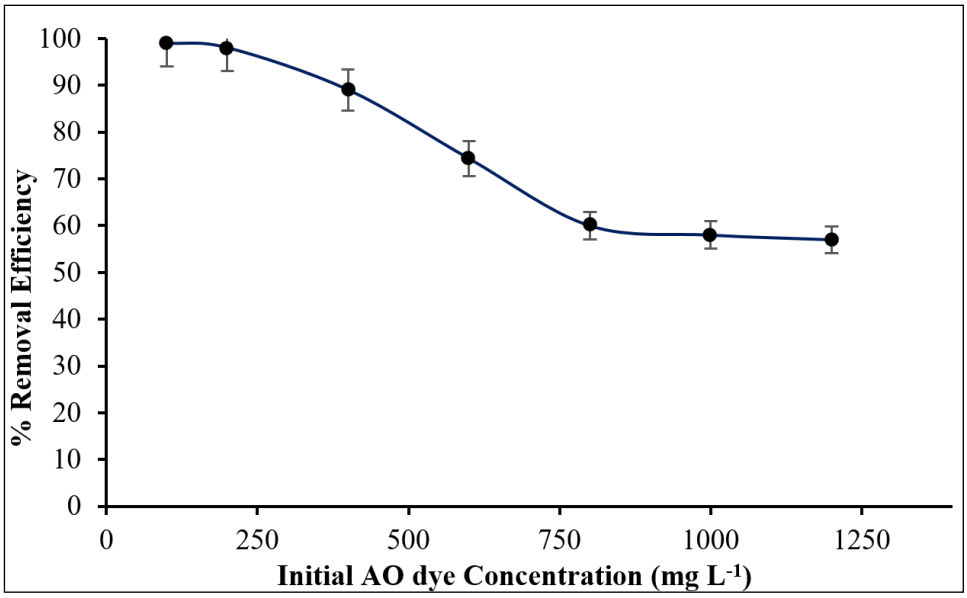

Fig. 6. Effect of AO dye initial concentration on removal efficiency

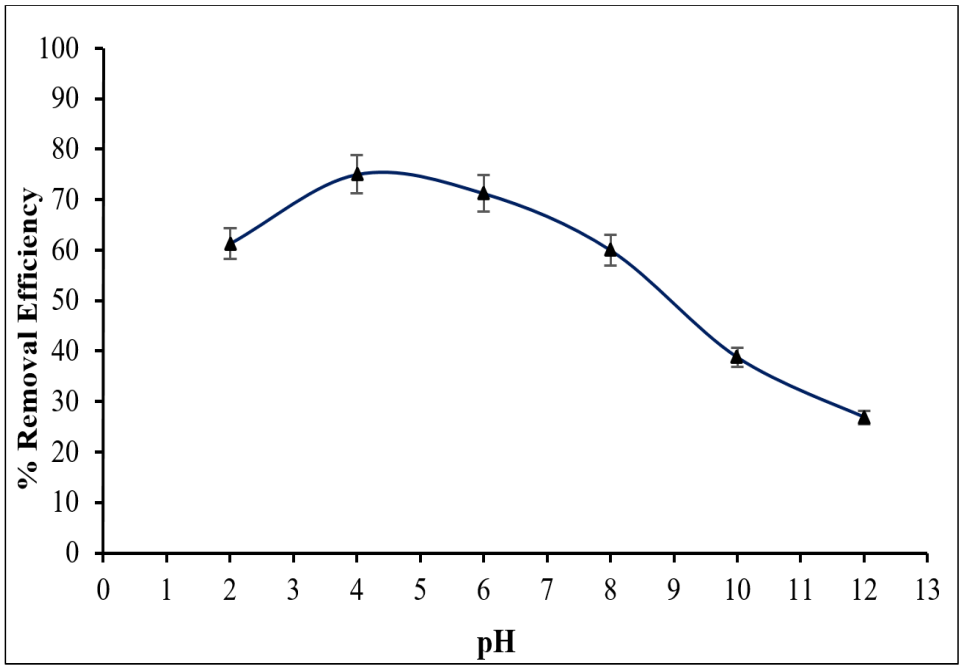

Fig. 7. Effect of dye solution pH value on removal efficiency

3.1.3.Effect of H_2O_2/ Fe^{2+} Ratio in the Dye Removal

The optimization study for ratio of H_2O_2/ Fe^{2+} in Figure 8, indicates that the maximum removal efficiency gets at ratio 1:4 and then decline in trend in the ratio of 1:8 to 1:10, this behavior is explained by the fact that H_2O_2 cannot oxidize AO dye in the absence of iron ions; instead, the presence of ferrous (Fe^{3+}) ions caused the (OH) radical to develop, which in turn triggered the oxidation process. Controlling the ferrous ion concentration in the Fenton reaction is crucial and highly influential since, in contrast, excessive H_2O_2/Fe^{2+} ratios exceeding 1:4 led to a decrease in the efficiency of dye degradation.

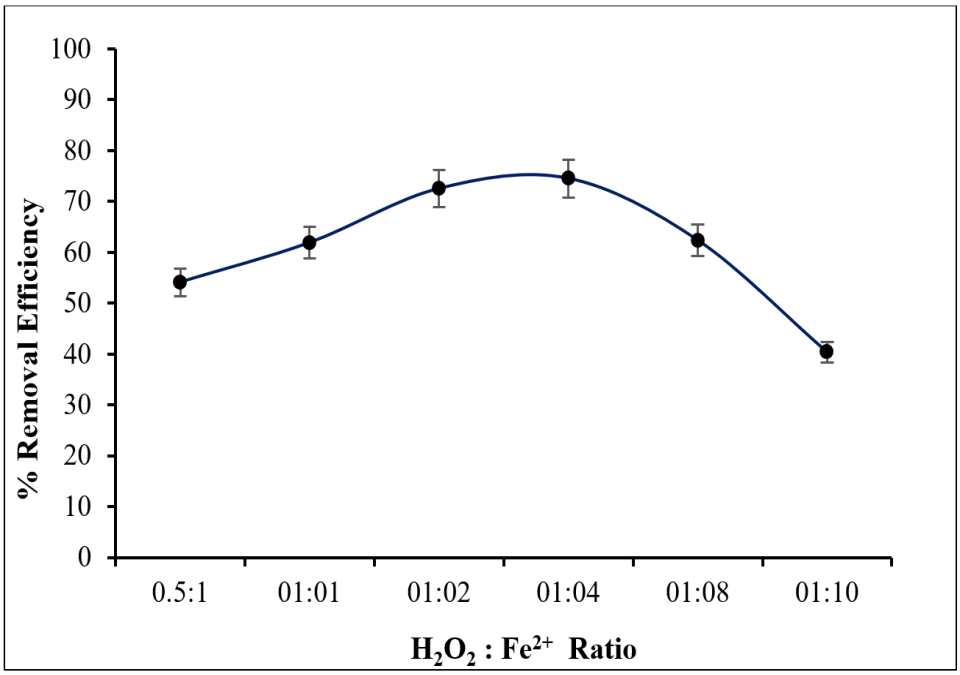

Fig. 8. Effect of H_2O_2/Fe^{2+} ratios on removal efficiency

3.1.4. The Effect of Time on the Dye Removal

The effect of time on AO dye removal efficiency was applied at optimal conditions obtained in previous experiments. The results showed that, when reaction times increased from 2 to 10 minutes, the removal efficiency first showed an ascending trend, but later on, because of intermediate compounds formation that reacted with (OH) radicals, quench potential and eliminate hydroxyl [31]. Within the initial few minutes of the Fenton reaction, a significant amount of hydroxyl free radicals are created [32,33]. However, the degree of color removal decreases significantly over time due to the generation of hydroxyl radicals [34]. The impact of reaction time on the elimination of AO dye is shown in Figure 9.

3.2. Adsorption of AO dye onto prepared Hardener Epoxy Resin

3.2.1. Effect of pH

For all adsorbents, the impact of pH on the adsorption capacities (qe) was investigated at an initial AO dye concentration of 500.0 mg L^{-1}. The pH influence of the adsorption capabilities at various pH values ranging from 2.0 to 12.0 at 25°C is shown in Figure 10.

The data indicates a notable increase in AO dye adsorption from 2.0 to 10.0 pH, with adsorption capacity remaining constant at 12 for adsorbents E1-E4. However, with the increasing pH values, this fact was also reported by other studies [33]. Adsorption of adsorbents tends to be favorable with rising pH values, because the electrostatic attraction between adsorbate species of cationic dyes (AO) increased.

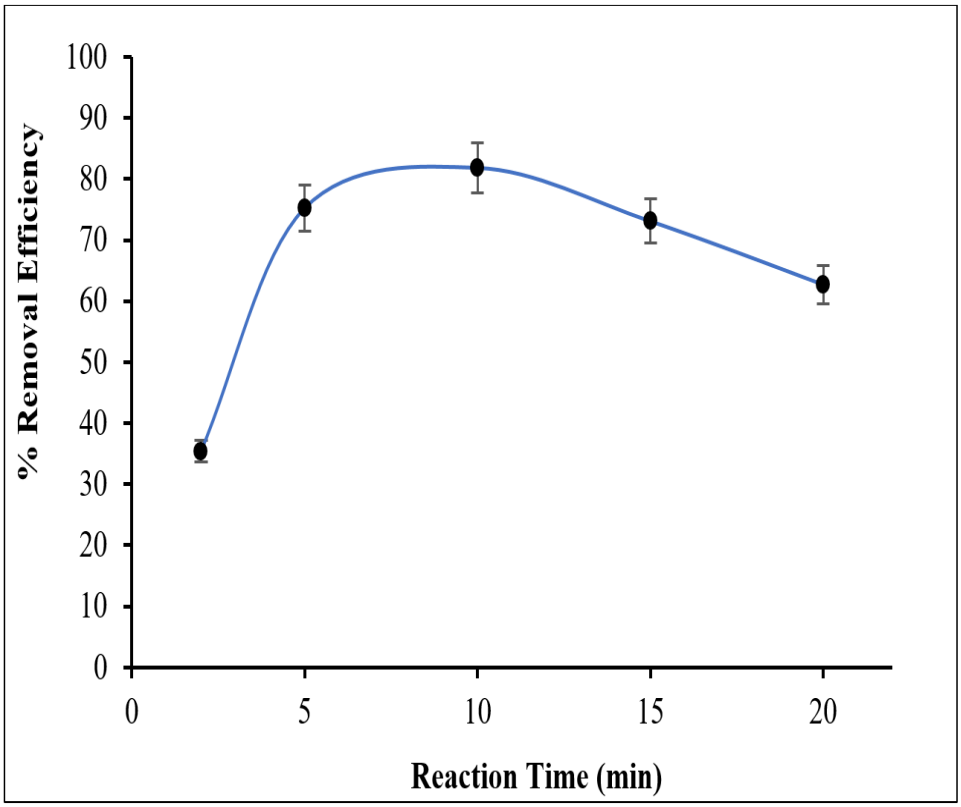

Fig. 9. Effect of reaction time on removal efficiency

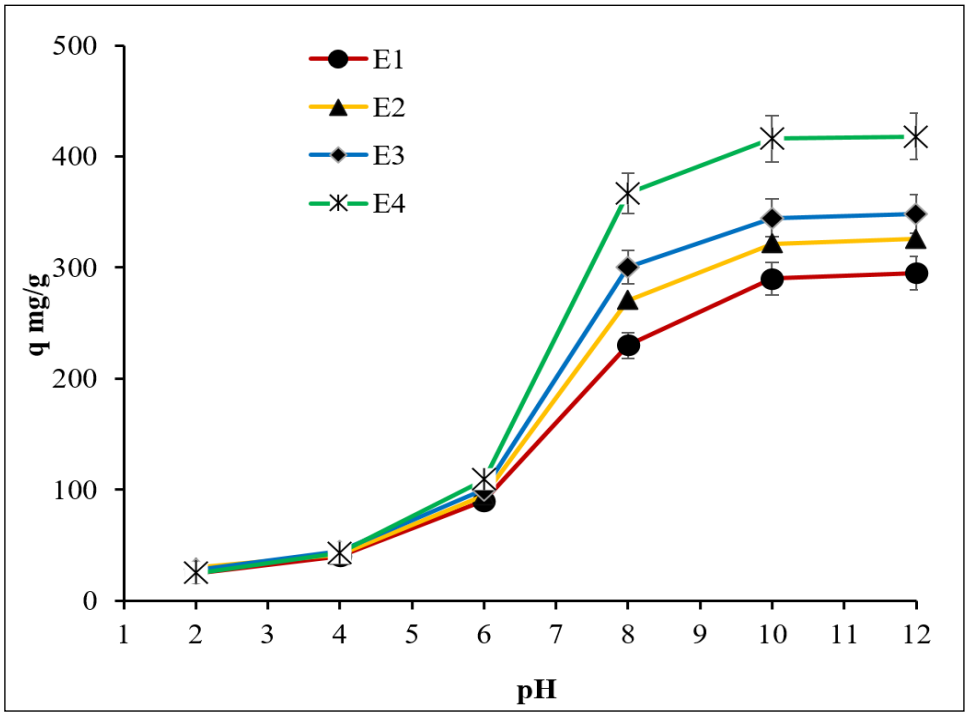

Fig. 10. Effect of dye solution pH value on adsorption capacity

3.2.2.Agitation time effect on the adsorption

Figure 11 shows the influence of shaking time on the adsorption of AO dye at pH 10.0 onto adsorbents E1-E4. The adsorption of AO increases sharply for a period of time (15–60 min), and then the trend reaches a steady state within a period of time (60–180 min) for all adsorbents.

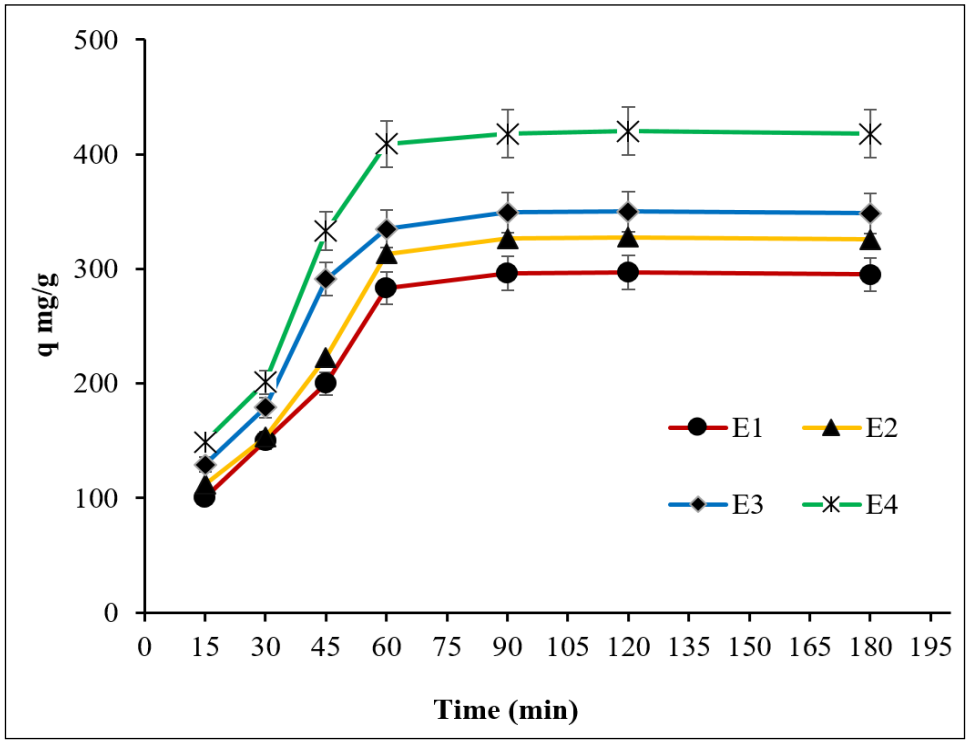

Fig. 11. Effect of agitation time on adsorption capacity

3.2.3.Adsorption Isotherm

The distribution of molecules between the liquid and solid phases at equilibrium is displayed by the adsorption isotherm. One of the most important steps in determining which model best describes the adsorption process is to analyze the isotherm data by plotting the data to various isotherm models [34]. The experimental data in this work are analyzed using the Langmuir and Freundlich models. The limitation of the Langmuir isotherm is the maximum adsorption that fits with the saturated monolayer of liquid (adsorbate) molecules on the solid (adsorbent) surface [35]. Figure 12 exhibits the plots of Langmuir adsorption isotherms. The linearized form of the Langmuir model is given in Equation 3.

$$\frac{C_e}{q_e} = \frac{1}{q_{max} + K_L} + \frac{C_e}{q_{max}}$$

(Eq.3)

The heterogeneous exponentially decaying distribution that underlies the Freundlich isotherm [35] fits the tail region of the heterogeneous distribution of adsorbed nicely. The empirical equation for a general Freundlich isotherm is as Equation 4.

$$lnq_e = lnK_F + {}^{1}/_{n}\, lnC_e$$

(Eq.4)

where K_F (L mg^{-1}) is a constant for the adsorption or distribution coefficient, and it reflects the adsorption capacity at equilibrium concentration, Freundlich adsorption isotherms represented in Figure 13, Table 2 displays results obtained from the isotherm study.

Table 2. Langmuir and Freundlich Isotherm Parameters for Adsorption of AO dye onto E1-E4 at 25°C.

Adsorbents	Langmuir			Freundlich		
	q_{max}	K_L	R^2	K_F	n	R^2
E1	980.39	0.0019	0.9989	15.376	1.8228	0.9883
E2	1515.2	0.0014	0.9969	10.305	1.5221	0.9944
E3	1694.9	0.0015	0.9918	11.353	1.4921	0.9879
E4	1851.9	0.0029	0.9898	25.237	1.6255	0.9927

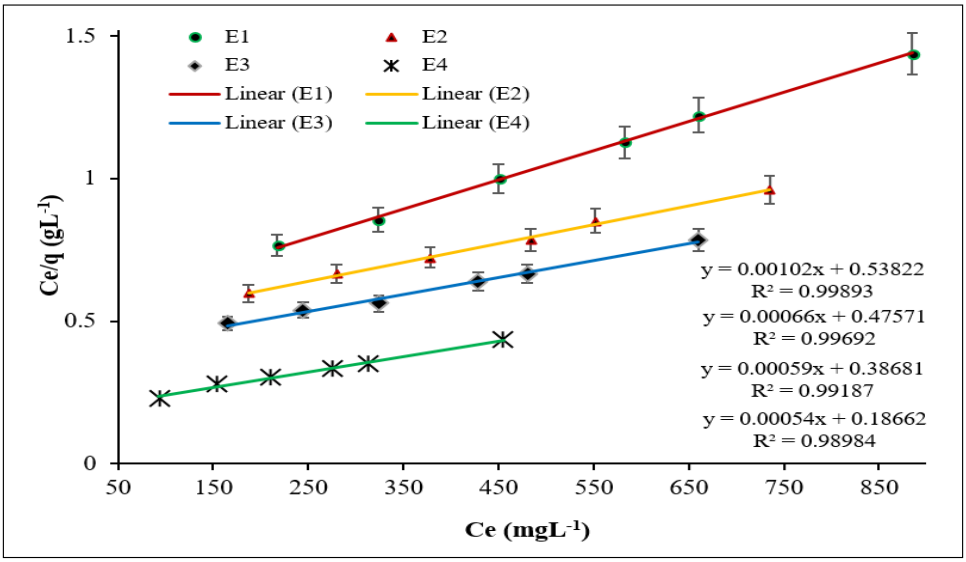

Fig. 12. Langmuir model adsorption isotherms for AO dye onto E1-E4

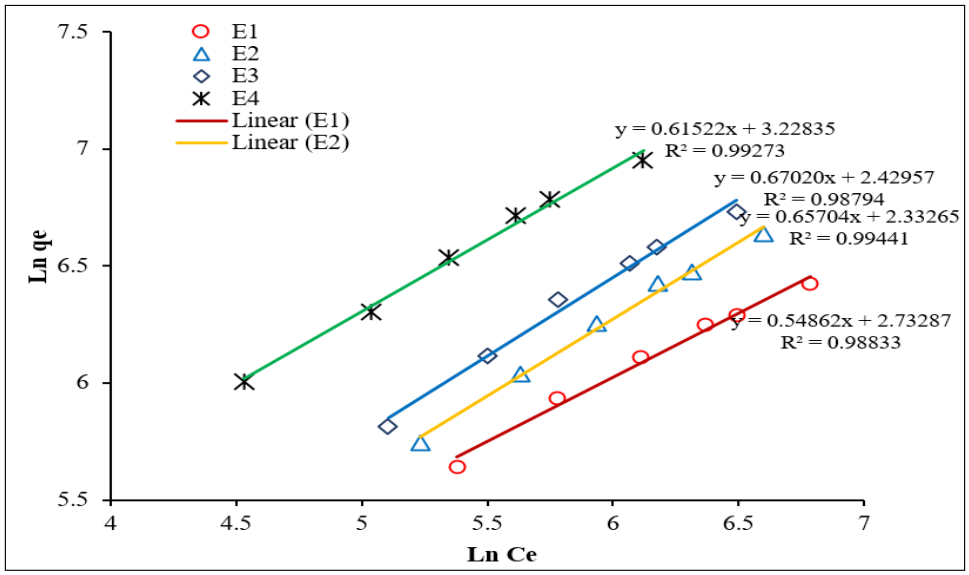

Fig. 13. Freundlich model adsorption isotherms for AO dye onto E1-E4

3.3. Performance Evaluation

The maximum adsorption capacity of AO dye has been compared with the literature values of other adsorbents and listed in Table 3. All of the methods used for AO have considerably higher max values than the adsorption onto thermosetting epoxy resin E1-E4 used in this study.

4. Conclusion

This study employed adsorption and Fenton methods for removal of cationic AO dye, the efficient removal from aqueous solutions by using the new hardener epoxy resins E1-E4 as adsorbents. The maximum adsorption of AO was obtained at pH 10. From closed R^2 values to one of the

Table 3. Summary of AO adsorption capacities of various adsorbents

Type of adsorbent	q_{max} , (mg g^{-1})	Reference
BG/GO; IL-MWCNTs; CQDs	200-350	[36-38]
sugar beet pulp	324.85	[39]
Gt/Cu-AC np	95.43	[40]
MGA-PP-RFHN	202.63	[41]
dry biomass of Bacillus cereus	210.46	[42]
Watermelon rinds	69.44	[43]
E1	980.39	This Study
E2	1515.2	This Study
E3	1694.9	This Study
E4	1851.9	This Study

BG/GO; IL-MWCNTs; CQDs: Bismuth oxide coupled to heterogeneous graphene/graphene oxide; Ionic liquid coated on MWCNTs; Carbon Quantum Dots
Gt/Cu-AC np: Green tea/copper-activated carbon nanoparticles
MGA-PP-RFHN: Mesoporous glutamic acid-g-polyacrylamide/plaster of paris/riboflavin hydrogel nanocomposite

Langmuir model plots for all adsorption systems, we concluded the chemosorption mechanism. From the calculation of the Langmuir equation (qmax), values for E1-E4 were 980.39, 1515.2, 1694, and 1851.9 mg g^{-1} respectively. On the other hand, the optimum parameters of the Fenton process were investigated: pH =3, H_2O_2/Fe^{2+} ratio of 1:4, contact time = 10 minutes, and the dye concentration of 800mg.L^{-1} was obtained. In addition, the results showed that the initial dye concentration influenced the concentration of hydrogen peroxide and iron sulfate. The percentage of Acridine Orange removal was 81.87%, and the results of this study showed that the Fenton process was a practical approach to remove AO dye from its solution.

5. Acknowledgements

The authors thank the University of Basra, Al-Ashar–Corniche Street, Basra, Iraq.

6. References

[1] M. S. Tsuboy, J. P. F. Angeli, M.S. Mantovani, S. Knasmuller, G.A. Umbuzeiro, L.R. Ribeiro, Genotoxic, mutagenic and cytotoxic effects of the commercial dye CI Disperse Blue 291 in the human hepatic cell line HepG2, Toxicol. In Vitro, 21 (2007) 1650–1655. https://doi.org/10.1016/j.tiv.2007.06.020

[2] S. Sultana, M.D. Khan, S. Sabir, K.M. Gani, M. Oves, M.Z. Khan, Bio-electro degradation of azo-dye in a combined anaerobic–aerobic process along with energy recovery, New J. Chem., 39 (2015) 9461–9470. https://doi.org/10.1039/C5NJ01610J

[3] C. Zhang, P.C. Zhu, L. Tan, J.M. Liu, B.E. Tan, X.L. Yang, H.B. Xu, Triptycene-based hyper-cross-linked polymer sponge for gas storage and water treatment, Macromol., 48 (2015) 8509–8514. https://doi.org/10.1021/acs.macromol.5b02222

[4] N.R. Paluvai, S. Mohanty, S.K. Nayak, Synthesis and modifications of epoxy resins and their composites: A review, Plast. Technol. Eng., 53 (2014) 1723–1758. https://doi.org/10.1080/03602559.2014.919658

[5] J. Xu, J. Yang, X. Liu, H. Wang, J. Zhang, S. Fu, Preparation and characterization of fast-curing powder epoxy adhesive at middle temperature, Royal Soc. Open Sci., 5 (2018) 180566. https://doi.org/10.1098/rsos.180566

[6] P.S. Beata, W. Monika, K. Łukasz, Synthesis, characterization and sorption ability of epoxy resin-based sorbents with amine groups, Polymers, 13 (2021) 4139. https://doi.org/10.3390/polym13234139

[7] G. Samaresh, A. Mridula, Removal of azo dye molecules from aqueous solution using novolac resin based network polymer, Bull. Chem. Soc. Japan, 84 (2011) 349–351. https://doi.org/10.1246/bcsj.20100245

[8] M. M. Asl, F. Atabi, Functionalized graphene oxide with bismuth and titanium oxide nanoparticles for efficiently removing formaldehyde from the air by photocatalytic degradation–adsorption process, J. Anal. Test., 7 (2023) 444-458. https://doi.org/10.1007/s41664-023-00272-0

[9] S. Teimoori, A. H. Hassani, M. Panahi, N. Mansouri, An immobilization of aminopropyl trimethoxysilane-phenanthrene carbaldehyde on graphene oxide for toluene extraction and separation in water samples, Chemosphere, 316 (2023) 137800. https://doi.org/10.1016/j.chemosphere.2023.137800

[10] S. Teimoori, Rapid extraction of BTEX in water and milk samples based on functionalized MWCNTs by dispersive homogenized-micro-solid phase extraction, Food Chem., 421 (2023) 136229. https://doi.org/10.1016/j.foodchem.2023.136229

[11] S. Teimoori, A. H. Hassani, New extraction of toluene from water samples based on nano-carbon structure before determination by gas chromatography, Int. J. Environ. Sci. Technol., 20 (2023) 6589–6608. https://doi.org/10.1007/s13762-023-04906-9

[12] F. Golbabaei, On-line micro column preconcentration system based on amino bimodal mesoporous silica nanoparticles as a novel adsorbent for removal and speciation of

chromium (III, VI) in environmental samples, J. Environ. Health Sci.Eng., 13 (2015) 47. https://doi.org/10.1186/s40201-015-0205-z

[13] M. Asl, N. Mansouri, S. A. R. Haji Seyed Mirzahosseini, F. Atabi, Simultaneity comparative evaluation of toluene removal from the air by adsorption and UV semi-degradation-based adsorption procedure, Int. J. Environ. Sci. Technol., 21 (2024) 6677-6694. https://doi.org/10.1007/s13762-024-05503-0

[14] S. Ghosh, M. Acharyya, Pyridine-Rich Novolac-Based Network as an Effective Adsorbent for Removing Azo Dyes, Chem. Select, 5 (2020) 10727-10735 https://doi.org/10.1002/slct.202002024

[15] L. Feng, Y. Wang, Y. Wang, H. Liu, Study on reaction kinetics of epoxy resin cured by a modified dicyandiamide, J. Appl. Polym. Sci., 127 (2013) 1895-1900. https://doi.org/10.1002/app.37917

[16] P. Ranpara, P.N. Bhalerao, Curing of epoxy resin by using commercial amine/hydrazine and its effect on ultra violet spectrum advances in chemical, bio and environmental engineering, Conference paper, Environ. Sci. Eng., (2022) 949–956. http://dx.doi.org/10.1007/978-3-030-96554-9_63

[17] S. Yu, X. Li, M. Zou, X. Guo, H. Ma, S. Wang, Effect of the aromatic amine curing agent structure on properties of epoxy resin-based syntactic foams, ACS Omega, 5 (2020) 23268–23275. https://doi.org/10.1021/acsomega.0c03085

[18] H. Yamasaki, S. Morita, Epoxy curing reaction studied by using two-dimensional correlation infrared and near-infrared spectroscopy, J. Appl. Polymer Sci., 119 (2011) 871–881. https://doi.org/10.1002/app.32787

[19] H.S. Al-Niaeem, Thermal stability of some new metal containing polymers based on resol- bisphenol A formaldehyde resin, Res. J. Sci. Technol., 7 (2015) 2349-2988. https://doi.org/10.5958/2349-2988.2015.00025.X

[20] A.A. Abdulwahid, A.A. Alwattar, A. Haddad, M. Alshareef, J. Moore, G. Y. Yeatesb, P. Quayleb, An efficient reusable perylene hydrogel for removing some toxic dyes from contaminated water, Polymer Int., 70 (2021) 1234–1245. http://dx.doi.org/10.1002/pi.6186

[21] Y. Chen, Y. Ma, Q. He, Q. Qiuxia Han, Construction of pyridinium/*N*-chloramine polysiloxane on cellulose for synergistic biocidal application, Cellulose, 26 (2019) 5033–5049. https://doi.org/10.1007/s10570-019-02437-6

[22] E. Ulker, M. Kavanoz, Synthesis of poly (Vinylferrocene) perchlorate/poly(3,3'-diaminobenzidine) modified electrode in dichloromethane for electroanalysis of hydroquinone, J. Braz. Chem. Soc., 26 (2015) 1947-1955. http://dx.doi.org/10.5935/0103-5053.20150173

[23] M. R. Rezaei Kahkhaa, A. Faghihi Zarandi, A review in analytical methods: Removal and extraction of pollutants in different matrixes by nanotechnology, Anal. Methods Environ. Chem. J., 7 (2024) 51-82. https://doi.org/10.24200/amecj.v7.i03.1004

[24] M. González González, J. Carlos Cabanelas, J. Baselga, Applications of FTIR on epoxy resins - identification, monitoring the curing process, phase separation and water uptake, materials science, engineering and technology, Intech Open Publisher Book, 2012. https://doi.org/10.5772/36323

[25] F. Moghadam, N. N. Kohbanan, Removal of reactive blue 19 dye using Fenton from aqueous solution, Avicenna J. Environ. Health Eng., 5 (2018) 50-55. https://doi.org/10.15171/ajehe.2018.07

[26] H. Lee, M. Shoda, Removal of COD and color from livestock wastewater by the Fenton method, J. Hazard. Mater., 153 (2008) 1314-1319. https://doi.org/10.1016/j.jhazmat.2007.09.097

[27] S. Meric, D. Kaptan, T. Olmez, Color and COD removal from wastewater containing Reactive Black 5 using Fenton's oxidation process, Chemosphere., 54 (2004) 435-441. https://doi.org/10.1016/j.chemosphere.2003.08.010

[28] P. Bautista, A.F. Mohedano, J.A. Casas, An overview of the application of Fenton oxidation to industrial wastewaters treatment, J. Chem. Technol. Biotechnol., 83 (2008) 1323-1338. https://doi.org/10.1002/jctb.1988

[29] L. Szpyrkowicz, C. Juzzolino, S.N. Kaul, A Comparative study on oxidation of disperse dyes by electrochemical process, ozone, hypochlorite and fenton reagent, Water Res., 35 (2001) 2129- 2136. https://doi.org/10.1016/S0043-1354(00)00487-5

[30] B.H. Hameed, T.W. Lee, Degradation of malachite green in aqueous solution by Fenton process, J. Hazard. Mater., 164 (2009) 468-472. https://doi.org/10.1016/j.jhazmat.2008.08.018

[31] P.V. Nidheesh, R. Gandhimathi, Electro Fenton oxidation for teh removal of Rhodamine B from aqueous solution in a bubble column reactor under continuous mode, Desalin. Water Treat., 55 (2015) 263-271. https://doi.org/10.1080/19443994.2014.913266

[32] A.A. Zorpas, C.N. Costa, Combination of Fenton oxidation and composting for the treatment of the olive solid residue and the olive mile wastewater from the olive oil industry in Cyprus, Bioresour. Technol., 101 (2010) 7984-7987. https://doi.org/10.1016/j.biortech.2010.05.030

[33] Y. Yang, P. Wang, S. Shi, Y. Liu, Microwave enhanced Fenton-like process for the treatment of high concentration pharmaceutical wastewater, J. Hazard. Mater.,168 (2009) 238-245. https://doi.org/10.1016/j.jhazmat.2009.02.038

[34] A.A. Albaheli, PhD Thesis(chemist), Basrah university, Basrah, 2020. https://www.researchgate.net/profile/Alaa_Mizhir

[35] S.M. Saleh, PhD Thesis(chemist), Basrah university, Basrah, 2024. https://doi.org/10.13140/RG.2.2.19385.42086

[36] A. Faghihi-Zarandi, J. Rakhtshah, B. B. Yarahmadi, A rapid removal of xylene vapor from environmental air based on bismuth oxide coupled to heterogeneous graphene/graphene oxide by UV photo-catalectic degradation-adsorption procedure, J. Environ. Chem. Eng., 8 (2020) 104193. https://doi.org/10.1016/j.jece.2020.104193

[37] R. Ashouri, N. Mansouri, Dynamic and static removal of benzene from air based on task-specific ionic liquid coated on MWCNTs by sorbent tube-headspace solid-phase extraction procedure, Int. J. Environ. Sci. Technol., 18 (2021) 2377-2390. https://doi.org/10.1007/s13762-020-02995-4

[38] R. Ashouri, S. A. Hajiseyed Mirzahosseini, N. Mansouri, Synthesis of carbon quantum dots from olive stones for efficient adsorption of benzene from the ambient air, J. Nanostruct., 11 (2021) 480-497. https://doi.org/10.22052/JNS.2021.03.007

[39] V. M. Vučurović, V. S. Puškaš, U. D. Miljić, Removal of acridine orange dye from aqueous solution by adsorption onto dried sugar beet pulp, Acta Periodica Technologica, 48 (2017) 307-314. https://doi.org/10.2298/APT1748307V

[40] K. Chandrika, A. Chaudhary, T. Mareedu, Adsorptive removal of acridine orange dye by green tea/copper-activated carbon nanoparticles (Gt/Cu-AC np), Mater. Today: Proceedings, 44 (2021) 2283–2289. https://doi.org/10.1016/j.matpr.2020.12.391

[41] N. Abbasi, S. A. Khan, T. Alam Khan, Statistical evaluation of liquid phase sequestration of acridine orange and Cr6+ by novel mesoporous glutamic acid-g-polyacrylamide/plaster of paris/riboflavin hydrogel nanocomposite, Environ. Res., 213 (2022) 113712. https://doi.org/10.1016/j.envres.2022.113712

[42] S. Bag, M.I. Hasan, D Halder, Biosorption of organic dye Acridine orange from aqueous solution using dry biomass of Bacillus cereus M116, Arch. Microbiol., 203 (2021) 3811-3823. https://doi.org/10.1007/s00203-021-02355-x

[43] S. Ahmed, S.H. Siham, A. Nuri, E.A. Marwa, Watermelon rinds as cost-efficient adsorbent for acridine orange: a response surface methodological approach, Environ. Sci. Pollut. Res., 30 (2023) 71554-71573. https://doi.org/10.1007/s11356-021-13652-9

Anal. Methods Environ. Chem. J. 8 (1) (2025) 115-132

AMECJ

Research Article, Issue 1
Analytical Methods in Environmental Chemistry Journal
Journal home page: www.amecj.com/ir

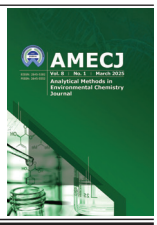

Spectroscopic determination of the minoxidil drug by charge transfer complex using Schiff base

Muhammed, N. Tawfeeq[*,a] , Eman Thiab Al Samarrai[b] , and Sattar R. Majeed[c]
[a] *Iraqi Ministry of Education, Anbar Education, Ramadi, Anbar, Iraq*
[b] *Department of Chemistry, College of Science, University of Anbar, Ramadi, Anbar, Iraq*
[c] *Department of Chemistry, College of Education, University of Samarra, Iraq*

ARTICLE INFO:
Received 13 Nov 2024
Revised form 30 Jan 2025
Accepted 29 Feb 2025
Available online 28 March 2025

Keywords:
Spectroscopic methods,
Charge transfer complex,
Schiff base,
Drug azo reagent,

ABSTRACT
This work includes the synthesis and characterization of a charge transfer complex from Schiff base-minoxidil with a new azo reagent, 1-(4-hydroxy-3-(4-nitrophenyl diazenyl) phenyl) ethan-1-one, and the determination of minoxidil drug in pharmaceuticals. The charge transfer complex gives a red-colored product that gives its highest absorption at the wavelength of 505 nm. UV-visible, FT-IR, and GC-mass characterized azo reagent, Schiff base-drug, and charge transfer complex. The nature of the complex was determined by studying the Job method and the molar ratio method, which showed that the acceptor-to-donor ratio was (1:1). Simple, easy, highly sensitive, and inexpensive spectrophotometric methods for the determination of minoxidil have been developed. Optimal conditions were studied, which gave good sensitivity. It displayed a linear range of 1–12.5 µg mL^{-1} and a correlation value 0.9979. The Sandel sensitivity, the detection limit (LOD), and the quantitative limit (LOQ) were obtained at 0.0110 µg cm^{-2},, 0.1019 µg mL^{-1}, and 0.3089 µg mL^{-1}, respectively, respectively. The average recovery (%)was 102.47.

1. Introduction

The scientist Mulliken assumed that the charge transfer complexes were a resonant hybrid resulting from the union of electron-donating molecules with low ionization potential. These represent Lewis bases, with electron-accepting molecules with high electronic affinity, representing Lewis's acids [1, 2]. As the scientist Weiss explained, the donor molecule (D+) has a partial positive charge, while the receiving molecule (A-) carries a partial negative charge [3]. The transition occurs from the highest HOMO of the electron-donating molecule to the lowest LUMO of the electron-receiving molecule [4,5]. Electron-donating and electron-accepting compounds were classified as potent donating compounds if they contain atoms with a double or more non-coupled bearing, in addition to the presence of propelling groups that increase their ability to donate an electron, as well as weak donating compounds, which donate the electron from a cooperating orbital. Likewise, electron-accepting compounds are strong if they contain an empty orbital and weak receptor compounds if they include a π type bond [6]. Molecules in charge transfer complexes were connected by bonds not only by van der Waals forces and electrostatic polarization, and sometimes they contained hydrogen bonds, but also by electronic charge transfer, and the strength of the interaction depended on the amount of electronic transfer from the donor to the acceptor. As a result, the excited electronic state is an internal redox process. The

*Corresponding Author: Muhammed, N. Tawfeeq
Email: mohamed_tawfiq@uosamarra.edu.iq
https://doi.org/10.24200/amecj.v8.i01.1016

active pharmaceutical compound was often the donor, and the analytical challenge was to find a suitable acceptor. The products of these reactions were formed very quickly and show absorption in the visible region. The compound formed depends on the solvent polarity [7-9]. Charge transfer complexes have broad applications, including OLED electronic devices based on organic materials that emit light as a result of the application of an electrical voltage [10-12], solar cells [13, 14], photodetectors [15, 16], and as electrocatalysts due to their conductivity and electrochemical activity [17, 18]. In addition to its biological applications [19, 20] and estimation of pharmaceutical compounds [21, 22]. Minoxidil, also known as 2,4-diamino-6-piperidinopyrimidine 3-oxide chemically, was a white powder drug with the molecular weight of 209.25 g mol^{-1} and chemical formula $C_9H_{15}N_5O$. It was used to treat severe hypertension in patients whose blood pressure was not sufficiently controlled with combinations of conventional antihypertensive medications. Approximately 80% of patients had favorable outcomes [23]. It opens potassium channels in the smooth muscles of the peripheral arteries, causing the cell membrane to become hyperpolarized [24]. One of the reasons the medication was found to be beneficial in treating androgenic alopecia (AGA), initially in males and then in females, was because it caused adverse effects, such as excessive hair growth [25, 26]. Since it significantly impacted drug development, developing analytical methods is critical in pharmaceutical analysis.

2. Experimental

2.1. Materials and Instrumentation

All experiments used high-purity chemicals. Minoxidil (CAS Number: 38304-91-5, Macklin 98%, China), p-Hydroxy acetophenone (CAS Number: 99-93-4, Aldrich 98%, China), p-nitro anline (CAS Number: 100-01-6, Fluka 98%), DMSO (CAS Number: 67-68-5, HiMedia 99%, India), sodium hydroxide (CAS Number: 1310-73-2, ACS CHEMICALS, India), Hydrochloric acid (CAS Number: 7647-01-0, CDH, India) and ethanol (CAS Number: 64-17-5, Honeywell 99.8%). Electro thermal (Melting points SMP20), Infrared spectra (Shimadzu (FT–IR)–8400S), pH meter (HANNA HI2210-02), UV-Visible spectrophotometer (INESA SHANGFEN N4S UV-Visible) and mass spectra (Shimadzu GCMS-QP2010 SE) were used in this study.

2.2. Reagent and chemical solutions

The reagent solution (1000 µg mL^{-1}) was prepared by dissolving 0.1 g of azo reagent in a small amount of ethanol, transferring it to a 100 mL volumetric flask, and supplementing it to the mark with the same solvent. Schiff-Drug solution (100 µg mL^{-1}) was prepared by dissolving 0.01 g in ethanol, transferring it to a 100 mL volumetric flask, and supplementing it to the mark with the same solvent. Hydrochloric acid solution (0.1 M) is prepared by diluting 0.83 mL of concentrated acid to 11.97 molarity by adding it to distilled water and bringing the volume to the mark in a 100 mL bottle. Sodium hydroxide solution (0.1M) was prepared by dissolving 0.4 g of sodium hydroxide in distilled water, transferring it to a 100 mL volumetric vial, and completing the volume with distilled water.

2.3. Analysis of minoxidil in the pharmaceutical preparations

Steadfast Medishield Pvt Ltd, New Delhi, India, produces the pharmaceutical preparation Minoxidil Tablets. Each tablet contains 5 milligrams. Twenty tablets were ground and dissolved in 25 mL of ethanol. The solution was filtered and transferred to a 100 mL volumetric flask, then completed to the mark by ethanol to produce 1000 µg mL^{-1}. 13 mL of 4-hydroxyacetophenone solution with a concentration of 1000 µg mL^{-1} was withdrawn. A drop of glacial acetic acid was added, then mixed with 10 mL of the pharmaceutical solution of the drug Minoxidil. The mixture was stirred and heated at 70°C for 6 hours, then cooled and transferred to a 100 mL volumetric vial and completed by ethanol to the mark to produce a Schiff base solution for the drug with a concentration of 100 µg mL^{-1}.

2.4. Synthesis of reagent 1-(4-hydroxy-3-(4-nitrophenyl diazenyl)phenyl) ethan-1-one

We dissolved 4-nitroaniline (0.345 g, 2.5 mmol) into a clear solution by stirring in a mixture of ethanol (10 mL) and hydrochloric acid (2 mL). A range of 0 to 5 °C was kept constant. Then, while keeping the temperature below 5°C, an aqueous solution comprising 1.0 g of sodium nitrite that has been dissolved in 10 mL of water has been added gradually, dropwise. After that, the mixture was swirled for five minutes. The 0.34 g, 2.5 mmol 4-hydroxy acetophenone was dissolved in 20.0 mL of ethanol and then cooled in an ice bath. The precipitate was dried and filtered after mixing the final solution with cooling solution 1 [27, 28]. Scheme 1 demonstrates the brown precipitate that resulted in a melting point of 84.6%.

2.5. Synthesis of Schiff base-Drug ($C_{23}H_{23}N_5O_3$)

Minoxidil (0.52 g, 2.5 mmol) was dissolved by stirring and heating in a beaker containing ethanol (40 mL), and 4-hydroxyacetophenone (0.68 g, 5 mmol) was dissolved by stirring and heating in a beaker containing ethanol (40 mL), then adding 2-3 drops of glacial acetic acid. We mixed and refrigerated the solutions for six hours at 70°C. The solution was cooled and collected into a white precipitate [29,30]; Scheme 2 shows that the yield was 72.8%.

2.6. procedure method

One mL of azo reagent (1000 µg mL^{-1}) was added to the beaker containing 0.5 mL (100 µg mL^{-1}) of Schiff base-minoxidil to produce a red solution rapidly. After diluting the flask's contents with ethanol to the appropriate level, the sample's absorbance was compared to a blank solution [31,32]. The spectrum showed a broad peak with the highest absorbance at 505 nm.

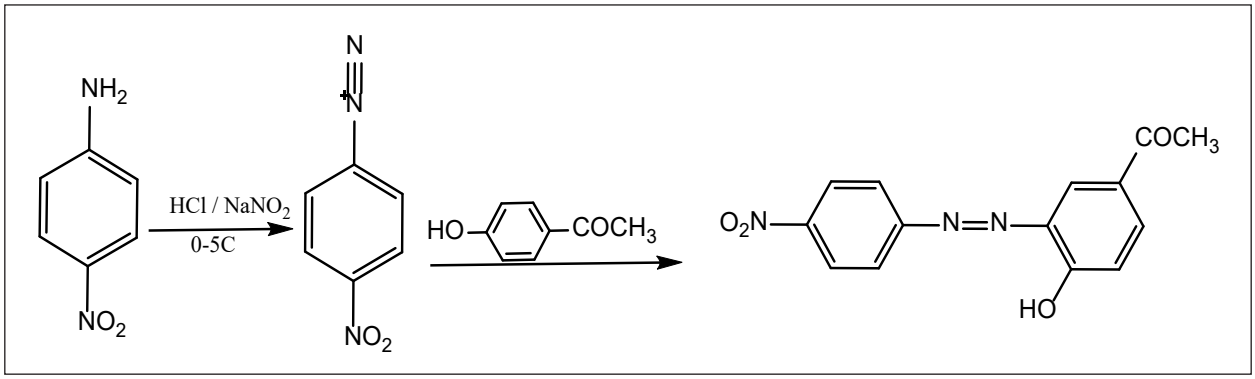

Scheme 1. Synthesis of Azo reagent

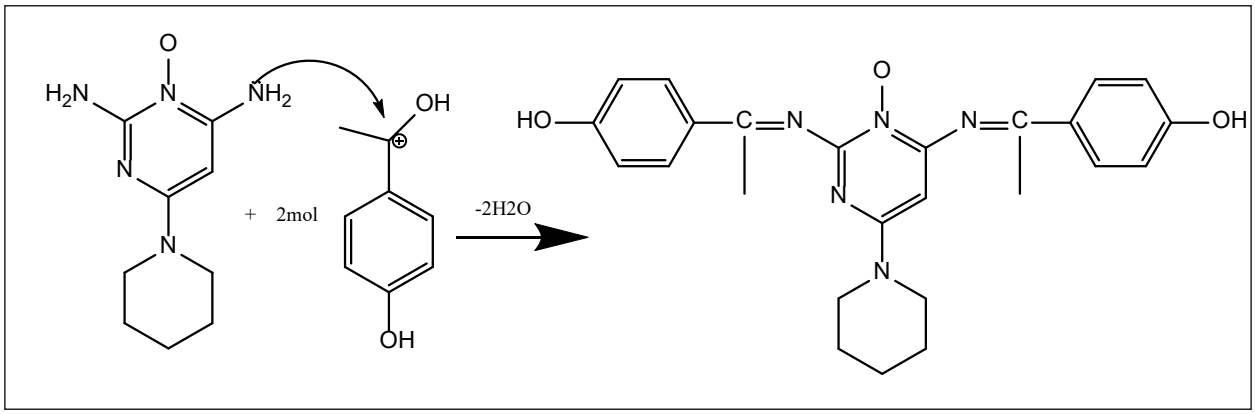

Scheme 2. Synthesis of Schiff base-Minoxidil

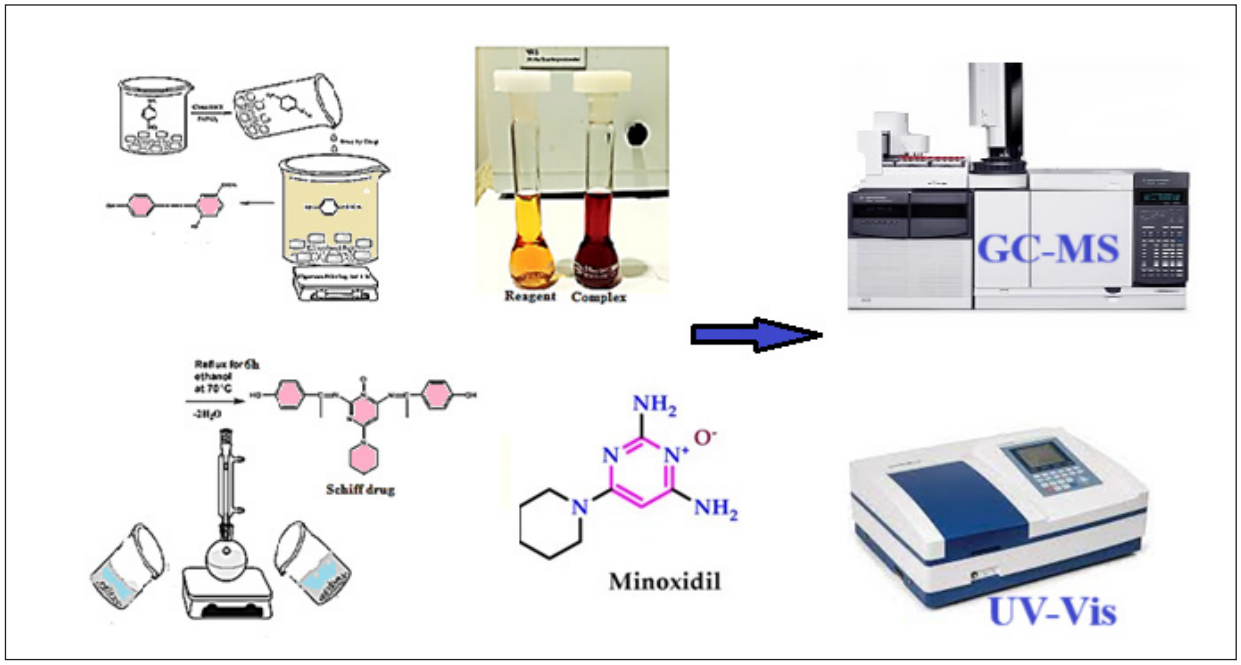

Schema 3. Determination Minoxidil drug by GC-MS and UV-Vis

3. Results and Discussion

3.1. FT-IR spectral data

The infrared spectra of the azo reagent, Schiff base-minoxidil, and charge transfer complex were summarized in Table 1 and Figures 1-5. The spectrum showed absorption at 3437 cm^{-1} to the hydroxyl group in the azo reagent [33]; the (-N=N-) group absorption was observed at 1433 cm^{-1} [34]; the (C=O) group absorption was observed at 1681 cm^{-1}; and (C=C) absorption was observed at 1602 cm^{-1}. The ketone's spectrum revealed three bands: one at 1662 cm^{-1} owing to the carbonyl group's vibration, another at 1577 cm^{-1} due to the (C=C) group's vibration, and a band at 3309 cm^{-1} owing to the hydroxyl group's stretching frequency. The disappearance of absorption of the amine group in the minoxidil drug and the carbonyl group of the compound 4-hydroxyacetophenone and the appearance of absorption at 1620 cm^{-1} belong to the (C=N-) group [35], indicating the formation of the Schiff base drug. The charge transfer complex also appeared to absorb at 3448 cm^{-1}, which belongs to the hydroxyl group, in addition to the possibility of forming hydrogen bonds [36]. The spectrum showed absorption of the carbonyl group at 1658 cm^{-1} and absorption of the azo group at 1435 cm^{-1}.

Table 1. The bands of the FTIR Spectra

Compounds	OH	NH_2	C=O	C=N-Aromatic	C=N	C=C	N=N
Azo reagent	3437	-----	1681	-----	-----	-----	1433
Minoxidil	-----	3417	-----	-----	------	1450	----
4-Hydroxy acetophenone	3309	-----	1662	-----	-----	1577	----
Schiff base-minoxidil	3456	-----	-----	1651	1581	1496	----
Charge transfer complex	3448	-----	1658	-----	----	----	1435

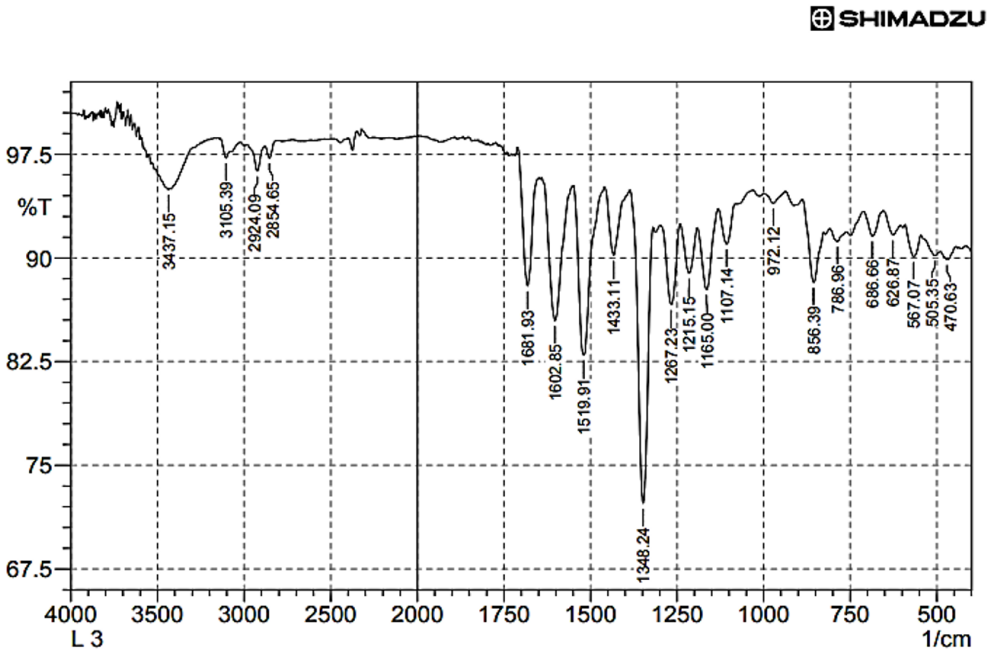

Fig. 1. IR Spectrum of Azo reagent

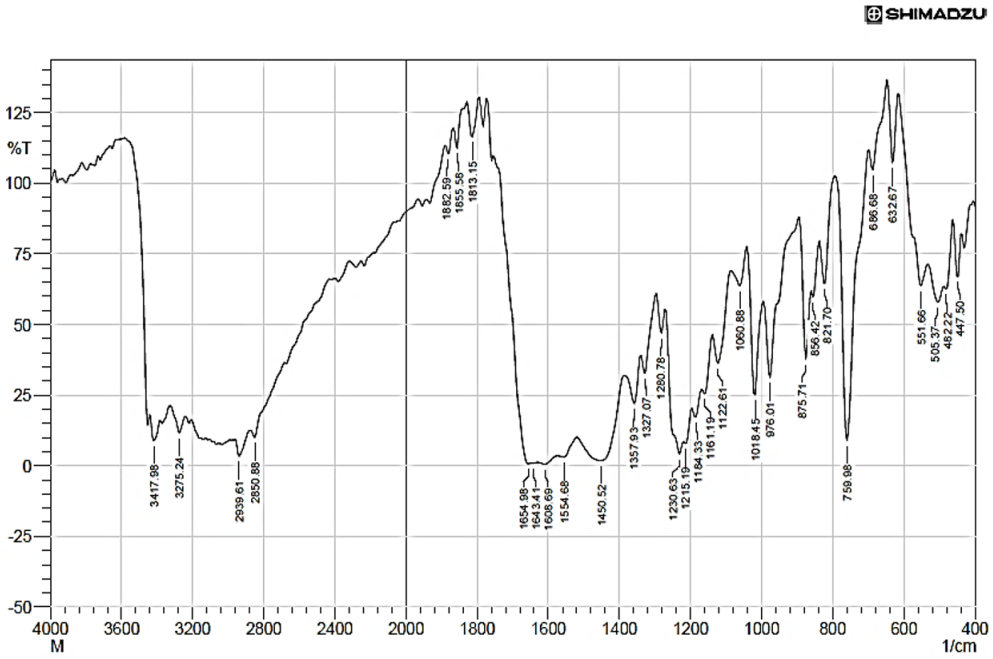

Fig. 2. IR Spectrum of minoxidil drug

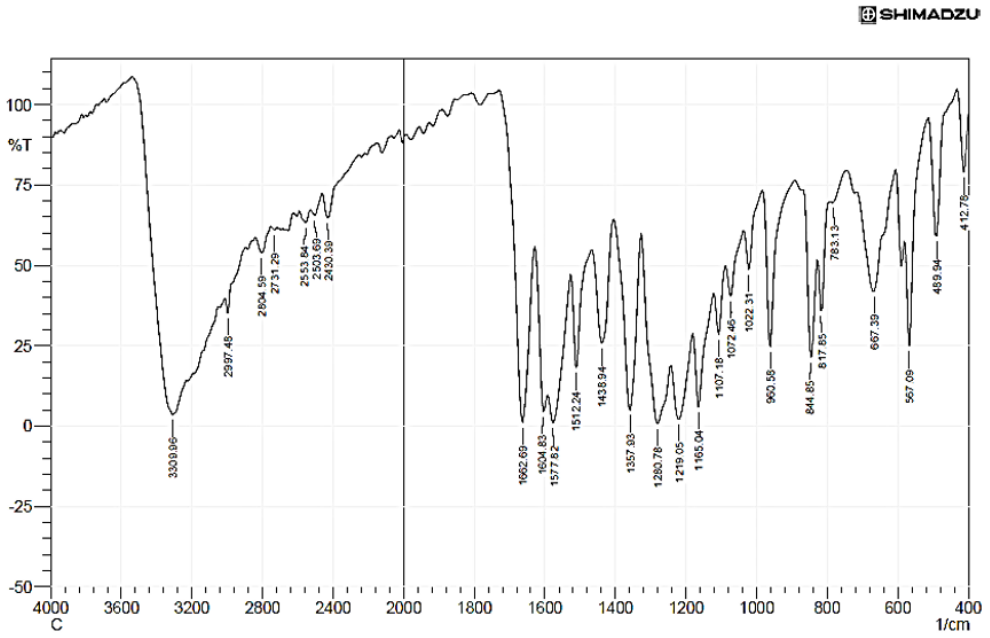

Fig. 3. IR Spectrum of 4-Hydroxy acetophenone

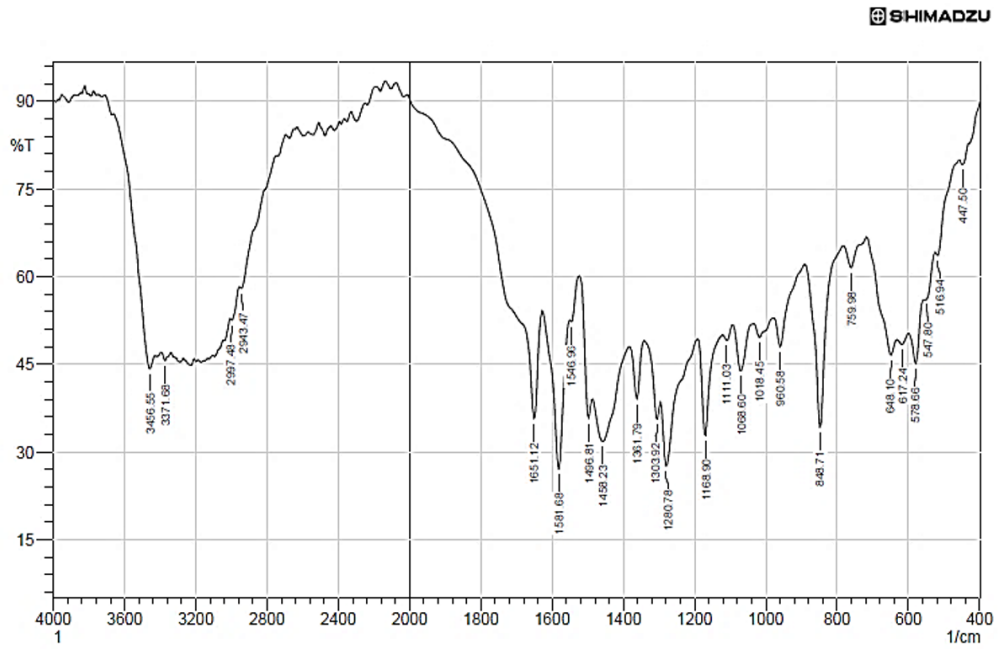

Fig. 4. IR Spectrum of Schiff -drug

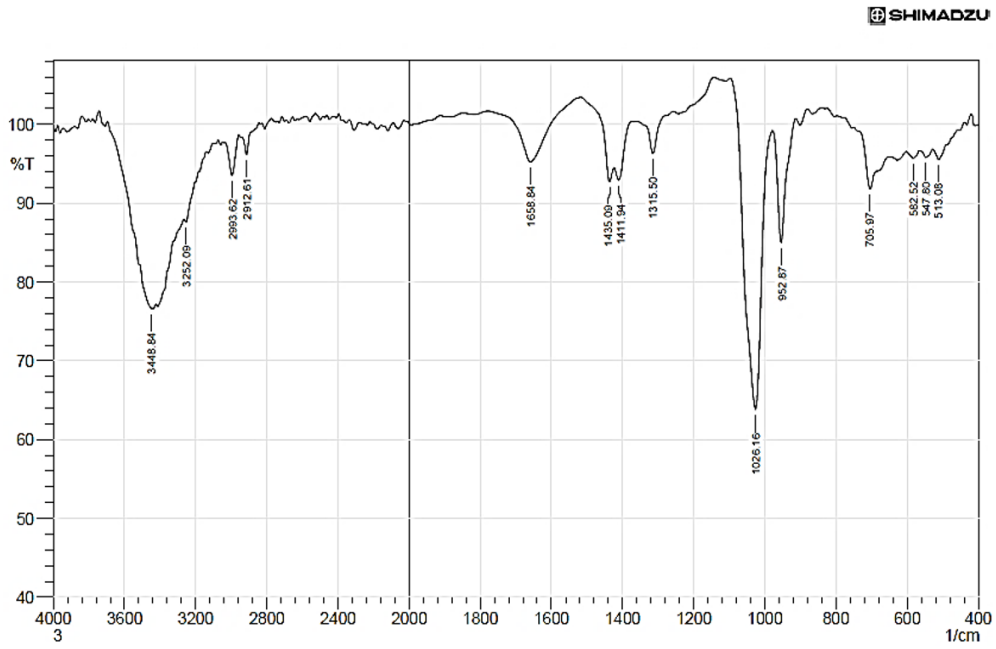

Fig. 5. IR Spectrum of Charge transfer complex

3.2. Mass spectra of Azo reagent, Schiff base-minoxidil and CT complexe

The mass spectrum of the azo reagent was shown in Figure 6. The molecular weight of the azo reagent (286) created a parent peak at m/z = 285 (M+) in its mass spectrum. Figure 7 shows the mass spectrum of Schiff base-minoxidil, which has a parent peak at m/z = 445 (M+) and a molecular weight of 445.21. The mass spectrum of the charge transfer complex, which has a molecular weight of 1015.36, is shown in Figure 8. It indicated a parent peak at m/z = 1015 (M+) [37].

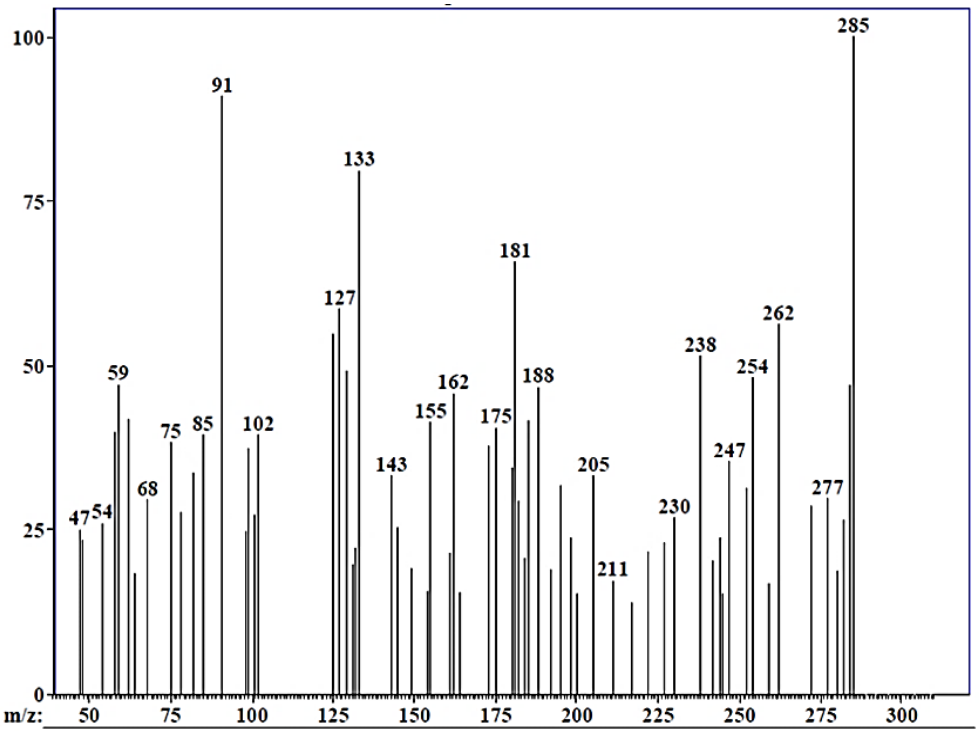

Fig. 6. Mass spectrum of Azo reagent

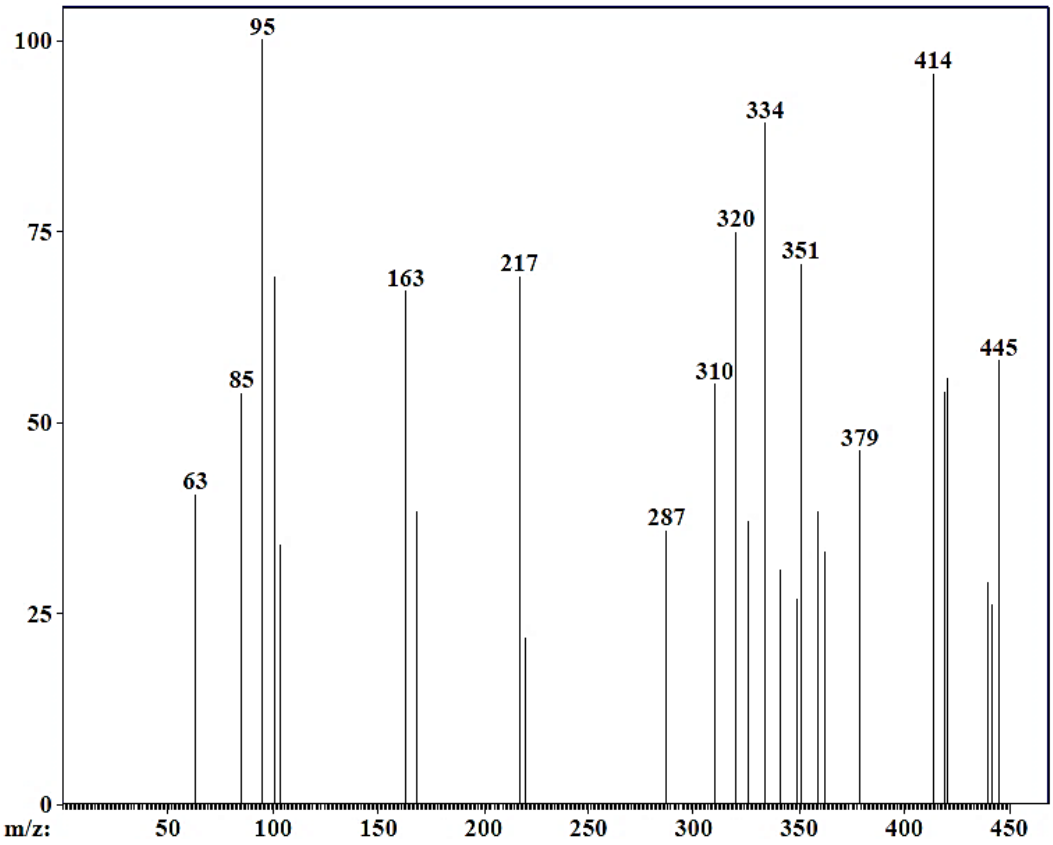

Fig. 7. Mass spectrum of Schiff base-Minoxidil

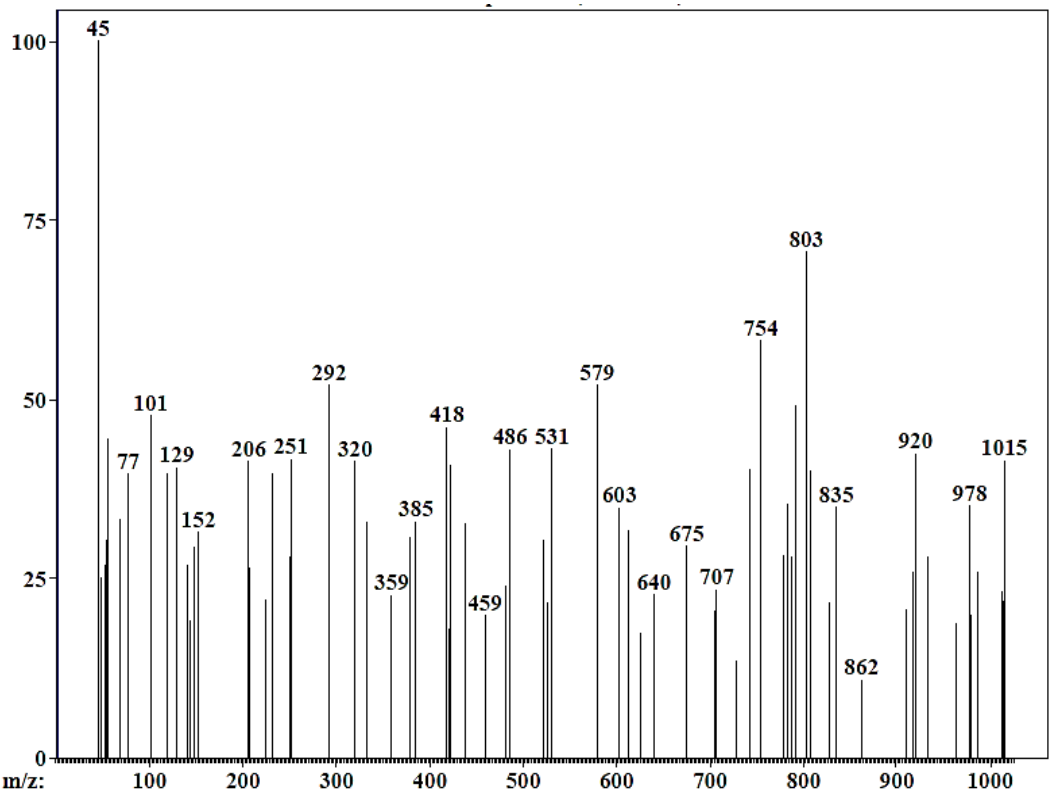

Fig. 8. Mass spectrum of Charge transfer complex

3.3. UV-Vis Spectral data

Table 2 summarizes UV spectrum data for the azo reagent, Schiff-Minoxydil base, and charge transfer complex (Figures 9 and 10). Absorption peaks were seen in the azo reagent spectra at 245 and 275 nm, which indicated a (π→π∗) transition, and at 325 and 390 nm, which showed a (n → π*) transition. Two absorption peaks appeared in the Schiff base-minoxidil spectra at 235 and 280 nm, indicating a (π→π∗) transition, and a new absorption peak at 330 nm, indicating a shift (n→π*) for the group (-N=C); comparison with p-hydroxy acetophenone had peaks appearing at 220 nm. and 279 nm for (π→π∗); minoxidil peaks appeared at 230 nm, 260 nm, and 285 nm for (π→π∗). The spectrum of the charge transfer complex also showed a new band at 505 nm, which indicates charge transfer within the visible range [38].

Table 2. UV spectrum data for reagent, Schiff base-minoxidil and CT complex

No.	compounds	λ max (nm)	Transition
1	Azo reagent	245	π → *π
		275	π → *π
		325	n → *π
		390	n → *π
2	Schiff base-minoxidil	235	π → *π
		280	π → *π
		330	n → *π
3	Charge transfer complex	230	π → *π
		274	π → *π
		325	n → *π
		505	C.T

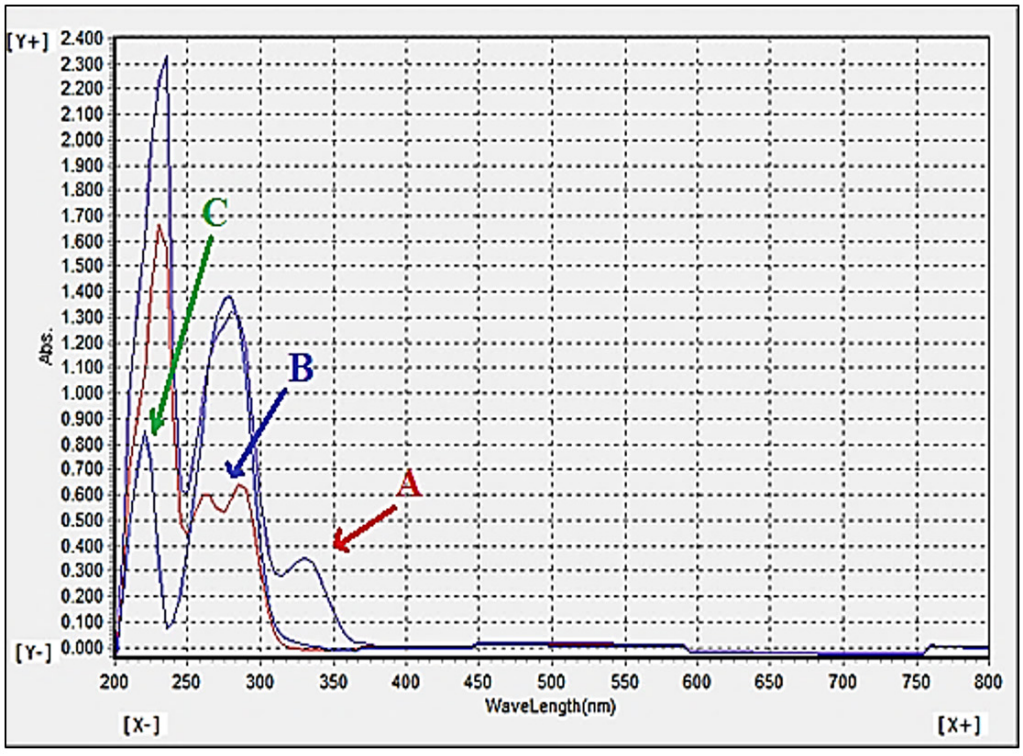

Fig. 9. Absorption spectrum of Schiff base-Minoxidil spectrum **(A)**, Minoxidil drug **(B)** and p-hydroxy acetophenone spectrum **(C)** versus blank

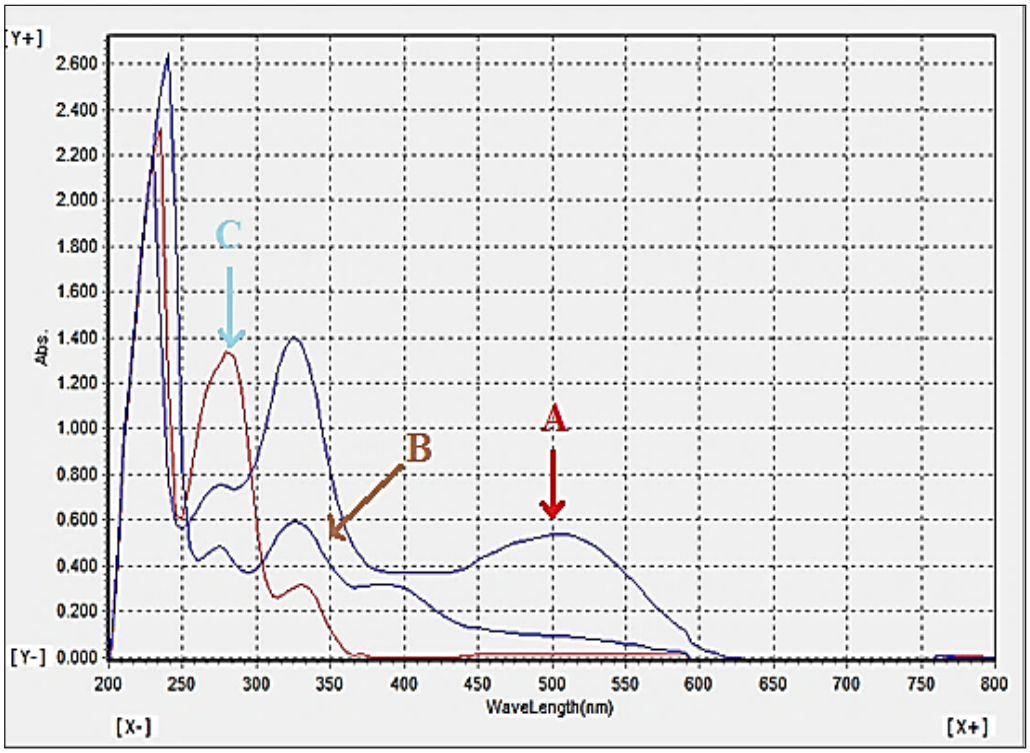

Fig. 10. Absorption spectrum of charge transfer complex (**A**), Azo reagent spectrum (**B**) and Schiff base-Minoxidil spectrum (**C**) versus blank

3.4. The analytical approach

Using the synthesized reagent, quick and straightforward spectroscopic techniques were created to estimate minoxidil. The ideal circumstances and the maximum wavelength for the complex (effects of various reagent types on CT complex absorption, temperature, time, and buffer solution) were investigated.

3.4.1.Impact of different reagent types on CT complex absorption

Several receptor reagents were used to obtain the detector that gave the best peak. As shown in Table 3. The azo reagent showed the highest absorption compared to other acceptor reagents, so it was adopted in other experiments.

Table 3. Impact of different reagent types on CT complex absorption

Reagent	max (nm)ג	Abs
8-hydroxy quinoline	372	0.143
2,3-dichloro-5,6-dicyano-1,4-benzoquinone	425	0.134
Chloranail	540	0.060
1-(4-hydroxy-3-((4-nitrophenyl) diazenyl) phenyl) ethan-1	505	0.358

3.4.2.Effect of azo reagent size

The optimal size of the azo reagent was studied, where different volumes ranging from (0.5-2.5) ml of the reagent were withdrawn. Then 0.5 ml of 100 µg/ml Schiff base-minoxidil was added. The solution was transferred to a 10 ml volumetric flask, and the volume was completed with ethanol; the absorbance was measured at a 505 nm wavelength. Absorption values were recorded in Table 4. The highest absorption value was at 1 ml of the reagent, which was adopted in subsequent experiments.

3.4.3.Effect of acid and base

Increasing amounts of base and acid were added to determine the optimal pH of the complex, as shown in Table 5. It was noted that adding a base or acid decreases absorption, so adding a buffer solution was excluded.

3.4.4.Effect of temperature

The effect of temperature on the resulting complex was studied over a wide range of temperatures to choose the optimal temperature that gives the best absorption, as shown in Table 6. The optimal temperature is 25 degrees Celsius.

3.4.5.The effect of time

The effect of time on the stability of the CT complex was studied by measuring the absorption versus the blank solution for different periods and under the same conditions as the previous experiments, as shown in Table 7. The table clearly shows that the complex has high stability for up to 30 minutes.

Table 4. Effect of azo reagent size on Abs

Volume of reagent + 0.5ml Schiff drug (100 µg mL^{-1})	Abs
0.5	0.358
1.0	0.520
1.5	0.513
2.0	0.439
2.5	0.342

Table 5. Effect of acid and base on Abs

	HCl (0.1M) VmL	Abs	NaOH (0.1M) VmL	Abs
Charge transfer complex	0	0.520	0	0.520
	0.1	0.026	0.1	0.092
	0.2	0.008	0.2	0.054
	0.3	----	0.5	0.032

Table 6. Effect of temperature

Temperature(C°)	Abs
5	0.507
10	0.515
15	0.518
20	0.519
25	0.520
30	0.516
35	0.513
40	0.512
45	0.510
50	0.498

Table 7. The effect of time

Min	0	5	10	15	20	25	30	35	40	45	50	55	60
Abs	0.520	522	520	520	520	521	0.518	0.516	0.513	0.510	0.506	0.502	0.493

3.4.6. Calibration curve

The calibration curve was prepared by taking increasing volumes of the Schiff base-minoxidil and the reagent (0.1-2.0 mL). The previous conditions were applied to each complex, and the volumes were completed to the mark with ethanol. Then, the absorbance of the solutions was measured at the specific wavelength of 505 nm, as shown in Figure 11, where the linearity range is from 1 to 12.5 µg mL^{-1}, and the estimation factor range is 0.9979 [39].

3.4.7. Accuracy and precision

The method's accuracy and precision were tested by calculating the average of Recovery% and RSD% and under optimal conditions by taking five readings for three different concentrations of the Schiff base-Minoxidil within the limits of Beer's Law in the calibration curve, which gave 102.4705% to the average of Recovery% and 0.092312 ≥ to RSD% no more than, as shown in Table 8. The detection and quantitative limits were calculated by taking five readings of the blank solution's absorbance to identify the standard deviation value. Table 9 shows the computed values [40].

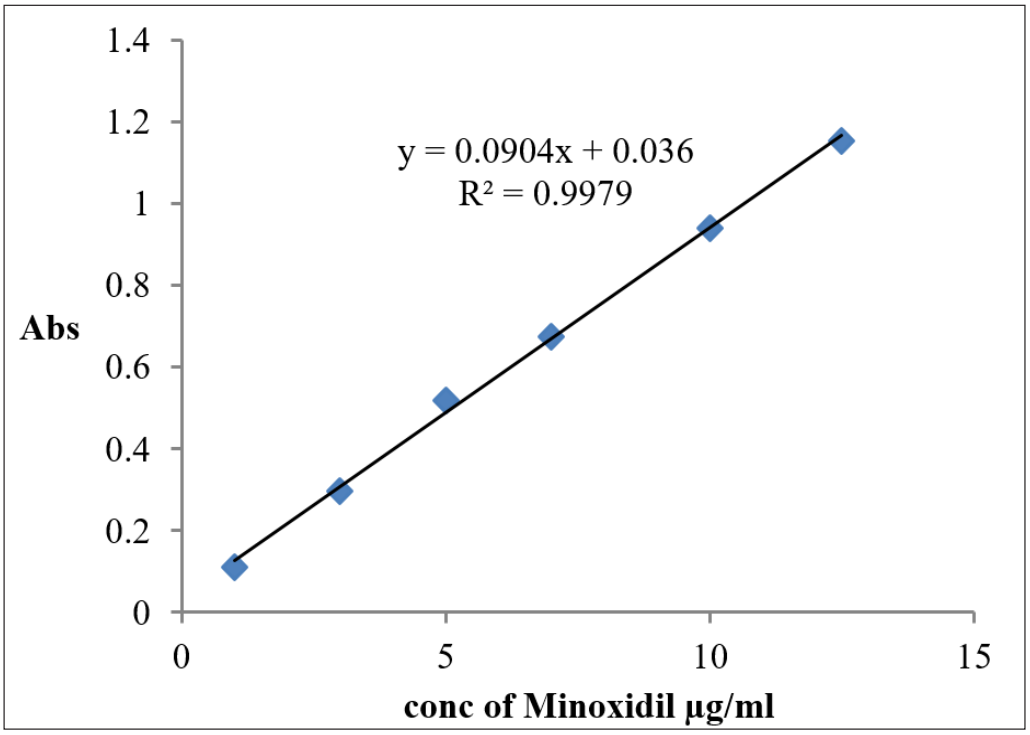

Figure 11. Calibration curve for CT complex

Table 8. Accuracy and precision

Taken (µg mL^{-1})	Abs	Found (µg mL^{-1})	R%	Average of Recovery%	RSD%
3	0.310	3.0331	101.1062	102.4705	0.0923
7	0.705	7.4026	105.7522		0.0378
10	0.945	10.0553	100.5531		0.0278

Table 9. The detection limit and quantitative limit

Slope	SD	LOD (µg mL^{-1})	LOQ (µg mL^{-1})
0.0904	0.0028	0.1019	0.3089

3.5. Stoichiometry to CT complex

To determine the rate and nature of the compound bonding, the molar ratios and continuous changes (JOB) methods were performed as follows:

3.5.1.Molar ratio method

It involved taking azo reagent concentrations increasing in quantities (0.25-2.5 mL) of 1x 10^{-4} M into a series of 10 mL volumetric flasks; a fixed volume of 1 mL of Schiff base-Minoxidil solution was added at the same concentration, 1x 10^{-4} M, and the volume was finished to the appropriate level [41]. Also, many other nanotechnology methods are used to determine organic compounds by GC-MS or GC-FID [42-45]. Then 5 minutes passed, at a wavelength of 505 nm, the absorbance values were measured concerning the blank solution, showing a ratio of 1:2, as shown in Figure 12.

3.5.2.Continuous changes method (Job method)

It included taking different volumes of azo reagent (0.1-0.9 mL) (1 x 10^{-4} M) into a series of 10 mL volumetric flasks. Then volumes (0.9-0.1) mL of Schiff base-minoxidil solution (1 x 10^{-4} M) were added so that the final volume of the reagent and the Schiff-Drug was 1 ml; the volume was completed to the mark [46]. Then, after 5 minutes, the absorbance values were recorded against the blank solution at 505 nm of wavelength, where the ratio was 1:2, as shown in Figure 13.

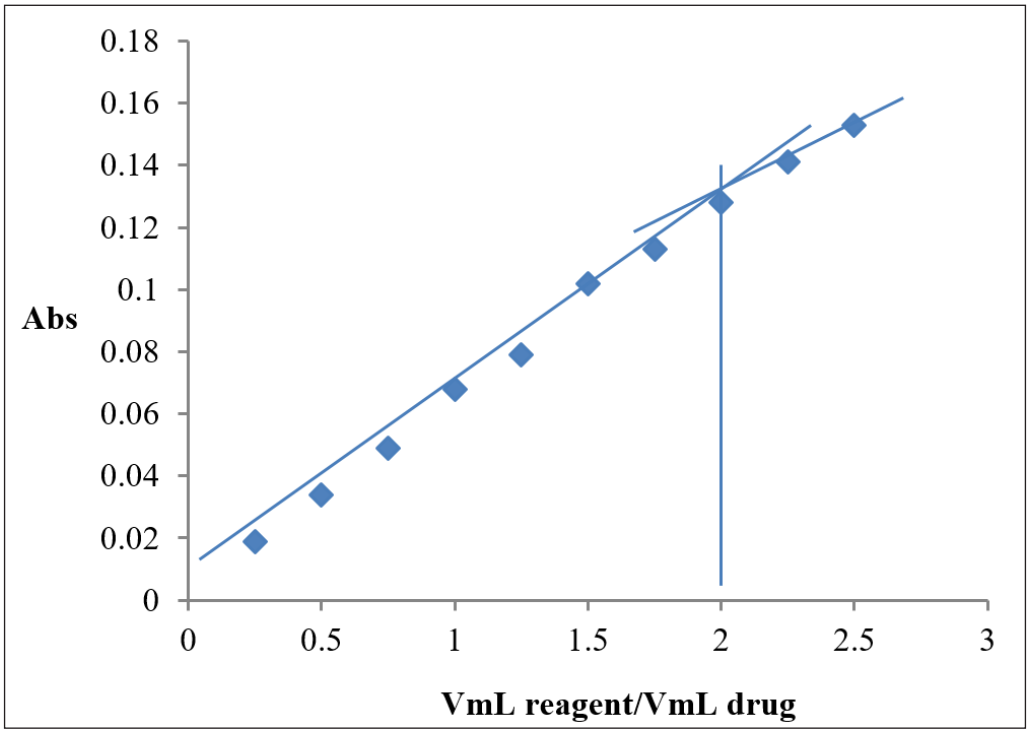

Fig. 12. Curve of the molar ratio method for the determination of CT complex

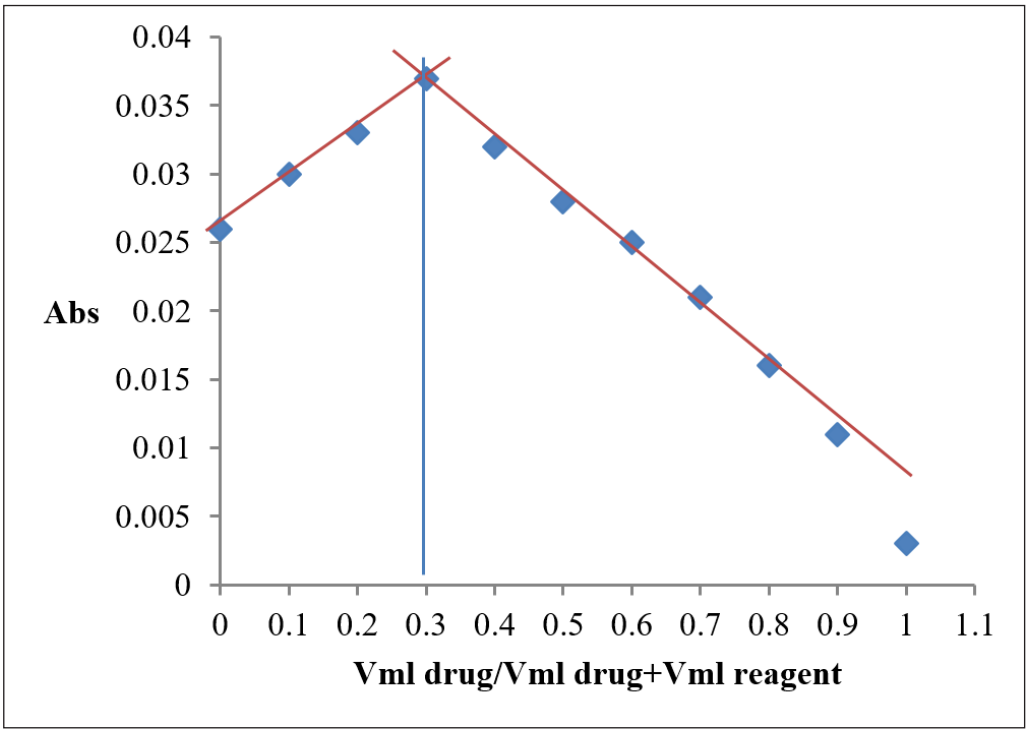

Fig. 13. Curve of the Job method for the determination of CT complex

3.5.3.Application of the method

Theproposedmethodwasappliedtothepharmaceutical preparation of Schiff base-minoxidil, where three different concentrations (4, 6, and 8) µg mL^{-1} were taken from the preparation with a concentration of 100 µg mL^{-1} by withdrawing volumes of 0.4, 0.6, and 0.8 ml, respectively, into a 10 mL volumetric flask under the same conditions, then adding ethanol to the volume to the required level. The solutions' absorbance was measured at a wavelength of 505 nm, where the value of the average of recovery% reached 100.852% in the pharmaceutical preparation, and the value of the RSD% did not exceed 0.0111%, as shown in Table 10.

3.5.4.Summary of optical characteristics for the method proposed

The analytical characteristics for determining minoxidil by the charge transfer complex method and at the optimum conditions are summarized in Table 11.

Table 10. Application of the method for the determination of Minoxidil in a pharmaceutical preparation (µg mL^{-1})

Pharmaceutical preparation	Abs	Found	R%	RSD%
4	0.400	4.0309	100.7743	0.0694
6	0.583	6.0575	100.9587	0.0462
8	0.767	8.0951	101.1892	0.0345

Table 11. The analytical parameters

Parameter	Value
λmax nm	505
Beer's Law Limit (μg mL^{-1})	1-12.5
Molar Absorptivity ($Lmol^{-1}cm^{-1}$)	$1.8916x10^4$
Limit of Detection (μg mL^{-1})	0.1019
Limit of Quantification (μg mL^{-1})	0.3089
Slope	0.0904
Intercept	0.036
Correlation Coefficient (R^2)	0.9979
Sandell's Sensitivity (μg cm^{-2})	0.0110
% RSD	0.0923%≤
Average of % Recovery	102.4705%

4. Conclusion

A simple, rapid, and sensitive method for determining minoxidil in pharmaceuticals. Mixing the Schiff base of the drug with the azo reagent gave a stable red complex that showed a maximum absorption peak at 505 nm compared to the blank solution. Beer's law demonstrated linearity within the 1-12.5 μgmL^{-1} concentration range, with a molar absorptivity of $1.8916x10^4$ L mol^{-1} cm^{-1}. The RSD% was discovered to range from 0.0278% to 0.0923%. The recommended method for detecting minoxidil in pharmaceutical samples has the benefits of being inexpensive, straightforward, and sensitive. The technique was effectively used for determination in pharmaceuticals.

5. Acknowledgements

The authors thank the Department of Chemistry, College of Science, University of Anbar, Ramadi, Anbar, Iraq and University of Samarra, Iraq

6. References

[1] R.S. Mulliken, Molecular compounds and their spectra. II, J. Am. Chem. Soc., 74 (1952) 811-824. https://doi.org/10.1021/ja01123a067

[2] J.N. Murrell, The theory of charge-transfer spectra, Quarterly Rev. Chem. Soc., 15 (1961) 191-206. https://doi.org/10.1039/QR9611500191

[3] J. Weiss, The formation and structure of some organic molecular compounds, J. Chem. Soc., (1942) 245-252. https://doi.org/10.1039/JR9420000245

[4] H. Miyasaka, Control of charge transfer in donor/acceptor metal–organic frameworks, Accounts Chem. Res., 46 (2013) 248-257. https://doi.org/10.1021/ar300102t

[5] Y. Kato, H. Matsumoto, T. Mori, Absence of HOMO/LUMO transition in charge-transfer complexes of thienoacenes, J. Phys. Chem., A 125 (2021) 146-153. https://doi.org/10.1021/acs.jpca.0c08925

[6] G.R. Anderson, Symmetry classification and selection rules for some electron donor-acceptor complexes, J. Am. Chem. Soc., 92 (1970) 3552-3560. https://doi.org/10.1021/ja00715a005

[7] D. Booth, Charge-transfer molecular complexes and their role in chemical reactions, Sci. Progress, 48(1960) 435-455. https://www.jstor.org/stable/43417573

[8] A. Müllertz, T. Rades, Evaluating oral drug delivery systems: dissolution models, Springer Publisher, Anal. Tech. Pharm. Sci., (2016) 753-771. https://doi.org/10.1007/978-1-4939-4029-5

[9] C. Arrell, L. Longetti, M. Chergui, J. Helbing, Charge-transfer and impulsive electronic-to-vibrational energy conversion in ferricyanide: Ultrafast photoelectron and transient infrared

studies, Phys. Chem. Chem. Phys., 19 (2017) 17052-17062. https:// doi.org/ 10.1039/ C7CP03337K

[10] S. S. Swayamprabha, D. K. Dubey, Shahnawaz, R.A.K. Yadav, M.R. Nagar, A. Sharma, F. Tung, J. Jou, Approaches for long lifetime organic light emitting diodes, Adv. Sci. 8 (2021) 2002254. https://doi.org/10.1002/advs.202002254

[11] H.J. Kim, T. Yasuda, Narrowband emissive thermally activated delayed fluorescence materials, Adv. Optic. Mater., 10 (2022) 2201714. https:// doi.org/ 10.1002/adom.202201714

[12] A. Hillier, G. Mao, Charge-transfer complexes: Fundamentals and advances in catalysis, Sensing, and optoelectronic applications, Adv. Mater., 36 (2024) 2406083. https://doi.org/10.1002/adma.202406083

[13] M. Cai, C. Shang, F. Bi, F. Feng, Z. Du, C. Sun, Y. Li, X. Bao, Regulating intramolecular charge transfer and resonance effects to realize ultrawide bandgap conjugated polymer for high-performance all-Polymer solar cells, Adv. Funct. Mater., 33 (2023) 2301701. https://doi.org/10.1002/adfm.202301701

[14] M. Waqas, Z. Aloui, M. Essid, M. Ibrahim, R. Khera, M. Shaban, M. Ans, Exploring the electronic, optical, and charge transfer properties of ADA-type IDTV-ThIC-based molecules to enhance photovoltaic performance of organic solar cells, ACS Omega, 8 (2023) 45384-45404. https://doi.org/10.1021/acsomega.3c04437

[15] L. Liu, S. Zhao, S. Yang, D. Si, Q. Wu, Q. Wu, Y. Huang, R. Cao, Rapid charge transfer in covalent organic framework via through-bond for enhanced photocatalytic CO_2 reduction, Chem. Eng. J., 458 (2023) 141360. https://doi.org/10.1016/j.cej.2023.141360

[16] W. Jung, S. Gonzalez-Carrero, J. Durrant, H. Cha, T. Park, Understanding charge carrier dynamics in organic photocatalysts for hydrogen evolution, Energ. Environ. Sci., 17(2024) 7999-8018. https://doi.org/10.1039/D4EE01808G

[17] Liu, L. Fu, J. Liu, M. Wang, J. Zhou, Structure regulation of 2D materials by atom confinement for electrocatalysis, Coord. Chem. Rev., 520 (2024) 216164. https://doi.org/10.1016/j.ccr.2024.216164

[18] S. Mal, S. Bhattacharyya, Deciphering interfacial charge transfer mechanisms in electrochemical energy systems through impedance spectroscopy, J. Mater. Chem. A, 12 (2024)14334-14353. https://doi.org/10.1039/D4TA00537F

[19] M. Islam, S. K. Mustafa, A. Alessa, M. Al Ahjohani, N. Omer, R. Jame, I. Alatawi, M. Sagheer, Analysis the formation of H-bonded charge transfer complex of M-nitroaniline with oxalic acid in ethanol: Investigation its antimicrobial studies, DNA binding and molecular docking, DNA binding and molecular docking, Available at SSRN 4791207. https:/ /dx.doi.org/ 10.2139/ ssrn.4791207

[20] M.S. Refat, A.M. Alsuhaibani, M. Islam, Biological and computational exploration of a hydrogen-bonded charge transfer complex between 8-Hydroxyquinoline and Benzene-1, 4-diol in different polar solvents: synthesis and spectrophotometric analysis, Available at SSRN 4847578. https://dx.doi.org/10.2139/ssrn.4847578

[21] N. Alam, M. Islam, H. Najnin, S. Shakya, I. Khan, M. Hossain, R. Zaidi, Design and characterization of a binary CT complex of imidazole-oxyresveratrol: exploring its pharmacological and computational aspects, J. Biomol. Struct. Dyn., 42 (2024) 1319-1335. https://doi.org/10.1080/07391102.2023.2199088

[22] A. Radwan, N. Alzoman, I. Darwish, Formation and characterization of charge transfer complex between alectinib and 2, 3-dichloro-5, 6-dicyano-1, 4-benzoquinone: Application to development of microwell spectrophotometric method, Sustain. Chem. Pharm., 39 (2024) 101524. https://doi.

org/10.1016/j.scp.2024.101524

[23] A. Nies, Minoxidil, Ann. Intern. Med., 94 (1981) 61-65. https://www.acpjournals.org/doi/abs/10.7326/0003-4819-94-1-61

[24] N. Farjo, S. Picksley, V. Randall, Human hair follicles contain two forms of ATP-sensitive potassium channels, only one of which is sensitive to minoxidil, FASEB J., 22 (2008)1725-1736. https://doi.org/10.1096/fj.07-099424

[25] G.R. Zins, The history of the development of minoxidil, Clin. Dermatol., 6 (1988) 132-147. https:// doi.org/ 10.1016/ 0738-081X(88)90078-8

[26] M. Talukder, G. Williams, Comparison of oral minoxidil, finasteride, and dutasteride for treating androgenetic alopecia, J. Dermatol. Treat., 33 (2022) 2946-2962. https://doi.org/10.1080/09546634.2022.2109567

[27] M.G. Fraile, Theoretical characterization of new dynamic bonds for responsive materials and their optical properties, Diss. Universidad del País Vasco-Euskal Herriko Unibertsitatea, 2023. https://dialnet.unirioja.es/servlet/tesis?codigo=322971

[28] Y. Tang, G. Han, Recent advances in the synthesis of aromatic azo compounds, Molecules, 28 (2023) 6741. https://doi.org/10.3390/molecules28186741

[29] I. Mushtaq, M. Ahmad, M. Saleem, A. Ahmed, Pharmaceutical significance of Schiff bases: An overview, Futur. J. Pharm. Sci., 10 (2024) 16. https://doi.org/10.1186/s43094-024-00594-5

[30] L. Ahamed, S. AL-Khazraji, Synthesis, characterization, and study of anticancer activities of new Schiff bases and 1, 3-oxazepine containing drug, Russ. J. Bioorg. Chem., 50 (2024) 28-33. https://doi.org/10.1134/S1068162024010102

[31] H. Nassar, M. Abou-El-Wafa, H. Elkik, Synthesis and characterization of some coordinated metal and charge transfer complexes of isonicotinic acid hydrazide ligand with 2-hydroxyacetophenonylidene, Spectrochim. Acta A: Mol. Biomol. Spectrosc., 309 (2024) 123759. https://doi.org/10.1016/j.saa.2023.123759

[32] M. Ayaz, A. Alam, Zainab, A. Elhenawy, N. Rehman, S. Rahman, M. Ali, Abdul Latif, A. Al-Harrasi, M. Ahmad, Designing and synthesis of novel fexofenadine-derived hydrazone-Schiff bases as potential urease inhibitors: In-vitro, molecular docking and DFT investigations, Chem. Biodivers., 21 (2024) e202400704. https://doi.org/10.1002/cbdv.202400704

[33] F. Dai, Q. Zhuang, G. Huang, H. Deng, X. Zhang, Infrared spectrum characteristics and quantification of OH groups in coal, ACS Omega, 8 (2023) 17064-17076. https://doi.org/10.1021/acsomega.3c01336

[34] L.A. Mohammed, R. T. Mehdi, A. A. Mohammed Ali, Synthesis and biological screening of the gold complex as anticancer and some transition metal complexes with new heterocyclic ligand derived from 4-Amino Antipyrine, Nano Biomed., 10 (2018) 199-212. https://doi.org/10.5101/nbe.v10i3.p199-212

[35] S. O. Aljazzar, Composition and decomposition of several Schiff base metal complexes containing Co (II) and Ni (II) ions: Spectroscopic analysis, Mor. J. Chem., 12 (2024) 180-198. https://doi.org/10.48317/IMIST.PRSM/morjchem-v12i1.43061

[36] F. Naaz, S. Shakya, M. Islam, A. Khan, M. Ahmad, Photocatalytic activity, DFT/TD-DFT, and spectrophotometric studies of a synthesized charge transfer complex of p-toluidine with 1, 2, 4, 5-benzenetetracarboxylic acid in various polar solvents, J. Mol. Liq., 399 (2024) 124412. https://doi.org/10.1016/j.molliq.2024.124412

[37] D. Ivanov, Y. Yang, Mass spectrometry-based methods to characterize highly heterogeneous biopharmaceuticals, vaccines, and nonbiological complex drugs at the intact-mass level, Mass Spect. Rev., 43

(2024) 139-165.https://doi.org/10.1002/mas.21829

[38] S. Munusamy, M. Saravanakumar, M. Sekar, K. Muthusamy, M. Kumar, G. Vinitha, Exploring the structural and optical characteristics of the charge transfer complex 2, 3-dimethylquinoxaliniumpicrate: a comprehensive investigation through experimental and computational approaches, J. Mater. Sci.: Mater. Electron., 35 (2024) 1314. https://doi.org/10.1007/s10854-024-12989-4

[39] N. Alalam, S. Bashir, Analytical applications of some N, NBPAD Schiff's base for spectrophotometric determination of Chromium (VI), Chem. Res. J., 9 (2024) 86-93. https:// doi.org/ 10.5281/zenodo.11275451

[40] M. Al Mufty, M. Hailat, R. Awad, M. Awad, M. Hamad, Development and validation of a method for analyzing the combination of etoricoxib and acetaminophen in tablet dosage form, J. Hunan Univ. Nat. Sci., 51 (2024) 1-13.https://doi.org/10.55463/issn.1674-2974.51.5.1

[41] A. Amin, A. Gouda, R. Sharaf, A. Elkhashab, G. Elasala, Validated spectrophotometric methods for determination of selegiline HCl as an irreversible inhibitor of monoamine oxidase in pure form and pharmaceutical formulations, TWIST Int. Multidiscip. J., 19 (2024) 176-186. https://twistjournal.net/twist/article/view/156

[42] Sh. Teimoori, H. Shirkhanloo, A. Hassani, M. Panahi, N. Mansouri, Toxicological profile for ethylbenzene, benzene and xylene, Food Chem., 421 (2023) 136229. https://doi.org/10.1016/j.foodchem.2023.136229

[43] J. Rakhtshah, H. Shirkhanloo, N. Esmaeil, A rapid extraction of toxic styrene from water and wastewater samples based on hydroxyethyl methylimidazolium tetrafluoroborate immobilized on MWCNTs by ultra-assisted dispersive cyclic conjugation-micro-solid phase extraction Author links open overlay panel, Microchem. J., 170 (2021) 106759. https://doi.org/10.1016/j.microc.2021.106759

[44] S. Teimoori, A. H. Hassani, M. Panahi, N. Mansouri, An immobilization of aminopropyl trimethoxysilane-phenanthrene carbaldehyde on graphene oxide for toluene extraction and separation in water samples, Chemosphere, 316 (2023) 137800. https://doi.org/10.1016/j.chemosphere.2023.137800

[45] S. Teimoori, A. H. Hassani, M. Panahi, N. Mansouri, Rapid extraction of BTEX in water and milk samples based on functionalized MWCNTs by dispersive homogenized-micro-solid phase extraction, Food Chem., 421 (2023) 136229. https://doi.org/10.1016/j.foodchem.2023.136229

[46] A.M. Ali, M. Abdulzahra, M. Abdali, Spectrophotometric determination of gancyclovir drug by combination reaction with NQS as a reagent, AIP Conf. Proc., 3092 (2024) 030007. https://doi.org/10.1063/5.0199700

Anal. Methods Environ. Chem. J. 8 (1) (2025) 133-151

AMECJ

Research Article, Issue 1
Analytical Methods in Environmental Chemistry Journal
Journal home page: www.amecj.com/ir

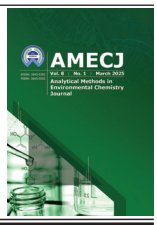

Analysis of BTEX in ambient air using gas chromatography-flame ionization detector to assess health risks

Ahmad Zarei-chargoud [a], Ali Faghihi- Zarandi [b,*],and Maryam Faraji [c,d,*]

[a]Student Research Committee, Kerman University of Medical Sciences, Kerman, Iran.
[b] Department of Occupational Health Engineering and Safety at Work, Faculty of Public Health, Kerman University of Medical Sciences, Kerman, Iran.
[c] Environmental Health Engineering Research Center, Kerman University of Medical Sciences, Kerman, Iran.
[d]Department of Environmental Health Engineering, Faculty of Public Health, Kerman University of Medical Sciences, Kerman, Iran.

ARTICLE INFO:

Received 8 Oct 2024
Revised form 29 Dec 2024
Accepted 4 Feb 2025
Available online 29 March 2025

Keywords:
BTEX,
Analysis,
Gas chromatography flame ionization detector,
Ambient air

ABSTRACT

The United States Environmental Protection Agency (USEPA) classified benzene, toluene, ethylbenzene, and xylene (BTEX) as a hazardous air pollutant (HAPs). This study aimed to investigate the spatiotemporal variations of BTEX and its health risks in the ambient air of Kerman, Iran. Sampling was actively done using the NIOSH-1501 standard method in 2022. BTEX compounds were analyzed in the laboratory using a gas chromatography flame ionization detector (GC-FID). The effect of BTEX on tropospheric ozone production has been investigated through the calculation of the ozone formation potential (OFP). The average BTEX concentrations during winter and summer were analyzed using GC-FID, resulting in the following order: xylene > toluene > benzene > ethylbenzene. The average total concentration of benzene, toluene, ethylbenzene, and xylene compounds was 29.87, 103.34, 16.89, and 109.44 µg m^{-3}, respectively. In general, the concentration of BTEX in winter was higher than in summer. Due to the average OFP, total BTEX compounds were obtained to be 908.80 µg m^{-3} and 376.48 µg m^{-3} in winter and summer, respectively. The non-cancer risk was at a safe level of less than one (HQ<1) in both seasons. The carcinogenicity of benzene in summer and winter was found to be 7.55×10^{-5} and 1.76×10^{-4}, which is more than the recommended limit of EPA. Motor vehicles were Kerman's main potential sources of BTEX in the study period. Based on the results, it can be concluded that motor vehicles were the main potential sources of BTEX in Kerman during the study period. Therefore, based on the BTEX analysis, gasoline control, green space development, and public transportation can be suggested to diminish the number of BTEXs in Kerman City.

1. Introduction

Air pollution has received much attention over the past decade, mainly caused by traffic and industrial and residential activities [1]. It is one of the most prominent threats to public health and the environment in developed and developing countries due to the industrialization and growth of urban populations resulting from the migration to cities [2, 3]. Air pollution and its impacts on public health have raised significant concerns among the World Health Organization (WHO), environmental regulatory agencies, and the general

*Corresponding Author: A. Faghihi Zarandi and M. Faraji
Email: alifaghihi60@yahoo.com; m.faraji@kmu.ac.ir
https://doi.org/10.24200/amecj.v8.i01.1028

public [4]. Air pollutants are typically classified into particulate matter and gaseous contaminants. Gaseous pollutants consist of sulfur dioxide (SO_2), carbon monoxide (CO), nitrogen dioxide (NO_2), volatile organic compounds (VOCs), and ozone (O_3) [5,6]. The most prevalent VOCs are benzene, toluene, ethylbenzene, and xylene (BTEX). Natural sources of BTEX included volcanic eruptions, forest fires, and biomass burning, which emitted them in small amounts [7]. Motor vehicles, fuel stations, and industrial processes are the human sources of BTEX in urban air[8]. When BTEX compounds interact with atmospheric NO2, they undergo reactions that produce tropospheric O_3 and various other harmful compounds [9]. Exposure to tropospheric O_3 may result in asthma, reduced lung capacity, coughing, shortness of breath, and eye discomfort[10]. The significance of VOC species in O_3 production is primarily determined by the ozone formation potential (OFP), which quantifies the ozone volume generated per unit mass of emitted VOCs [10]. OFP is influenced by temperature, solar radiation, wind speed, other climatic factors, and the concentration of volatile organic compounds (VOCs) and their reactions in the surrounding air [11,12]. Ozone isn't released directly; instead, it forms through the interaction of VOCs and nitrogen oxides (NOx) when exposed to sunlight in a process known as photochemical reactions. The production of ozone in the lower atmosphere, namely tropospheric ozone, is considered a worldwide air pollution challenge [13] that negatively impacts the environment and human health. Ozone presents a significant risk to the vegetation, including crops and ecological plants, affecting their physiological functions at various levels [14]. The short-term effects of ozone exposure are irritation of the respiratory system, inflammatory processes, cough, shortness of breath, headaches, and inflammation of the mucous membranes. Its long-term consequences, such as asthma, bronchitis, and other respiratory diseases, as well as a decrease in lung function, can be mentioned [10,15,16]. Different types of VOCs have different potential for ozone formation due to the unique chemical behavior of each species. Therefore, identifying VOCs is essential in terms of quantity and quality as potential contributors to ozone formation in an area. This process aids in comprehending how ozone is produced and assists in determining effective strategies for managing and controlling VOC emissions [13]. BTEX compounds have been classified as hazardous air pollutants (HAPs) by the US Environmental Protection Agency (USEPA)[17, 18,19]. Contact and inhalation are the primary pathways to BTEX exposure [20]. Acute and chronic exposure to these compounds can cause severe adverse health effects, including leukemia, brain damage, birth defects, allergies, inflammation of the skin and central nervous system, eye irritation, and breathing problems [21]. The national maximum annual benzene concentration is 5.0 µg m^{-3}[22]. Many studies have been conducted to assess ambient BTEX concentration levels and analyze their impact on human health [1,23-26]. In research by Kermani et al., levels of BTEX compounds, spatial and seasonal distribution, sources, and health risks were explored in Tehran, Iran [27]. Dehghani et al. researched the characteristics and health effects of BTEX in the bus terminal in Shiraz, Iran [28]. Maleky et al. assessed the concentration, spatiotemporal variation, and health risk of BTEX in the ambient air of Zarand, an industrial city in southeast Iran [26]. Caselli et al. investigate BTEX compounds and the impact of vehicle traffic on air quality in the main roads in Italy [29]. Given the mentioned health effects and the multiple sources of BTEs, it is essential to measure the concentration of these compounds, assess exposure levels, and investigate their impact on the health of exposed individuals. This study aimed to determine the amounts of BTEX and OFP from BTEX compounds in Kerman City's ambient air. This study aimed to assess the health risks, identify potential sources, and analyze the spatial distribution of the BTEXs in Kerman City, Iran, as the first investigation.

2. Materials and Methods

2.1. Study area

Kerman city (30° 28' N, 57° 08' E), the capital of Kerman province, is in southeast Iran. As of the 2015 census, the city had a population of approximately 738,000 people, covering an area of nearly 240 square kilometers. This city is located in an arid and semi-arid region at 1756 meters above sea level. The average air temperature ranges between -8 and 37°C, respectively. Twenty sampling points were selected at all five urban areas across the city. Sampling points are illustrated in Figure 1.

2.2. Sampling and Analysis

This descriptive-analytical study was conducted in 20 stations in Kerman City for two months in the summer and winter of 2022. Active sampling was done using the NIOSH-1501 standard method, using an SKC sampling pump with a flow rate of 0.3 liters per minute for 2 hours between 7 and 9 am at 1.5 meters above the ground level using activated carbon adsorbent tubes. Each station was sampled twice. In this way, at the sampling sites, the two ends of the adsorbents were broken and connected to the calibrated sampling pump using the connecting tube. After the end of the sampling, the two heads of adsorbents were closed with a plastic cap. Samples were transported to the laboratory and kept at 4°C until analysis. BTEXs were first extracted in the laboratory for chemical analysis with 1 mL of carbon disulfide (CS2). Extracted BTEXs were analyzed via a gas chromatography flame ionization detector (GC-FID, 5890 Series GC-FID from Agilent Technologies Inc., Santa Clara, CA, USA). Details of the GC-FID analysis are reported in Table 1. Also, some different methods were used to determine BTEX in water samples using GC-FID and GC-MS analyzers[30-39].

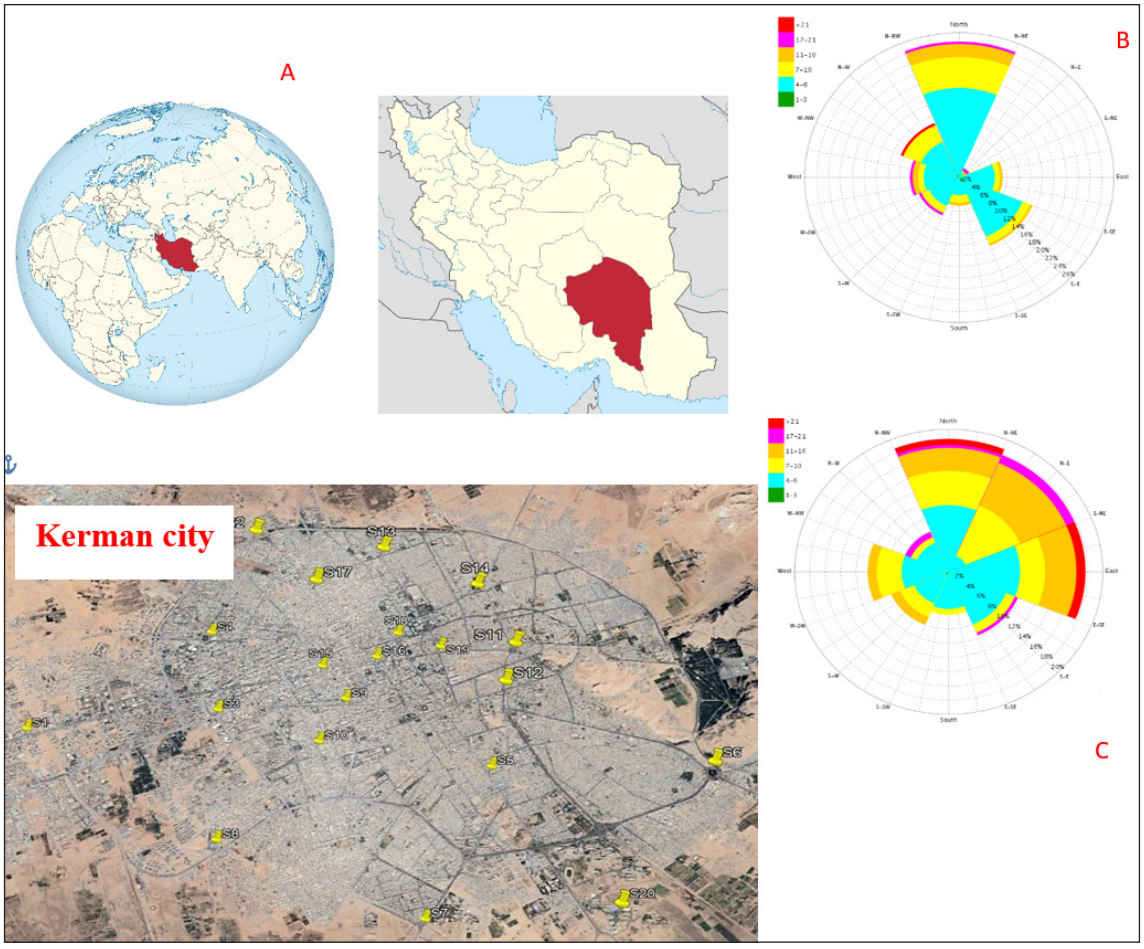

Fig.1. The study area (a) as well as wind rose in winter (b) and summer (c)

Table 1. Details of the GC-MS analysis

Characteristics	Description
Column model	HP5
Column characteristics	30 m × 0.32 mm × 0.25 µm
Carrier gas	N2 (purity 99.995%) with a flow rate of 1.5 mL min^{-1}
Injection port temperature	250-300 ºC
Oven temperature	40ºC for ٤ min and increased with a rate of 3ºC to 80ºC per min

2.3. Quality assurance and control (QA/QC)

The BTEX standard used was manufactured by Sigma Aldrich and measured 1 × 1 mL with 2000 µg mL^{-1} in methanol. Techniques for quality control and assurance were applied throughout the entire analytical process. Five standard solutions with different concentrations were used to do the calibrations. A blank sample was given before and after each of the three samples. After completing linear calibrations, the BTEX were located by comparing their area and retention times with standard values. The relevant calibration curves, a limit of detection (LOD), and a limit of quantification (LOQ) were obtained, $R^2 > 0.97$, 0.01 µg m^{-3}, and 0.03 µg m^{-3} for all BTEX chemicals, including benzene, toluene, ethylbenzene, and xylene.

2.4. Statistical Analysis

The data was reported as the mean±standard deviation of BTEX and OFP. An ANOVA analysis was employed to compare the average concentrations of BTEXs between two seasons. Various methods were used to identify the sources of BTEX, including correlation analysis, principal component analysis (PCA), and evaluations of inter-species relationships among compounds. These methods were used to illustrate the correlation patterns among species, identify the primary causal factor, and determine the sources of pollutant emissions. The statistical analysis was performed using R software version 3.6.2, and a p-value of less than 0.05 was defined as the significance level.

2.5. Spatial Analysis

Spatial distribution refers to the visualization of areas with specific characteristics. To illustrate BTEX's spatial distribution in the study area, we employed ArcGIS 10.8.2 software and the Inverse Distance Weight (IDW) interpolation method. In environmental research, the IDW technique is commonly used to evaluate the spatial dispersion of environmental pollutants. This method forecasts the levels of environmental contaminants at unsampled sites by relying on data collected from other designated sampling points [26].

2.6. Ozone formation potential

The calculation of OFP involves utilizing both the concentration of BTEX and the MIR (Maximum Incremental Reactivity) coefficient. Carter's first calculation of the MIR coefficient in 1994 was updated in 2009. These modifications aimed to refine its application in assessing the quantity of ozone generated per unit of emitted VOCs. Equation 1 utilizes the adjusted MIR coefficients for benzene, toluene, ethylbenzene, and xylene, which are set at 0.69, 3.88, 2.93, 7.44, and 7.4, respectively [40].

$$\text{OFP } (\mu g\ m^{-3}) = \text{BTEX Concentration } (\mu g\ m^{-3}) \times \text{MIR (g O3 per g VOCs)} \quad \text{(Eq.1)}$$

2.7. Health risk assessment

The non-carcinogenic and carcinogenic risks of BTEX compounds from the inhalation route were assessed based on USEPA guidelines using two indicators: The Hazard Quotient (HQ) is a risk ratio used to evaluate non-carcinogenic risks associated with exposure to certain substances. Incremental Lifetime Cancer Risk (ILCR) represents the probability of developing cancer over a person's lifetime due to exposure to specific carcinogens [41]. Notably, the non-carcinogenic risk was

calculated for all four compounds in the present study. Still, cancer risk calculations were specific to benzene due to its classification as a definite carcinogen [42,43]. To evaluate the human health risks associated with BTEX compounds through the inhalation route, exposure levels were assessed using Equations (2-5). The risk parameters used for ILCR and HQ assessments are defined in Table 2.

$$EC = (C \times ET \times ED \times EF) / AT \quad \text{(Eq.2)}$$

$$CDI = (C \times IR \times EF \times ED \times CF) / (BW \times AT) \quad \text{(Eq.3)}$$

$$LTCR = CDI \times CSF \quad \text{(Eq.4)}$$

$$HQ = EC/RFC \quad \text{(Eq.5)}$$

A Hazard Quotient (HQ) less than 1 suggests the absence of potential non-carcinogenic effects. At the same time, an HQ of more than 1 indicates the potential occurrence of non-carcinogenic effects in the exposed population. The calculated carcinogenic risk level is compared against the EPA's recommended maximum acceptable risk, typically set at 10^{-4} or 10^{-6}, representing the thresholds considered acceptable for risk related to cancer [26].

3. Results and Discussion

3.1. BTEX characteristics in the ambient air

The BTEX concentrations measured in the current study are shown in Table 3. During the summer season, the total BTEX levels measured were 78.19±46.75 µg m^{-3}, while in the winter, they were found to be 181.34±69.73 µg m^{-3}. The BTEX concentration measured during the summer and winter sampling periods was 259.54±81.05 µg m^{-3}. The average levels of all BTEX compounds were higher during winter than summer. However, based on the ANOVA analysis (Table 3), the observed mean difference between the two sampling seasons was not statistically significant. Studies in China, France, Turkey, Tehran, and South Pars Jam in Iran have reported similar results consistent with our findings [22,43-47]. The higher concentration of BTEX in the winter can be attributed to the emission from the heating sources of houses, temperature inversion, stability of the atmosphere, and reduction of pollutant dilution.

According to Table 3, it can be seen that in the winter

Table 2. Risk parameters applied for ILTCR and HQ assessment

Parameter	Define	UNIT	Value
RFC	Reference concentrations	mg m^{-3}	Benzene=0.03 Toluene=5 Ethylbenzene=1 Xylene=0.1
C	Concentration	µg m^{-3}	Measured
IR	Inhalation rate	m^3 per day	20
AT	Averaging time	day	ED×365 y
CF	Conversion factors	mg per µg	10^{-3}
CSF	Cancer slope factor	$(mg\ per\ kg \times d)^{-1}$	0.029
ET	Exposure time	Hours per day	8.0
EF	Exposure frequency	Day per year	365
ED	Exposure duration	Year	70
BW	Body weight	kg	70

Reference:Maleki, Asadgol et al. 2022, Maleky and Faraji 2023

Table 3. Statistical descriptive of the BTEXs in air samples (μg m^{-3})

Parameters	Benzene	Toluene	Ethylbenzene	Xylene	BTEX
Summer (n:20)					
Min	5.56	8.33	4.17	8.33	30.56
Mean	8.89	33.33	5.90	30.07	78.19
Standard deviation	4.12	29.20	1.68	18.17	46.75
Max	20.83	113.89	12.50	86.11	215.28
Winter (n:20)					
Min	5.21	13.54	4.17	12.50	35.42
Mean	20.98	70.00	10.99	79.37	181.34
Standard deviation	8.10	26.10	4.20	35.47	69.73
Max	38.33	138.33	25.00	173.33	375.0
Overall					
Min	10.76	44.10	9.72	20.83	85.42
Mean	29.87	103.34	16.89	109.44	259.54
Standard deviation	9.40	34.72	4.28	41.11	81.05
Max	55	173.06	31.94	219.17	479.17
[1] p-value for two seasons	0.72	0.36	0.52	0.74	0.76

[1] p-value is significant at the 0.05 level

season, the average concentration of benzene, toluene, ethylbenzene, and xylene compounds, as well as total BTEX, were found to be 20.98 μg m^{-3}, 70 μg m^{-3}, 10.99 μg m^{-3}, 79.37 μg m^{-3}, and 181.34 μg m^{-3}, respectively. It can be seen that xylene was the highest amount and ethylbenzene the lowest. However, in the summer season, the average concentration of benzene, toluene, ethylbenzene, and xylene compounds, as well as total BTEX, were measured as 8.89 μg m^{-3}, 33.33 μg m^{-3}, 5.90 μg m^{-3}, 30.07 μg m^{-3}, and 78.19 μg m^{-3}, respectively. It can be seen that toluene had the highest amount, and ethylbenzene had the lowest amount, which could be related to the higher vapor pressure of toluene. The order of total concentration of BTEX compounds (μg m^{-3}) during the study period followed xylene (109.44) > toluene (103.34) > benzene (29.87) > ethylbenzene (16.89), which have been reported in the same way by studies in Tehran, Urmia, Yazd, and Tabriz [5,40,48,49].

3.2. Spatio-temporal Variation

The spatial distribution of average BTEX concentration in the summer and winter seasons is shown in Figure 2. The spatial distribution showed that the highest concentration of BTEX was detected during the winter season at sampling stations S2 and S6. The stations S2, S11, S14, and S17 exhibited the highest benzene concentrations among the BTEX compounds. Toluene displayed its highest levels at stations S2 and S6, while ethylbenzene recorded its peak concentrations at stations S2 and S17. The highest BTEX concentration was also identified for xylene at stations S2 and S9. The presence of medium-density fiberboard (MDF) workshops and furniture workshops, gas stations, high traffic, and heavy vehicle traffic in station 2 and the gas station, and high traffic in station 6 could be the reason for the maximum concentration of BTEX in these stations.

The spatial distribution showed that the highest concentration of BTEX was detected during the summer season at the sampling stations S16 and S18. The highest compound concentration was found at the S16 and S18 stations for benzene, stations of S2, S16, and S18 for toluene, stations of S16 and S18 for ethylbenzene, and station S18 for xylene. According to Figure 1 of Golbad, in the summer season, it can be noted that the direction

of the winds is from north to south. S16 station is located at the center of medical centers and has high traffic. There was a gas station and high traffic density near the S18 station. The concentration of BTEX decreased with increasing distance from emission sources, and according to the distribution maps, the level of BTEX compounds was higher in winter than in summer. This could be associated with a temperature inversion in the cold season, atmospheric stability, and pollutant accumulation.

3.3. Ozone formation potential

Through the computation of OFP, the impact of BTEXs on tropospheric ozone generation has been examined in this work. Figure 3 shows the OFP values seasonally in air samples from Kerman City. The ranking of average values of the OFP in winter and summer followed as xylene > toluene > ethylbenzene > benzene. Xylene exhibited the highest OFP values due to the maximum MIR coefficient and the highest concentration. In both studied seasons, benzene exhibited the lowest involvement in ozone formation, similar conclusions drawn from studies conducted in Saudi Arabia, Korea, and Iran[5, 23,50].

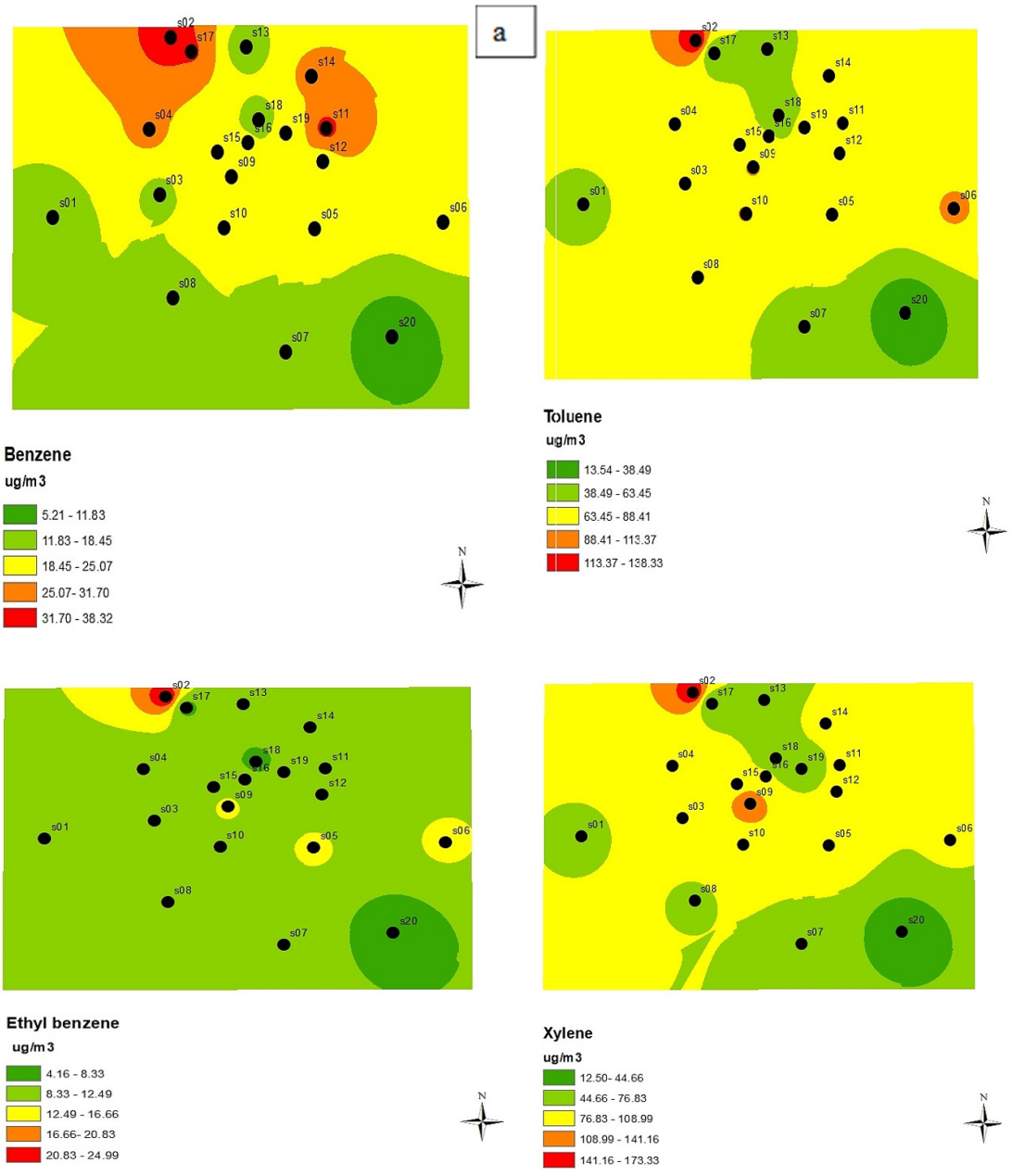

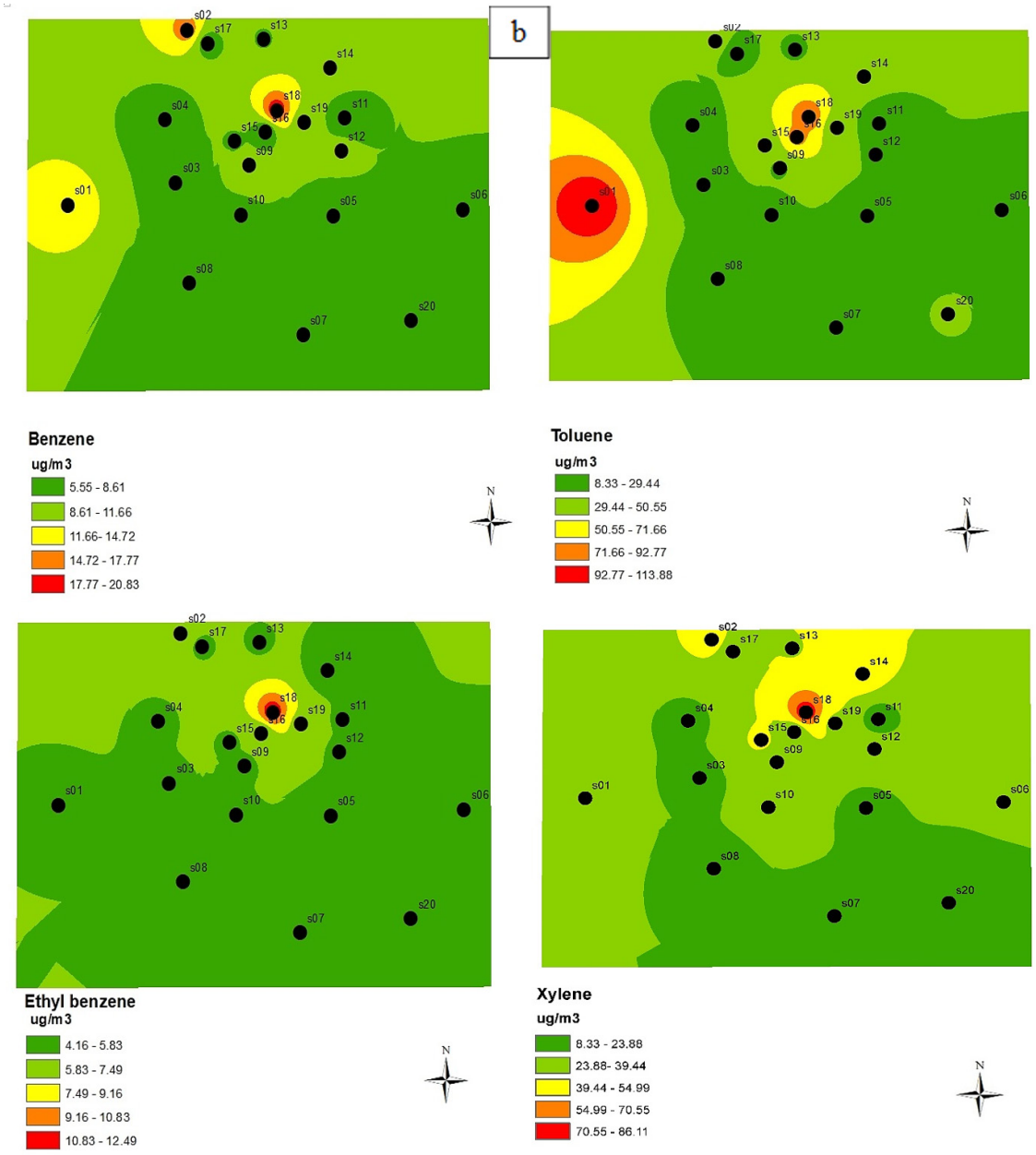

Fig. 2. Spatial changes in the concentration of BTEX compounds in winter (**a**) and summer (**b**)

3.4. Source identification

3.4.1.Specific ratios of VOCs

Researchers suggest using the proportions of BTEX compounds to identify the source of emissions and the photochemical behaviors of these substances in the surrounding atmosphere. Variations in the BTEX ratios due to different photochemical reactions offer valuable insights into the diverse characteristics of BTEX impacting various urban regions [5]. Many researchers analyzed BTEX based on nanotechnology in different matrixes, such as food and water samples[51-54]. Benzene and toluene, present in gasoline, can potentially be emitted into the atmosphere via vehicle exhaust emissions. A toluene/benzene ratio (T/B) in the range of 1.5-4.5 indicates traffic-related pollution emission sources, and a ratio higher than this range

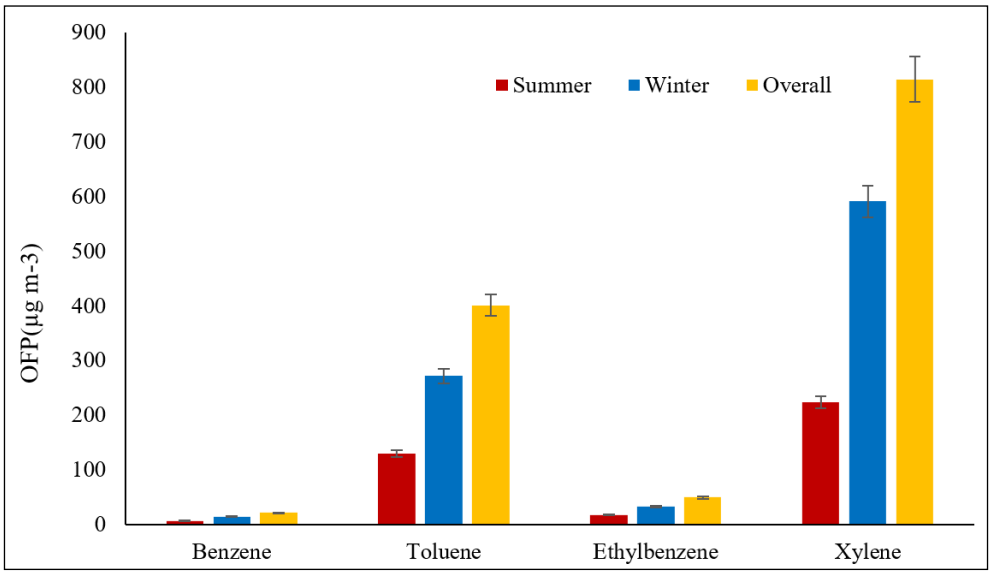

Fig. 3. OFP Values associated with the BTEXs in winter, summer, and overall

indicates that these pollutants mainly originated from sources other than vehicular traffic, such as fixed point sources (industries) [5,12]. In this study, the T/B ratio was 3.68 and 3.47 for summer and winter, respectively. Therefore, it can be concluded that the source of pollution was related to urban traffic and transportation, consistent with the results of the study in Ahvaz, Yazd, and Azerbaijan in Iran [1,5, 25]. The xylene/benzene (X/B) and xylene/ethylbenzene (X/E) ratios serve as metrics for estimating the tropospheric ozone formation potential (OFP). Increased X/B ratios typically signify emissions from a nearby source. In contrast, lower values suggest the air mass has undergone photochemical aging, indicating that the pollutant is already formed and exists within the environment. On average, the X/B ratio was 3.27 in summer and 3.89 in winter, and the X/E ratio was 5.03 in summer and 7.06 in winter.

3.4.2.Correlation analysis between the concentration of BTEX

The correlation between the concentration of benzene, toluene, ethylbenzene, and xylene compounds is shown in Figure 4. The sources of BTEX were determined by correlation analysis, which determines the correlation pattern between species. The Pearson correlation test was utilized to examine the correlation between each pair of BTEX compounds based on their normal distribution. As indicated in Figure 4, a statistically significant positive correlation existed between the concentrations of all BTEX compounds during both sampling periods (summer and winter). Benzene, primarily associated with urban traffic, can indicate the existence of BTEX compounds within urban regions. Also, the significant positive correlation between ethylbenzene and xylene suggests the possibility of their simultaneous emission from gasoline vehicles and gas stations. This strong positive correlation among BTEX compounds in the air has also been documented in other cities, including Yazd, Bandar Abbas, and Maragheh in Iran [1,5,12]. These results further emphasize the importance of transportation and traffic as sources of these pollutants.

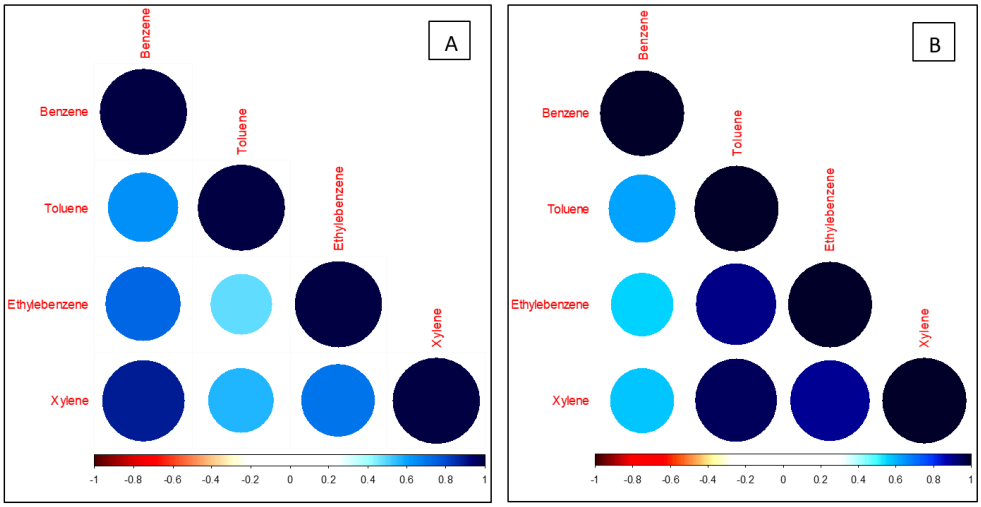

Fig. 4. Correlation coefficients (r) of BTEX compounds in summer (**A**) and winter (**B**)

3.4.3.Principal Component Analysis of BTEX

The outcomes of the PCA for various BTEX compounds can be found in Table 4. Two primary components, PC1 and PC2, were obtained during the analysis. In the summer season, two primary components were responsible for 90% of the overall variation among the variables. The initial principal component, denoted as PC1 and corresponding to factor 1, captures 76% of the overall variance and encompasses benzene, toluene, ethylbenzene, and xylene. During the winter season, two primary components were responsible for 96% of the overall variation among the variables. The primary principal component denoted as PC1 and corresponding to factor 1, captures 82% of the total variance. It comprises benzene, toluene, ethylbenzene, and xylene, similar to the winter season. According to the findings of PCA, the first component significantly contributes to the total variance. Consequently, it significantly impacts BTEX levels and effectively identifies vehicles as potential primary sources of BTEX emissions in the study area.

Table 4. Principal Component Analysis of BTEXs as well as regression factor scores

Variables	Factor 1	Factor 2
Summer		
Benzene	0.95	-0.07
Toluene	0.76	0.64
Ethylbenzene	0.85	-0.31
Xylene	0.92	-0.17
Initial eigenvalues	3.03	0.54
% of variance	76.0	14.0
Cumulative % of variance	76.0	90.0
Winter		
Benzene	0.74	0.68
Toluene	0.97	-0.12
Ethylbenzene	0.94	-0.21
Xylene	0.95	-0.19
Initial eigenvalues	3.28	0.55
% of variance	82.0	14.0
Cumulative % of variance	82.0	96.0

3.5. Health Risks

Human health can assess risks due to exposure to BTEX compounds. To assess the risk posed to human health by BTEX compounds, the components' non-carcinogenic risk, and benzene's cancer risk were evaluated using Monte Carlo simulation conducted within Crystal Ball software (version 11.1.2.4, Oracle, Inc, USA). Figure 5 compares the EC, CDI, and HQ index values for the studied BTEX compounds through inhalation exposure. According to Figure 5, the order of EC in the winter followed as xylene > toluene > benzene > ethylbenzene. In the summer, the order was as toluene > xylene > benzene > ethylbenzene, the same for CDI in both seasons. EC and CDI of total BTEX were higher in winter than it in summer. The HQ ranking for the investigated BTEX compounds was xylene > benzene > toluene > ethylbenzene in winter and summer, which is consistent with the results of the study in Zarand city in Iran [26]. In addition, the HQ of total BTEXs was higher in winter than summer.

The distribution of non-carcinogenic risk (HQ) and sensitivity analysis using Monte Carlo simulations due to exposure to environmental BTEXs in the summer and winter are shown in Figures 6 and 7, resoectively. According to Figures 6 and 7, with a probability of 95%, the average HQ in both seasons was less than one (HQ<1), which is at a safe level. Assessment of non-cancer risks indicated that exposure to BTEX compounds among Kerman residents during summer and winter does not adversely impact their health. This study's results were consistent with those of studies in Maragheh, Zarand, Tehran, Iran, and Brazil [1, 26, 43, 55]. According to the findings of the sensitivity analysis in Figures 6 and 7, during the summer season, the significant factors influencing the Hazard Quotient (HQ) were the exposure time (ET) for benzene and toluene, exposure duration (ED) for ethylbenzene, and exposure frequency (EF) for xylene. However, toluene, ethylbenzene, and xylene concentrations were identified as the most critical variables affecting the Hazard Quotient (HQ) during the winter. Figure 8 displays the distribution of ILTCR resulting from benzene inhalation during both summer and winter. This information was derived using Monte Carlo simulation techniques and sensitivity analysis. The average value of LTCR in the summer season was 7.55 x 10^{-5}, more than the level recommended by EPA (10^{-6}). Also, the value of ILTCR in winter was 1.76 x 10^{-4}, which is more than the level recommended by the EPA, which was similar to the results of the study of Urmia and Maragheh in Iran [1,49]. The most important variables for ILTCR in summer were CSF and, for winter, IR respiration rate. Although the amount of benzene in the samples was lower than xylene and toluene, the same amount that was measured showed that it exceeded the safe level and was dangerous.

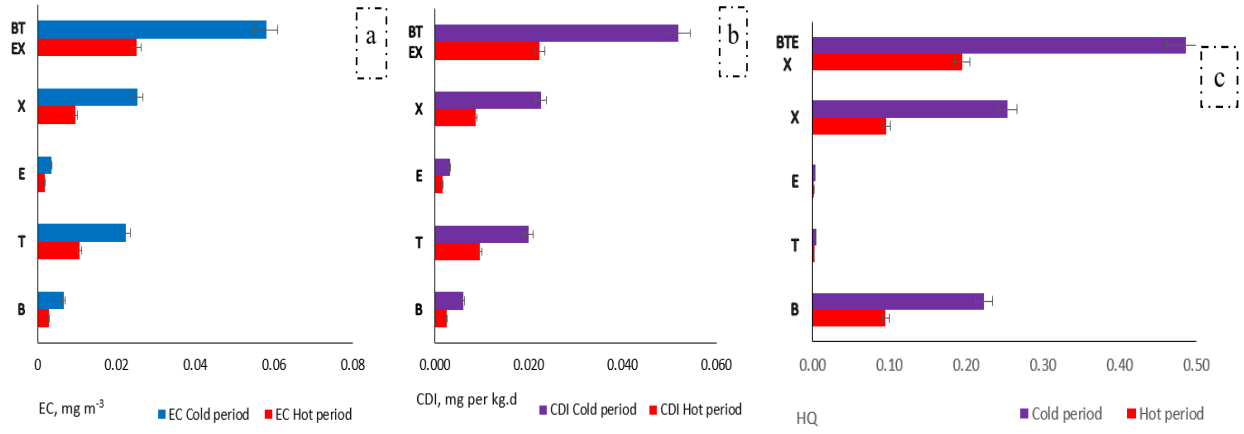

Fig. 5. Comparison of exposure concentration (EC) (**a**), chronic daily intake (CDI) (**b**) and hazard quotient (HQ) (**c**)

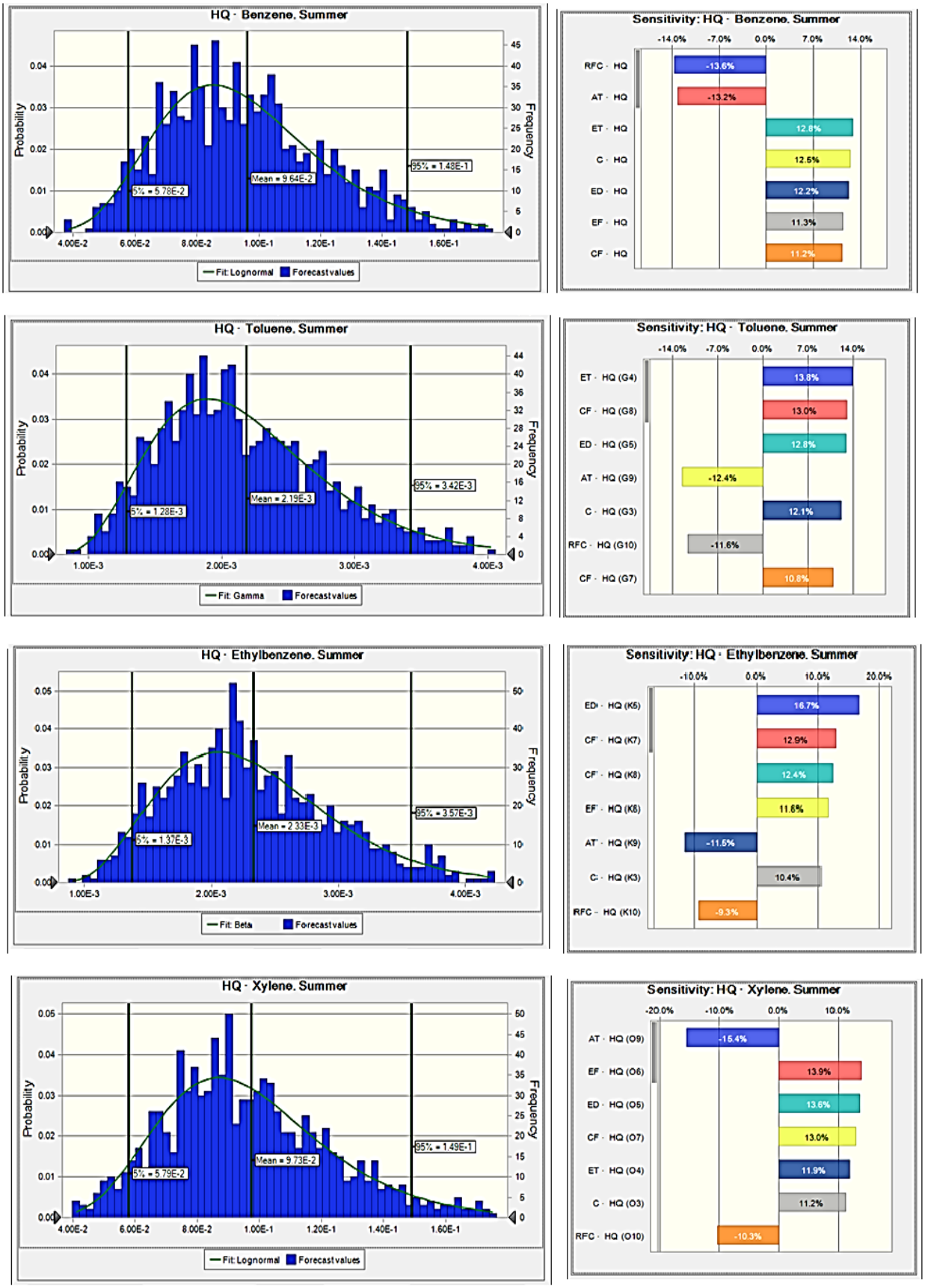

Fig. 6. Distribution of non-cancer risk due to exposure to environmental BTEXs during the summer period and their sensitivity analysis using the Monte Carlo simulation

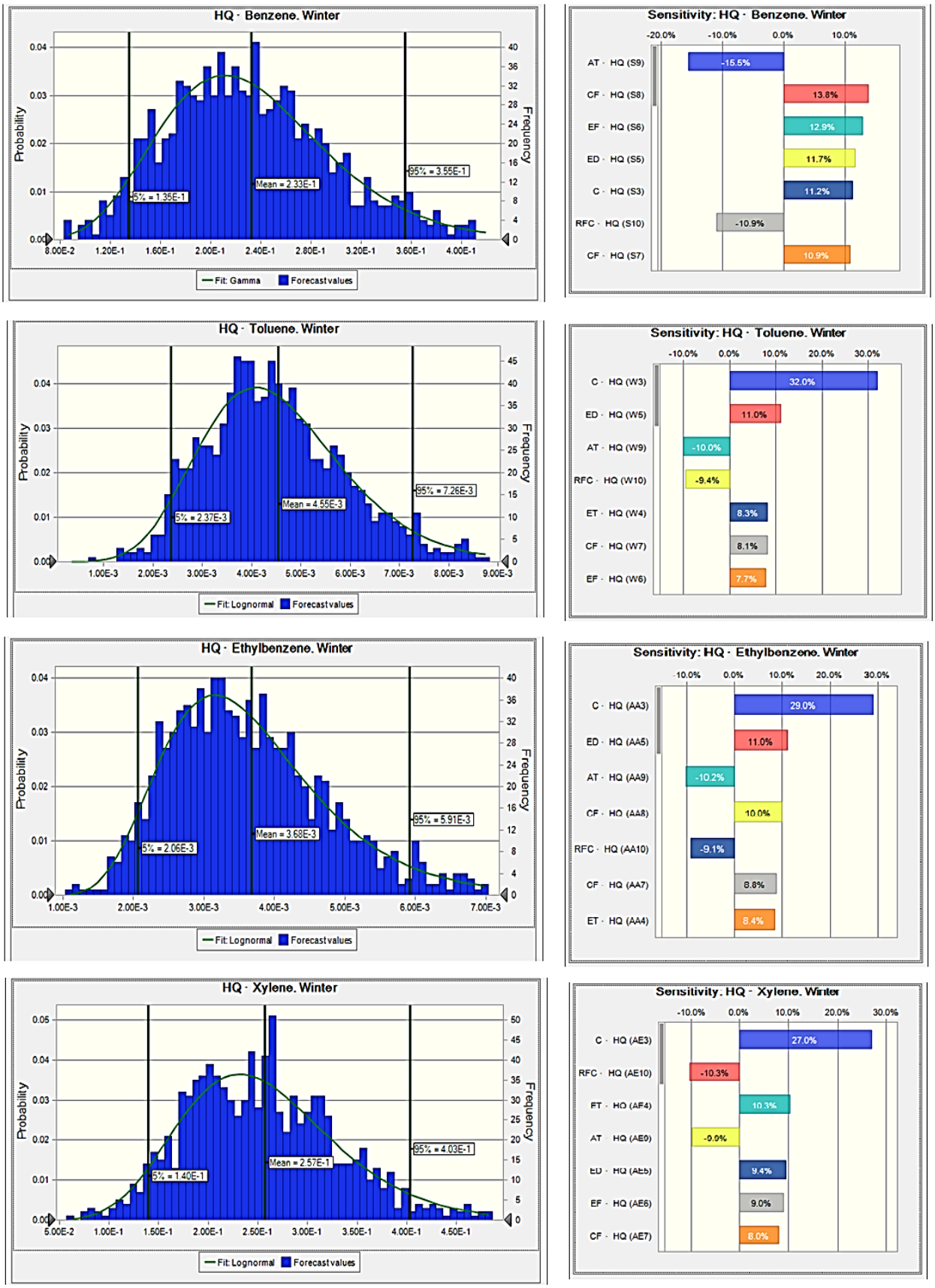

Fig. 7. Distribution of non-cancer risk due to exposure to environmental BTEXs in winter and their sensitivity analysis using Monte Carlo simulation

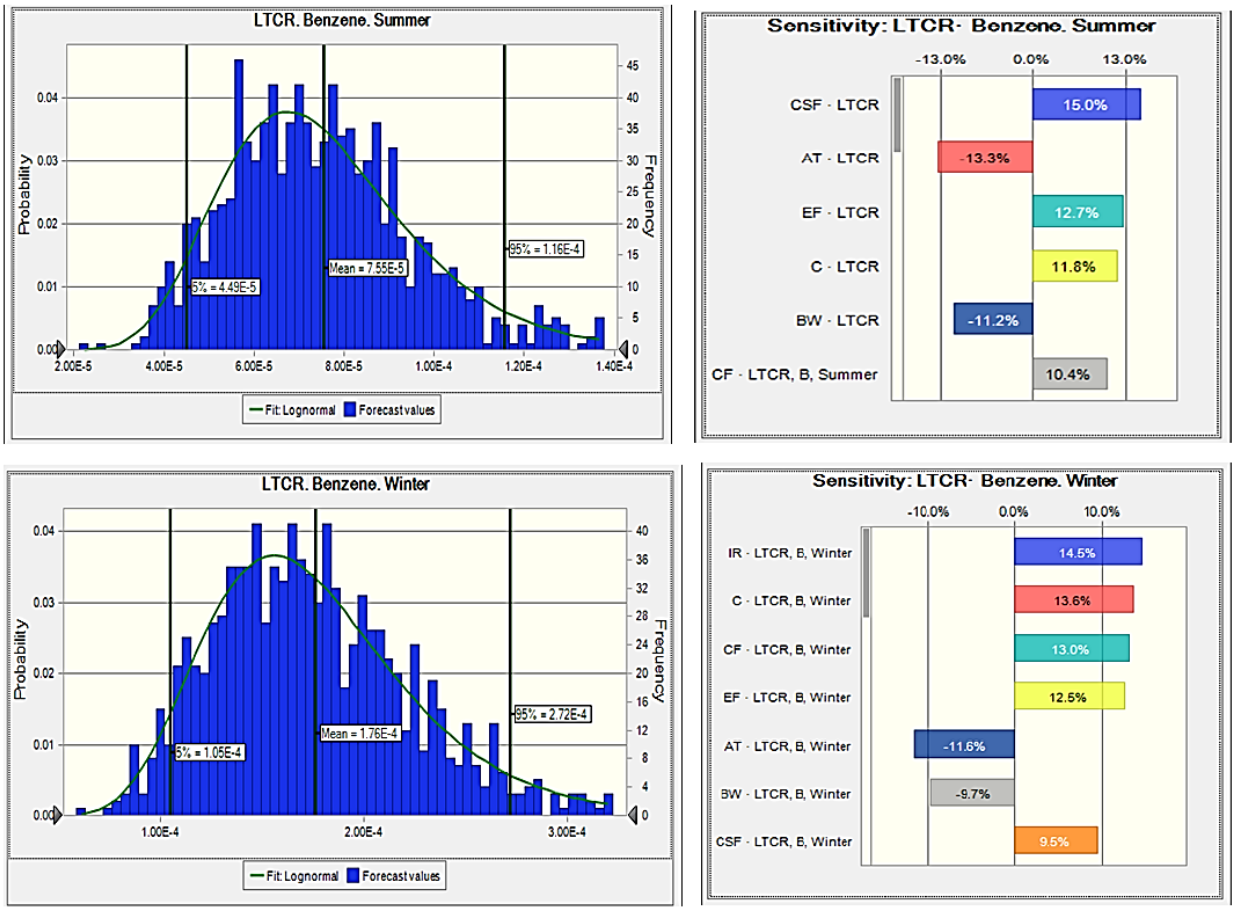

Fig. 8. Distribution of cancer risk due to benzene exposure during summer and winter periods and their sensitivity analysis using Monte Carlo simulation

4. Conclusion

This study was conducted to determine the concentration of BTEX compounds and the potential for ozone formation caused by these compounds and to evaluate the health risks of these pollutants (carcinogenic and non-carcinogenic) for the residents of Kerman City for the first time. The average total concentration of benzene, toluene, ethylbenzene, and xylene compounds was 29.87μg m^{-3}, 103.34 μg m^{-3}, 16.89 μg m^{-3}, and 109.44 μg m^{-3}, respectively. The order of the average total concentration of BTEX compounds during winter and summer is followed by xylene > toluene > benzene > ethylbenzene. The concentration of pollutants was higher in winter than in summer. The BTEX compounds showed no statistically significant differences between the summer and winter. The higher average concentration of BTEX in the winter can be related to the emissions from residential heating sources, temperature inversion, stability of the atmosphere, increase in the concentration of pollutants, and low mixing height. The T/B ratio in the summer and winter seasons was 3.68 and 3.47, respectively, in the range of 1.5 to 4.5. Therefore, it can be said that the source of pollution was related to urban traffic and transportation. According to the location analysis, the highest amount of pollutants was found in S2 and S6 stations in the winter and S16 and S18 stations in the summer. The average OFP values in winter are higher than in summer, and the average OFP values in both seasons are followed by xylene > toluene > ethylbenzene > benzene. The evaluation of non-cancer health risks related to exposure to BTEX compounds during both summer and winter indicated no adverse effects on the health of Kerman city residents because HQ was less than one (HQ<1) and at a safe level. The carcinogenicity of benzene

in the summer and winter seasons was more than the recommended limit by the EPA (>10^{-6}) and is dangerous.

5. Acknowledgments

The authors are grateful for Kerman University of Medical Sciences' financial support and also to Engineer Abdullah Bagheri, who helped calibrate the laboratory sampling pump. This work was part of the Master of Science thesis that was approved by the Vice-Chancellor for Research and Technology of Kerman University of Medical Sciences under the code of research ethics certificate IR.KMU.REC.1401.257. This research did not receive any grants from funding agencies in the public, commercial or non-profit sectors. The authors declare that this study has no any financial and non-financial competing interests. All authors contributed to the study's conception and design. Ahmad Zarei-Chargoud, Methodology, Data curation, writing-original draft, editing, data analysis, software; Ali Faghihi-Zarandi: Methodology, Providing equipment (sampling pump); Maryam Faraji: Methodology, Supervision, data analysis, reviewing and editing, software. All authors read and approved the final manuscript.

6. References

[1] A. Behnami, N. Jafari, K. Z. Benis, F. Fanaei, A. Abdolahnejad, Spatio-temporal variations, ozone and secondary organic aerosol formation potential, and health risk assessment of BTEX compounds in east of Azerbaijan Province, Iran, Urban Climate, 47 (2023) 101360. https://doi.org/10.1016/j.uclim.2022.101360

[2] R. Fouladi Fard, M. R. Hosseini, M. Faraji, A. Omidi Oskouei, Building characteristics and sick building syndrome among primary school students, Sri Lanka J. Child Health, 47 (2018) 332-337. https://doi.org/10.4038/sljch.v47i4.8595

[3] S. Dehhaghi, H. Hasankhani, A. Taheri, Spatiotemporal variations, photochemical characteristics, health risk assessment and mid pandemic changes of ambient BTEX in a west Asian metropolis, Stoch. Environ. Res. Risk Assess., 37 (2023) 4091–4107. https://doi.org/10.1007/s00477-023-02476-3

[4] M. Osanloo, O. Q. Dadras, Nobel method for toluene removal from air based on ionic liquid modified nanographene, Int. J. Occup. Hyg., 6 (2014) 1-5. https://ijoh.tums.ac.ir/index.php/ijoh/indexing

[5] Y. Hajizadeh, M. Mokhtari, M. Faraji, A. Abdolahnejad, A. Mohammadi, Biomonitoring of airborne metals using tree leaves: Protocol for biomonitor selection and spatial trend, Methods X, 6 (2019) 1694-1700. https:// doi.org/ 10.1016/ j.mex.2019.07.019

[6] J.G. Cerón Bretón, R.M. Cerón Bretón, S. Martínez Morales, J.D. Kahl, C. Guarnaccia, R.d.C. Lara Severino, M. Rangel Marrón, E. Ramírez Lara, M.d.l.L. Espinosa Fuentes, M.P. Uc Chi, Health risk assessment of the levels of BTEX in ambient air of one urban site located in Leon, Guanajuato, Mexico during two climatic seasons, Atmosphere, 11 (2020) 165. https://doi.org/10.3390/atmos11020165

[7] M. Słomińska, P. Konieczka, J. Namieśnik, The fate of BTEX compounds in ambient air, Crit. Rev. Environ. Sci. Technol., 44 (2014) 455-472. https://doi.org/10.1080/10643389.2012.728808

[8] F. Abbasi, H. Pasalari, J.M. Delgado-Saborit, A. Rafiee, A. Abbasi, M. Hoseini, Characterization and risk assessment of BTEX in ambient air of a Middle Eastern City, Process Saf. Environ. Prot., 139 (2020) 98-105. https://doi.org/10.1016/j.psep.2020.03.019

[9] J. Mehralipour, M.R. Samarghandi, R. Rahimpoor, Evaluation of exposure to BTEX in hookah smokers and carcinogenic and non-carcinogenic risk assessment, Iran. J. Health Safe. Environ., 5 (2018) 1128-1131. https://ijhse.ir/index.php/IJHSE/article/view/343

[10] M. Malakootian, S. Maleki, S. Rajabi, F. Hasanzadeh, A. Nasiri, A. Mohammdi, M. Faraji, Source identification, spatial distribution and ozone formation potential of benzene, toluene, ethylbenzene, and xylene (BTEX) emissions in Zarand, an industrial city of southeastern Iran, J. Air Pollut. Health, 7 (2022) 1-13. https://doi.org/10.18502/japh.v7i3.10537

[11] N. Fakkaew, S. Bualert, T. Thongyen, T. Rungratanaubon, Ozone formation potential of ambient volatile organic compounds at roadside in Bangkok, Thailand, Appl. Environ. Res., 43 (2021) 14-28. https://doi.org/10.35762/AER.2021.43.4.2

[12] H.R. Ghaffari, Z. Kamari, M.S. Hassanvand, M. Fazlzadeh, M. Heidari, Level of air BTEX in urban, rural and industrial regions of Bandar Abbas, Iran; indoor-outdoor relationships and probabilistic health risk assessment, Environ. Res., 200 (2021) 111745. https://doi.org/10.1016/j.envres.2021.111745

[13] Y. Hajizadeh, M. Mokhtari, M. Faraji, A. Mohammadi, S. Nemati, R. Ghanbari, A. Abdolahnejad, R.F. Fard, A. Nikoonahad, N. Jafari, Trends of BTEX in the central urban area of Iran: A preliminary study of photochemical ozone pollution and health risk assessment, Atmos. Pollut. Res., 9 (2018) 220-229. https://doi.org/10.1016/j.apr.2017.09.005

[14] N. Pinthong, S. Thepanondh, V. Kultan, J. Keawboonchu, Characteristics and impact of VOCs on ozone formation potential in a petrochemical industrial area, Thailand, Atmosphere, 13 (2022) 732. https://doi.org/10.3390/atmos13050732

[15] T. Masui, H. Imadzu, N. Matsuyama, N. Imanaka, Total oxidation of toluene on Pt/CeO_2–ZrO_2–Bi_2O_3/γ-Al_2O_3 catalysts prepared in the presence of polyvinyl pyrrolidone, J. Hazard. Mater., 176 (2010) 1106-1109. https://doi.org/10.1016/j.jhazmat.2009.11.108

[16] W.-W. Liu, L. Fang, X.-R. Guo, L. Nie, M.-Y. Wang, Emission characteristics and ozone formation potential of VOCs in printing enterprises in Beijing-Tianjin-Hebei, Environ. Sci., 40 (2019) 3942-3948. https://doi.org/10.13227/j.hjkx.201901043

[17] Y. Sahranavard, S. Zare, S. Kalantary, L. Omidi, M. Karami, Determining benzene, toluene, ethylbenzene and xylenes (BTEX) concentrations in the hydrometallurgical environment of sarcheshmeh copper complex, J. Occup. Hyg. Eng., 2 (2016) 9-13. https://doi.org/10.21859/johe-02042

[18] A.E. Ojimelukwe, M.O. Nafagha-Lawal, K.E. Lelei, A.O. Uche, E.P. Kika, S. Igbiri, B.B. Babatunde, F.D. Sikoki, Petroleum hydrocarbon pollution in the Niger Delta: human health risk assessment of BTEX in biota, J. Toxicol. Environ. Health Sci., 13 (2021) 65-72. https://doi.org/10.1007/s13530-020-00072-4

[19] A. Tabrizi, F. Golbabaei, M. Jafarizaveh, R. Yarahmadi, Evaluation of the adsorption capacity of nano-graphene and nano-graphene oxide for xylene removal from air and their comparison with the standard adsorbent of activated carbon to introduce the optimized one, J. Health Saf. Work, 6 (2016) 25-34. https://journals.tums.ac.ir/jhsw/article-1-5415-en.html

[20] M. Moridzadeh, S. Dehghani, A. Rafiee, M.S. Hassanvand, M. Dehghani, M. Hoseini, Assessing BTEX exposure among workers of the second largest natural gas reserve in the world: a biomonitoring approach, Environ. Sci. Pollut. Res., 27 (2020) 44519-44527. https://doi.org/10.1007/s11356-020-10379-x

[21] A.R. Moslem, H. Rezaei, S. Yektay, M. Miri, Comparing BTEX concentration related to surgical smoke in different operating rooms, Ecotoxicol. Environ. Saf., 203 (2020) 111027. https://doi.org/10.1016/j.ecoenv.2020.111027

[22] A. Keramati, R. Nabizadeh Nodehi, R. Rezaei Kalantary, S. Nazmara, A. Zahed, A. Azari, H. Bahramifar, A.H. Mahvi, TVOCs and BTEX concentrations in the air of south pars special

economic energy zone, J. Mazandaran Univ. Med. Sci., 25 (2016) 236-244. http://jmums.mazums.ac.ir/article-1-6988-en.html

[23] K. Na, K.-C. Moon, Y. P. Kim, Source contribution to aromatic VOC concentration and ozone formation potential in the atmosphere of Seoul, Atmos. Environ., 39 (2005) 5517-5524. https://doi.org/10.1016/j.atmosenv.2005.06.005

[24] A.N. Baghani, A. Sorooshian, M. Heydari, R. Sheikhi, S. Golbaz, Q. Ashournejad, M. Kermani, F. Golkhorshidi, A. Barkhordari, A.J. Jafari, A case study of BTEX characteristics and health effects by major point sources of pollution during winter in Iran, Environ. Pollut., 247 (2019) 607-617. https://doi.org/10.1016/j.envpol.2019.01.070

[25] M. Jafarizaveh, F. Golbabaei, A. Tabrizi, K. Azam, M. Ghasemkhani, Nobel method for xylene removal from the air on nano activated carbon adsorbent compared to NIOSH approved carbon adsorbent, J. Health Saf. Work, 6 (2016) 23-30. https://jhsw.tums.ac.ir/browse.php?a_id=5374&sid=1&slc_lang=en

[26] S. Maleky, M. Faraji, BTEX in ambient air of Zarand, the industrial city in southeast of Iran: concentration, spatio-temporal variation and health risk assessment, Bull. Environ. Contamin. Toxicol., 111 (2023) 25. https://doi.org/10.1007/s00128-023-03778-6

[27] M. Kermani, Z. Asadgol, M. Gholami, A.J. Jafari, A. Shahsavani, B. Goodarzi, H. Arfaeinia, Occurrence, spatial distribution, seasonal variations, potential sources, and inhalation-based health risk assessment of organic/inorganic pollutants in ambient air of Tehran, Environ. Geochem. Health, 43 (2021) 1983-2006. https://doi.org/10.1007/s10653-020-00779-w

[28] M. Dehghani, M. Fazlzadeh, A. Sorooshian, H.R. Tabatabaee, M. Miri, A.N. Baghani, M. Delikhoon, A.H. Mahvi, M. Rashidi, Characteristics and health effects of BTEX in a hot spot for urban pollution, Ecotoxicol. Environ. Saf., 155 (2018) 133-143. https://doi.org/10.1016/j.ecoenv.2018.02.065

[29] M. Caselli, G. de Gennaro, A. Marzocca, L. Trizio, M. Tutino, Assessment of the impact of the vehicular traffic on BTEX concentration in ring roads in urban areas of Bari (Italy), Chemosphere, 81 (2010) 306-311. https://doi.org/10.1016/j.chemosphere.2010.07.033

[30] R. Ashouri, N. Mansouri, Dynamic and static removal of benzene from air based on task-specific ionic liquid coated on MWCNTs by sorbent tube-headspace solid-phase extraction procedure, Int. J. Environ. Sci. Technol., 18 (2021) 2377-2390. https://doi.org/10.1007/s13762-020-02995-4

[31] R. Ashouri, S. A. Hajiseyed Mirzahosseini, N. Mansouri, Synthesis of Carbon Quantum Dots from Olive Stones for Efficient Adsorption of Benzene from the Ambient Air, J. Nanostruct., 11 (2021) 480-497. https://doi.org/10.22052/JNS.2021.03.007

[32] A. Faghihi-Zarandi, J. Rakhtshah, B. B. Yarahmadi, A rapid removal of xylene vapor from environmental air based on bismuth oxide coupled to heterogeneous graphene/graphene oxide by UV photo-catalectic degradation-adsorption procedure, J. Environ. Chem. Eng., 8 (2020) 104193. https://doi.org/10.1016/j.jece.2020.104193

[33] M. Mohammadi Asl, N. Mansouri, S. A. R. Haji Seyed Mirzahosseini, F. Atabi, Simultaneity comparative evaluation of toluene removal from the air by adsorption and UV semi-degradation-based adsorption procedure, Int. J. Environ. Sci. Technol., 21 (2024) 6677-6694. https://doi.org/10.1007/s13762-024-05503-0

[34] M. M. Asl, F. Atabi, Functionalized graphene oxide with bismuth and titanium oxide nanoparticles for efficiently removing formaldehyde from the air by photocatalytic degradation–adsorption process, J. Anal. Test., 7 (2023) 444-458. https://doi.org/10.1007/s41664-023-00272-0

[35] A. Faghihi-Zarandi, H. Shirkhanloo, C. Jamshidzadeh, A new method for removal of hazardous toluene vapor from air based on ionic liquid-phase adsorbent, Int. J. Environ. Sci. Technol., 16 (2019) 2797-2808. https://doi.org/10.1007/s13762-018-1975-5

[36] C. Jamshidzadeh, A new analytical method based on bismuth oxide-fullerene nanoparticles and photocatalytic oxidation technique for toluene removal from workplace air, Anal. Methods Environ. Chem. J., 2 (2019) 73-86. https://doi.org/10.24200/amecj.v2.i01.55

[37] M. B. H. Abadi, H. Shirkhanloo, J. Rakhtshah, Air pollution control: The evaluation of TerphApm@ MWCNTs as a novel heterogeneous sorbent for benzene removal from air by solid phase gas extraction, Arabian J. Chem., 13 (2020) 1741-1751. https://doi.org/10.1016/j.arabjc.2018.01.011

[38] Rakhtshah, H. Shirkhanloo, N. Esmaeil, A rapid extraction of toxic styrene from water and wastewater samples based on hydroxyethyl methylimidazolium tetrafluoroborate immobilized on MWCNTs by ultra-assisted dispersive cyclic conjugation-micro-solid phase extraction Author links open overlay panel, Microchem. J., 170 (2021) 106759. https://doi.org/10.1016/j.microc.2021.106759

[39] M. Arjomandi, H. Shirkhanloo, A review: analytical methods for heavy metals determination in environment and human samples, Anal. Methods Environ. Chem. J., 2 (2019) 97-126. https://doi.org/10.24200/amecj.v2.i03.73

[40] L. Tohid, Z. Sabeti, P. Sarbakhsh, K.Z. Benis, M. Shakerkhatibi, Y. Rasoulzadeh, R. Rahimian, S. Darvishali, Spatiotemporal variation, ozone formation potential and health risk assessment of ambient air VOCs in an industrialized city in Iran, Atmos. Pollut. Res., 10 (2019) 556-563. https://doi.org/10.1016/j.apr.2018.10.007

[41] US. EPA, Exposure factors handbook, 2011. https://www.epa.gov/expobox/exposure-factors-handbook-2011-edition

[42] F.A. Esteve-Turrillas, A. Pastor, M. de la Guardia, Assessing air quality inside vehicles and at filling stations by monitoring benzene, toluene, ethylbenzene and xylenes with the use of semipermeable devices, Anal. Chim. Acta, 593 (2007) 108-116. https://doi.org/10.1016/j.aca.2007.04.055

[43] R. Maleki, Z. Asadgol, M. Kermani, A. Jonidi Jafari, H. Arfaeinia, M. Gholami, Monitoring BTEX compounds and asbestos fibers in the ambient air of Tehran, Iran: Seasonal variations, spatial distribution, potential sources, and risk assessment, J. Environ. Anal. Chem., 102 (2022) 4220-4237. https://doi.org/10.1080/03067319.2020.1781836

[44] Y. Zhang, Y. Mu, J. Liu, A. Mellouki, Levels, sources and health risks of carbonyls and BTEX in the ambient air of Beijing, China, J. Environ. Sci., 24 (2012) 124-130. https://doi.org/10.1016/S1001-0742(11)60735-3

[45] L.H. Tecer, S. Tagil, Impact of urbanization on local air quality: differences in urban and rural areas of Balikesir, Turkey, Clean Soil Air Water, 42 (2014) 1489-1499. https://doi.org/10.1002/clen.201200640

[46] N. Bauri, P. Bauri, K. Kumar, V. Jain, Evaluation of seasonal variations in abundance of BTXE hydrocarbons and their ozone forming potential in ambient urban atmosphere of Dehradun (India), Air Qual. Atmos. Hlth., 9 (2016) 95-106. https://doi.org/10.1007/s11869-015-0313-z

[47] F. Borhani, M. Mirmohammadi, A. Aslemand, Experimental study of benzene, toluene, ethylbenzene and xylene (BTEX) concentrations in the air pollution of Tehran, Iran, J. Res. Environ. Health, 3 (2017) 105-115. https://jreh.mums.ac.ir/article_9457_en.html?lang=fa

[48] M. Asadi, M. Mirmohammadi, Experimental study of benzene, toluene, ethylbenzene, and xylene (BTEX) contributions in the air pollution of Tehran, Iran, Environ. Qual. Manag., 27 (2017) 83-93. https://doi.org/10.1002/tqem.21510

[49] A. Mohammadi, Y. Ghassoun, M.-O. Löwner, M. Behmanesh, M. Faraji, S. Nemati, A. Toolabi, A. Abdolahnejad, H. Panahi, H. Heydari, Spatial analysis and risk assessment of urban BTEX compounds in Urmia, Iran, Chemosphere, 246 (2020) 125769. https://doi.org/10.1016/j.chemosphere.2019.125769

[50] A. Alahabadi, I. Fazeli, M.H. Rakhshani, M.L. Najafi, H. Alidadi, M. Miri, Spatial distribution and health risk of exposure to BTEX in urban area: a comparison study of different land-use types and traffic volumes, Environ. Geochem. Health, 43 (2021) 2871–2885. https://doi.org/10.1007/s10653-020-00799-6

[51] S. Teimoori, A. H. Hassani, M. Panahi, N. Mansouri, An immobilization of aminopropyl trimethoxysilane-phenanthrene carbaldehyde on graphene oxide for toluene extraction and separation in water samples, Chemosphere, 316 (2023) 137800. https://doi.org/10.1016/j.chemosphere.2023.137800

[52] S. Teimoori, A. H. Hassani, M. Panahi, N. Mansouri, Rapid extraction of BTEX in water and milk samples based on functionalized MWCNTs by dispersive homogenized-micro-solid phase extraction, Food Chem., 421 (2023) 136229. https://doi.org/10.1016/j.foodchem.2023.136229

[53] S. Teimoori, A. H. Hassani, New extraction of toluene from water samples based on nano-carbon structure before determination by gas chromatography, Int. J. Environ. Sci. Technol., 20 (2023) 6589–6608. https://doi.org/10.1007/s13762-023-04906-9

[54] F. Golbabaei, A. Ebrahimi, A. Koohpaei, A. Faghihi-Zarandi, Single-Walled Carbon Nanotubes (SWCNTs), as a Novel Sorbent for Determination of Mercury in Air, Glob. J. Health Sci., 8 (2016) 273-280. https://doi.org/10.5539/gjhs.v8n7p273

[55] G. Dantas, I. Gorne, C.M. da Silva, G. Arbilla, Benzene, toluene, ethylbenzene and xylene (BTEX) concentrations in urban areas impacted by chemical and petrochemical industrial emissions, Bull. Environ. Contamin. Toxicol., 108 (2022) 204-211. https://doi.org/10.1007/s00128-021-03336-y